

**Synthesis, functionalization and characterization of  
zirconium - and hafnium based metal-organic  
frameworks and improved impact of modulators on  
water adsorption, catalytic and sensor applications**

**D I S S E R T A T I O N**

zur Erlangung des akademischen Grades

**Doctor rerum naturalium**

vorgelegt der

**Fakultät Mathematik und Naturwissenschaften**

**der Technischen Universität Dresden**

von

**M. Sc. Franziska Drache**

**geboren am 26.03.1987 in Radebeul**

**Eingereicht am .....**

**Die Dissertation wurde in der Zeit von 03 / 2013 bis  
09 / 2016 im Institut für Anorganische Chemie I angefertigt.**

Erstgutachter Prof. Dr. rer. nat. habil. Stefan Kaskel

Zweitgutachter Prof. Dr. rer. nat. habil. Eike Brunner

Tag der Verteidigung 26.04.2018



Wissenschaftler, 1988

Heinz Drache

Tempera

*This work is dedicated to my grandmother Regina E. I. Drache*



---

<b>1. MOTIVATION AND INTRODUCTION.....</b>	<b>8</b>
<b>2. STATE OF THE ART.....</b>	<b>11</b>
<b>2.1 Metal-organic frameworks.....</b>	<b>11</b>
2.1.1 General.....	11
2.1.2 Chemically stable MOFs.....	13
2.1.3 Functionalization routes of Zr based MOFs .....	20
2.1.4 Applications of Zr-based MOFs as catalysts.....	23
2.1.5 Applications of Zr-based MOFs as luminescence based sensors.....	26
<b>3. CHARACTERIZATION METHODS.....</b>	<b>31</b>
<b>3.1 Adsorption.....</b>	<b>31</b>
3.1.1 Definitions and terminology.....	31
3.1.2 Adsorption of gases .....	33
3.1.3 Determination of the specific surface area according to Brunnauer, Emmet and Teller .....	36
3.1.4 Determination of the total pore volume.....	38
3.1.5 Determination of the pore size distribution.....	38
3.1.6 Water vapour physisorption.....	40
<b>3.2 X-ray crystallography.....</b>	<b>42</b>
3.2.1 Fundamentals.....	42
3.2.2 Single crystal X-ray diffraction.....	47
3.2.3 Powder X-ray diffraction.....	50
<b>4. EXPERIMENTAL PART.....</b>	<b>57</b>
<b>4.1 Used chemicals.....</b>	<b>57</b>
<b>4.2. Instrumental Setup.....</b>	<b>58</b>
4.2.1 Physisorption measurements.....	58
4.2.2 Thermogravimetric- and differential thermal analysis.....	59
4.2.3 Elemental analysis.....	59
4.2.4 Nuclear magnetic resonance measurements.....	59

---

4.2.5 Contact angle measurements.....	59
4.2.6 Scanning electron microscopy.....	59
4.2.7 Gas chromatography coupled with mass spectroscopy.....	59
4.2.8 Luminescence measurements.....	60
4.2.9 Crystal structure simulation.....	61
4.2.10 X-ray diffraction.....	61
<b>4.3 Synthetic protocols.....</b>	<b>63</b>
4.3.1 Synthesis of metal-organic frameworks.....	63
4.3.2 Post-synthetic exchange of modulator molecules.....	65
4.3.3 Catalysis.....	65
<b>4.4 Crystallographic data.....</b>	<b>66</b>
<b>5. RESULTS AND DISCUSSION.....</b>	<b>69</b>
<b>5.1 Modulator driven polymorphism.....</b>	<b>70</b>
5.1.1 Synthesis and characterization of DUT-126.....	70
<b>5.2 Post-synthetic inner surface functionalization of DUT-67.....</b>	<b>78</b>
5.2.1 Synthesis and characterization of DUT-67 with various modulators.....	79
5.2.2 Post-synthetic inner surface functionalization of DUT-67 with hydrophobic fluorinated ligands.....	82
5.2.3 Post-synthetic inner surface functionalization of DUT-67 with chiral ligands.....	95
5.2.4 Post-synthetic inner surface functionalization of DUT-67 with fluorescein.....	99
<b>5.3 Post-synthetic treatment of DUT-67 with inorganic acids.....</b>	<b>101</b>
<b>5.4 Catalytic studies of DUT-67 in Meerwein-Pondorf-Verley reduction.....</b>	<b>109</b>
<b>5.5 DUT-122 and its application as sensor material.....</b>	<b>121</b>
5.5.1 Synthesis and characterization of DUT-122.....	122
5.5.2 Application as solvent vapour sensor.....	127
<b>6. CONCLUSIONS AND OUTLOOK .....</b>	<b>133</b>
<b>7. REFERENCES.....</b>	<b>137</b>

<b>8. LIST OF ABBREVIATIONS.....</b>	<b>153</b>
<b>9. APPENDIX.....</b>	<b>156</b>
<b>10. ACKNOWLEDGEMENT.....</b>	<b>164</b>
<b>11. LIST OF PUBLICATIONS.....</b>	<b>166</b>
<b>12. VERSICHERUNG UND ERKLÄRUNG.....</b>	<b>167</b>

## 1. MOTIVATION AND INTRODUCTION

Porous materials have been known and used for centuries by humans. Especially materials like clays and charcoals have a long history to look upon. Already in 1550 BC the Egyptians and Sumerians utilized charcoal to purify water and later, in 460 BC, Hippocrates reported the application of charcoal for medical therapies for various diseases as well.<sup>1</sup> During the industrial revolution in the 18<sup>th</sup> century wood charcoal was employed to purify and decolourize sugar products. In the time of World War I, adsorbent materials with high surface areas became essential for the use in respirators to protect people from poisonous gases. At the present time, porous materials are extensively used in industry as adsorbents as well as in smaller scale for special applications. The usage as filter to purify water and air is still an issue as well as the capture and decomposition of hazardous gases, such as volatile organic compounds<sup>2</sup> and nerve agents<sup>3-5</sup>. The selective adsorption of gases and other mixtures of substances is a serious alternative to e.g. distillation techniques which are usually energy consuming. Thereby, the separation processes are based either on size exclusion or on different polarities of the substrates, which interact differently with the adsorbent surface. Because porous materials provide high surface areas and good mass transport, they are extremely suitable as heterogenous catalyst or as catalyst support. Heterogenous catalysts have some prominent benefits compared to homogenous ones, since their separation from the reaction mixture and their recycling is much simpler.

In general, porous materials can be distinguished into four different classes. Besides the class of carbon based porous materials, which includes activated carbons, carbide derived carbons etc. and the class of inorganic porous materials, which includes metal oxides, aluminium phosphates - and silicates, the class of porous polymers and coordination polymers joined recently and aroused considerably greater interest since the 1990s. According to IUPAC, coordination polymers are defined as “compounds with repeating coordination entities extending in 1, 2, or 3 dimensions”, which “do not need to be crystalline”.<sup>6</sup> One subsection of the coordination polymers are coordination networks. Coordination networks differ from coordination polymers only in the point that the repeating coordination entities extending in one dimension are cross-linked in between, if they do not have repeating coordination entities in 2 or 3 dimensions. Then again, metal-organic frameworks (MOFs) are a subsection of coordination networks and are defined as “a coordination network with organic ligands containing potential voids”.<sup>6</sup> They are built up by inorganic metal-(oxo)-clusters, which are connecting organic linkers. This material class has the highest surface areas known so far and



stands out clearly from other materials on this matter. In addition, the sheer endless pool of framework components enables a purposive design of the resulting frameworks and makes the tuneability of pore sizes and topologies feasible. Also the possibility of framework functionalization opens new application fields, like storage of energy providing gases<sup>7-13</sup> such as hydrogen and methane, separation of gases<sup>13-25</sup> e.g. the selective separation of carbon dioxide from methane or enantioselective separations of substance mixtures, catalysis<sup>26-33</sup>, sensor technology<sup>34-39</sup> and even drug delivery<sup>40-46</sup> and medical diagnostics<sup>44-46</sup>. Recently, heat transformations applications through reversible water ad- and desorption are under discussion.<sup>47-52</sup> Despite the versatile application fields serious disadvantages makes them challenging for industrial scaled employment, such as high costs, complex linker synthesis, differing reproducibility, and most important factor the instability against moisture, which limits their application and commercial use. Therefore a lot of effort and progress is made to overcome these limiting factors. Normally the synthesis of MOFs is done in laboratory scale by solvothermal procedures, which often involves toxic solvents like dimethylformamide and high energy consumption. Therefore, environmentally friendly synthesis routes could be developed for some MOFs to avoid toxic and expensive solvents. Also the use of environmental friendly and sustainable reactants has been a focus, like in bio-MOF-1<sup>53</sup> and bio-MOF-100<sup>54</sup>, which use adenine as a biomolecular building block or in MOFs that are based on the lignocellulose derived 2,5-furandicarboxylic acid<sup>55-57</sup>. Even the use of water as reaction medium in the synthesis of some zirconium based MOFs like UiO-66 type MOFs, DUT-67 and MOF-808 has been reported to be feasible.<sup>58-60</sup> Thereby microwave irradiation was utilized to shorten the reaction times and to save energy. Also the scalability of the synthesis of UiO-66-NH<sub>2</sub> and Zr-fumarate with a continuous flow reactor could be shown. Another approach is aimed to abandon any solvents or at least to minimize their amount in the synthesis procedure. A solid phase reaction allows a fast synthesis of MIL-101(Cr) without the usage of solvents and the problematic additive hydrofluoric acid.<sup>61</sup> Mechanochemical continuous syntheses *via* extruders were demonstrated for various MOFs.<sup>62-63</sup> For instance, the production of ZIF-8 could be pushed by this approach to get space time yields of up to  $144 \times 10^3$  kg per m<sup>3</sup> per day<sup>63</sup>. Such progresses in the large-scale synthesis of MOFs make them attractive for commercial purposes. For some years, BASF is even producing MOFs in ton scale under the trade name “Basolite”.<sup>64</sup>

As mentioned above, some applications of MOFs are limited by their instability against water. Consequently, the focus in MOF research is on water stable MOFs, especially on zirconium and hafnium based MOFs. These MOFs are synthesised by the modulated approach<sup>65</sup>, where

monocarboxylic acids act as directing agent in the framework formation. In many cases, the resulting framework is formed of metal clusters with reduced connectivity, which can be utilized for various applications and functionalization approaches. Compared to functionalization approaches that comprises the pre- or post-synthetically functionalization of linkers, the functionalization of MOFs *via* the metal cluster is less complex and easier executed. Main obstacles of linker functionalization are that desired structures may not be formed if functionalized linkers are used in the synthesis or that the MOF may be vulnerable for a wanted post-synthetic functionalization. In addition, the syntheses of functionalized organic linkers are often time-consuming and expensive, whereas for the functionalization of the metal cluster commercially available monocarboxylic acids can be utilized.

In this thesis zirconium and hafnium based MOFs are investigated, wherein the focus lies on the role of modulators in the structure formation and the resulting properties, such as textural properties, framework stability against higher temperatures and moisture, hydrophobicity, and catalytic activity. Thereby, MOFs are investigated that are built up by the commercially available linker 2,5-thiophenedicarboxylate (tdc). With proper choice of the modulator a new structure, namely DUT-126 (DUT = Dresden University of Technology), could be presented in the course of this work, besides the already known polymorphs of DUT-67, DUT-68 and DUT-69. Further, DUT-67, which can be produced with good reproducibility in large-scale – and also in an alternative environmental friendly synthesis route, is chosen as a model structure to functionalize the framework by exchanging the modulator post-synthetically. The strategy of the post-synthetic modification approach is based on the selective introduction of functionalities into the framework, whereby surface properties are changed, amplifying the application fields. Therefore, a focal point of this work is the tuning of surface polarities and the framework stability against water removal, particularly in regard to potential application as adsorbent material for heat pumps or desiccants. Another focal point of this work is the application of DUT-67 as heterogenous catalyst in a catalytic transfer hydrogenation reaction, which plays a significant role in upgrading biomass-derived feedstocks to fuels and valuable chemicals<sup>66</sup>. Thereby, the impact of coordinated modulator molecules in the framework on the catalytic performance is carefully investigated. Furthermore, the UiO-67 analogue DUT-122, which contains the luminescent linker 9-fluorenone-2,7-dicarboxylate (fdc), is tested as sensor material to detect solvent vapours.

## 2. STATE OF THE ART

### 2.1 Metal-organic frameworks

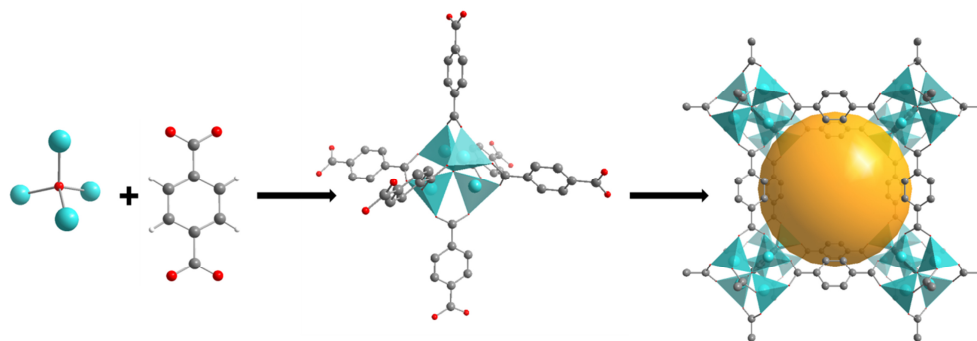
#### 2.1.1 General

According to the proposed terminology from IUPAC<sup>67</sup>, metal-organic frameworks are defined as inorganic coordination networks with organic ligands, wherein a coordination network consists of a coordination polymer which contains repeating coordination entities in two or more dimensions or only in one dimension but with cross-links in between. In contrast to coordination polymers, the existence of potential voids is obligatory in MOFs.

The formation of polymeric structures out of coordinative bonds between organic ligands and metal ions was already studied in the late 1950s and early 1960s.<sup>68-69</sup> These compounds were labelled then as “coordination polymers” or “chelate polymers” and were reviewed by several authors, like Berlin in 1960<sup>70</sup>, Rode in 1963<sup>71</sup> or Bailar Jr. in 1964<sup>72</sup>. But it took some decades until this field of research was further developed. Only in 1989 Hoskins and Robson<sup>73-74</sup> published a three-dimensional crystalline framework, built from tetrahedral coordinated Cu-centres and 4,4',4'',4'''-tetracyanotetraphenylmethane. In their work, they already pointed out the versatile potential application fields of these materials and proposed to expand it through linker functionalization. In 1995, the term “metal-organic framework” was introduced by Yaghi<sup>75</sup> and established for this class of materials since.

In general, MOFs are built from molecular building blocks, consisting of metal-(oxo)-clusters and multidendate organic ligands. These two basic modules form the secondary building unit SBU. Thereby, the metal clusters function as nodes and are linked through the organic ligands, which work as linkers or spacers. The connectivity of the metal cluster, the number of connecting functional entities of the linker, and their geometric constitution define the resulting framework topology. As ligands, usually multifunctional carboxylates, but also neutral N-heterocyclic ligands, are used. In case of the N-donor-ligands, negative charged counter-ions, which are usually provided by the metal salts used in synthesis, serve for charge balance. MOF-5 is counted as the prototype of MOFs and was reported by Li *et al.* in 1999<sup>76</sup>. The SBU of MOF-5 consists of a tetrahedral  $Zn_4O^{6+}$  cluster, which is edge-bridged by six 1,4-benzenedicarboxylates (BDC). Thereby, the  $Zn_4O^{6+}$  clusters are octahedrally coordinated by the BDC ligands, which form together the framework (Figure 1). MOF-5 crystallizes in a primitive cubic structure, whereas every  $Zn_4O^{6+}$  cluster represents the corner of the unit cell. After solvent removal, MOF-5 shows permanent porosity and has a specific surface area of

3800 m<sup>2</sup> g<sup>-1</sup> and a pore volume of 1.55 cm<sup>3</sup> g<sup>-1</sup>, derived by nitrogen adsorption measurements performed at 77 K.<sup>77</sup>



**Figure 1.** Formation of the metal-organic framework MOF-5 from Zn<sub>4</sub>O<sub>6</sub><sup>6+</sup> metal cluster and BDC linker molecules. Zinc polyhedra and atoms are illustrated in light blue, carbon atoms in grey, oxygen atoms in red and hydrogen atoms in white.

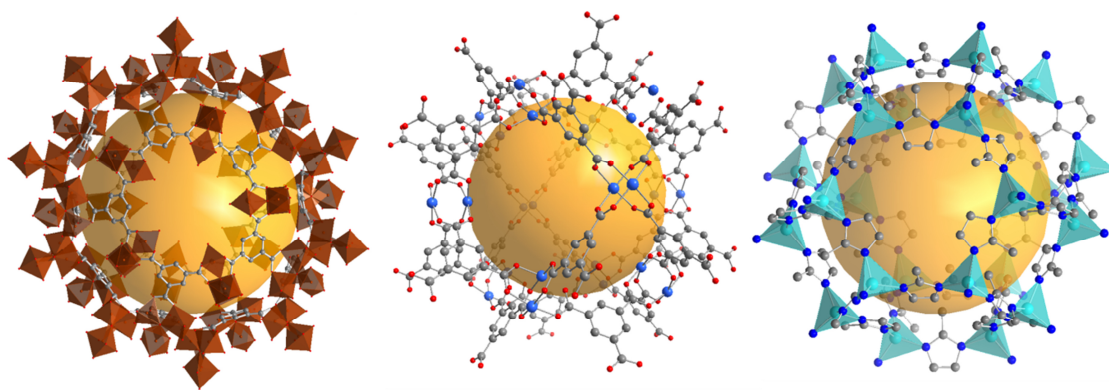
At the time of publication, this was an exceptionally high value, which surpasses surface areas of other microcrystalline materials like zeolites and carbons. Due to the modular concept of MOFs, higher surface areas can be generated by using longer linkers. If just the length of the linker is extended, the framework topology remains unchanged but the pore sizes increase. For example with the usage of linkers, which are extended each by one additional phenyl unit, the pore diameter can be varied from 18.5 Å (MOF-5, IRMOF-1) to 24.5 Å (IRMOF-14) and to 28.8 Å (IRMOF-16).<sup>78</sup> Yet, this concept, which is known as the isorecticular approach, is limited by network interpenetration. If pore sizes are approaching a size, allowing that metal-clusters have enough space to form a second network inside one, potential free voids are occupied and pore sizes decrease. There exist some strategies to avoid this phenomenon, like using alternative synthesis routes such as liquid phase epitaxy<sup>79</sup>, varying the solvothermal conditions<sup>80</sup> or using ligands, which feature spatial protecting groups<sup>81-82</sup>. Also some structures are not so prone to framework interpenetration, like paddlewheel connected networks<sup>83</sup> or IRMOF-74<sup>84</sup> (also known as CPO-27). IRMOF-74 is based on M<sub>3</sub>O<sub>3</sub>(CO<sub>2</sub>) (M = Mg, Zn) SBUs, forming metal oxide rods, which are arranged into an hexagonal framework. One-dimensional channels are generated, whose diameter can be adjusted from microporous 10 Å (IRMOF-74-I) to even mesoporous 85 Å (IRMOF-74-XI), wherein linker molecules are used that consist of minimum one and maximum 11 phenyl units. Though, interpenetration can also be used as a tool to enhance the stability of the network or to adjust pores to desired sizes. Thereby it enables to study new applications like separation and storage of small molecules. For example, an interpenetrated MOF-5 shows a significant higher uptake

for H<sub>2</sub> at 77 K up to 1 bar than a non-interpenetrated one.<sup>85</sup> Nevertheless, with the isoreticular approach, endless high surface areas cannot be generated. Schnobrich *et al.* calculated that there is a theoretical upper limit of 10.436 m<sup>2</sup> g<sup>-1</sup> if an infinite number of phenyl units are added to the MOF-5 structure.<sup>86</sup> Also frameworks that are built from paddle-wheel SBUs (HKUST-1 structure) and are based just on phenyl units do not give higher values (10.577 m<sup>2</sup> g<sup>-1</sup>, 9950 m<sup>2</sup> g<sup>-1</sup>).<sup>83, 86</sup> But if ethynyl moieties are applied, the theoretical maximum surface area could be increased up to 14.600 m<sup>2</sup> g<sup>-1</sup>.<sup>83</sup> This value is in good agreement to the work of Sarkisov, who estimated a theoretical upper limit to ~ 15.000 m<sup>2</sup> g<sup>-1</sup> for crystalline and disordered structures of porous materials.<sup>87</sup> So far, a series of MOFs was published, whose experimentally estimated surface areas are approaching these high values. MOFs, which exhibit surface areas > 5000 m<sup>2</sup> g<sup>-1</sup> are mostly based on Zn<sub>4</sub>O<sup>6+</sup>-cluster, like UMCM-2 (5200 m<sup>2</sup> g<sup>-1</sup>)<sup>88</sup>, MOF-210 (6240 m<sup>2</sup> g<sup>-1</sup>)<sup>89</sup> and DUT-32 (6411 m<sup>2</sup> g<sup>-1</sup>)<sup>89-90</sup>. But also Cu based paddle-wheel structures can achieve ultra-high surface areas, examples are DUT-49 (5476 m<sup>2</sup> g<sup>-1</sup>)<sup>91</sup>, DUT-76 (6344 m<sup>2</sup> g<sup>-1</sup>),<sup>92</sup> NU-109 (7010 m<sup>2</sup> g<sup>-1</sup>)<sup>83</sup> and NU-110 (7140 m<sup>2</sup> g<sup>-1</sup>)<sup>83</sup>. These high porosities open new application fields, like the storage of various gases such as hydrogen, carbon dioxide or methane. Yet, one of the main obstacles to employ these MOFs to industrially relevant applications is their low stability against moisture and protic solvents. Especially Zn<sub>4</sub>O<sup>6+</sup>-cluster based MOFs are prone to hydrolysis of the metal-ligand bonds. Therefore, a lot of research was devoted to strategies increasing the tolerance against water.

### 2.1.2 Chemical stable MOFs

The instability towards water arises from several factors and degradation mechanisms. If water molecules or other nucleophiles attack the metal cluster, ligands can be displaced or a hydrolysis reaction takes place.<sup>93</sup> In case of a hydrolysis reaction, water dissociates, forming a hydroxylated metal cation and a free protonated ligand. Thereby the metal-linker-bond is broken. In contrast, in the ligand displacement reaction, water is first inserted into the metal-linker bond and afterwards a hydrated metal cation and a free linker molecule is generated. When a critical number of linker molecules are removed, the framework becomes unstable and collapses. From a thermodynamic point of view, a high metal-ligand-bond strength is essential. Though, a kinetic factor must be also taken into account. A high activation energy barrier for ligand displacement/hydrolysis is a constraint for chemical stability. If the energy barrier is too low, even a strong metal-ligand-bond cannot ensure stability.<sup>94-95</sup> Yet, the activation barriers can be tuned by making it more difficult for water molecules to attack.

As mentioned, MOFs which are based on Zn-clusters and carboxylates linkers do not have a high bonding strength.  $\text{Zn}^{2+}$  prefers a tetrahedral coordination environment, since it has a  $d^{10}$ -electron configuration and is not affected by any ligand field stabilization energy. Thus, this  $\text{Zn}_4\text{O-SBU}$  is found in most of the MOFs, where only carboxylates function as linkers. These MOFs usually start to decompose after a short time of water exposure, even at low humidity levels.<sup>96-97</sup> This instability arises from very low activation energies for the ligand displacement hydrolysis reaction on this specific SBU that are one of the lowest found in MOFs.<sup>93</sup> Despite the tetrahedral SBU,  $\text{Zn}^{2+}$  can form also other coordination geometries, which tend to be more stable. One example is the MOF  $\text{Zn}_2(\text{bdc})_2(\text{dabco})$  which consists of a pillared paddle wheel structure. In this structure, the two metal atoms are bridged by four carboxylates, building 2D-nets. The two axial positions that are left are coordinated by the heterocyclic nitrogen of the dabco, connecting the nets into a 3D network. This framework is only stable under low relative humidity (RH) of 30%.<sup>98-99</sup> Alkyl chains that are incorporated into linker molecules are able to shield the metal cluster. Such an increase of the kinetic stability enables even several water adsorption-desorption cycles without crystallinity loss, up to a loading of  $p/p_0 = 0.9$ .<sup>100</sup> Another route to increased kinetic stability is framework interpenetration, which hinders ligand displacement by locking them inside the framework.<sup>101</sup> Since MOFs can be seen as Lewis acid-base coordination complexes, the basicity of the coordinating atom of the ligand plays also an important role. Thereby, higher  $\text{pK}_a$  values lead to higher bond-strengths.<sup>93</sup> Besides, also the concept of Pearson – the theory of the “hard and soft acids and bases” (HSAB) – helps to predict the thermodynamic stability of a given metal-ligand-bond. Low oxidation state metal ions, like  $\text{Zn}^{2+}$  or  $\text{Co}^{2+}$ , are softer metal ions and form stronger bonds to softer heterocyclic N-donor-ligands, such as imidazoles<sup>102-103</sup> or pyrazoles<sup>104-105</sup>. Zeolitic imidazolate frameworks (ZIFs), for example, show exceptional high chemical stability against acids, boiling water and in some cases even against 8 M aqueous sodium chloride solution.<sup>106-107</sup> The term ZIF is derived from their structure, which is topologically isomorph to zeolites. They consist mostly of Zn(II)- or Co(II) metal ions, which are bound to imidazoles. Thereby, the bridging angle between the metal ions and the imidazolate is similar to the Si-O-Si angle in zeolites, enabling the isomorph structure (Figure 2). Their improved hydrolytic stability originates not only from the fact that the coordination bonds formed to imidazoles are more hydrolytically stable than to carboxylates. They exhibit also a hydrophobic pore surface and in some cases alkyl side chains, which protect the metal cluster.



**Figure 2.** Selection of framework structures and pore environments of MIL-100(Fe) (left), HKUST-1 (middle) and ZIF-8 (right). Iron polyhedra and atoms are illustrated in brown, copper atoms are displayed in blue, zinc polyhedra and atoms are illustrated in light blue, carbon atoms in grey, oxygen atoms in red and nitrogen in dark blue.

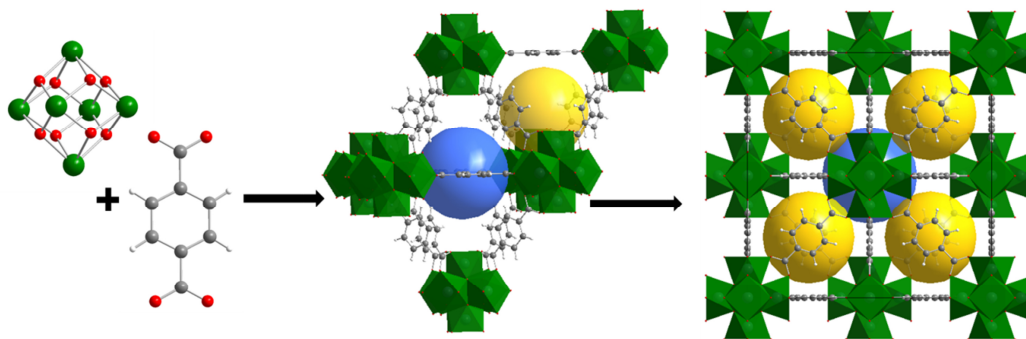
To reduce the lability of the metal-ligand bond in Zn(II)-carboxylate based SBUs,  $Zn^{2+}$  ions can be replaced by more stable ones, such as copper. These frameworks should be less prone to ligand replacement due to the fact that  $Cu^{2+}$  has a  $d^9$  electron configuration and features therefore some ligand field stabilization energy. One of these frameworks is HKUST-1<sup>108</sup>. Its SBU is based on paddlewheel structure, forming a 3D-network. Two  $Cu^{2+}$  ions are bridged by three 1,3,5-benzene-tricarboxylate (BTC) ligands and each of the axial positions are occupied by one water molecule (Figure 2). Thereby, these water molecules can be easily removed by a thermal treatment and/or under vacuum conditions, releasing free coordination sites, which can be used for various application purposes, such as catalysis. Nevertheless, HKUST-1 shows indeed an increased chemical stability, compared to  $Zn_4O$ -based frameworks, yet its stability is still low. It decomposes in pure liquid water and cannot be stored in air over a longer range of time.<sup>109</sup> After one water adsorption-desorption cycle, its porosity is already reduced to  $\sim 50\%$ .<sup>110</sup>

Metal ions, which have higher charge densities, such as  $Fe^{3+}$ ,  $Cr^{3+}$  or  $Al^{3+}$ , should also increase the metal-ligand-bond strength by increasing the electrostatic interaction. Unlike  $Zn^{2+}$ , these metal ions are hard acids, which form stronger coordination bonds to the hard carboxylate linkers. Another stabilization effect of these metal ions is their high coordination number. If some of the linker molecules in the framework are removed by hydrolysis, enough linkers are left to prevent a framework collapse. MIL-101(Cr)<sup>111</sup> for example consists of a trimeric SBU. This building block includes three Cr atoms, which share one  $\mu_3$ -O atom and are each octahedrally coordinated by four oxygen ions that originate from carboxylate ligands and by one hydroxide or by one fluoride anion, depending on the used synthesis route. Four of

these building blocks are linked by six BDC linkers and form a so called super-tetrahedron, creating microporous cavities. On the corners of the super-tetrahedra are also BDC linkers coordinated, building a 3D-network with two different mesoporous cages. MIL-101(Cr) reaches thereby high specific surface areas of  $>3000 \text{ m}^2 \text{ g}^{-1}$ . Also MIL-100(Fe)<sup>112</sup>, which has an isostructural SBU to MIL-101, but is linked by tridendate BTC linkers, has high surface areas of  $>1500 \text{ m}^2 \text{ g}^{-1}$  (Figure 2). Remarkably, both MOFs show high stability against liquid water, despite their hydrophilic pore surfaces.<sup>110</sup>

Also MOFs based on oxophilic M(IV) transition metal clusters ( $M = \text{Zr}, \text{Hf}, \text{Ti}$ ) and carboxylates as linkers enhance their chemical stability by increased bonding strength. Especially Zr-based frameworks are in the focus, since hafnium metal sources are more expensive and titanium based frameworks tend to be difficult to generate in direct synthesis. Up to now, two different Zr metal clusters geometries are known in MOF chemistry. In the MIL-140 series  $\text{ZrO}_2$ -chains are responsible for framework formation.<sup>113</sup> All other Zr-based SBUs are derived by the one of UiO-66. It consists of a  $\text{Zr}_6$ -octahedron, whose triangular faces are alternately capped by  $\mu_3\text{-O}$  and  $\mu_3\text{-OH}$  groups and whose edges are bridged by twelve carboxylate linkers. Thereby, every Zr atom is eight-fold coordinated by oxygen atoms, forming a square-antiprismatic coordination geometry. The resulting  $\text{Zr}_6(\mu_3\text{-O})_4(\mu_3\text{-OH})_4(\text{CO}_2)_{12}$  SBU leads to the dense fcc packing. Two kinds of pores originate from this structure. One octahedral shaped pore is located at the centre of the elementary cell and is surrounded by eight smaller tetrahedral shaped pores (Figure 3). The size of these pores can be increased by using 4,4'-biphenyldicarboxylate (UiO-67) or terphenyldicarboxylate (UiO-68) as linker, instead of 1,4-benzenedicarboxylate (UiO-66) (

Table 1).<sup>114</sup>



**Figure 3.**  $\text{Zr}_6(\mu_3\text{-O})_4(\mu_3\text{-OH})_4^{12+}$  cluster and  $\text{bdc}^{2-}$  (left) react to the framework UiO-66, which exhibits octahedral pores (blue sphere) and smaller tetrahedral pores (yellow spheres) and consists of fcc crystal structure (right) .

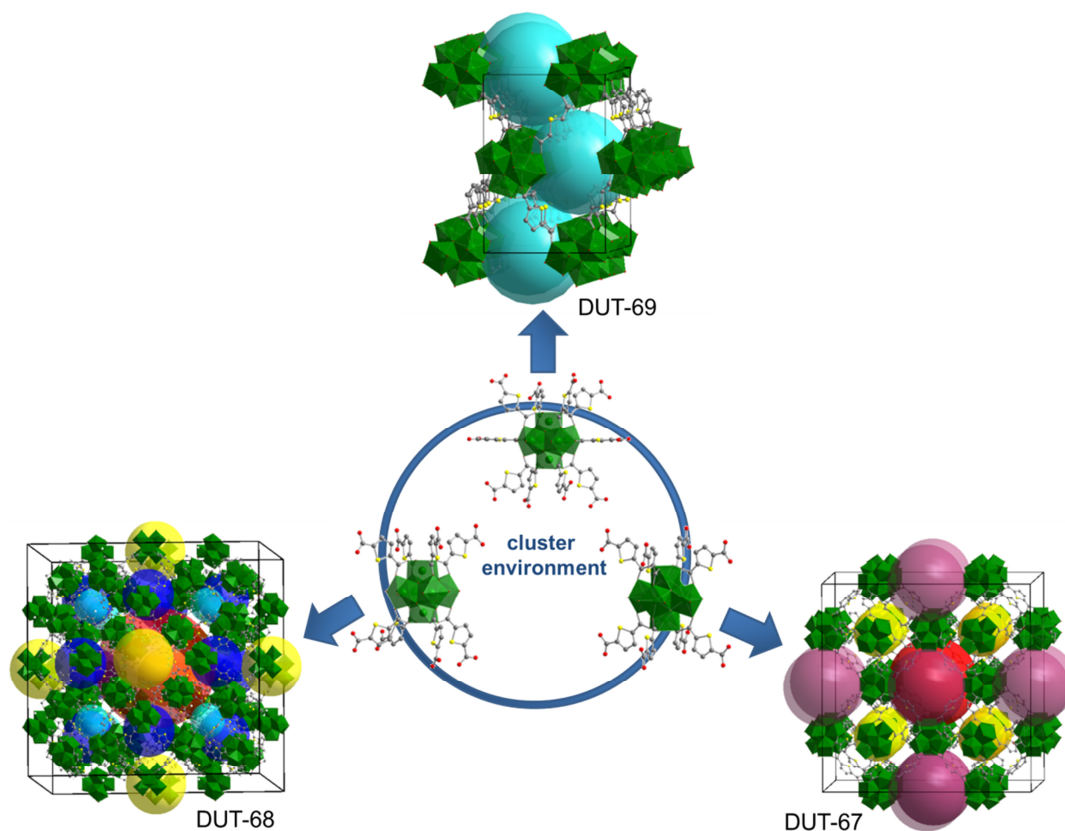


**Table 1.** Textural properties of UiO-66, UiO-67 and UiO-68-C=O derived by Poreblazer program<sup>115</sup>.

	UiO-66	UiO-67	UiO-68-C=O
Geometrical surface area, m <sup>2</sup> g <sup>-1</sup>	1656	3023	4055
Geometrical total pore volume, cm <sup>3</sup> g <sup>-1</sup>	0.577	1.057	1.714
Pore limiting diameter, Å	3.30	5.78	6.28
Maximum pore diameter, Å	8.57	12.25	17.35
Diameter of tetrahedral pore, Å	7.00	9.80	14.65
Diameter of octahedral pore, Å	8.10	12.02	16.67

The isoreticular approach cannot be applied here without any stability loss. UiO-66 is known to be stable in liquid water, in 0.1 M hydrochloric acid solution and also after thermal activation from water. On the contrary, MOFs that are based on this SBU and on biphenyldicarboxylate (bpdc) or 2,2'-bipyridine-5,5'-dicarboxylate (bipy) linkers are less stable. These MOFs, which are known under the name UiO-67 and UiO-67(bipy) or MOF-867, respectively, do not decompose in liquid water, but framework collapse appears after water desorption.<sup>116</sup> Remarkably, a solvent exchange from water to acetone preserves the porosity after thermal activation. Therefore, the instability does not primarily originate from potential hydrolysis instability of the Zr-cluster but from capillary forces, which are occurring during the evacuation process.<sup>117</sup> It is stated that the decreased stability of these isostructural MOFs arises from the higher torsional strain that the linker molecules operate on the metal cluster.<sup>116, 118-119</sup> It is also reported that these frameworks are more susceptible to an acid induced decomposition. For example, if such a MOF is brought into contact with hydrochloric acid, a Cl<sup>-</sup> anion displaces the carboxylate ligand and in the process, the ligand-metal-bond breaks. The ligand is now protonated and can leave the framework. In contrast, the Cl<sup>-</sup> anion coordinating on a Zr atom, leaves one coordination site on the metal-oxo-cluster unoccupied. Thus, such linker vacancies can be tuned by a post-synthetic treatment with acids. These free coordination sites are catalytically active and can be used for Lewis acid catalysed reactions. On the other hand, almost all of the Zr-based MOFs are instable in strong basic conditions. Thus, in contact with an aqueous NaOH solution, the metal-ligand-bond breaks and the OH<sup>-</sup> ions coordinate the metal cluster so that the framework decomposes successive into sodium carboxylates and probably transforming further into hydroxo zirconates under base conditions. So far, only NO<sub>2</sub>-functionalized UiO-66<sup>120</sup> preserves its crystallinity at pH 14 for a

short time of two hours and the porphyrinic PCN-225<sup>121</sup> was reported to retain crystallinity and porosity after exposure to aqueous solutions in a pH range of 1–11 for at least 12 hours. Zr- and Hf -based MOFs are synthesised by solvothermal synthesis. To increase their degree of crystallinity, modulating agents are added to the reaction mixture. These modulators consist of monocarboxylic acids. During the synthesis, these monocarboxylic acids coordinate to the metal cluster, forming the twelve connected SBU. Afterwards they are successively replaced by linker molecules, generating the framework. In some cases, not all of the modulators are exchanged. Thereby, the connectivity of the metal cluster can be reduced from twelve to ten, eight, or even six, expanding the number of possible framework structures that can be formed. Different factors, such as metal to linker ratio, amount, size, polarity and  $pK_a$  value of the modulator agent, are responsible for the resulting connectivity and structure. For instance, DUT-67, DUT-68 and DUT-69 all consist of the same linker (2,5-thiophenedicarboxylate;  $tdc^{2-}$ ) and the same modulator agent (acetic acid).<sup>122</sup> Just by varying the metal-linker-ratio and the amount of modulator, different SBUs are generated, leading to different networks (Figure 4).



**Figure 4.** The different cluster environments (inside the circle) lead to the respective crystal structures of DUT-67, DUT-68 and DUT-69 (outside the circle).

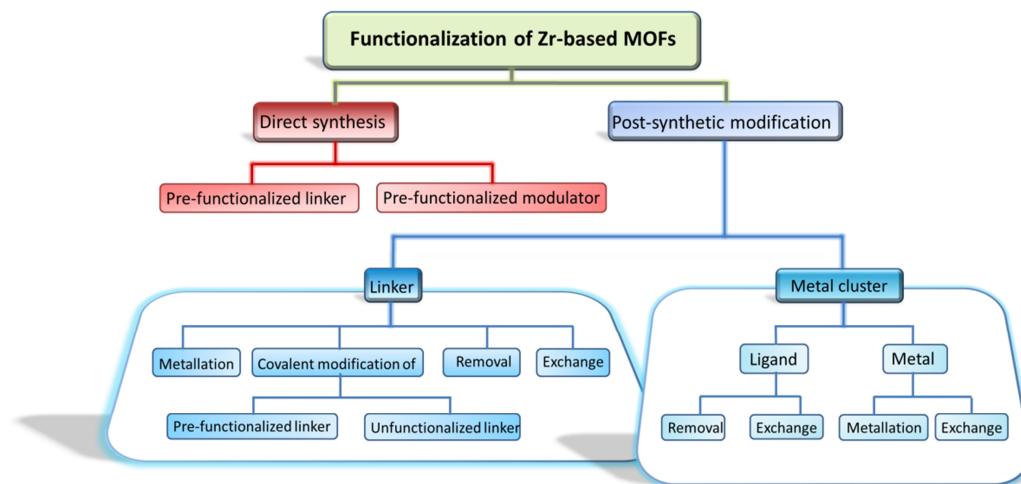
By using a metal-linker-ratio of 1:1 and 50 eq of acetic acid in the synthesis, a 10-connected SBU is formed. The resulting network, named DUT-69, has **bct** topology and crystallizes in an orthorhombic  $P2_12_12_1$  space group. It has open octahedral cages. These cages are interconnected and form channels, running along the  $c$ -axis. If the metal-linker-ratio is decreased to 1:0.66 and the amount of modulator is increased to 120 eq, the polymorphic DUT-67 is formed. Thereby the connectivity of the metal cluster is reduced to eight, forming a network with **reo** topology. The pores of this framework are shaped octahedral – and cuboctahedral. Moreover, DUT-67 has a cubic crystal system and an  $Fm\bar{3}m$  space group. The third polymorph DUT-68 is formed if the metal-linker ratio is increased to 1:1.5 and the amount of acetic acid is also increased to 180 eq. The resulting framework crystallizes in the cubic  $Im\bar{3}m$  space group. DUT-68 contains also an eight-connected metal cluster, but the linkers are differently oriented than in DUT-67. DUT-68 has even two independent SBUs, which differ from each other only in the orientation of two linker molecules. The resulting pore system contains octahedral, square-antiprismatic and cuboctahedral shaped pores as well as rhombicuboctahedral mesopores.

Remarkably, the twelve connected UiO-66 and its analogues can also show domains in crystals, where its connectivity is reduced. These defects can be generated and tuned by the choice of modulator and its amount. During the synthesis, not every monodentate modulator molecule is necessarily replaced by the bidentate linker. Therefore, linkers are missing and the defective positions are compensated either with the terminating modulator ligands and/or terminal OH-units and/or with water molecules.<sup>123-133</sup> Also, whole metal clusters can be missing.<sup>134-137</sup> In this case, the connectivity of the remaining nearby clusters is reduced to eight. Such defects exist in nanoregions, where then the network topology changes from **fcu** to **reo**. By increasing the amount of the modulator and by using a modulator with a low  $pK_a$  value, the defect concentration can be increased. This creates extra cavities, which consequently leads to higher pore volumes. Additionally, the reduced connectivity provides free coordination sites on the metal cluster, which can be utilised for catalysis<sup>127</sup>, enhanced adsorption processes<sup>128-132, 134</sup> or functionalization purposes<sup>138</sup>.

Furthermore, with the modulated synthesis approach, the crystal size can be controlled. With a raised amount of modulator agent, the size of the crystals is increasing. This aspect becomes relevant if the MOF is intended for applications where the size of the crystals plays a role, for example diffusion influenced applications, packing of columns or creating thin films.

### 2.1.3 Functionalization routes in Zr based MOFs

Functional groups can be introduced into frameworks either *via* direct synthesis or *via* post-synthetic modifications (PSM) (Figure 5).



**Figure 5.** Overview of different functionalization approaches for zirconium based MOFs.

In the direct synthesis linkers or modulators are used where the functional moieties are already included. With this strategy not every framework can be obtained, due to various possible reasons. For example, poor solubility of the linker or its poor chemical or thermal stability, as well as steric hindrance or coordinating capabilities of the functional groups can be the cause for restricted formation of the desired MOF. Nevertheless, some functional group containing MOFs are accessible by direct solvothermal synthesis. A few examples, which are based on UiO-66, UiO-67 or UiO-68 are listed in Table 2.

**Table 2.** Selection of Zr based MOFs with functional moieties which are accessible via direct synthesis.

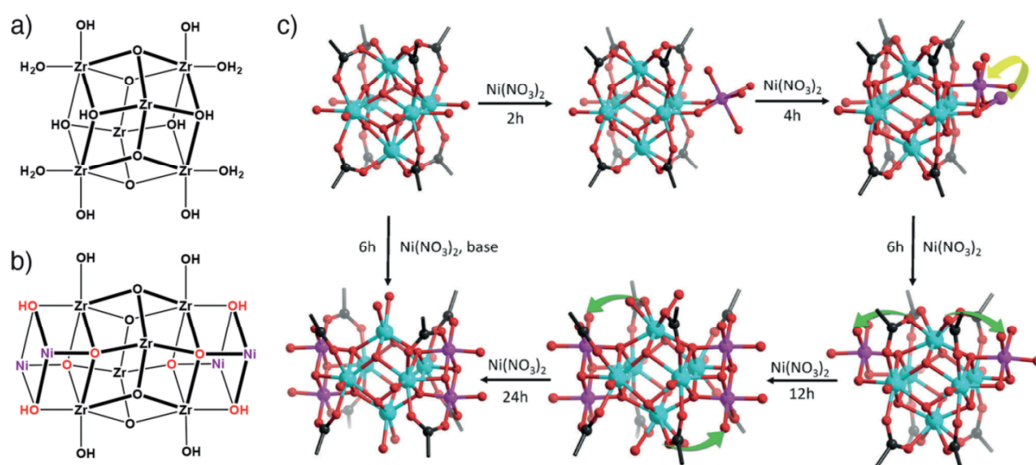
entry	linker	MOF	reference
1	2-amino-1,4-benzenedicarboxylate	UiO-66-NH <sub>2</sub>	120, 139
2	2-bromo-1,4-benzendicarboxylate	UiO-66-Br	120
3	2-nitro-1,4-benzendicarboxylate	UiO-66-NO <sub>2</sub>	120
4	1,4-dicarboxybenzene-2,5-dithiol	UiO-66-(SH) <sub>2</sub>	140
5	1,2,4-benzenetricarboxylate	UiO-66-CO <sub>2</sub> H	141
6	1,2,4,5-benzenetetracarboxylate	UiO-66-(CO <sub>2</sub> H) <sub>2</sub>	141
7	2-azidobiphenyl-4,4'-dicarboxylate	UiO-67-N <sub>3</sub>	142
8	2',5'-dihydroxy-p-terphenyl-4,4''-dicarboxylate	UiO-68-(OH) <sub>2</sub>	143

Such functional group tagged MOFs can be used to integrate a broader range of functional moieties. For example, the amine group in UiO-66-NH<sub>2</sub> reacts with amino acids or acid anhydrides to an amide-functionalized MOF. In this way, chiral information can be easily introduced into the network.<sup>144</sup> UiO-66-NH<sub>2</sub> can also be modified by condensation reactions with aldehydes to form alkylamine moieties or by a treatment with Cl<sub>2</sub> gas to form UiO-66-NH<sub>2</sub>-Cl. UiO-66-Br, on the contrary, can undergo a cyanation with CuCN to form UiO-66-CN, which is not so easily obtained by direct synthesis. Since Zr based MOFs are relatively chemically stable, harsher conditions for the PSM can be employed. For instance, even an aqueous 30% H<sub>2</sub>O<sub>2</sub> solution can be used to oxidize UiO-66-(SH)<sub>2</sub>.<sup>145</sup> With this procedure, sulfonic acid groups can be incorporated into the network without significant crystallinity loss. Also hydroxyl radicals, generated from aqueous H<sub>2</sub>O<sub>2</sub> solutions, can be utilized to modify the non-functionalized linker in UiO-66 post-synthetically. With this synthesis method UiO-66-OH can be obtained under preservation of crystallinity. In addition, hydroxyl-, carboxyl- or thiol units as well as heterocyclic atoms in linkers can provide metal chelation sites. An appropriate candidate for post-synthetic metallation is UiO-67(bipy), where transition metals can be inserted. So far, various metal salts or metal complexes are reported to be suitable for this purpose, for example CuCl<sub>2</sub><sup>146</sup>, CoCl<sub>2</sub><sup>146</sup>, Cr(CO)<sub>6</sub><sup>146</sup>, FeBr<sub>2</sub><sup>146</sup>, Re(CO)<sub>5</sub>Cl<sup>147</sup>, IrCl<sub>3</sub>·H<sub>2</sub>O<sup>147</sup>, Mn(CO)<sub>5</sub>Br<sup>148</sup>, and many more<sup>148-149</sup>. Consequently, such metalated MOFs are predestinated materials for heterogeneous catalysis.

Another way to introduce functionalized linkers into the network is a solvent assisted linker exchange (SALE)<sup>150-154</sup>. This method is performed under mild conditions and under moderate temperatures. Thereby, the parent MOF is exposed to a solution of functionalized ligands, which are then incorporated into the framework under simultaneous release of the original linker molecules. With SALE, a broad range of functional group containing MOFs can be provided, which are not accessible *via* direct synthesis. Furthermore, the metal cluster environment can also be modified. Modulator molecules can be hydrolytically removed from the metal cluster by a treatment with diluted solutions of inorganic acids.<sup>126</sup> In case of treatment with HCl, it is stated that terminating OH-units and water molecules are then coordinated on the metal cluster.<sup>138</sup> Afterwards non-bridging ligands, such as carboxylates<sup>126, 138, 155</sup>, phosphonates<sup>138</sup> or sulphonates<sup>156</sup>, can be coordinated to the metal cluster by the so called “solvent assisted ligand incorporation” (SALI) approach, without affecting the metal core.<sup>138, 157-158</sup> In this method, the MOF is soaked into a solution of the desired ligand. The incorporation rate depends thereby on the used solvent, the temperature, the pK<sub>a</sub> value of the ligands, as well as on diffusion and steric factors. An example of this method is the

functionalization of NU-1000 with perfluorinated aliphatic carboxylates. NU-100 is not stable if activated directly from water. Due to the functionalization, the water stability could be slightly enhanced.<sup>155</sup> Another example is the incorporation of oxalic acid in defective UiO-66, where the vacant positions are used. After the functionalization, this material shows one of the highest adsorption capacities for SO<sub>2</sub> and NO<sub>2</sub> for MOFs at room temperature and pressures < 0.1 bar.<sup>158</sup>

Furthermore, a post-synthetic exchange of the metal species itself is possible.<sup>150</sup> For example, parts of the Zr ions can be replaced with Ti(IV) up to a loading of ~ 50%.<sup>159</sup> Because of the reduced molecular weight of the heterometallic MOF, the specific surface area can be significantly increased. Furthermore, such a transmetalation generates smaller pores due to smaller ionic radius of Ti. In case of UiO-66, the tetrahedral cages remain unchanged, but the pore width of the octahedral cages decreases about ~ 1 Å. For this reason, the adsorption enthalpy can be increased and therefore also the CO<sub>2</sub> uptake enhances by 81% (T = 273 K, p = 120 bar).<sup>159</sup> In addition, bimetallic UiO-66(Zr/Ti) is also an excellent catalyst for a photocatalytic CO<sub>2</sub> reduction.<sup>160</sup> Moreover, a post-synthetic metallation of the Zr-cluster is feasible. Different metal species can be grafted onto the metal cluster of the MOF. Thereby, the μ<sub>3</sub>-OHs, as well as terminal OH-units are utilized. For example, the μ<sub>3</sub>-OH groups of the Zr-cluster in UiO-67 react with a solution containing [AuMe(PMe<sub>3</sub>)] under a simultaneous release of methane. The eight connected PCN-700, on the other hand, is qualified to incorporate Ni(II) or Co(II) under solvothermal conditions. In this case, M(NO<sub>3</sub>)<sub>2</sub> (M = Co, Ni) salts are brought into reaction with terminal water – and OH-units of the Zr-cluster.



**Figure 6.** a) The eight connected Zr<sub>6</sub>(μ<sub>3</sub>-O)<sub>4</sub>(μ<sub>3</sub>-OH)<sub>4</sub>(OH)<sub>4</sub>(H<sub>2</sub>O)<sub>4</sub> cluster of PCN-700. b) The formed bimetallic [Zr<sub>6</sub>Ni<sub>4</sub>O<sub>8</sub>(μ<sub>3</sub>-OH)<sub>4</sub>(OH)<sub>4</sub>(H<sub>2</sub>O)<sub>8</sub>] cluster (terminal water ligands are omitted for clarity reasons). c) Incorporation and migration mechanism of Ni ions for the PCN-700 cluster.<sup>161</sup> Reprinted with permission from Yuan, S.; Chen, Y.-P.; Qin, J.; Lu, W.; Wang, X.; Zhang, Q.; Bosch, M.; Liu, T.-F.; Lian, X.; Zhou, H.-C., Cooperative Cluster Metalation and Ligand Migration in Zirconium Metal–Organic Frameworks. *Angewandte Chemie International Edition* 2015, 54 (49), 14696-14700. Copyright 2015 Wiley-VCH.

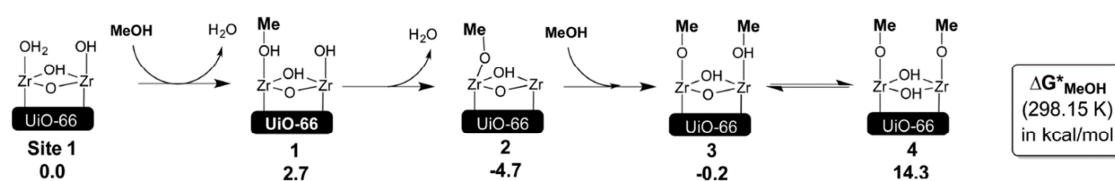
In the end four M(II) species per Zr-cluster are coordinated to the  $\mu_3$ -OH groups of the Zr-cluster, wherein linker migration is observed from Zr to the M(II) species during the reaction, so that every linker is coordinated to both metal species (Figure 6).<sup>161</sup> Another way to attach metal complexes on the Zr-cluster is gas phase metallation. The terminal OH-units of NU-1000, for example, can react within minutes with  $\text{Al}(\text{Me})_3$  or  $\text{Zn}(\text{Et})_2$  via atomic layer deposition, whereas Zn atoms can be post-synthetically exchanged with Cu, Co or Ni.<sup>162-164</sup>

#### 2.1.4 Applications of Zr-based MOFs as catalysts

Already in the beginning of MOF research, its application as heterogenous catalyst was in the focus. As porous material it ensures adequate mass transport and good accessibility for substrates. In contrast to zeolites that have usually small pore windows, the pores of MOFs can be tuned by the modular building concept and therefore adjusted for particular problems. The catalytic activity of MOFs can be achieved by different strategies. Catalysed reactions can be catalysed either by the metal cluster itself<sup>26</sup> or by other metal species incorporated in the network. For example, catalytic active nanoparticles, such as noble metal nanoparticles or metal oxide nanoparticles, can be encapsulated into MOF particles.<sup>165-166</sup> MOFs provide enough porosity for this purpose and can disperse the catalytic agent on its surface. Also the functional sites of linkers can be utilised. As mentioned in the previous chapter, organic moieties can be metallated. For example UiO-67, containing 2-phenylpyridyl- or bipyridyl ligands, was metallated with transition metal complexes. These functionalized UiO-67 analogues showed catalytic activity in various organic reactions, like C-H borylation of arenes, water -and sulfide oxidation, amine coupling, aza-Henry-reactions and  $\text{CO}_2$  reduction.<sup>147</sup> Also Zr-PCN-221(Fe), which has the iron coordinated to the porphyrine linkers, exhibit additional active centres due to metallation. The selective oxidation of cyclohexane with *tert*-butyl hydroperoxide as oxidant, for example, shows fast conversion and good selectivities with the usage of this catalyst, wherein the selectivity for cyclohexanone is 86.9% and for cyclohexanol 5.4%.<sup>167</sup> It was also reported that an incorporation of 3d metals such as Cr, V, Mn, Fe, Co and Ni on the Zr-clusters in defect UiO-66 and UiO-67 is feasible.<sup>126, 168-169</sup> Yet, the mode of coordination of these metals is still unclear. Nevertheless, these functionalized MOFs show good catalytic activity. In case of Cr(III) incorporated UiO-67, trimerization of acetaldehyde is successfully catalyzed at room temperature with conversions up to 96 %.<sup>126</sup> Furthermore, Zn- and Al complexes, which are attached on the Zr-cluster of

NU-1000 exhibit catalytic activity in Knoevenagel condensation reactions without leaching effects.<sup>162</sup>

As mentioned, the free coordination sites of the Zr-cluster can act as catalytic active sites. Due to reduced connectivity or defects in the MOF structure, open metal sites are present and function as electron pair acceptors. Thereby, the catalytic activity is for many reactions directly dependent on the amount of the open metal sites. This circumstance was recently pointed out for the hydrolysis of the phosphate ester dimethyl 4-nitrophenyl phosphate (DMNP), which is a nerve agent. The twelve connected UiO-67 shows a turnover frequency (TOF) of 13.68 h<sup>-1</sup>, whereas the amount of defects of the used sample was not described in the literature.<sup>170</sup> Nevertheless, the eight-connected NU-1000, which had water thermally removed at 300 °C, show 100% degradation of DMNP in 10 min and a TOF of 32.4 h<sup>-1</sup>.<sup>3</sup> Consequently, the six-connected MOF-808 is even faster in the decomposition of DMNP with a TOF of 504 h<sup>-1</sup>.<sup>4</sup> Furthermore, the catalytic active metal sites can be tuned by the choice of the modulator in the synthesis and by its amount. In the Meerwein-Ponndorf-Verley (MPV) reduction of 4-tert-butylcyclohexanone, UiO-66 that was synthesised without any modulator, shows almost no activity. In contrast, UiO-66 that exhibit defects and was modulated either by trifluoroacetic acid (Tfa) or HCl is able to catalyse this reaction and shows conversions up to 93% in 24 h. Thereby, the small modulators, which can be also thermally removed in case of Tfa, provide more space at the catalytic centres, which is needed for the simultaneous activation of the reactants.<sup>127</sup>



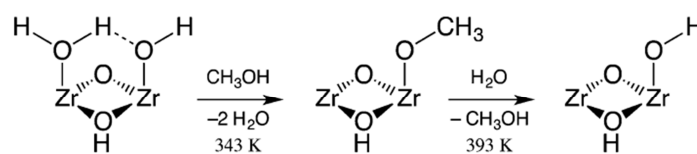
**Figure 7.** Relative free energies in kcal/mol at 298.15 K of possible products from methanol substitution on UiO-66.<sup>171</sup> Reprinted with permission from Yang, D.; Bernales, V.; Islamoglu, T.; Farha, O. K.; Hupp, J. T.; Cramer, C. J.; Gagliardi, L.; Gates, B. C., Tuning the Surface Chemistry of Metal Organic Framework Nodes: Proton Topology of the Metal-Oxide-Like Zr<sub>6</sub> Nodes of UiO-66 and NU-1000. *Journal of the American Chemical Society* 2016, 138 (46), 15189-15196. Copyright 2016 American Chemical Society.

To examine the constitution of -OH and -OH<sub>2</sub> groups as well as vacancies on the Zr-cluster, detailed investigations were done in case of UiO-66 and NU-1000 with the help of IR spectroscopy in combination with DFT calculations.<sup>171</sup> After synthesis, terminal -OH units and water are coordinated on the metal cluster (Site 1 in Figure 7). In presence of methanol or ethanol, which are often used in washing processes of MOFs, a range of possible substitution



products can be built that contain alkoxy groups. Their relative free energies were calculated. Thereby, product 2 in Figure 7, where one methoxy group and one vacant Zr site is formed, is the most likely one, since it has the lowest free energy of -4.7 kcal/mol. The actual formation of this product was also confirmed by IR spectroscopy.

In reaction with water, methanol is eliminated and one terminal OH group is formed (Figure 8). Residual water is removed by heating the MOF to 393 K in vacuum. The OH-units function as Lewis base sites, and are located in direct neighbourhood of the Lewis acid site (vacant Zr site), which can be crucial in some catalysis reactions, like in MPV-reduction, CO<sub>2</sub> cycloaddition of styrene oxide or hydrolysis of phosphate esters.



**Figure 8.** Constitution of the Zr-cluster of UiO-66 and how it changes after exposed to methanol and water.<sup>171</sup> Reprinted with permission from Yang, D.; Bernales, V.; Islamoglu, T.; Farha, O. K.; Hupp, J. T.; Cramer, C. J.; Gagliardi, L.; Gates, B. C., Tuning the Surface Chemistry of Metal Organic Framework Nodes: Proton Topology of the Metal-Oxide-Like Zr<sub>6</sub> Nodes of UiO-66 and NU-1000. *Journal of the American Chemical Society* 2016, 138 (46), 15189-15196. Copyright 2016 American Chemical Society.

The OH-units can also take on the function as Brønsted acid. The amount and strength of Brønsted acidities of various MOFs were measured by Klet *et al.* via potentiometric titration.<sup>172</sup> As expected, a defect-free UiO-67 exhibits only one type of titratable proton. Due to the absence of unoccupied metal sites, only  $\mu_3$ -OHs are present. In case of defects containing UiO-66,  $\mu_3$ -OHs, terminal-OHs and -OH<sub>2</sub> could be determined, wherein the ratio of terminal -OH units and -OH<sub>2</sub> is 1:1. The corresponding acid strengths of UiO-66 accounts to pK<sub>a1</sub> = 3.52 for  $\mu_3$ -OH, pK<sub>a2</sub> = 6.79 for -OH<sub>2</sub> and pK<sub>a3</sub> = 8.3 for -OH.

Furthermore, the acid strengths of Zr based MOFs can be influenced. One possible way is a post-synthetic treatment of the MOF with H<sub>2</sub>SO<sub>4</sub>.<sup>156</sup> After the acidic treatment, the sulphate ions are coordinated to the Zr-cluster and former modulator molecules are released. In case of MOF-808, the Hammet acidity can be changed from > 2.8 to ≤ - 14.5. Thus, organic reactions are now possible, which require catalysts with high acid strength. For example, the isomerization of  $\alpha$ -pinene is not catalysed by MOF-808, whereas the modified MOF-808-SO<sub>4</sub> shows conversions up to 99% in 1.5 days. Also the cyclization of citronellal to ( $\pm$ )-isopulegol and its isomers can be drastically improved. Whereas MOF-808 achieves a conversion of only 8% in eight hours, the sulphated analogue show a conversion up to 98%. Furthermore, steric

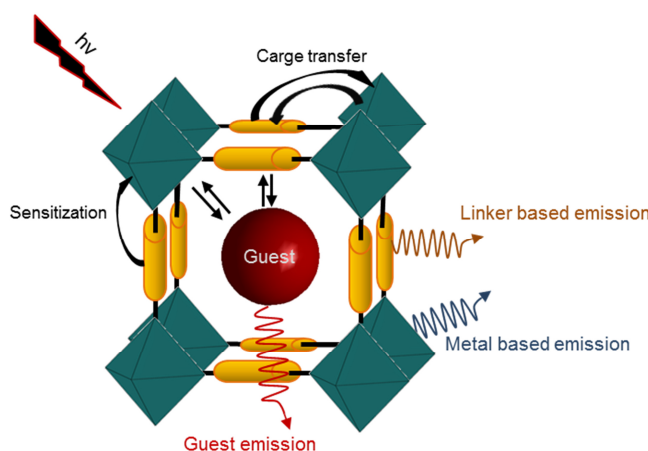
and electronic effects of ligands play a role. The cyclization of citronellal to isopulegol was also investigated for UiO-66 with BDC-X linkers, whereas X = H, NH<sub>2</sub>, CH<sub>3</sub>, OCH<sub>3</sub>, F, Cl, Br, NO<sub>2</sub>.<sup>173</sup> Electron-withdrawing groups on the linker can affect the Lewis acidity and increase the reaction rates. Especially the introduction of the NO<sub>2</sub>-group has a huge impact. Compared to UiO-66-H, a 56-fold increase of the conversion rate takes place. The trend was also observed for other Lewis-acid catalysed reactions, such as the conversion of geraniol in the Oppenauer oxidation with furfural.<sup>173</sup> With the functionalization of linkers, also Brønsted acid sites can be incorporated into the MOF. The sulfonic acid functionalized UiO-66-SO<sub>3</sub>H, for example, outperforms other MOFs in the transfer hydrogenation (Lewis acid catalysed) of levulinic acid and its esters to  $\gamma$ -valerolactone (Brønsted acid catalysed). In case of UiO-66, the yield for  $\gamma$ -valerolactone is only 36% after 9 h, whereas UiO-66-SO<sub>3</sub>H can reach yields up to 80% under the same conditions.<sup>174</sup> Also aromatic sulfonic acid groups in linkers can provide Brønsted acidity. In the work of Miao *et al.* *o*-sulfobenzoic acid was reacted with UiO-66-NH<sub>2</sub> to give UiO-66-RArSO<sub>3</sub>H.<sup>175</sup> This catalyst shows an exceptional good TOF in the acetalization of benzaldehyde. In contrast to UiO-66-NH<sub>2</sub> that has a TOF of 14 h<sup>-1</sup> for this reaction, UiO-66-RArSO<sub>3</sub>H gives a TOF value of 490 h<sup>-1</sup>.

### 2.1.5 Applications of Zr-based MOFs as luminescence based sensors

One feasible application of MOFs is to use them as chemical sensors. For this function, a broad range of signal-transduction mechanisms exist, which take advantage of mechanical, electrical or optical properties of the MOFs. In this chapter, only luminescence as signal-transduction is discussed.

In an ideal case, materials which are used as sensors should be selective to the analytes, be highly sensitive and have short response times. Also the stability and reusability should be considered for an application as sensor. MOFs as porous materials with high surface areas are eligible to concentrate analytes in their pore system. There, guest molecules may be able to affect the emission properties, leading to changed intensities, wavelength shifts or new emission peaks. Thereby, the sensitivity is also dependent on the size of the pores, since analytes are usually stronger adsorbed in smaller pores than in larger ones. In general, selectivity can be achieved by various strategies. One strategy is based on size exclusion.<sup>176-178</sup> The pore dimensions can be designed according to the modular concept of MOFs. Thus, small analytes are able to diffuse into the pore system, while molecules that are too bulky to

cross the pore windows are excluded. Such tunability can provide a high degree of selectivity. Furthermore, specific interactions of the analyte with the MOF can provoke selectivity, like electron donor/acceptor interactions,  $\pi$ - $\pi$ -interactions, electrostatic interactions, or the presence of hydrogen- or coordinative bonds. Such interactions often require the presence of functional groups in the linker. Though, some analytes are preferably adsorbed on open metal sites. If the local coordination environment of the metal cluster changes, the emission properties can be also affected. Thereby, the luminescence can be generated either by the metal species or by the linker (Figure 9).



**Figure 9.** Schematic illustration of emission processes and electronic transfers between the building blocks of metal-organic frameworks.<sup>34</sup> Adapted from Allendorf, M. D.; Bauer, C. A.; Bhakta, R. K.; Houk, R. J. T., Luminescent metal-organic frameworks. *Chemical Society Reviews* 2009, 38 (5), 1330-1352.

MOFs which exhibit metal based emission, feature f-elements as nodes. Lanthanide ions or actinide ions emit with sharp peaks but show weak luminescence. Yet, the luminescence can be enhanced by antenna effects, where an energy transfer from the excited state of a highly absorbing linker to the metal occurs. Linker based luminescence is caused by conjugated organic ligands, which are absorbing in the UV and visible region. Fluorescent emission typically involves a spin-allowed singlet-singlet transition from the lowest singlet excited state to lower lying states and to the ground state. Also a non-radiative transfer to the triplet state can occur. Emission from this state to the singlet-ground state is spin-forbidden and is defined as phosphorescence. In case of MOFs, the emission depends not only on the linker itself, but also on the size of the metal, the SBU and the orientation of the linker in the framework. The degree of isolation of the linkers to each other is one important factor, since effects such as  $\pi$ - $\pi$ -stacking can be avoided. That has also an influence on lifetimes and quantum yields. Another factor is the metal species itself. MOFs that are based on transition

metals emit mostly from the linker. Thus, a ligand-to-metal charge transfer (LMCT) or a metal-to-ligand charge transfer (MLCT) can be involved. MOFs containing metal ions without unpaired electrons, especially those with  $d^{10}$  configuration, usually exhibit a strong linker-based emission. If transition-metal ions with unpaired electrons are involved, quenching effects are possible due to strong reabsorption or charge transfer through partially filled d orbitals.<sup>34</sup> Despite the character of the frontier orbitals, the luminescence properties depend also on the energy gap between the highest occupied and the lowest unoccupied molecular orbitals (HOMO-LUMO). If the energy gap gets smaller, the luminescence intensity is enhanced. Electron donating groups on linkers are able to reduce these gaps.<sup>179</sup>

In most cases, the signal transduction of luminescent MOFs is based on quenching or enhancement of the emission intensity. For example, adsorbed analytes can inhibit linker motion. That reduces non-radiative decays of the photoexcited states, leading to enhanced intensities. On the other hand, quenching can occur if energy transfers are involved or exciplexes are formed. An exciplex is an excited complex, which can be built e.g. by  $\pi$ - $\pi$ -interactions between the linker and the guest molecule. However, the main disadvantage of so called “turn on” or “turn off” sensors is their low selectivity. The intensity change can be often caused by other phenomena than the analyte interaction or is not specific for the analyte. A sensing mechanism based on solvchromatic shifts is more reliable and gives more detailed information, but is not so frequently observed.

In Zr-based MOFs, the luminescence originates typically from the linker. So far, only a few Zr-based MOFs are reported to be suitable as a sensor. One of them is the eight-connected PCN-225. Due to its porphyrine linker, which contains pyridine-type N atoms, a non-linear pH-dependent fluorescence is observed. In acidic solution, the linkers are protonated, which destroys their  $\pi$ -electron conjugated double bond system. Therefore fluorescence quenching occurs, whereas intensity is enhanced with higher pH values.<sup>121</sup> Also UiO-66-NH<sub>2</sub> is sensitive to the pH in the range from 1 to 9. The emission intensity increases thereby exponentially with the pH value.<sup>180</sup> UiO-66-NH<sub>2</sub> appears to be useful also for other sensing applications. By taking advantage of the possibility to create missing linker defects in UiO-66-NH<sub>2</sub>, the free coordination sites can be utilized to form strong coordinative bonds to phosphates. Normally, the fluorescence of this linker is weakened by LMCT. If phosphates bond to the Zr-oxo-cluster, the electron density at the Zr atoms is reduced. This leads to raised 3d electron-binding energies and LMCT is inhibited. Thus, fluorescence is recovered and the emission intensity is enhanced. A linear detection range of the phosphates is found to be from 5 to 150  $\mu$ M with a detection limit of 1.25  $\mu$ M.<sup>181</sup> Furthermore, an enhancement of emission

intensity occurs also in the presence of a buffered aqueous solution of Aspirin. Amongst other mechanisms, the enhancement is caused by the intermolecular hydrogen-bonding interaction between the  $\text{NH}_2$ -moiety of the linker and the Aspirin. Thereby, the detection range is linear and lies between 0.02 and 200  $\mu\text{M}$  of Aspirin.<sup>182</sup> Another mechanism is utilized to detect nitric oxide in aqueous phase, whereat a deamination of the linker takes place to give UiO-66, whose luminescence is significantly weaker.<sup>183</sup> Decreased emission intensity takes also place if nitrobenzene is present. In the range of 10-100 ppm of nitrobenzene, a “turn off” mechanism can be observed. At 100 ppm of nitrobenzene 95% quenching efficiency is achieved. Since UiO-66- $\text{NH}_2$  has defects, an electron transfer from the excited state of the free Zr sites to nitrobenzene occurs. Furthermore, the electron-deficient NO-group coordinates to the electron-rich Zr-OH sites. Thereby the distance between the benzene rings of the linker and the nitrobenzene is reduced, which leads to  $\pi$ - $\pi$ -stacking. Other aromatic molecules like benzene, toluene or chlorobenzene cannot coordinate to the Zr-cluster in such a way. That leads to increased distances between the molecules and the linker, and therefore to weaker  $\pi$ - $\pi$  interactions. Nevertheless, these molecules have quenching efficiencies < 40% at 100 ppm.<sup>184</sup> Additionally, formaldehyde in aqueous solution influences also the luminescence of UiO-66- $\text{NH}_2$ . Formaldehyde forms non-covalent bonds to the linker, whereas the HOMO-LUMO gap decreases. This leads to fluorescence quenching. A linear correlation of fluorescence quenching and the concentration of formaldehyde is found in the range of 10-100 ppm. In case of other aldehydes, such as propionaldehyde or butyraldehyde, UiO-66- $\text{NH}_2$  is not so sensitive, since their HOMO-LUMO gaps are larger.<sup>185</sup>

Other Zr-based MOFs whose signal-transduction is based on fluorescence intensity change are UiO-66- $\text{N}_3$  and UiO-66- $\text{NO}_2$ . They are “turn on” sensors for a selective sensing of  $\text{H}_2\text{S}$ . In case of UiO-66- $\text{N}_3$ ,  $\text{H}_2\text{S}$  reduces it rapidly to UiO-66- $\text{NH}_2$  and in case of UiO-66- $\text{NO}_2$  it reacts to UiO-66- $\text{NH}_2$ . Other reducing agents, such as halogens,  $\text{NO}_2$  or amino acids do not provoke a responding behaviour of the MOF, but in combination with  $\text{H}_2\text{S}$  they induce a specific signal change. These MOFs were tested under physiological conditions and since they have low toxicity, their application as sensor in living cells and in biological systems is feasible.<sup>186-187</sup> Another MOF which works under physiological conditions and is used for bioimaging applications is a UiO-66 analogue MOF that is functionalized with maleimide derivate moieties. These groups can sense selectively the thiol containing amino acids cysteine and glutathione in living cells. If a thiol adduct of the maleimide moieties is built, the fluorescence signal is turned on. Then, the emission intensities are increased in a linear correlation of thiol concentration in a range of  $10^{-11}$ - $10^{-3}$  M.<sup>188</sup> An  $\text{O}_2$  sensitive detection in living cells is

achieved by an UiO-type MOF, where phosphorescent Pt(II)-porphyrine ligands are incorporated. With increasing O<sub>2</sub> partial pressure, the sensor responds by decreasing phosphorescence intensities and decays.<sup>189</sup>

Another application field for UiO-type MOFs is the detection of nitro explosives, such as 2,4,6-trinitrophenol (TNP), in aqueous media. Even low concentrations of 2.6 mM can be detected, if 2-phenylpyridine-5,4'-dicarboxylate is used as linker. In this case, not only the fluorescence intensity is influenced, also the emission peak is shifted to higher wavelengths.<sup>190</sup> Another case, where both signal-transduction mechanisms – luminescence quenching and vapochromism – take place, is the sensing of electro-donating alkylamines by the UiO-67 analogue MOF that has electron-deficient methylated 2,2'-bipyridinium as linkers.<sup>191</sup>

Furthermore, Zr-based MOFs, whose linkers contain metal binding sites on their moieties (like the linker p,p'-terphenyldicarboxylate) can be utilized to sense transition metals with unpaired d electrons. The coordination of such metal ions to the MOF lead to significant quenching effects, caused by reasons mentioned above. Especially the detection of Mn(II) is very sensitive with a detection limit of <0.5 ppb.<sup>192</sup>

### 3. CHARACTERIZATION METHODS

#### 3.1 Adsorption

##### 3.1.1 Definitions and terminology

*Adsorption* describes a spontaneous enrichment of one or more components (molecules, atoms or ions) in the gaseous or liquid phase on the phase interface. Thereby, the component in the fluid phase is defined as *adsorptive* and in the adsorbed state as *adsorbate*. The solid itself, where the components are adsorbed is defined as *adsorbent*, and the occupied surface as *adsorption space*. The reverse process of adsorption is *desorption*, whereat adsorbed components are removed from the surface by supplying the required energy to return to the fluid phase (Figure 10). Between the adsorbent and the adsorptive, intermolecular forces and specific molecular interactions are involved. Depending on the strength of the interactions, they are classified as *chemisorption* or *physisorption*. Chemisorption takes place if adsorption enthalpies  $> 40 \text{ kJ mol}^{-1}$  are involved. Then, usually chemical bonds, such as covalent or coordinative bonds, are at play and monolayers are built. In that case, the adsorption is mostly irreversible or at least the desorption process is incomplete. On the contrary, in the physisorption process, despite attractive dispersion- and short range repulsive forces, only weak van-der Waals interactions are formed and adsorption enthalpies are less than  $40 \text{ kJ mol}^{-1}$ . Physisorption is also characterized by the formation of multilayers and the complete reversibility of the adsorption/desorption process.

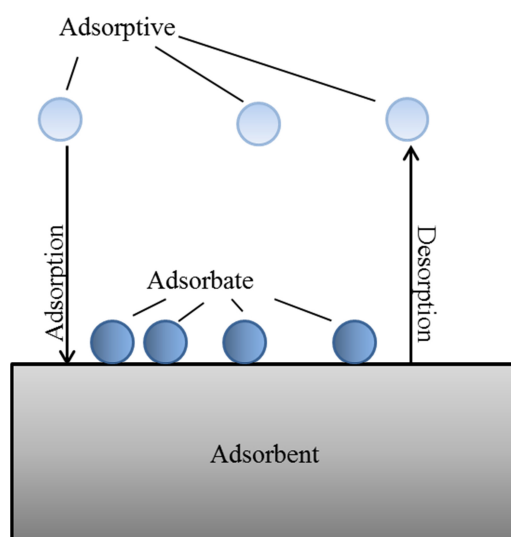
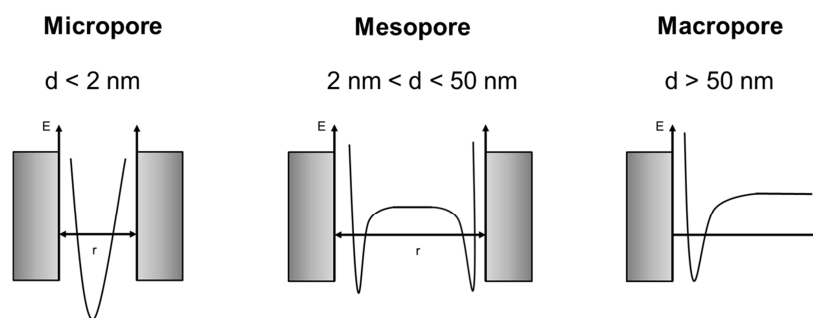


Figure 10. Terminology and definitions of the adsorption process.

The adsorption process can be utilized to characterize porous materials. Thereby, there are three classifications of pores, which are differentiated by their sizes. According to IUPAC they are classified as *macropores*, *mesopores* and *micropores*.<sup>193</sup> Macropores include pore widths exceeding 50 nm, whereas the size of mesopores lies between 2 nm and 50 nm. Micropores are smaller than 2 nm and are further subdivided into *supermicropores* that exhibit diameters between 0.7 nm and 2 nm, and *ultramicro-pores* whose diameters are smaller than 0.7 nm. The adsorption of molecules in these different pore types differ by their potential energies. The free energy of a gas molecule in dependence of its distance to the surface wall of the adsorbent is described by the *Lennard-Jones potential* (Figure 11). This energy potential consists of long range attracting forces, like van-der Waals forces or dispersion forces, as well as of short range repelling forces, which originate from overlapping electron orbitals and the resulting Pauli-repulsion. At the distance, where the potential energy reaches its minimum (potential well), the attractive and the repulsive forces are in equilibrium and the gas molecule can be adsorbed on the pore wall. This is only valid for non-porous or macroporous materials, where no interaction of the gas molecule with the opposite pore wall can occur. In case of micro- and mesoporous materials, the potential energy is influenced also by the geometric properties of the pores. In micropores, attractive adsorbate-adsorbent-interactions are prominent. The adsorption potentials of both pore walls are overlapping and reinforce each other. This results in a deeper potential well and thus to higher adsorption energies. The more the distance between the opposite pore walls is reduced the more is the depth of the potential well increased. Therefore, even at very low pressures adsorption takes place and the small micropores are filled very fast. In mesopores, the adsorption potentials are not overlapping in such an extent. The potential wells are clearly separated from each other. Despite the adsorbate-adsorbent-interactions, which are responsible for mono- and multilayer adsorption, also the interactions between the gas molecules with themselves play a role, with increasing layer thickness.



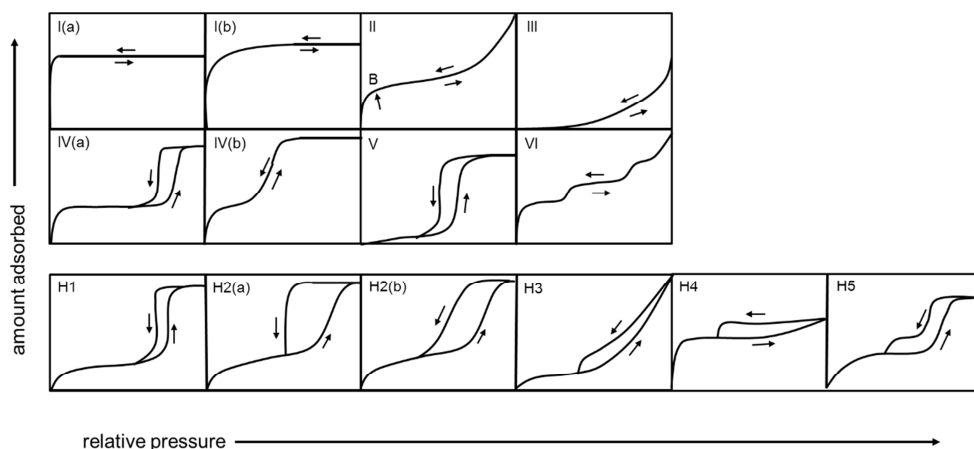
**Figure 11.** Classification of pore sizes according to IUPAC and the corresponding Lennard-Jones potentials.



### 3.1.2 Adsorption of gases

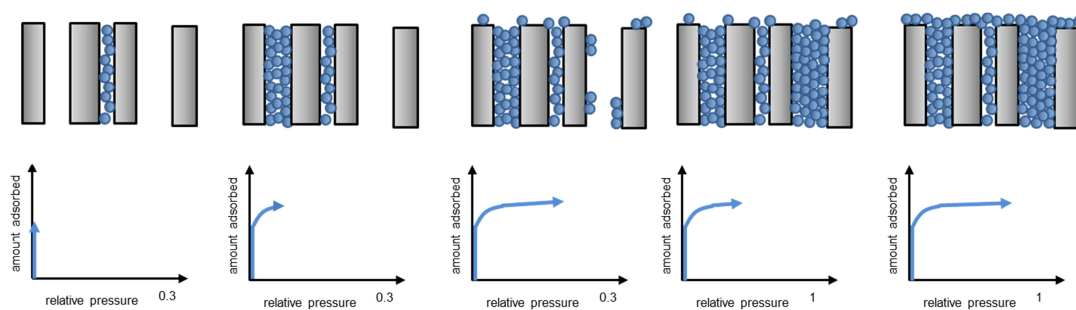
The physisorption of gases is a powerful tool for the characterization of the inner surface of porous materials. It is a non-destructive method and relevant information, such as the specific surface area, pore volumes, pore size distributions and adsorption enthalpies can be gained. As a routine method, the physisorption of nitrogen at its boiling temperature of 77 K has been established. Compared to other inert gases, nitrogen has some economic advantages. The supply of gaseous nitrogen is relative cheap, as well as liquid nitrogen, which is needed to secure the low measurement temperature. For special cases, like the analysis of small micropores, argon physisorption measurements can be expedient, since it has a smaller radius and no quadrupole moment, polar interactions with the solid material are minimized. Before the actual measurement can be executed, the sample must be activated in vacuum at higher temperatures (RT-200 °C, depending on nature of the material) to remove remained solvent molecules or physisorbed gases and to determine the exact mass of the sample. For the sorption process, a gravimetric or a manometric technique can be applied. In case of the manometric technique, defined amounts of gas are dosed into the loaded sample cell at constant temperature until the equilibrium pressure is established for each dose and the final target pressure is reached. The process must be repeated for several times at different target pressures. For low-pressure physisorption isotherms, the highest targeted pressure does not exceed 1 bar and the measuring temperature is usually below the critical temperature of the adsorptive to avoid condensation in the sample cell. For such an isotherm the adsorbed amount of gas at standard temperature and pressure conditions (STP = 0 °C, 1.013 bar) is plotted versus the relative pressure in relation to the sample mass. Thereby, the relative pressure  $p/p_0$  is defined as the proportion of the equilibrated pressure to the saturation vapour pressure at the operational temperature. The resulting form of the isotherm is influenced by various factors, like adsorptive-adsorbent interactions, polarities, pore sizes and pore geometries. A classification of isotherms was done by IUPAC in 1985<sup>193</sup> and extended in 2015<sup>194</sup> (Figure 12). Type I isotherms are characteristic for microporous materials with small portion of external surface. In micropores the adsorbate-adsorbent interactions are enhanced due to overlapping energy potentials of the narrow pores. Consequently, a strong adsorption at very low relative pressures takes place. At higher pressures only adsorption on the external surface occurs. These processes are reflected by the concave shape to the abscissa and a steep uptake of the isotherm at low  $p/p_0$ . Typically, the isotherm approaches a saturation plateau very fast. The  $p/p_0$ -region, where the plateau is reached depends thereby on the pore size.

Type I(a) isotherms, whose plateau is already attained at very low  $p/p_0$ , are generated by narrow micropores with pore width smaller than  $\sim 1$  nm, whereas type I(b) isotherms are attributed to materials with a broader range of pore sizes, including small mesopores ( $< \sim 2.5$  nm).



**Figure 12.** Classification of isotherms and hysteresis loops according to IUPAC.<sup>194</sup>

Therefore the beginning of the plateau of type I(b) isotherms are shifted to higher  $p/p_0$ , compared to type I(a). In general, different sized pores are filled at different pressures. First, the smallest pores are filled. Parallel to the filling of wider micropores, an adsorption on small mesopores takes also place. Such an adsorption process with the corresponding development of the isotherm is shown in Figure 13.

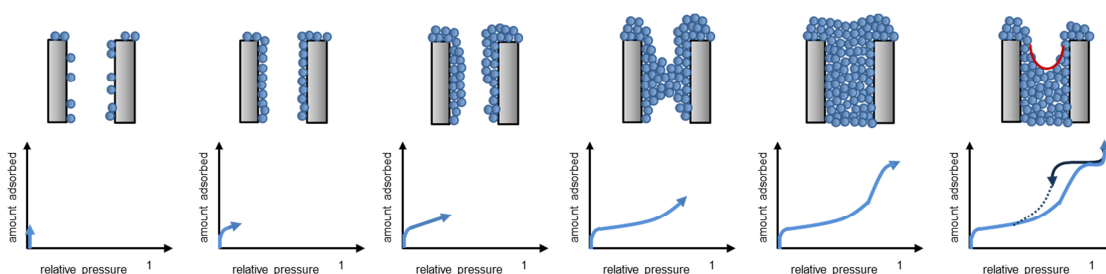


**Figure 13.** Pore-filling mechanism of micropores and small mesopores.

The adsorption on non-porous and macroporous materials is displayed by type II and III isotherms. For such materials the adsorption process is characterized by the formation of monolayers on the pore walls/solid surface, followed by the unrestricted multilayer adsorption. Type II isotherms exhibit a concave shape, followed by a linear section. The

beginning of this section is marked by a point B, which represents the transition between mono- and multilayer adsorption. If this point is distinct, the monolayer capacity and therefore the specific surface area can be determined. At higher pressures the shape of the isotherm gets convex to the abscissa due to adsorptive condensation. A convex shape over the whole pressure region is typical for type III isotherms. Here, adsorption appears only on the most favourable sites at higher pressures. The reason for this behaviour is that just relatively weak interactions between the adsorbate and the adsorbent are at play. A similar shape of isotherm is of type V, where also only weak interactions between adsorbent and adsorbate are present. At higher  $p/p_0$ , molecules are clustered and pores are filled. Type V isotherms exhibit a hysteresis and are typical for water vapour adsorption on micro or mesoporous materials, which have a hydrophobic pore surface. Type VI isotherms consist of multiple steps and originate from non-porous materials, which offers a highly uniform surface. Each step of the isotherm represents one layer of adsorption, whereas the height of the step is dependent on the layer capacity and its sharpness is dependent on the given system and temperature.

Mesoporous materials are described by type IV isotherms. At low relative pressures, the shape of the isotherm resembles the one of type II. In this region initial monolayers are built, followed by multilayer adsorption on the mesopore walls. At a certain pressure, capillary condensation of the adsorptive in the pores occurs, depending on the pore width. Thereby the adsorptive condenses in a liquid-like state under formation of a concave meniscus at pressures that are lower than the saturation pressure of the bulk liquid (Figure 14). These mechanisms are displayed by a steep increase of the isotherm in the corresponding pressure region until a saturation plateau is reached. Then the pores are completely filled. The existence of a hysteresis is typical for type IV(a) isotherms and only occurs if the pore width exceeds a critical point. This point depends also on the given system and temperature but is usually observed for pores that are wider than  $\sim 4$  nm. For materials with smaller mesopores, isotherms of type IV(b) are usually observed, which do not have a hysteresis.



**Figure 14.** Pore-filling mechanism of mesopores.

In general, the formation of a hysteresis is linked to the metastability of the adsorbed multilayer.<sup>195</sup> Condensation requires the building of condensation nuclei. This process is inhibited so that the process is delayed and the adsorption process is not in the thermodynamic equilibrium. On the contrary, the desorption branch is in the equilibrated thermodynamic state. Then, the adsorption- and desorption branches are not identical and the desorption branch is shifted to lower relative pressures. Despite of the pore sizes, the formation and the shape of the hysteresis are also dependent on network effects and pore geometries. The IUPAC classified the hysteresis loops into six different types.<sup>193-194</sup> Materials with a narrow range of uniform pores are responsible for the formation of the hysteresis of type H1. The shape of these hysteresis loops is relatively steep and narrow. H2 type hysteresis loops are caused by more complex materials with a broader range of pore sizes. Therefore, the hysteresis loop is broadened. In case of H2(a) hysteresis types, pore blocking caused by uniform pore necks and cavitation-induced evaporation are responsible for a very steep desorption branch. The loops of H2(b) type are also associated with pore blocking effects. Their slope is less steep due to a broader range of pore neck sizes. Type H3 hysteresis loops originate from plate-like particles and not completely filled macropores. Due to the lack of micropores, the adsorption branch resembles isotherms of type II. On the contrary, the adsorption branch of type H4 hysteresis is a composite of type I and II isotherms. These hysteresis loops are therefore generated by materials which exhibit micro- and mesopores. Type H5 hysteresis loops are associated with open and partially blocked mesopores.

### **3.1.3 Determination of the specific surface area according to Brunnauer, Emmet and Teller**

The specific surface area of a material is generally determined by the application of the Brunnauer-Emmet-Teller (BET) equation<sup>196</sup>. In contrary to the Langmuir approach<sup>197-198</sup>, which takes only monolayer formation into account, the BET approach considers also the existence of multilayer adsorption of a fluid on a solid surface. The BET-theory is based on the assumption that the first adsorbed molecular layer is stronger bonded to the adsorbent than the following layers, whereas the amount of the adsorbed layers is assumed to be unlimited. To apply the BET-method, the physisorption isotherm is transferred into the linearized form of the BET equation, which is given in (1). Thereby  $n$  is the total amount of adsorbed gas,  $n_m$  is the capacity of one monolayer and  $C$  is the adsorption constant that describes the strength of

the interactions between adsorbate and adsorbent.

$$\frac{p}{n \cdot (p_0 - p)} = \frac{1}{C \cdot n_m} + \frac{C - 1}{C \cdot n_m} \cdot \frac{p}{p_0} \quad (1)$$

A plot of  $p/n(p_0 - p)$  against  $p/p_0$  gives a linear regression in a certain pressure region, which is usually in  $p/p_0$  range of  $\sim 0.05 - 0.3$ . For microporous materials, the appropriate range is sometimes shifted to lower relative pressures and usually lies between values of  $0.02 - 0.1$ .<sup>199-200</sup> By the extrapolation of the line to the intersection of the ordinate, the capacity of one monolayer  $n_m$  can be determined. The slope of the line can also be used for its determination (Figure 15).

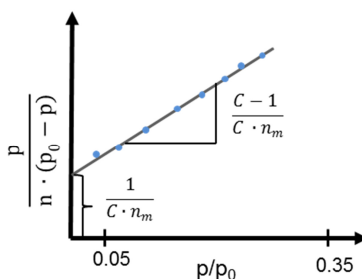


Figure 15. Graphic analysis of nitrogen isotherms according to the BET-plot.

From the monolayer capacity, the specific surface area  $a_s$  of the adsorbent can be finally calculated. The relation is given by equation (2), whereas  $m$  is mass of the adsorbent,  $N_a$  is the Avogadro constant and  $\sigma_m$  is molecular cross sectional area. The molecular cross sectional area describes the surface area of one gas molecule on a flat surface. For  $N_2$ , the value of  $\sigma_m$  is  $0,162 \text{ nm}^2$  at  $77\text{K}$ .

$$a_s = \frac{n_m^a \cdot N_a \cdot \sigma_m}{m} \quad (2)$$

For microporous materials, some criteria for the application of the BET method were recommended by IUPAC. By choosing the linear range of the BET plot, it should be taken care of that in this range the term  $p/n(p_0 - p)$  continuously increases with  $p/p_0$ , and that the  $p/p_0$  value that corresponds to the completeness of the monolayer  $n_m$  should be included. Furthermore, the value of the adsorption constant  $C$  should be positive. This constant gives also useful information about the shape of the isotherm. If the value is  $< 2$ , than the BET method is not applicable and the isotherm is either of type III or V. If  $C$  is lower than  $\sim 50$ , an

overlap mono and multilayer adsorption takes place and  $n_m$  cannot be identified. For a confident identification of  $n_m$ , the value of  $C$  should be at least  $\sim 80$ . Values over  $\sim 150$  indicate the filling of small micropores and an adsorption on high-energy sites.

### 3.1.4 Determination of the total pore volume

Despite the useful information that the specific surface area gives, the pore volume of a material is also an important characterization tool. According to Gurvich<sup>201</sup>, the pores are completely filled by the adsorptive if the saturation pressure is reached. For micro- and mesoporous materials, such a reliable point is at  $p/p_0 = 0.95$ . For the determination of the total pore volume, the adsorbed volume of the gas  $V_{ads}$  is converted into the corresponding volume of the adsorptive in its condensed state  $V_{liq}$  at STP. Thereby,  $V_m$  is the molar volume of the liquid adsorbate ( $34.7 \text{ cm}^3 \text{ mol}^{-1}$  for nitrogen). The assumption is made that the volume  $V_{liq}$  equates to the total pore volume  $V_{pore}$  of the sample.<sup>202</sup>

$$V_{liq} = \frac{p_0 \cdot V_{ads} \cdot V_m}{R \cdot T} \quad (3)$$

Macroporous materials are often not filled completely, even at high relative pressures. In this case the isotherm does not have a plateau. Therefore, the determination of the total pore volume cannot be done by this method. In case of a material that exhibit micropores as well as mesopores, a discrimination of their pore volumes can be done. The specific micropore volume of a material and its portion to the total pore volume can be determined by the method of de Boer, which is also known as “statistical thickness method” (t-plot).<sup>203</sup>

### 3.1.5 Determination of the pore size distribution

For the calculation of pore sizes, various methods exist which are based on the information that are obtained from isotherms. If capillary condensation takes place, the radius of the formed meniscus  $r_{menisc}$  inside the pores can be calculated by the Kelvin equation<sup>204-205</sup> (4). Thereby,  $\gamma$  is the surface tension and  $\varphi$  is the wetting angle.

$$\ln \frac{p}{p_0} = \frac{-2\gamma \cdot V_m}{r_{menisc} \cdot R \cdot T} \cdot \cos\varphi \quad (4)$$

The adsorbed multilayers, which do not take part in the formation of the meniscus, are not taken into account by the Kelvin equation. The thickness of those multilayers, in dependence of the relative pressure, can be calculated with the help of the Wheeler equation (5)<sup>206</sup>.

$$t = 4.3 \left( \frac{5}{\ln(p_0/p)} \right)^{1/3} \quad (5)$$

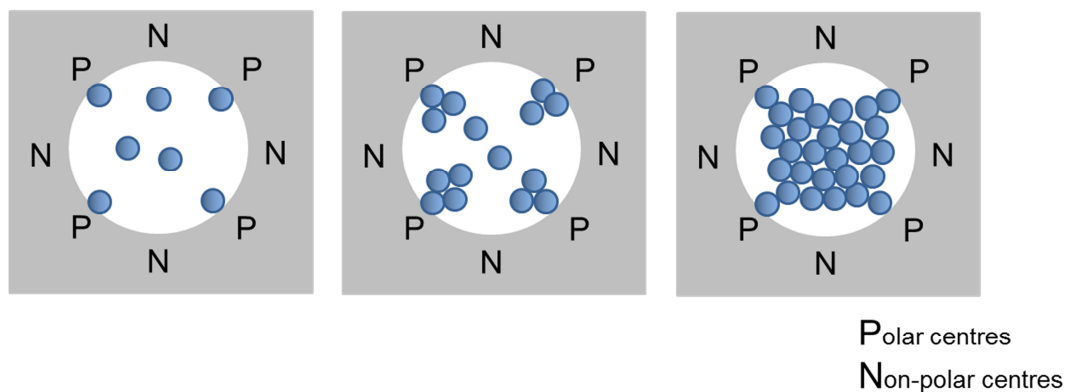
The Barrett-Joyner-Halender (BJH) method<sup>207</sup> combines both equations. The pore radius  $r_{pore}$  results from the sum of  $r_{menisc}$  and  $t$ . Yet, the BJH method is only applicable on materials that exhibit mesopores. The radii of pores smaller mesopores and micropores cannot be calculated due to the lack of capillary condensation. For these materials, a method based on the density functional theory (DFT) is eligible. The DFT theory was first established by Evans and Tarazona<sup>207-211</sup>. On contrary to the BJH method, which assumes that the condensed phase has bulk-like properties, this method takes fluid-fluid as well as fluid-solid interactions into account and is therefore more precise. In consideration of temperature, pore geometries, pore sizes and material properties, the density profiles of the adsorbate at its equilibrated state, in dependence to its distance to the solid surface at different pressures can be calculated. Using these density profiles, theoretical isotherms can be derived. Thereby, every theoretical isotherm is related to a defined pore size. These theoretical isotherms are summarized in a so called “kernel”, whereas each kernel refers to the given system. By linear combination of the theoretical isotherms, they are fitted to the experimental derived isotherm. The weighting of each isotherm in this mathematical process is then displayed in the resulting pore size distribution.

For the calculation of the density profiles, different methods are established. The non-local-density functional theory (NLDFT) is the most widely used method and is used as a standard<sup>212</sup> for characterizing micro and mesoporous materials. Another method is the quenched solid density functional theory (QSDFT) that takes also the surface roughness into account. This method is therefore suitable for materials exhibiting pore wall heterogeneity. The isotherms derived from these calculated density profiles are collected in libraries. In most cases, they are calculated for silica, zeolites or carbon materials with pore morphologies, like slit-pores, cylindrical pores or spherical pores, for different adsorptive gases (nitrogen (77 K), argon (87 K) or CO<sub>2</sub> (195 K)).<sup>213</sup> Up to now, no kernels exist that are customized for MOF materials. Nevertheless, kernels, which were developed for silica and carbon materials, were successfully applied on MOFs. Yet, the implementation of these kernels to MOFs should be

done with precaution and verified by other methods.

### 3.1.6 Water vapour adsorption

To characterize the polarity or to be more precise the hydrophobicity/hydrophilicity of a material the adsorption of water vapour can be utilized.<sup>214</sup> In contrast to nitrogen or other inert gases like argon, water is a strongly polar molecule. Depending on the surface properties of the adsorbent, not only van-der Waals interactions play a role, but also the formation of hydrogen bonds. Therefore, not only physisorption but also chemisorption can be involved in the adsorption process. In case of a polar material with only small micropores, like zeolites or silicas, continuous monolayers are built and the resulting isotherm is of type I. If the polar material has wider micropores or even mesopores, also multilayer adsorption takes place. The adsorption branch is then shifted to higher relative pressures. Water vapour isotherms of non-polar materials, like activated carbons or ZIFs, have usually a convex shape and the pore filling takes place at relatively high relative pressures.



**Figure 16.** Adsorption of water molecules (blue spheres) on polar and non-polar centres of the pore wall (grey solid).<sup>110</sup> Adapted from Küsgens, P.; Rose, M.; Senkovska, I.; Fröde, H.; Henschel, A.; Siegle, S.; Kaskel, S., *Characterization of metal-organic frameworks by water adsorption*. *Microporous and Mesoporous Materials* 2009, 120 (3), 325-330.

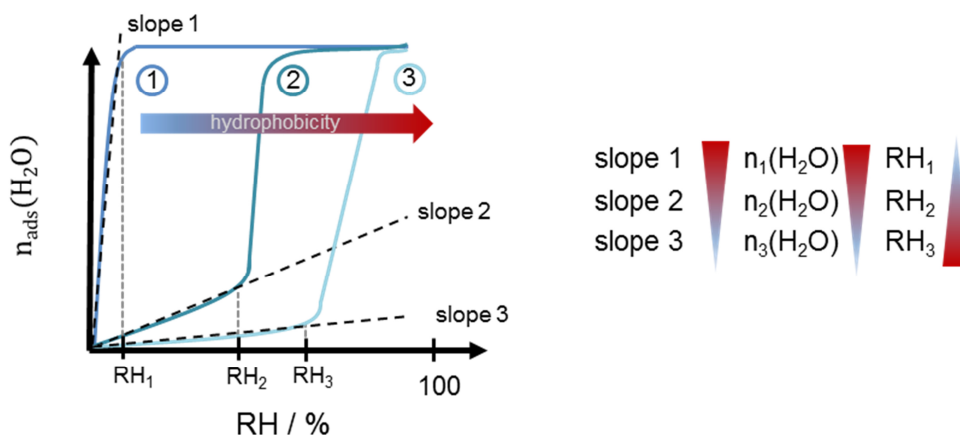
MOFs usually have non-polar surface sites due to their aromatic organic linkers, but highly polar metal clusters. On these hydrophilic centres, water nucleation sites are formed, whereas the hydrophobic areas of the linker are avoided (Figure 16). By building hydrogen bridges, more and more water molecules coordinate to the already adsorbed water. Then, small water clusters are formed until they unite with other water clusters, which were formed from other areas of the pore surface. Thereby, the hydrophobic areas are spared till a certain point, leaving free space.<sup>110</sup> Thus, the total pore volume derived by water adsorption can be smaller



than the one derived by nitrogen adsorption. The free space, where no water adsorption takes place, can be quantified by the pore filling degree and can be calculated according equation (6):

$$\text{pore filling degree} = \frac{V_{\text{total}}(\text{H}_2\text{O})}{V_{\text{total}}(\text{N}_2)} \cdot 100\% \quad (6)$$

With the help of the pore filling degree, materials with similar pore geometries can be compared in matters of their hydrophobicity. For a reliable comparison, the pore volumes should be determined at the same relative pressures, usually at high relative pressures ( $p/p_0 \sim 0.95$ ). High pore filling degrees point to hydrophilic pore surfaces, while lower degrees indicate more hydrophobic surfaces.



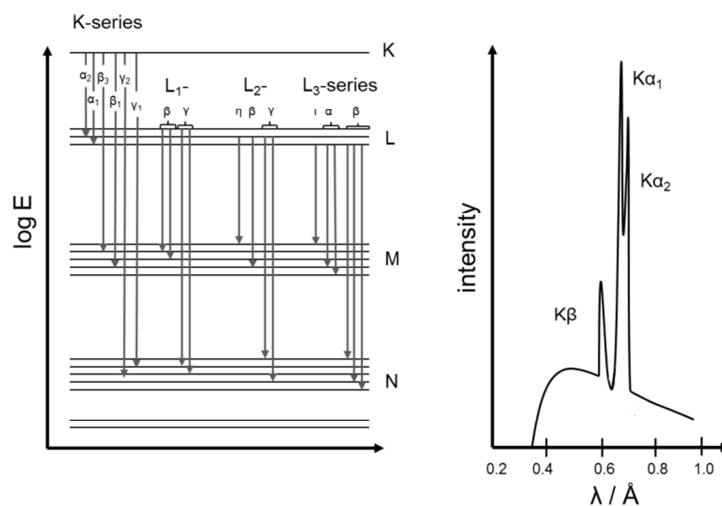
**Figure 17.** Various shapes of water vapour adsorption isotherms. The more hydrophilic a material is the higher is the slope of the isotherm and the higher is the uptake of water at lower relative humidity (RH).

Through strong interactions of water with the adsorbent, some materials can be transformed or start to decompose. Thus, water vapour adsorption experiments can be a useful tool to characterize the water stability of a material – or the stability against water evaporation. Some materials are stable in water, but collapse if capillary forces appear during water removal. A hysteresis indicates such moisture instability. Since the equilibration of water isotherms is often much slower than for non-polar adsorptives (up to hours for one point), the origin of hysteresis may thus also be caused by insufficient equilibration.

## 3.2 X-ray crystallography

### 3.2.1 Fundamentals

With the help of X-ray diffractometry, the structure of crystalline materials can be investigated. Useful information can be obtained such as lattice parameters, the space group, phase purities or the portion of amorphous fractions. The required X-rays are usually generated by an X-ray tube in a lab diffractometer. Thereby, the characteristic X-ray spectrum with defined wavelengths is not only dependent on the accelerating voltage, but also on the used anode material of the X-ray tube.



**Figure 18.** X-ray energy level diagram with the Siegbahn notations of the permitted transitions (right); spectrum of a Mo-X-ray tube (right).

Furthermore, these wavelengths depend on the energy levels of the transferred electrons. For example, if the expelled electron is located in the K shell (K-series) and the transferred electron originates from the L III state, the resulting X-ray radiation has the wavelength of  $K\alpha_1$ . The wavelength of  $K\alpha_2$  results from an electron transfer from the L II state (Figure 18). Usually the wavelength of  $K\alpha_1$  is used for measurements, since it has the highest intensity, and other wavelengths are generally separated by monochromators.

For special cases, such as small scattering crystals, synchrotron radiation can be expedient. Especially for MOF crystals the higher intensity of synchrotron radiation is essential, since they have usually large cell parameters, a high amount of disordered solvent molecules and small particle sizes. Synchrotron radiation occurs when electrons are accelerated in a magnetic field with kinetic energies in the range of Giga eV.

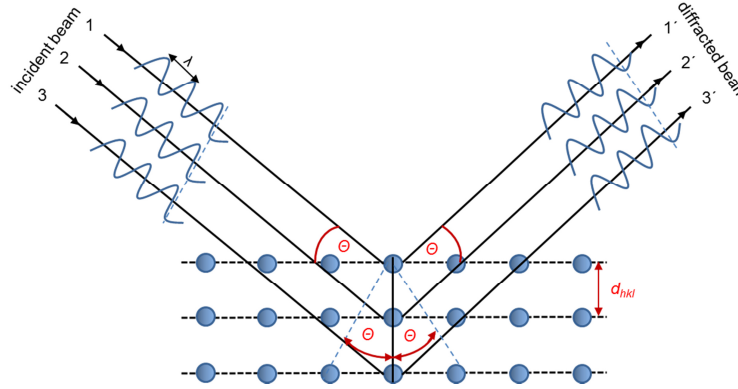


Figure 19. Schematic drawing of Bragg's law.

Materials with long range ordered atoms lead to a scattering of X-ray radiation from their lattice planes. A possible description is given by Bragg's law<sup>215</sup>, which is illustrated in Figure 19 and is given in equation (7), whereas  $n$  is a positive integer:

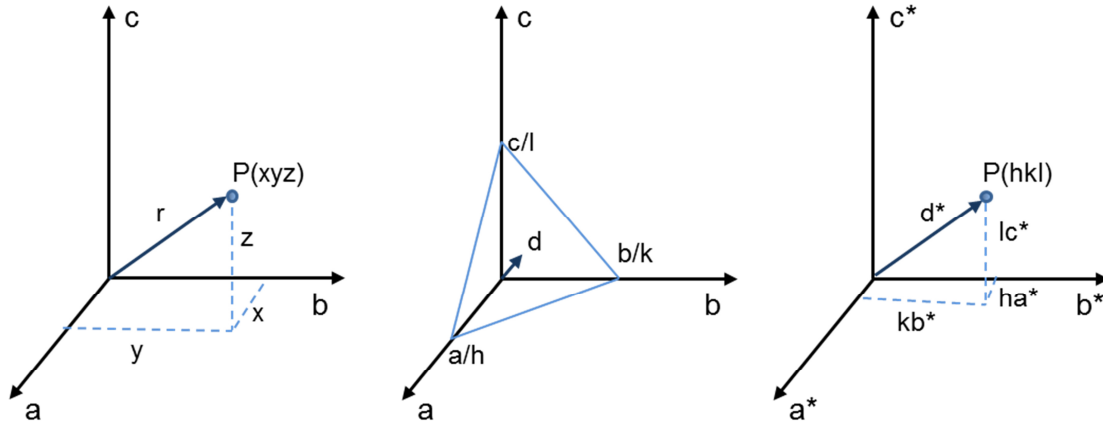
$$n \cdot \lambda = 2d \cdot \sin\theta \quad (7)$$

Thereby, the lattice planes are spaced by the distance  $d$ , which has to be in the range of the X-ray radiation wavelength  $\lambda$ , and the exit angle  $\theta$  of the scattered waves of the X-ray radiation is the same as the incident angle. If the Bragg condition is fulfilled, the scattered waves undergo constructive interference. Otherwise destructive interference takes place and leads to extinction. By measuring the scattered wave intensities as a function of the angle  $2\theta$ , a diffraction pattern is obtained and the distance of the lattice planes  $d$  can be calculated. The positions of the Bragg-reflections are thereby dependent on lattice parameters and symmetry. To obtain information about the crystal system and to describe the lattice planes, the Bragg-reflections of the diffractogram have to be indexed. The smallest repeating unit in the space is described by length and direction of the three basis vectors  $a$ ,  $b$  and  $c$  (8):

$$r = n_1a + n_2b + n_3c \quad (8)$$

The smallest unit of this lattice with the highest symmetry density is defined as unit cell and is characterized by the amount of the vectors  $a$ ,  $b$  and  $c$  (lattice constants) and their corresponding angles  $\alpha$ ,  $\beta$  and  $\gamma$ , which are known together as lattice parameters. The position of atoms in the unit cell are described by the fractional atomic coordinates  $x$ ,  $y$  and  $z$ , which consist of a fraction of the lattice constants. All of these atoms are located on a set of

crystallographic planes. The orientation and the distance of these planes are characterised by the Miller indices  $hkl$  and by the vector  $d$ . Thereby, the crystallographic planes intersect the axes intercepts of the real crystal lattice at  $\frac{a}{h}$ ,  $\frac{b}{k}$  and  $\frac{c}{l}$  (Figure 20). Due to the Laue conditions reciprocal lattice vectors are actually measured, which can be determined from the diffraction pattern. The reciprocal lattice can be Fourier-transformed into the real lattice and *vice versa*, wherein the reciprocal axes intercepts has to be integer.<sup>216</sup>



**Figure 20.** Illustration of the position of an atom in the unit cell described by the distance equation (left), description of the  $d$ -vector in the real crystal lattice with the corresponding lattice plane (middle) and description of the  $d^*$ -vector in the reciprocal lattice (right).<sup>217</sup>

With the help of the quadratic Bragg-equation, the individual Bragg-reflections can be indexed with the corresponding  $hkl$  values and the lattice constants can be calculated afterwards. The quadratic Bragg-equation of the simple case of an orthorhombic system is given in equation (9) and simplified to the distance equation (10):

$$\frac{1}{d^2} = \frac{4\sin^2\theta}{\lambda^2} = \frac{h^2}{a^2} + \frac{k^2}{b^2} + \frac{l^2}{c^2} \quad (9)$$

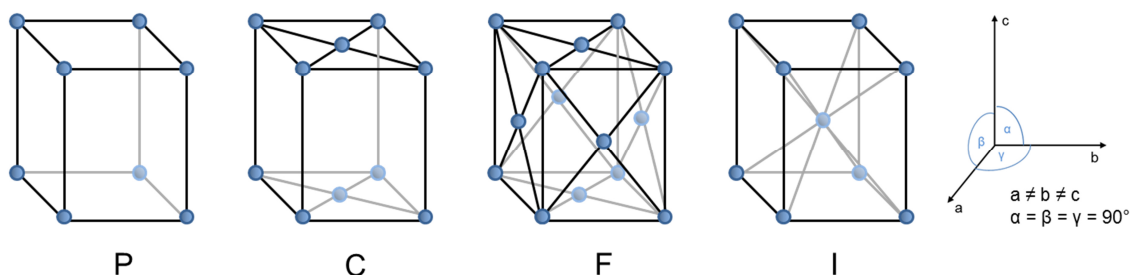
$$d^{*2} = h^2 a^{*2} + k^2 b^{*2} + l^2 c^{*2} \quad (10)$$

with

$$d^* = \frac{1}{d}, a^* = \frac{1}{a}, b^* = \frac{1}{b}, c^* = \frac{1}{c} \quad (11)$$

The lower the symmetry of the crystal system is the more complicated gets the quadratic Bragg-equation. Whereas the quadratic Bragg-equation for the orthorhombic system is simple and  $d$  is dependent on the lattice constants  $a$ ,  $b$  and  $c$ , the triclinic crystal system is not only dependent on  $a$ ,  $b$  and  $c$ , but also on  $\alpha$ ,  $\beta$  and  $\gamma$ . In general, seven crystal systems exist, namely the cubic, the hexagonal, the rhombohedral, the tetragonal, the orthorhombic, the monoclinic and the triclinic system.

To describe the positions of lattice points to each other in a crystallographic cell, symmetry elements can be used. By translation symmetry operations in three-dimensional space 14 allowed non-redundant translation lattices can be generated that are not reducible anymore. These translation lattices are named as Bravais lattice<sup>218-219</sup>. If only the cell corners are occupied by lattice points, the lattice is primitive (P). If an additional lattice point is located at the centre of each face that belongs to one pair of parallel faces, the lattice is base-centred. Depending on which faces are occupied, the base-centred lattice is labelled as A, B or C. A lattice which is face-centred (F) has all the cell corners and each face of the cell at their centre occupied. In a body-centred lattice (I) the cell corners are occupied and additionally the centre of the cell. In case of the orthorhombic crystal system, four Bravais lattices can occur, which are displayed in Figure 21.



**Figure 21.** Unit cells and Bravais types of the orthorhombic crystal system.

To describe the symmetry in a given crystal structure, symmetry elements are used, such as mirror planes ( $m$ ), diagonal glide planes ( $n$ ), rotation axes ( $2, 3, 4, 6$ ) and rotoinversion axes ( $\bar{1}, \bar{3}, \bar{4}, \bar{6}$ ). With these non-translational symmetry elements 32 crystal classes can be described. If translation symmetry elements and therefore also screw axes ( $2_1, 3_1, 3_2, 4_1$ ) and glide planes vertical to the axis  $a$ ,  $b$  or  $c$  ( $a, b, c$ ) are taken into account, every possible combination of symmetry operations leads to 230 space groups. Every space group is thereby represented by the Hermann-Mauguin notation. The short form of the Hermann-Mauguin notation contains the Bravais type and the symmetry elements, which describe sufficiently the space group. The

longer version of the Hermann-Mauguin notation includes additional symmetry elements, such as screw axes. A detailed description of the 230 space groups can be found in the International Tables of Crystallography Volume A<sup>220</sup>.

Furthermore, the position of every possible point in the unit cell is described by the Wyckoff position. These positions are related to the space groups and are distinguished into two types. Special positions are located on a symmetry centre, a rotation axis or a mirror plane. All other positions are defined as a general position. Overall, 1731 Wyckoff positions exist, which are labelled by small Latin letters and can be looked up in Wyckoff's book "The Analytical Expression of the Results of the Theory of Space Groups"<sup>221</sup> or in the International Tables of Crystallography Volume A<sup>220</sup>.

In general, the intensity of a given Bragg-reflection  $hkl$  is proportional to the square of the structure factor  $F_{hkl}$ :

$$I_{hkl} \sim |F_{hkl}^2| \quad (12)$$

The structure factor describes the scattering power of all atoms within the unit cell and is expressed in equation (13):

$$F_{hkl} = \sqrt{\sum_i (f_i A_i)^2 + \sum_i (f_i B_i)^2} \quad (13)$$

with

$$A_i = \sum_i \cos 2\pi(hx_i + ky_i + lz_i) \quad (14)$$

and

$$B_i = \sum_i \sin 2\pi(hx_i + ky_i + lz_i) \quad (15)$$

Thereby,  $x_i, y_i, z_i$  are the coordinates of the Wyckoff positions – and  $f_i$  is the scattering factor of the  $i$ th atoms. The scattering factor is dependent on the amount of electrons and the scattering angle. It increases with the atomic number and decreases with  $(\sin\theta)/\lambda$ . This relation explains the relatively weak scattering behaviour and low intensities of MOF crystals, since they possess a lot of free space and therefore a low structure density and since a main component of them, the organic linkers, are built of light elements. The structure factor expresses also the amplitude and the phase of the beam, which is diffracted by  $(hkl)$  planes. Besides the structure factor other factors do also affect the measured intensities such as the multiplicity factor, the temperature factor, the absorption factor as well as the Lorentz- and the polarisation factor.

### 3.2.2 Single crystal X-ray diffraction

Before a measurement can be started on an X-ray diffractometer, a suitable crystal has to be chosen. This crystal should not be twinned, should exhibit no cracks or inclusions and ideally should have defined faces and edges. In case of air and moisture sensitive materials like MOFs, the crystal is prepared from its solution in a closed glass capillary. Afterwards the prepared crystal is mounted on the diffractometer. Thereby it is centred in the primary beam and needs to be rotated around its own axis, which is done with the help of a goniometer. Then, a random trial scan is done for indexing and to receive the orientation matrix, Afterwards, the actual measurement can be executed. The generated raw data have to be processed. With the help of software programmes like CCP4<sup>222</sup> or X-Area<sup>223</sup>, the detected peaks with its count rates can be transformed into integral net intensities. For the integration process a background correction is done and the data has to be scaled, because the detected intensities are time dependent. The net intensities  $I_{Net}$  are then transformed into the structure factor  $F_0$ , which is dependent on the Lorentz factor  $L$  and on the polarisation factor  $P$  (16). Whereas the polarisation factor is independent on the measuring instrument, the Lorentz factor contains experiment specific information about the measurement geometry.

$$F_0 = \sqrt{\frac{I_{Net}}{LP}} \quad (16)$$

Thus the amplitudes of the structure factor  $F_0^2$  can be calculated as well as the standard deviation  $\sigma$  for the structure factor amplitudes and the intensities. For weak Bragg-reflections, the background correction can result in negative intensities. Therefore only Bragg-reflections with  $0 > I > -2\sigma(I)$  are considered to give trustworthy information. Intensities having values smaller than  $-2\sigma(I)$  are physically impossible and are thus omitted.

Because the X-ray beam is extenuated by various physical processes during its way through the crystal, a numerical absorption correction is normally done. However, because an absorption correction is technically not possible at some beamlines (e.g. BESSY MX BL14.2 beamline of Helmholtz Zentrum Berlin für Materialien und Energie) and because MOF crystals exhibit only small absorption coefficients, an absorption correction may be omitted.

With the known unit cell and the obtained information of the intensities of the Bragg-reflections, the space group, or at least a selection of suitable space groups, can then be

determined. The software program XPREP<sup>224</sup> can be helpful for the corresponding calculations. It calculates also the average value  $R_{int}$ , which correlates the structure factor amplitude  $F_0^2$  of one Bragg-reflection with average of the amplitudes of all structure factors  $\overline{F^2}$  that are symmetry equivalent (17). The  $R_{int}$  value gives an estimate for the quality of the collected data and the chosen crystal system.

$$R_{int} = \frac{\sum(F_0^2 - \overline{F^2})}{\sum F_0^2} \quad (17)$$

For determination of the exact positions of the atoms a Fourier transformation should be executed of the structure factors with their phases into the position depending electron density function  $\rho$  (18).

$$\rho_{xyz} = \frac{1}{V} \sum_{hkl} F_{hkl} \cdot \{ \cos[2\pi(hx + ky + lz)] + i \cdot \sin[2\pi(hx + ky + lz)] \} \quad (18)$$

The main problem is that only the modulus of the structure factors is obtained by the transformation of the intensities into amplitudes. Therefore the important phase information is lost and the phase angles cannot be determined directly. To receive this information different approaches exist, like the direct approach, the historical Patterson approach or dual-space algorithm based approaches, such as charge-flipping.

Like the name suggests, the direct method tries to find a direct solution of the phase problem, by utilizing the interrelation of the intensities of a set of Bragg-reflections with their phases. For that matter, the symmetry elements are connected with the structure factor amplitudes of particular reflection pairs by the inequations of Harker and Kasper<sup>225</sup>. Instead of the structure factor amplitudes these inequations uses the so called unitary structure factor amplitudes. They give a prediction about the portion of the electrons of a certain Bragg-reflection to the structure amplitude. Because it is difficult to compare amplitudes that are obtained by different diffraction angles, the structure factors are normalized (E-value). Of central importance is the Sayre equation<sup>226</sup> (19), which states that a structure factor of one Bragg-reflection can be obtained from the sum of products of structure factors from other Bragg-reflection pairs. One constraint is that their indices  $h'k'l'$  and  $h - h'k - k'l - l$  can be added



to the indices of the wanted Bragg-reflection. Another constraint is that the electron density must not get negative and are concentrated in punctual maxima.

$$F_{hkl} = \sum_{h'k'l'} F_{h'k'l'} \cdot F_{h-h'k-k'l-l'} \quad (19)$$

Is the phase information of an intensity rich Bragg-reflection (E-value > 2) pair known, the phase of a wanted Bragg-reflection can be determined by the so called  $\Sigma_2$  relation (20).

$$\Phi_{h'k'l'} + \Phi_{h-h'k-k'l-l'} - \Phi_{hkl} \cong 0 \quad (20)$$

The  $\Sigma_2$  relation applies to a triplet of Bragg-reflections that fulfils the Sayre equation. From this over-determined system of equations the unknown variables  $x, y, z$  can be calculated. In the beginning of a structure solution a set of Bragg-reflections with known phases is required. Afterwards, eligible reflection-triplets are selected until enough phase information of new Bragg-reflections are gathered. Then a Fourier transformation gives proposals for a reliable structure model. The software program SHELXS<sup>227</sup> works with a huge amount of Bragg-reflections, whose phases are generated statistically. Therefore a large set of solution proposals is generated, whereas not every structure is chemically reasonable. Thus, the various structure solutions are checked by the so called figures of merit (FOM). They give a valuation of the quality of the chosen structures.

The calculated atomic coordinates  $x, y, z$  contain some errors, which can be minimised by a structure refinement. The difference of the observed structure factor amplitudes  $F_0^2$  and the calculated structure factor amplitudes  $F_c^2$  should be as small as possible. The software program SHELXL<sup>228</sup> uses for this matter the method of least squares. To evaluate the quality of the obtained model for the structure, confidence factors are established. The un-weighted  $R_1$  factor is based on  $F$  and equates to the average derivation of the observed and the calculated structure factors (21). Structure solutions with  $R_1$  values smaller than 2.5% are usually considered as solutions of high quality and  $R_1$  values smaller than 5% as good solutions. In case of MOFs, poorly or non-ordered solvent molecules remain in the pores and cause residual electron density, which cannot be refined. Therefore,  $R_1$  values in a range 5-15% are considered as high quality solutions and values smaller than 30% as good solutions.

$$R_1 = \frac{\sum_{hkl} ||F_0| - |F_c||}{\sum_{hkl} |F_0|} \quad (21)$$

The weighted  $wR_2$  factor refers to the structure factor amplitudes. It gives the derivation of the observed and calculated structure factor amplitudes, taking the error sums of squares into account (22). In general this confidence factor has higher values than the  $R_1$  factor.

$$wR_2 = R_w(F^2) = \sqrt{\frac{\sum_{hkl} w (F_0^2 - F_c^2)^2}{\sum_{hkl} w (F_0^2)^2}} \quad (22)$$

In contrast to the  $R$  factors, the goodness of fit (GooF or  $S$ ) is independent of the signal-to-noise ratio. It refers also on the structure factor amplitudes, but takes also the number of independent Bragg-reflections  $N_{Ref}$  and the number of parameters  $N_{Par}$  into account (23). The GooF should always approach the value 1. If it is higher than 1, a poor model was applied.

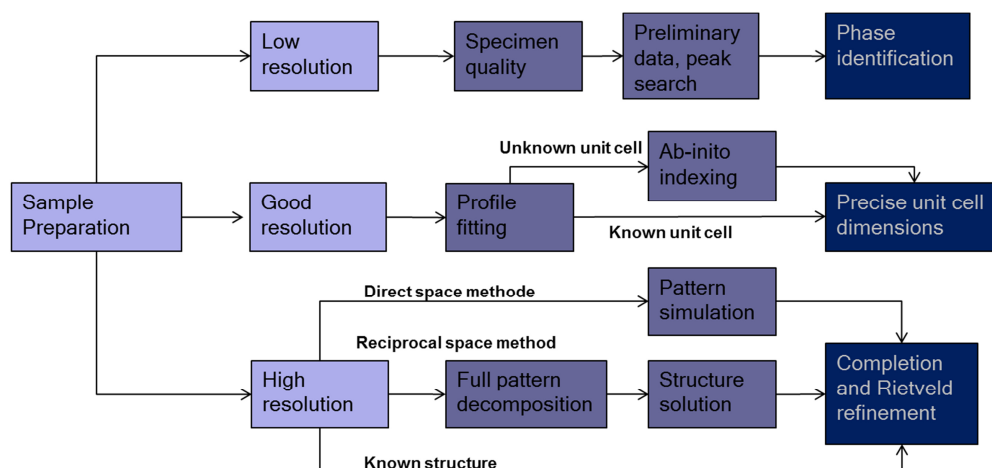
$$GooF = S = \sqrt{\frac{\sum_{hkl} w (F_0^2 - F_c^2)^2}{N_{Ref} - N_{Par}}} \quad (23)$$

In case of MOFs, the unordered solvent molecules inside the pore system are responsible for a diffuse scattering contribution. Because of their non-periodicity their exact positions cannot be determined. Therefore, the confidence factors have relatively high values. The software program SQUEEZE<sup>229</sup> generates a new set of Bragg-reflections, wherein all Bragg-reflections are omitted that are not assigned to a located atom of the structure. Thus, the values of the confidence factors get smaller. The program adapts the raw data to the determined structure model and should therefore be used with caution.

### 3.2.3 Powder X-ray diffraction

A different situation applies to powder X-ray diffraction. In contrast to the single X-ray diffraction, not only one crystal is measured, but many. The crystals of the powder sample are distributed and randomly orientated. The X-ray beam is therefore diffracted by a statistically oriented number of lattice planes, which are orientated in such a way that the Bragg-equation

is fulfilled. Thus, the obtained data is a projection of a three-dimensional reciprocal space onto a one-dimensional space, which results in overlapping Bragg-reflections. Only the information about the length of the reciprocal lattice vectors remains, the information about their directions is lost. It can be therefore very challenging to extract structure factors for a structure solution from a powder diffraction pattern. Nevertheless, a structure solution from powder diffraction patterns can be expedient. For example, the size of crystals is sometimes too small for single X-ray diffraction measurements. In general, multiple information can be obtained by powder diffraction patterns, depending on their quality (Figure 22).



**Figure 22.** Schematic overview of powder X-ray diffraction analysis.<sup>230</sup> Adapted from Vitalij Pecharsky, P. Z., *Fundamentals of Powder Diffraction and Structural Characterization of Materials*, Second Edition. Springer US: 2009.

A powder diffraction pattern, generated by a fast experiment of several minutes or hours can give information about the specimen quality and be used for phase identification. Since the positions of the Bragg-reflections in diffraction pattern are characteristic for each compound, they can be compared with calculated diffraction patterns for a given structure or with diffraction patterns that are deposited in data bases<sup>231-237</sup>. By the shape and the broadening of the Bragg-reflections, an estimation of the degree of crystallinity can be done. Also the background gives information about the existence or the portion of an amorphous phase, respectively.

For generating good resolution diffraction patterns, it is sometimes necessary to perform multiple measurements, wherein the discrete scans are summed. With such a diffractogram, more information can be extracted, such as the crystal system, the Bravais type, the unit cell dimensions or space group symmetry. The positions of the Bragg-reflections are related to the lattice parameters, whereas their intensities contain information about the positions of atoms

in the unit cell. Therefore, it is crucial to determine the exact positions of the individual Bragg-reflections. For that reason, the shapes of individual Bragg-reflections are fitted to suitable profile functions. As mentioned, Bragg-reflections are overlapping and may contain  $K\alpha_1$  and  $K\alpha_2$  components. The intensity the  $i^{\text{th}}$  point  $Y(i)$  of an  $k^{\text{th}}$  Bragg-reflection is assembled by the contributions of  $m$  overlapped individual Bragg-reflections and can be expressed by the following generalised equation (24):

$$Y(i) = b(i) + \sum_{k=1}^m I_k [y_k(x_k) + 0.5y_k(x_k + \Delta_{xk})] \quad (24)$$

wherein  $b(i)$  is the background,  $y(k)$  is the contribution from the individual Bragg-reflection  $m$  ( $1 \leq k \leq m$ ) to the  $k^{\text{th}}$  Bragg-reflection's intensity  $I_k$ ,  $x_k = 2\theta_i - 2\theta_k$ , and  $\Delta_{xk}$  is the difference between the Bragg-angles of  $K\alpha_1$  and  $K\alpha_2$  components, if present.<sup>230</sup>

The most common profile functions are the Gauss function (25), the Lorentz function (26), the Pseudo-Voigt function (27) and the Pearson-VII function (28).

$$y(x) = G(x) = \frac{C_G^{1/2}}{\sqrt{\pi}H} e^{-C_G x^2} \quad (25)$$

$$y(x) = L(x) = \frac{C_L^{1/2}}{\pi H} (1 + C_L x^2)^{-1} \quad (26)$$

$$y(x) = PV(x) = \eta \frac{C_G^{1/2}}{\sqrt{\pi}H} e^{-C_G x^2} + (1 - \eta) \frac{C_L^{1/2}}{\sqrt{\pi}H} (1 + C_L x^2)^{-1} \quad (27)$$

$$y(x) = PVII(x) = \frac{\Gamma(\beta)}{\Gamma(\beta - 1/2)} \frac{C_P^{1/2}}{\sqrt{\pi}H} (1 + C_P x^2)^{-\beta} \quad (28)$$

The variable  $x$  consists of the difference between the Bragg-angle of the  $i$ th point  $\theta_i$  and the ideal Bragg-angle  $\theta_k$  of the  $k$ th Bragg-reflection, divided by the full width at half maximum  $H$  (26).  $C_G, C_L, C_P$  are normalization factors for the particular profile function. Since the Pseudo-Voigt function is composed of the Gauss-function and the Lorentz-function, the mixing parameter  $\eta$  gives the fractional contribution of the Gauss-function to the linear combination of the both profile functions  $G(x)$  and  $L(x)$ .  $\Gamma$  is the gamma-function  $\Gamma(z) = \int_0^\infty t^{z-1} \cdot e^{-t} dt$  which was established by Caglioti et al.<sup>238</sup>, whereas  $\beta$  consists of the free variables  $\beta_0, \beta_1, \beta_2$  and is related to the Bragg-angle by  $\beta = \beta_0 + \frac{\beta_1}{2\theta} + \frac{\beta_2}{(2\theta)^2}$ . The full width at half-maximum (FWHM)  $H$ , which applies to the Gauss-function, the Pseudo-Voigt function and the Pearson-

VII function, is known as the Caglioti formula (29). It consists of the free variables  $U, V$  and  $W$ .

$$H = \sqrt{U \tan^2 \theta + V \tan \theta + W} \quad (29)$$

For the Lorentz-function, the FWHM  $H'$  is differently calculated by the equation (30):

$$H' = \frac{U}{\cos \theta + V \tan \theta} \quad (30)$$

Depending on various instrumental factors, such as axial divergence, or non-ideal specimen geometry, the Bragg-reflections can exhibit an asymmetric shape, which is also dependent on the Bragg-angle. The asymmetry can be corrected by the intensity correction  $A(x_i)$  (31), whereas the asymmetric parameter  $\alpha$  is a free variable and  $z_i$  is defined as  $z_i = 2\theta_i - 2\theta_k$ .

$$A(x_i) = 1 - \alpha \frac{z_i \times |z_i|}{\tan \theta} \quad (31)$$

The precise determination of the Bragg-angles is crucial for a correct indexing, where the accurate value of  $d_{hkl}^*$  is needed. An *ab-initio* indexing has to be done, if no prior knowledge about unit cell dimensions and symmetry of the lattice exist. Then, Miller indices can be assigned only by the relationships between the Bragg-angles and the indexing becomes often a trial-and-error process. The higher the lattice symmetry is the lower is the probability for the existence of lattice vectors of the same length but different directions and the easier the indexing gets. The simplest case is the indexing of a cubic crystal system, where only one lattice parameter has to be determined instead of six (triclinic crystal system). As mentioned in the previous chapter (3.2.2), the interplanar distances are related with the  $hkl$  triplets and the lattice parameters by the quadratic Bragg equation. With the help of this equation the values of the corresponding  $hkl$  triplets can be determined and the indexing can be completed. But a manual indexing of lower symmetry lattices is extremely difficult and therefore done with the use of software programs such as DICVOL04<sup>239</sup> or TREOR90<sup>240</sup>, which utilizes various algorithms for an automatic indexing is crucial<sup>230</sup>. If the unit cell dimensions are known approximately, the indexing of Bragg-reflections becomes easier. Then, a list of all possible combinations of  $hkl$  triplets that are symmetrically independent is arrayed. Using this  $hkl$  triplet list and the best estimated unit cell dimensions, the corresponding interplanar distances are calculated. Afterwards, the  $hkl$  triplets are assigned to the observed Bragg-reflections so that the difference between the observed interplanar distance and the calculated  $d_{hkl}$  are minimized. Thus, the Bragg-angles can be now utilized

together with the assigned  $hkl$  triplets to refine the unit cell dimensions and to determine the space group.

To solve the crystal structure, a high resolution diffraction pattern with a high intensity to noise ratio is required. In general, a structure solution can be done by two different approaches. One approach is the direct space method, which does not include structure factors. Instead, a crystal structure is modelled in the direct space. For this task, different techniques can be utilized, such as purely geometrical modelling, testing different packing and conformations or minimization and optimization methods (including quantum-chemical energy, entropy, geometry optimizations). Also analogies with similar compounds can be of great help. For the direct space method, it is important to have an idea about the wanted structure. An advanced software program for structure modelling is Material Studio<sup>241</sup>, which can be recommended. After the assumed structure is modelled, a theoretical powder diffraction pattern can be calculated and checked against the experimental one.

If the structure is unclear, the reciprocal space method is applied. It uses procedures, which were originally established for structure solutions of single crystals, such as the Patterson method, the direct methods or charge flipping (see chapter 3.2.2). In contrast to the direct space method, the reciprocal space methods rely on the determination of structure factor amplitudes. These can only be calculated if the intensities of the corresponding Bragg-reflections  $I_{hkl}$  can be extracted by integration. Because of overlapping Bragg-reflections, the integration is often difficult. Therefore a decomposition of the diffraction pattern is required. This can be done by the so called full pattern decomposition techniques, established by Pawley<sup>242</sup> and Le Bail<sup>243</sup>.

The algorithm of Le Bail's method involves a refining of unit cell- and profile parameters. The first step of a Le Bail fit is to set all Bragg-reflection intensities to an arbitrary value and to label them as  $I_{calc}$ . The profile points  $y_{i(calc)}$  are then partitioned into pseudo-observed profile points, based on the profile functions (25-28). If an observed peak is composed of  $k$  Bragg-reflections, a set of  $k$  equations is required, where all profile points  $i$  are summated to pseudo-observed intensities (32).

$$\begin{aligned}
 I_{obs(1)} &= \sum \frac{y_{i(obs)} \times y_{i(1)}}{y_{i(calc)}} \\
 I_{obs(2)} &= \sum \frac{y_{i(obs)} \times y_{i(2)}}{y_{i(calc)}} \\
 &\vdots \\
 I_{obs(k)} &= \sum \frac{y_{i(obs)} \times y_{i(k)}}{y_{i(calc)}}
 \end{aligned} \tag{32}$$

Thereby the pseudo-observed intensities of the  $i^{\text{th}}$  point of the  $k^{\text{th}}$  reflection are adding up to the calculated profile point (33).

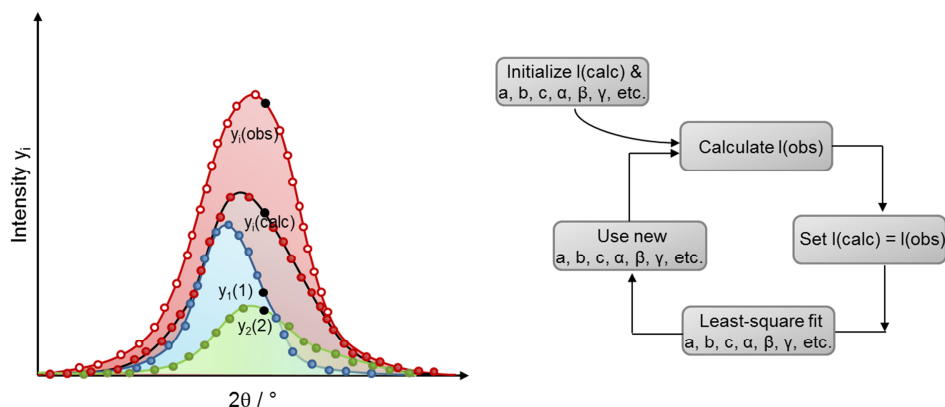
$$y_{i(\text{calc})} = y_{i(1)} + y_{i(2)} + \dots + y_{i(k)} \quad (33)$$

The pseudo-observed intensities of the Bragg-reflections are then used for a least-square fitting of the diffraction profile, wherein  $I_{\text{calc}}$  is set equal to  $I_{\text{obs}}$ . By doing so, the cell parameters (position of Bragg-reflections), the resolution of function parameters, such as the FWHM, and peak shape parameters can be refined. The process is iterated for several times. Each time, a new set of pseudo-observed intensities is calculated, which convert more and more to the true  $I_{hkl}$  (Figure 23). Based on these integrated intensities the structure factors amplitudes can be calculated and used to solve the structure.

The structure refinement is also based on the partitioning of observed profile points  $y_{i(\text{obs})}$  into  $y_{i(\text{calc})}$  based on the structural model obtained from the *ab initio* solution or structural analogy taking atomic positions and lattice constants into account. This technique was originally invented by Rietveld<sup>244</sup> in 1969. The Rietveld refinement utilizes the method of least-squares to minimize the difference between the calculated and the observed profile points (34),

$$\Delta = \sum_i w_i (y_{i(\text{obs})} - \frac{1}{c} y_{i(\text{calc})})^2 \quad (34)$$

wherein  $w_i$  is the statistical weight and  $c$  is a scale factor.



**Figure 23.** Schematic illustration (left) and process (right) of the whole pattern fitting *via* the LeBail method. The observed profile is displayed as a red line with white circles, the calculated one as a black line with red circles. The observed profile of peak 1 is shown as blue circles and of peak 2 as green circles.<sup>245</sup> Adapted from Dr. J. K. Cockcroft, P. P. B., Dr. M. P. Attfield, and others Advanced Certificate in Powder Diffraction on the Web. <http://pd.chem.ucl.ac.uk/pdnn/solve1/leball.htm> (accessed 30.06.2017).

Sometimes, the experimental intensities of a diffraction pattern do not fit the calculated ones, because of texture effects. If the crystallites exhibit a plate-like or a needle-like morphology, the correction factor  $P$  needs to be implemented in the Rietveld refinement. The correction factor is expressed in the Rietveld-Toraya equation (35) and depends on the refineable preferred orientation parameters  $G_1$  and  $G_2$ , as well as on the angle  $\alpha$  between the normal to the diffraction plane and the symmetry axis of the crystallites.

$$P = G_2 + (1 - G_2) \cdot e^{-G_1 \alpha^2} \quad (35)$$

To evaluate the quality of the Rietveld refinement, agreement factors are established. The profile factor  $R_p$  and the weighted profile factor  $R_{wp}$  are given in equation (36) and (37).

$$R_p = \frac{\sum_i |y_{i(obs)} - y_{i(calc)}|}{\sum_i y_{i(obs)}} \quad (36)$$

$$R_{wp} = \sqrt{\frac{\sum_i w_i (y_{i(obs)} - y_{i(calc)})^2}{\sum_i w_i (y_{i(obs)})^2}} \quad (37)$$

In contrast to the profile factors, where the deviation of the calculated and the observed profile points  $y_i$  is calculated, the Bragg-R-factor (38) takes the intensities of each Bragg-reflection into account.

$$R_B = \frac{\sum_k |I_{k(obs)} - I_{k(calc)}|}{\sum_k I_{k(obs)}} \quad (38)$$



## 4. EXPERIMENTAL PART

### 4.1 Used chemicals

Table 3. List of used chemicals.

Chemical	Formula	Purity	Producer
Acetone, dry	$(\text{CH}_3)_2\text{CO}$	99.8%	Acros Organics
Acetonitrile, dry	$\text{CH}_3\text{CN}$	99.8%	Sigma Aldrich
Ammonium nitrate	$\text{NH}_4\text{NO}_3$	p.a.	Sigma Aldrich
Ammonium sulfate	$(\text{NH}_4)_2\text{SO}_4$	99.0%	Sigma Aldrich
Benzene, dry	$\text{C}_6\text{H}_6$	99.8%	Sigma Aldrich
Benzene-1,4-dicarboxylic acid	$\text{C}_6\text{H}_4(\text{CO}_2\text{H})_2$	99.0%	Acros Organics
Benzoic acid	$\text{C}_6\text{H}_5\text{CO}_2\text{H}$	99.5%	Grüssing
Biphenyl-4,4'-dicarboxylic acid	$(\text{C}_6\text{H}_4)_2(\text{CO}_2\text{H})_2$	97.0%	Sigma Aldrich
2-Butanol, dry	$\text{C}_4\text{H}_9\text{OH}$	99.5%	Sigma Aldrich
Cyclohexane, dry	$\text{C}_6\text{H}_{12}$	99.5%	Sigma Aldrich
Cyclohexanone	$\text{C}_6\text{H}_{10}\text{O}$	>99.0%	Sigma Aldrich
Deuterium chloride solution	$\text{DCl}$ (35%)	>99.0%	Sigma Aldrich
Dichlormethane, dry	$\text{CH}_2\text{Cl}_2$	>99.8%	Sigma Aldrich
Diethylether, dry	$(\text{CH}_3\text{CH}_2)_2\text{O}$	>99.0%	Sigma Aldrich
N,N-Dimethylformamid	$(\text{CH}_3)_2\text{NCHO}$	p.a.	ABC R GmbH
1,4-Dioxane, dry	$(\text{CH}_2)_2\text{O}_2$	99.8%	Sigma Aldrich
Ethanol	$\text{CH}_3\text{CH}_2\text{OH}$	99.0%	ABC R GmbH
Ethanol, dry	$\text{CH}_3\text{CH}_2\text{OH}$	>99.8%	Sigma Aldrich
Ethyl acetate, dry	$\text{CH}_3\text{CH}_2\text{OCOCH}_3$	99.8%	Sigma Aldrich
Formic acid	$\text{HCO}_2\text{H}$	99.0%	Grüssing
9-Fluorenone-2,7-dicarboxylic acid	$\text{CO}(\text{C}_6\text{H}_3)_2(\text{CO}_2\text{H})_2$	85.0 %	Fluorochem Ltd.
Hafnium chloride	$\text{HfCl}_4$	98.0%	Sigma Aldrich
n-Heptane, dry	$(\text{CH}_2)_5(\text{CH}_3)_2$	99.0%	Sigma Aldrich
n-Hexadecane, dry	$(\text{CH}_2)_{14}(\text{CH}_3)_2$	99.0%	VWR chemicals
Hydrochloric acid	$\text{HCl}$ (37%)	p.a.	Merck
L-(+)-Lactic acid in water	$\text{C}_3\text{H}_6\text{O}_3$ (50%)	>99.0%	Sigma Aldrich
Magnesium chloride hexahydrate	$\text{MgCl}_2 \cdot 6\text{H}_2\text{O}$	99.0%	Sigma Aldrich
(R)-(-)-Mandelic acid	$\text{C}_6\text{H}_5\text{CH}(\text{OH})\text{CO}_2\text{H}$	98%	Sigma Aldrich
Methanol, dry	$\text{CH}_3\text{OH}$	99.8%	Sigma Aldrich
N-methyl-2-pyrrolidione	$\text{CH}_3\text{N}(\text{CH}_2)_3\text{CO}$	99.0%	ABC R GmbH
Nitrogen 5.0	$\text{N}_2$	0.99999	Air Liquide
Pentafluorobenzoic acid	$\text{C}_6\text{F}_5\text{CO}_2\text{H}$	99.0%	Alfar Aesar
Potassium acetate	$\text{KCH}_3\text{CO}_2$	99.0%	Grüssing
Potassium carbonate	$\text{K}_2\text{CO}_3$	99.0%	Grüssing
Potassium iodide	$\text{KI}$	p.a.	AppliChem
Potassium nitrate	$\text{KNO}_3$	>99.0%	Sigma Aldrich
1-Propanol, dry	$\text{CH}_3(\text{CH}_2)_2\text{OH}$	99.7%	Sigma Aldrich

2-Propanol, dry	$(\text{CH}_3)_2\text{CHOH}$	99.5%	Sigma Aldrich
Propionic acid	$\text{CH}_3\text{CH}_2\text{CO}_2\text{H}$	99.5%	Alfar Aesar
Sodium chloride	$\text{NaCl}$	99.0%	Chemsolute
Sodium hydroxide	$\text{NaOH}$	97.0%	VWR chemicals
Sulphuric acid	$\text{H}_2\text{SO}_4$	98.0%	Merck
DL-Tartaric acid	$\text{HOOC}(\text{CHOH})_2\text{COO}$	>99%	TCI
Tetrahydrofuran	$\text{H}$	>99.9%	Sigma Aldrich
2,5-Thiophenedicarboxylic acid	$(\text{CH}_2)_4\text{O}$	99.0%	TCI
Toluene, dry	$(\text{CH})_2\text{C}_2(\text{CO}_2\text{H})\text{S}$	99.8%	Sigma Aldrich
Trifluoroacetic acid	$\text{C}_6\text{H}_5\text{CH}_3$	99.0%	Alfar Aesar
4-Trifluoromethylbenzoic acid	$\text{CF}_3\text{CO}_2\text{H}$	98.0%	Alfar Aesar
Zirconium (IV) chloride	$\text{CF}_3\text{C}_6\text{H}_4\text{CO}_2\text{H}$ $\text{ZrCl}_4$	98.0%	Sigma Aldrich

## 4.2 Instrumental Setup<sup>†</sup>

### 4.2.1 Physisorption measurements

*Nitrogen physisorption* measurements were performed on BELSORP-max (MicrotracBEL, Japan) apparatus at 77 K up to 1 bar. For the measurements, high purity nitrogen gas was used (99.999%). The pore size distribution was determined with the help of DFT calculations. The applied Kernel is based on the NLDFT adsorption branch model and originally developed for silica materials with cylindrical pores.

*Water vapour physisorption* measurements were performed on a Hydrosorb 1000 apparatus (Quantachrome Co.) at 298 K with an equilibration time of 300 s for adsorption and desorption processes.

Before all adsorption measurements, the samples were outgassed in vacuum ( $p < 100$  Pa) at 373 K for at least 12 hours.

<sup>†</sup> parts of this chapter were literally adopted from publications<sup>246-248</sup>

Reprinted with permission from F. Drache, V. Bon, I. Senkovska, M. Adam, A. Eychmüller, and S. Kaskel, Vapochromic Luminescence of a Zirconium-Based Metal–Organic Framework for Sensing Applications, *European Journal of inorganic chemistry* 2016, 2016, 4483-4489. Copyright 2016 John Wiley and Sons.

Reprinted with permission from F. Drache, V. Bon, C. Marschelke, A. Synytska, and S. Kaskel, Postsynthetic Inner-Surface Functionalization of the Highly Stable Zirconium-Based Metal–Organic Framework DUT-67, *Inorganic Chemistry* 2016, 55, 7206-7213. Copyright 2016 American Chemical Society.

Reprinted with permission from F. Drache, V. Bon, I. Senkovska, J. Getzschmann, and S. Kaskel, The modulator driven polymorphism of Zr(IV) based MOFs, *Philosophical Transactions of the Royal Society A: Physical and Engineering Sciences* 2017, 375 by permission of the Royal Society.

#### 4.2.2 Thermogravimetric – and differential thermal analysis

The thermogravimetric analysis (TG) and differential thermal measurements (DTA) were performed on a STA 409 PC Luxx (Netzsch) thermal analyser in air with a heating rate of 2 K/min (range: 25-1000 °C).

#### 4.2.3 Elemental analysis

The CHN elemental analysis (EA) was performed using CHNS 932 analyzer (*LECO*).

#### 4.2.4 Nuclear magnetic resonance measurements

The  $^1\text{H-NMR}$  spectra were recorded on a Bruker DRX 500 P spectrometer at 500.13 MHz. The spectra were referenced against the deuterated solvent dimethyl sulfoxide (DMSO). The  $^{19}\text{F-NMR}$  spectra were carried out at 282.38 MHz on a Bruker AC 300 P. MOF digestion for NMR studies was achieved by mixing a small amount (ca. 15 mg) of CsF with 3 drops of deuterated hydrochloric acid (DCI) and adding this mixture to the same amount of sample under investigation. After 6 hours deuterated DMSO (0.9 ml) was added as well as  $\text{K}_2\text{CO}_3$  for neutralization of hydrochloric acid.

#### 4.2.5 Contact angle measurements

Contact angles were measured by the sessile drop method using a conventional contact angle and drop contour analysis system OCA 35 XL (DataPhysics Instruments GmbH, Germany). All measurements were carried out at 24 °C and 40% relative humidity. Deionized water was used for the measurements. Due to pinning effects, water receding angles could not be measured exactly.

#### 4.2.6 Scanning electron microscopy

The scanning electron microscopy (SEM) was carried out using a ZEISS DSM-982 Gemini and a SU8020 Hitachi with a detector system for secondary and low energy backscattered electrons.

#### 4.2.7 Gas chromatography coupled with mass spectrometry

For tracing the progress of the catalysis reactions, a Shimadzu gas chromatograph GC-17A coupled with a mass spectrometer QP5000 was used. A non-polar BPX5 column (SGE) with 5% of phenyl polysilphenylene-siloxane was utilized. As internal standard a 0.125 mol L<sup>-1</sup> solution of n-hexadecane in 2-propanol was applied.

#### 4.2.8 Luminescence Measurements

The *UV-VIS* absorption spectra were measured on a Cary 4000 (Varian) spectrophotometer and fluorescence spectra were recorded on a Cary Eclipse (Varian) fluorescence spectrophotometer. The determination of the spectrum maxima was done by calculating the zero of the derivation of the measured spectrum profiles. The error bars were calculated by preparing and measuring the spectra of DUT-122 in argon atmosphere for 20 times. The variation of the calculated spectrum maxima of these measurements was used for calculating the standard deviation (1.9 nm), which is used as error bar.

The fluorescence measurements were performed under argon atmosphere at room temperature in a quartz-glass cell with a cover slip mounted inside. The dried (in vacuum at 120 °C for at least 12 h) powder samples were fixed on the cover slip by double-faced adhesive tape in argon atmosphere in a glove box. The prepared samples were positioned in an angle of 45° in reference to the detector. For the measurements where a saturated solvent atmosphere was needed, 1 ml of dry solvent was placed into the sealed quartz cell. The measurement was started immediately after the solvent addition. For experiments involving water, the samples were exposed to the corresponding relative humidity in a desiccator. The desired relative humidity was achieved with the aid of saturated solutions of different salts. Up to a relative humidity of 75%, the MOF was exposed to the water vapour containing atmosphere for five minutes. At higher relative humidity, longer contact time was needed, so that the equilibration time was extended to 24 hours.

Photoluminescence lifetime measurements were conducted using a FluoroLog-3 spectrofluorometer (Horiba Jobin Yvon). The instrument was operated with a TCSPC module and pulsed light emitting diodes (LEDs) ( $\lambda_{\text{ex}} = 290 \text{ nm}$ ,  $\lambda_{\text{ex}} = 368 \text{ nm}$ ,  $\lambda_{\text{ex}} = 410 \text{ nm}$ ) at room temperature. For evaluating the response time (prompt) of the device at certain excitation wavelengths, a non-luminescent scatterer was measured, respectively. The fluorescence decay profiles were fitted by a multi exponential decay function. The fluorescence lifetimes were determined by setting the fluorescence intensity equal to  $10\,000/e$  and calculating the corresponding time of this value.

Photoluminescence quantum yield determinations experiments were performed on a FluoroLog-3 spectrofluorometer (Horiba Jobin Yvon) equipped with a Quanta- $\Phi$  integrating sphere. The MOF crystals and the fine powder of the linker were placed in a Spectralon-holder and covered by quartz-glass slip. The measurements were performed at room temperature.

#### 4.2.9 Crystal structure simulation

The crystal structures of functionalized DUT-67(Zr) materials were simulated using visualization module of Material Studio 5.0 software<sup>241</sup>. In order to obtain the substituted structure, consistent with the material composition, the symmetry of the crystal structure was reduced from  $Fm\bar{3}m$  (original structure) to  $Pa\bar{3}$ . Subsequently two modulator and one N,N-dimethylformamide (DMF) molecules were modelled in such a way that two modulator molecules are positioned in the cuboctahedral pores and DMF in the smallest octahedral cage. The geometry optimization tool with universal force field was used for the final structure optimization. The residual five positions of the terminal ligands are occupied by water molecules. The numbers of terminal ligands that are coordinated to the Zr cluster were derived from <sup>1</sup>H-NMR spectra, whereas their positions in the pore system were estimated by water vapour adsorption isotherms.

These structural models were used for the calculation of the pore size distribution using Zeo++ program<sup>249</sup>. A probe radius of 1.2 Å and bin size of 0.1 Å were used for the calculations.

#### 4.2.10 X-ray diffraction

Powder X-ray diffraction data were collected on a STOE STADI P diffractometer with  $\text{Cu-K}\alpha_1$  radiation ( $\lambda = 1.5405 \text{ \AA}$ ) at room temperature. The samples were placed between two sheets of adhesive tapes and measured in transmission mode. In case of temperature programmed X-ray diffraction measurements, the samples were prepared in quartz glass capillaries.

For the structure solution of DUT-126, a high-resolution PXRD pattern was measured on a laboratory powder diffractometer STOE STADI P, equipped with  $\text{Cu-K}\alpha_1$  monochromatic radiation and gas-filled 0D detector in transmission geometry using a capillary setup as a rotating sample holder. The data was collected in  $2\theta$  range of 1.5-90°. The PXRD pattern was indexed using the software program DICVOL91 program<sup>250</sup>. The obtained cell was imported to the Material Studio 5.0 program<sup>251</sup>, where Pawley refinement was performed using Reflex module. After analysing the extinction conditions, the space group  $P6/mmm$  was used for the structure solution. The positions of the  $\text{Zr}_6(\mu_3\text{-O})_4(\mu_3\text{-OH})_4$  clusters were located using the simulated annealing technique. In the next step, the ligand molecules were modelled in visualisation module of the program. The geometrical optimization without optimization of the unit cell was performed using Universal Force Field. The resulting structure was used as a starting model for the Rietveld refinement. Due to the poor data-to-parameter ratio in the

structure as well as reflection overlap at higher  $2\theta$  angles, some functional groups like carboxylates and thiophene moieties were refined as rigid bodies. The final structural model was obtained after hybrid Rietveld refinement with energy tool, built-in the Reflex tool (energy contribution 1%).

For the structure solution of DUT-122(Zr), DUT-122(Hf) and DUT-67(Zr)\_HCl, single crystal X-ray diffraction was used. The single crystals were placed into the glass capillary of 0.3 mm diameter with a small amount of solvent and sealed with melted wax. The dataset for DUT-122(Zr) and DUT-67(Zr) HCl was measured at BESSY MX BL14.2 beamline of Helmholtz Zentrum Berlin für Materialien und Energie. Diffraction experiments were performed at room temperature using the radiation with energy of 14 keV ( $\lambda = 0.88561 \text{ \AA}$ ). The  $\phi$ -scans with oscillation range of  $1^\circ$  were used for data collection. The images were integrated and scaled using CCP4 software package<sup>222</sup>. The data for DUT-122(Hf) were collected on a laboratory diffractometer STOE IPDS-II, equipped with monochromatic Mo- $K_\alpha$  radiation (graphite monochromator,  $\lambda = 0.71073 \text{ \AA}$ ). The dataset was integrated using X-Area software<sup>223</sup>. The numerical absorption correction was performed considering the real orientation of the single crystal on the diffractometer. The crystal structures were solved by direct methods and refined by full matrix least-squares on  $F^2$  using SHELX software<sup>228</sup>. All non-hydrogen atoms were refined in anisotropic approximation. Hydrogen atoms were refined in geometrically calculated positions using the “riding model” with  $U_{\text{iso}}(\text{H}) = 1.2U_{\text{iso}}(\text{C})$ . During the refinement of the structures, the positional disorder of the  $\mu_3$ -O3 and O4 atoms has been detected in all structures.

After refinement of the DUT-67(Zr)\_HCl framework, the position of the Cl<sup>-</sup> anion was determined from the difference Fourier map. The occupancy of the Cl<sup>-</sup> anion was refined free and then fixed in the final refinement cycle. In the final refinement, SWAT instruction was used in order to model the diffused solvent molecules in the pores.

The carbon atoms C2-C14 and O7 oxygen atom of DUT-122(Zr) and DUT-122(Hf) are affected by disorder showing obviously slight vibration of the fluorenone moiety with respect to the carboxylates. All trials to treat this disorder by splitting into two positions failed, therefore, similarity (SIMU, DELU) restraints were used during structure refinement. Because of the high symmetry of the crystal system, it was not possible to localise the disordered lattice solvent molecules in the pores. Therefore, SQUEEZE procedure<sup>229</sup> was used to correct reflection intensities, corresponding to disordered solvent molecules.

### 4.3 Synthetic protocols<sup>†</sup>

#### 4.3.1 Synthesis of metal-organic frameworks

##### Synthesis of UiO-66

An amount of 6.8 mmol of the metal precursor  $ZrCl_4$  (1.58 g) was dissolved in 390 ml of DMF by sonication for 10 minutes under atmospheric conditions. Afterwards, 6.15 mmol of 1, 4-benzenedicarboxylic acid (1.02 g) were added and the mixture was sonicated again for five minutes. Then, 30 eq of benzoic acid (24.9 g, 200 mmol) were added and the resulting mixture was placed into an oven for 96 h at 120 °C. The white precipitate was washed several times with DMF and then with ethanol. The drying process was done in vacuum at 120 °C.

##### Synthesis of UiO-67

An amount of 4.35 mmol (1 g) of  $ZrCl_4$  was dissolved in 400 ml DMF by sonication for 10 min in a 1 litre flask under atmospheric conditions. Afterwards, 4.13 mmol (1 g) of 4,4'-biphenydicarboxylic acid were added to the resulting solution and was sonicated for five more minutes. Then, 18.6 ml (325 mmol) of acetic acid was added and the resulting mixture was placed into an oven for three days at 120 °C. The resulting powder was separated, washed several times with DMF and after that the DMF was exchanged with ethanol. The powder was filtrated and dried under vacuum at 120 °C.

##### Synthesis of DUT-51

The metal precursor  $ZrCl_4$  (933 mg, 4 mmol) was dissolved together with dithieno[3,2-b;2',3'-d]-thiophene-2,6-dicarboxylic acid ( $H_2dttdc$ ) (710 mg, 2.5 mmol) in 16 ml DMF by sonication for five minutes under atmospheric conditions. Afterwards, 8 ml of formic acid and 16 ml of acetic acid were added to the solution, which was then sonicated again. The solution

---

<sup>†</sup> parts of this chapter were literally adopted from publications<sup>246-248</sup>

Reprinted with permission from F. Drache, V. Bon, I. Senkovska, M. Adam, A. Eychmüller, and S. Kaskel, Vapochromic Luminescence of a Zirconium-Based Metal–Organic Framework for Sensing Applications, *European Journal of inorganic chemistry* 2016, 2016, 4483-4489. Copyright 2016 John Wiley and Sons.

Reprinted with permission from F. Drache, V. Bon, C. Marschelke, A. Synytska, and S. Kaskel, Postsynthetic Inner-Surface Functionalization of the Highly Stable Zirconium-Based Metal–Organic Framework DUT-67, *Inorganic Chemistry* 2016, 55, 7206-7213. Copyright 2016 American Chemical Society.

Reprinted with permission from F. Drache, V. Bon, I. Senkovska, J. Getzschmann, and S. Kaskel, The modulator driven polymorphism of Zr(IV) based MOFs, *Philosophical Transactions of the Royal Society A: Physical and Engineering Sciences* 2017, 375 by permission of the Royal Society.

was transferred into a 50 ml Teflon-lined stainless steel autoclave and placed into an oven for 24 h at 120 °C. The resulting powder was filtered and washed several times with DMF. After that, the solvent was exchanged with ethanol and activated in vacuum at 100 °C for 12 h. Yield 75%.

#### Synthesis of DUT-122

The metal precursor (116 mg  $ZrCl_4$  or 160 mg  $HfCl_4$ , 0.5 mmol) was dissolved in DMF (25 ml) by sonication for 10 minutes under atmospheric conditions. Then 1 eq. of 9-fluorenone-2,7-dicarboxylic acid ( $H_2fdc$ ) (134 mg, 0.5 mmol) were added to the solution, as well as 30 eq. (1833 mg, 15' mol) of benzoic acid (HBa). The solution was sonicated for another 10 minutes. The mixture was sealed in a 50 ml vessel and heated to 120 °C for 2 days. After this treatment, small yellow octahedral shaped crystals were obtained. The resulting MOF was washed several times with DMF and activated at 120 °C in vacuum. Yield: 82%.

#### Synthesis of DUT-126

A solution of  $ZrCl_4$  (230 mg, 1 mmol) in DMF and N-Methyl-2-pyrrolidone (NMP) mixture (1:1, 50 ml) was sonicated for 10 min under atmospheric conditions. 2,5-thiophenedicarboxylic acid ( $H_2tdc$ ) (110 mg, 0.67 mmol) was added afterwards and the mixture was sonicated for additional 10 min. After that, the modulating agent trifluoroacetic acid (50 eq, 3810  $\mu$ l) was added. The resulting solution was transferred into a pressure tube and heated up to 120 °C and annealed for two weeks. After cooling down, the resulting precipitate was washed several times with DMF and dried in vacuum at 120 °C. Yield: 73%.

#### Synthesis of DUT67-Fa

$ZrCl_4$  (1.38 g, 6 mmol) was dissolved in 150 ml of a mixture of DMF and NMP (1:1 volume ratio) by sonication for 10 minutes under atmospheric conditions. 2, 5-thiophenedicarboxylic acid (0.66 g, 4 mmol) was added and the mixture was sonicated for five more minutes. Then, the modulating agent formic acid (26.8 ml, 120 eq) was added. The resulting mixture was placed into an oven for 48 h at 120 °C. The product (further denoted as DUT-67-Fa) was filtered, washed several times with DMF and ethanol and dried in vacuum at 120 °C. Yield: 89%.



### Synthesis of DUT-67-Ac

DUT-67-Ac is synthesised with the same procedure, but instead of formic acid, 150 eq of acetic acid (HAc) were used as modulating agent. Yield: 87%.

### Synthesis of DUT-67-Pa

DUT-67-Pa was synthesised using the same procedure, but instead of formic acid, 120 eq of propionic acid (HPa) were used as modulating agent. Yield: 85 %.

#### **4.3.2 Post-synthetic exchange of modulator molecules**

An amount of 150 mg of DUT-67-Fa was suspended in 5 ml of a 0.125 mol L<sup>-1</sup> DMF solution of the respective carboxylic acid (Table 9, Table 12) at room temperature for five days. Afterwards the resulting product was washed several times with DMF and ethanol and activated in vacuum at 100 °C for at least 12 hours.

#### DUT67\_HCl, DUT-67\_H<sub>2</sub>SO<sub>4</sub>

An amount of 150 mg of not-dried DUT-67 was suspended in 5 ml of a 2 wt% ethanolic solution of a HCl or H<sub>2</sub>SO<sub>4</sub> solution at room temperature for four hours. Afterwards, the resulting product was washed several times with ethanol and activated in vacuum at 100 °C for at least 12 hours.

#### **4.3.3 Catalysis**

20 μmol (0.03 eq) of catalyst, which was activated in vacuum at 100 °C overnight, was placed in a Schlenk tube and evacuated for two more hours at 120 °C. After this activation procedure, the catalyst was flushed with argon and 3 ml (39 mmol, 65 eq) of dry 2-propanol was added, as well as 0.6 mmol (1 eq) of cyclohexanone. The reaction mixture was stirred with 250 rpm to 120 °C and annealed for 20 hours.

The heterogeneity tests were done by filtering a small part of the reaction mixture off after a certain amount of time and transferring it into another vessel. The separated reaction mixture was then heated at 120 °C until the end of the origin reaction.

For the recycling tests, the catalyst was separated from the reaction mixture and washed with ethanol for at least five times. Subsequently, the catalyst was dried in vacuum at 100 °C and reused under the same conditions like the first run.

The reaction processes were monitored by using GC-MS analysis.

---

#### 4.4 Crystallographic data

**Table 4.** Crystallographic data of DUT-126 derived from powder X-ray diffraction patterns (Rietveld refinement).

<b>DUT-126</b>	
Empirical formula	Zr <sub>6</sub> O <sub>34</sub> C <sub>38</sub> S <sub>4</sub> H <sub>26</sub> N <sub>2</sub> F <sub>12</sub>
Formula weight	1958.19
Symmetry	hexagonal
Space group	<i>P6/mmm</i>
Unit cell dimensions	$a = 37.5757(2) \text{ \AA}$ , $c = 19.5244(1) \text{ \AA}$ , $V = 23873.97(7) \text{ \AA}^3$
Z	9
Zero point line shift	0.00555°
Profile function	Thompson-Cox-Hastings: $U = 0.23898$ , $V = -0.11824$ , $W = 0.01767$ $X = 0.62810$ , $Y = 0.08960$
Asymmetry correction function	Berar-Baldinozzi: $P_1 = -7.98812$ , $P_2 = -2.70412$ $P_3 = 15.84250$ , $P_4 = 5.38100$
Preferred orientation function	Rietveld-Toraya: $a^* = 0.56616$ , $b^* = 0.81145$ , $c^* = 0.14493$ $G_1 = 4.20142$ , $G_2 = 0.99000$
Lattice strain	$A = 0.90506$ , $B = 0.90506$ , $C = 0.00447$
Global isotropic temperature factors	$U = 0.06990$
Refined Motion Groups	23
Refined degree of freedom	57
$R_w$	21.88%
$R_p$	15.64%

**Table 5.** Crystallographic data of DUT-67(Zr)\_HCl derived by single crystal X-ray diffraction.

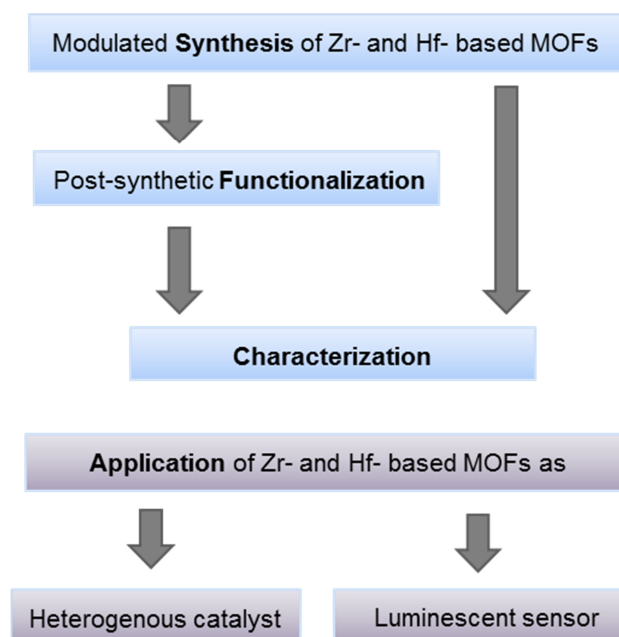
	<b>DUT-67(Zr)_HCl</b>
Empirical formula	$C_{24}H_8Cl_{0.86}O_{32}S_4Zr_6$
Formula weight	1514.23
Crystal system, space group	Cubic, $Fm\bar{3}m$
Unit cell dimensions, Å	$a = 38.650(4)$
Volume, Å <sup>3</sup>	57736(20)
<i>Z</i>	24
Calculated density, g/cm <sup>3</sup>	1.045
$\mu$ , mm <sup>-1</sup>	1.452
$T_{min}$ , $T_{max}$	0.972, 0.972
$\theta$ range, deg	1.149 – 32.48
	$-47 \leq h \leq 39$
Limiting indices	$-48 \leq k \leq 35$
	$-50 \leq l \leq 44$
Reflections collected / unique	54700 / 3520
$R(int)$	0.0995
Data / parameters	3520 / 93
GooF on $F^2$ [ $I > 2\sigma(I)$ ]	1.019
GooF on $F^2$ (all data)	1.019
$R_1$ [ $I > 2\sigma(I)$ ]	0.0872
$wR_2$ [ $I > 2\sigma(I)$ ]	0.3450
$R_1$ (all data)	0.1154
$wR_2$ (all data)	0.4062
Largest diff. peak / hole, eÅ <sup>-3</sup>	2.451 / -3.041

**Table 6.** Crystallographic data of DUT-122(Zr) and DUT-122(Hf) derived by single crystal X-ray diffraction.

	DUT-122(Zr)	DUT-122(Hf)
Empirical formula	C <sub>90</sub> H <sub>36</sub> O <sub>38</sub> Zr <sub>6</sub>	C <sub>90</sub> H <sub>36</sub> O <sub>38</sub> Hf <sub>6</sub>
CCDC number	1452907	1452908
Formula weight	2272.51	2796.13
Temperature, K	296	296
Crystal size, mm	0.08x0.08x0.08	0.06x0.06x0.06
Symmetry, space group		<i>Cubic, Pa<math>\bar{3}</math> (No 205)</i>
Unit cell dimensions, Å	<i>a</i> = 26.070(3)	<i>a</i> = 26.060(3)
Volume, Å <sup>3</sup>	17718(6)	17698(6)
Z	4	4
Calculated density, g/cm <sup>3</sup>	0.852	1.049
Absorption coefficient, mm <sup>-1</sup>	0.688	3.551
Tmin, Tmax	0.947, 0.947	0.783, 0.823
2θ range, deg	1.686 – 35.099	3.24 – 24.73
Wavelength, Å	0.88561	0.71073
Limiting indices	-31 ≤ <i>h</i> ≤ 32 -32 ≤ <i>k</i> ≤ 7 -33 ≤ <i>l</i> ≤ 14	-28 ≤ <i>h</i> ≤ 31 -31 ≤ <i>k</i> ≤ 20 -5 ≤ <i>l</i> ≤ 26
Reflections collected / unique	29097 / 6475	15294 / 5530
<i>R</i> <sub>(int)</sub>	0.0230	0.0478
Data / parameters	6475 / 203	5530 / 202
SQUEEZEd electrons / unit cell	6997	2456
GooF on <i>F</i> <sup>2</sup> [ <i>I</i> > 2σ( <i>I</i> )]	1.040	1.018
GooF on <i>F</i> <sup>2</sup> (all data)	1.049	1.018
<i>R</i> <sub>1</sub> [ <i>I</i> > 2σ( <i>I</i> )]	0.0437	0.0388
<i>wR</i> <sub>2</sub> [ <i>I</i> > 2σ( <i>I</i> )]	0.1080	0.0610
<i>R</i> <sub>1</sub> (all data)	0.0451	0.0678
<i>wR</i> <sub>2</sub> (all data)	0.1090	0.0629
Largest diff. peak / hole, eÅ <sup>-3</sup>	0.839 / -0.970	0.750 / -0.861
Residual coefficients before SQUEEZE		
<i>F</i> (000)	4336	1600
GooF on <i>F</i> <sup>2</sup> [ <i>I</i> > 2σ( <i>I</i> )]	1.109	0.757
GooF on <i>F</i> <sup>2</sup> (all data)	1.109	0.757
<i>R</i> <sub>1</sub> [ <i>I</i> > 2σ( <i>I</i> )]	0.0614	0.0440
<i>wR</i> <sub>2</sub> [ <i>I</i> > 2σ( <i>I</i> )]	0.1994	0.1131
<i>R</i> <sub>1</sub> (all data)	0.0683	0.0881
<i>wR</i> <sub>2</sub> (all data)	0.2045	0.1363
Largest diff. peak / hole, eÅ <sup>-3</sup>	1.849 / -2.028	1.765 -1.162

## 5. RESULTS AND DISCUSSION

In this work, the focus is the synthesis and functionalization of MOFs, which are based on Zr-oxo-clusters. In the synthesis of Zr- and Hf-based MOFs, the role of the modulator in framework formation is prominent<sup>60, 65, 127</sup>. The steric size, concentration and the nature of the modulator do not only influence the resulting crystal size of the MOF, but also the topology. In the synthesis of the already published structures of DUT-67, DUT-68 and DUT-69 (see chapter 2.1.2), which are all based on 2,5-thiophenedicarboxylic acid as linker molecule, acetic acid is used as modulator. The use of the hydrophobic molecule trifluoroacetic acid as modulator, instead of acetic acid, leads to a new phase which is described in chapter 5.1. The possibility to exchange the modulator - and therefore modify the MOFs properties - with a post-synthetic treatment is discussed in chapter 5.2, as well in chapter 5.3, where the removal of the modulator by inorganic acids is discussed. In chapter 5.4 the impact of this treatment on the catalytic activity is pointed out. In chapter 5.5, the applicability of a fluorenedicarboxylate based MOF as sensor material for small (solvent) molecules is elucidated.



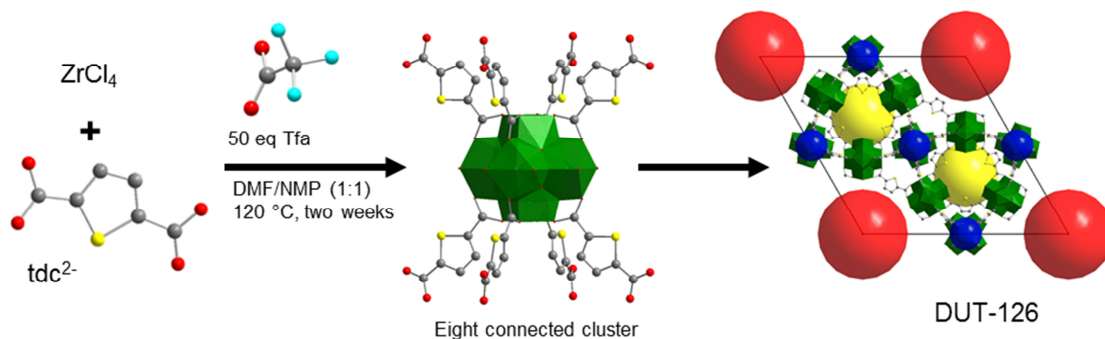
**Figure 24.** Overview of this thesis topics.

## 5.1 Modulator driven polymorphism<sup>†</sup>

By varying the synthesis procedure various structures can be obtained. So far, in the Zr-thiophenedicarboxylate system three individual structures are known, namely DUT-67, DUT-68 and DUT-69<sup>122</sup>. Depending on the cluster connectivity and the orientation of the linker, different framework topologies are formed. The 10-connected DUT-69 has a **bct** underlying topology whereas the eight-connected DUT-67 has a **reo** topology. DUT-68 has also an eight-connected cluster, but differs in the orientation of two tdc linkers of one from two independent clusters from DUT-67. This difference of the cluster environment leads to a **bon** topology. Consequently, the polymorphic frameworks exhibit a completely different pore system and texture properties. Such changes in structure and properties are caused by only minor changes in the synthesis procedure, like the metal to linker ratio and the amount of modulator. Yet, the influence is not only limited to the amount of modulator, also the molecular structure plays a crucial role. In the synthesis of DUT-67, DUT-68 and DUT-69 acetic acid is used as modulator. By replacing acetic acid with trifluoroacetic acid another polymorph is formed, which is named DUT-126. The synthesis and the characterization of DUT-126 are discussed in the following chapter.

### 5.1.1 Synthesis and characterization of DUT-126

A solvothermal reaction of  $\text{ZrCl}_4$  with  $\text{H}_2\text{tdc}$  and with 50 eq of trifluoroacetic acid as modulator leads to the formation of DUT-126 (Figure 25).



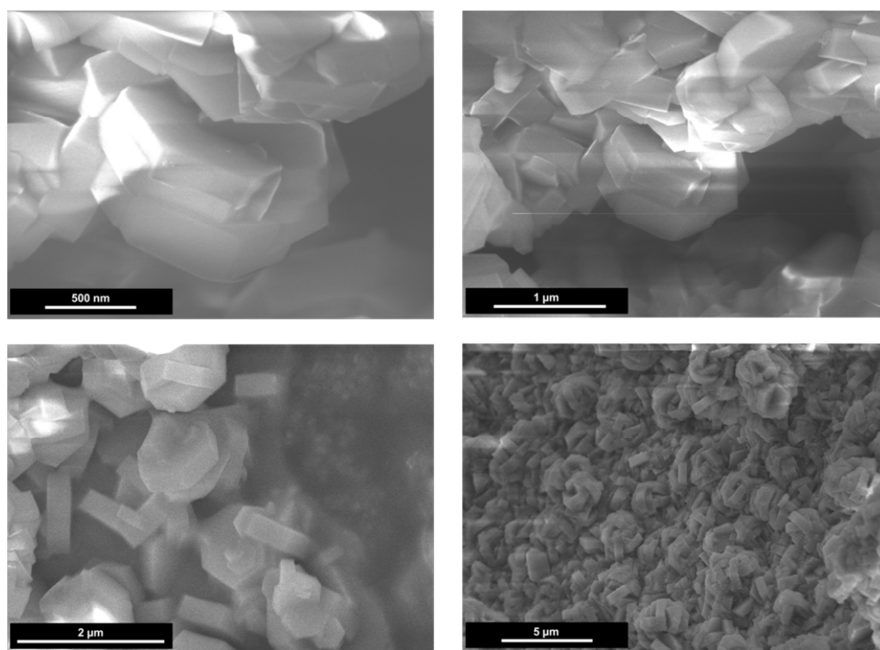
**Figure 25.** Reaction scheme of DUT-126 and synthesis conditions. Zirconium-clusters are shown in green, carbon atoms in grey, oxygen atoms in red and sulphur atoms in yellow. Hydrogen atoms are omitted for clarity.

<sup>†</sup> parts of this chapter were literally adopted from publication<sup>247</sup>.

Reprinted with permission from F. Drache, V. Bon, I. Senkovska, J. Getzschmann, and S. Kaskel, The modulator driven polymorphism of Zr(IV) based MOFs, *Philosophical Transactions of the Royal Society A: Physical and Engineering Sciences* 2017, 375 by permission of the Royal Society.

The composition of DUT-126 is  $Zr_6(\mu_3-O)_4(\mu_3-OH)_4(tdc)_4(tfa)_4(DMF)_2$ , and has been postulated according to various analytical methods, such as EA, TG and  $^1H$ -NMR. In the  $^1H$ -NMR (500 MHz, DMSO/ $D_2O$ ) spectrum of the dissolved MOF, the chemical shift of the  $tdc^{2-}$  linker and of DMF molecules are visible with  $\delta/ppm = 7.68$  (s, 2H,  $tdc$ ),  $\delta/ppm = 2.85, 2.68$  (s, 3H, DMF) and  $\delta/ppm = 7.90$  (s, 1H, DMF). Thereby, with the help of the integrated peaks of the spectrum, the ratio of  $tdc^{2-}/DMF$  has been calculated to 1:0.6. The amount of elements according to elemental analysis for the dried phase of DUT-126 is: C 23.14%, H 1.46%, S 5.82%, N 1.68%. Based on this data, the reasonable composition  $Zr_6(\mu_3-O)_4(\mu_3-OH)_4(tdc)_4(tfa)_4(DMF)_{2.3}(H_2O)_{13}$  could be deduced. The calculated values for this specific composition are: C 23.52%, H 2.74%, S 6.46%, N 1.62%. TG/DTA measurements confirm the ratio of the  $Zr_6(\mu_3-O)_4(\mu_3-OH)_4$  cluster to the  $tdc^{2-}$  linker of 1:4 and the ratio of  $Zr_6(\mu_3-O)_4(\mu_3-OH)_4$  cluster to DMF of 1:1.7 (FigureA 1 b). The amount of Tfa is with the ratio of 1:3.3  $Zr_6(\mu_3-O)_4(\mu_3-OH)_4/tfa$  less than the one found by elemental analysis. Nevertheless, considering the determined ratios, it could be concluded that the resulting SBU of DUT-126 has to consist of an eight-connected cluster.

The SEM images of DUT-126 (Figure 26) indicated a hexagonal morphology of the crystallites, which led to the assumption that DUT-126 crystallizes in the hexagonal crystal system. The obtained crystals were too small for a single X-ray diffraction measurement. Even an increase of modulator amount did not lead to suitable single crystals. Therefore, the crystal structure was solved *ab initio* from PXRD data.



**Figure 26.** SEM images of DUT-126 of different solutions.<sup>247</sup>

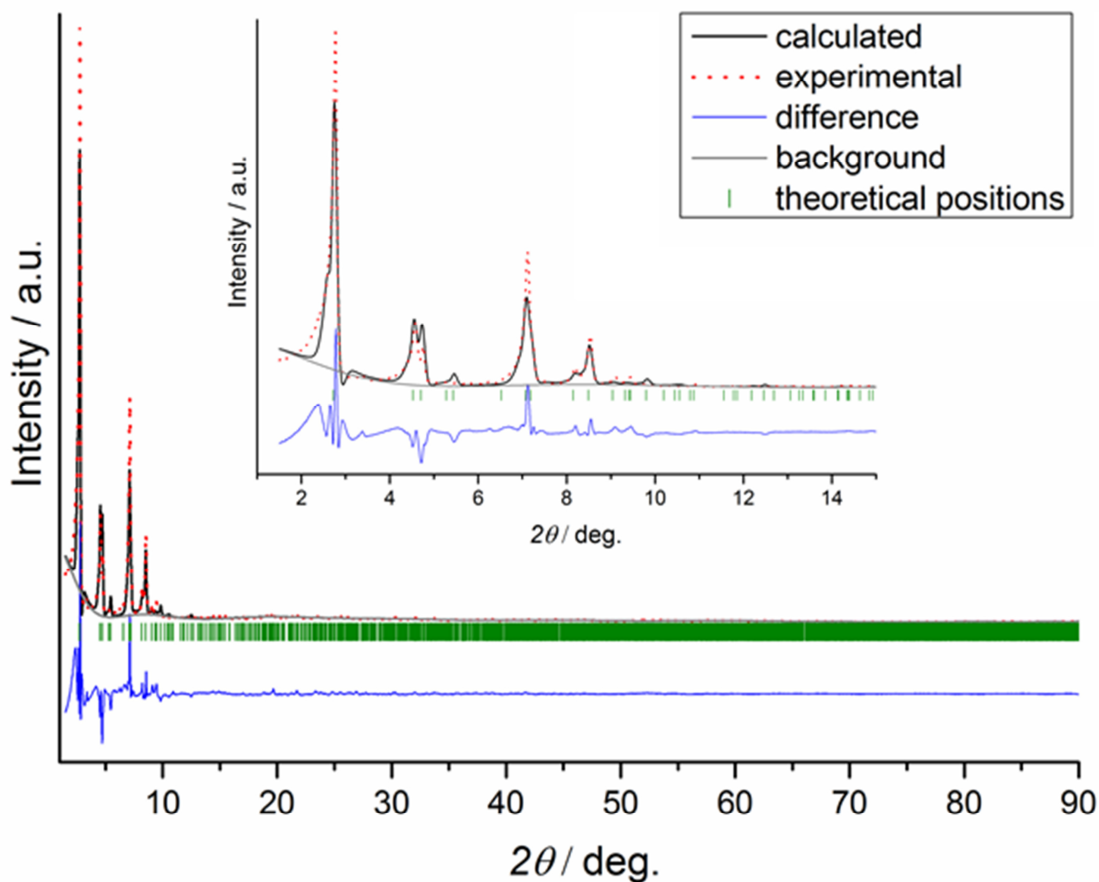
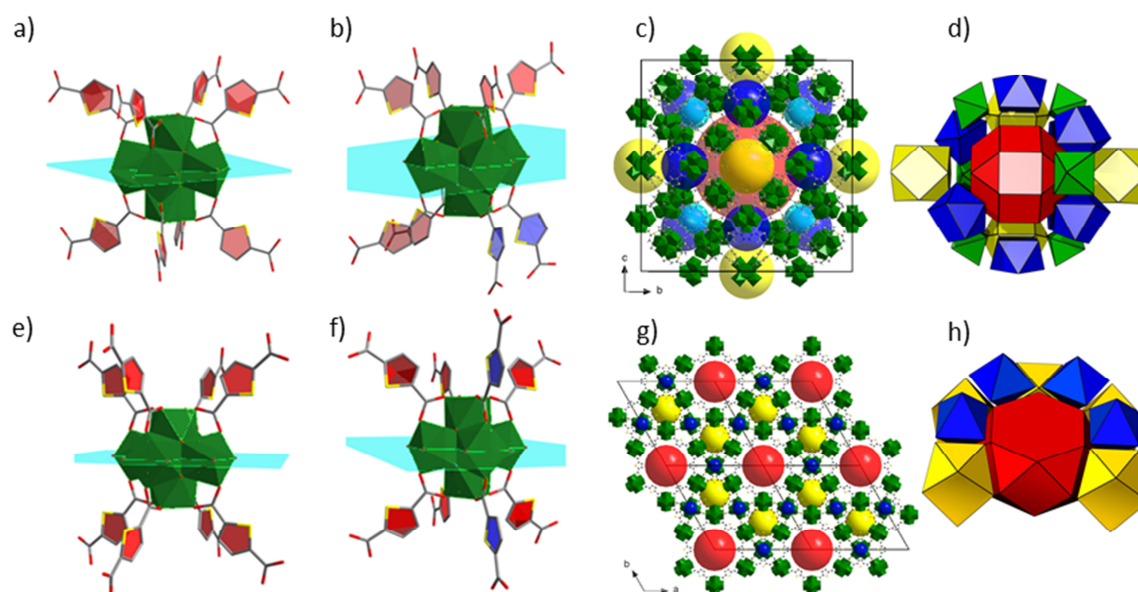


Figure 27. Rietveld plot for DUT-126.<sup>247</sup>

Assuming that DUT-126 has an eight-connected cluster and a hexagonal crystal system, a suitable structure was modelled with the help of the software program Materials Studio<sup>241</sup>. After comparing the theoretical simulated diffraction pattern with the experimental one, a Rietveld refinement was carried out (Figure 27). The structure of DUT-126 could be refined in the  $P6/mmm$  space group. Similar to the DUT-68 structure<sup>122</sup>, DUT-126 contains two symmetry independent  $Zr_6(\mu_3-O)_4(\mu_3-OH)_4$  SBUs. These SBUs are connected by  $tdc^{2-}$  linkers, resulting in a binodal 8,8-connected three dimensional framework. As in DUT-68, the sulphur atoms of the  $tdc^{2-}$  ligands of SBU1 point to the equatorial plane of the  $Zr_6$  octahedron, where the modulator molecules are located. In SBU2, the terminal ligands are also located in the equatorial plane, but the orientation of the  $tdc^{2-}$  ligands differ from DUT-68. In case of DUT-68, the SBU2 contains two adjacent  $tdc^{2-}$  ligands on the same side of the equatorial plane (marked blue in Figure 28 b), which are turned by  $180^\circ$  compared to the  $tdc^{2-}$  ligands of SBU1. Therefore, the sulphur atoms of these  $tdc^{2-}$  ligands point away from the equatorial plane. The constitution of this cluster environment leads to a cubic crystal structure and a

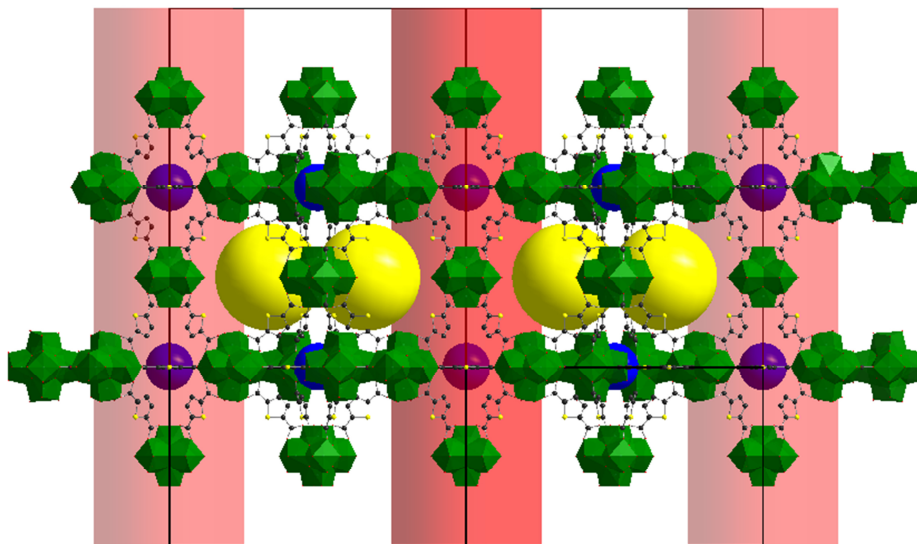


framework with **bon** topology (Figure 28 c). The SBU2 of DUT-126 shows one significant difference. Here, the  $\text{tdc}^{2-}$  ligands, whose sulphur atoms point away from the equatorial plane, are located on oppositional sides of the equatorial plane (marked blue in Figure 28 f). Such a different linker orientation results consequently in another framework topology. With the help of the software program ToposPro<sup>252</sup> the framework topology could be determined as **hbr**, which is according to the RCSR database<sup>253</sup> the very first MOF example. Therefore, a completely different pore system is established in DUT-126 compared to DUT-68, despite identical cluster connectivity.



**Figure 28.** Crystal structures of DUT-68 and DUT-126: a) SBU1 of DUT-68; b) SBU2 of DUT-68; c) Pores packing for DUT-68; d) Topological representation of DUT-68 as natural tiling; e) SBU1 of DUT-126; f) SBU2 of DUT-126; g) Pore packing for DUT-126; h) Topological representation of DUT-126 as natural tiling. Zirconium clusters are shown in green, carbon atoms in grey, oxygen atoms in red and sulphur atoms in yellow. Hydrogen atoms are omitted for clarity.<sup>247</sup>

A detailed analysis of the pore system leads to an identification of three different types of pores. With the help of the Zeo++<sup>254</sup> program the pore sizes were calculated, wherein the coordinated DMF molecules and  $\text{tfa}^-$  anions were neglected. Along the [001] direction small mesoporous hexagonal channels with a diameter of 22.8 Å are located (Figure 28 h, red polyhedron; Figure 29). The other two pore types are microporous and are arranged around the one dimensional hexagonal channels. Complete truncated triangular bipyramidal pores with diameter of 11.8 Å (Figure 28 h, yellow polyhedron; Figure 29) alternate with octahedral pores with diameter of 5.3 Å (Figure 28 h, blue polyhedron; Figure 29).



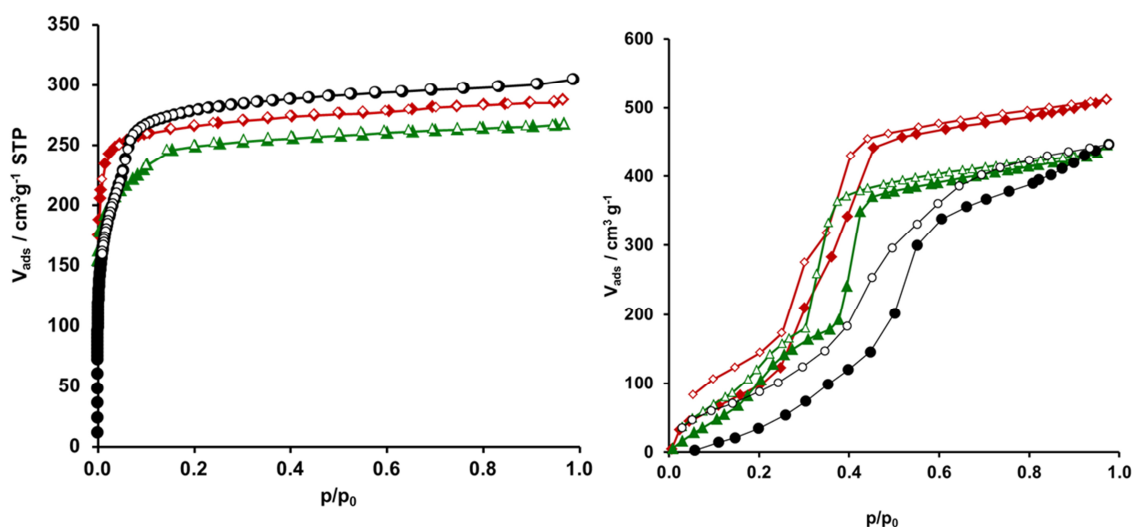
**Figure 29.** Pore system of DUT-126 viewed along *b*-axis. Zirconium-clusters are shown in green, carbon atoms in grey, oxygen atoms in red and sulphur atoms in yellow. Hydrogen atoms are omitted for clarity.

The different framework topology and – pore system affect the textural properties (Table 7). The crystallographic porosity amounts to 69% of the unit cell and the geometrical pore volume to  $0.73 \text{ cm}^3 \text{ g}^{-1}$ . Compared to the other eight-connected MOFs, DUT-67 ( $V_{\text{pore}} = 0.55 \text{ cm}^3 \text{ g}^{-1}$ ) and DUT-68 ( $V_{\text{pore}} = 0.50 \text{ cm}^3 \text{ g}^{-1}$ ), the calculated total pore volume of DUT-126 is significantly higher. The corresponding theoretical specific surface area of DUT-126 is  $2088 \text{ m}^2 \text{ g}^{-1}$  is accordingly also higher than the ones of DUT-67 ( $\text{SSA} = 1767 \text{ m}^2 \text{ g}^{-1}$ ) and DUT-68 ( $\text{SSA} = 1786 \text{ m}^2 \text{ g}^{-1}$ ). Due to the negligence of coordinated solvent molecules and modulators in the calculations and other reasons, such as chemical stability, the theoretical surface areas and pore volumes are larger than the experimental ones. After activation from DMF at  $120 \text{ }^\circ\text{C}$ , the experimental specific pore volume of DUT-126 amounts to  $0.48 \text{ cm}^3 \text{ g}^{-1}$  and the BET area is determined to be  $1297 \text{ m}^2 \text{ g}^{-1}$ .

**Table 7.** Textural properties of DUT-126 and other eight-connected Zr-tdc MOFs.<sup>122, 247</sup>

	<b>DUT-126</b>	<b>DUT-67</b>	<b>DUT-68</b>
Solvent accessible void, %	69	66	60
Theoretical pore volume $V_{\text{pore}}$ , $\text{cm}^3 \text{ g}^{-1}$	0.73	0.55	0.50
Theoretical surface area SSA, $\text{m}^2 \text{ g}^{-1}$	2088	1767	1786
Experimental pore volume, $V_{\text{pore}}$ $\text{cm}^3 \text{ g}^{-1}$	0.48	0.44	0.41
Experimental surface area SSA, $\text{m}^2 \text{ g}^{-1}$	1297	1064	891
Water pore filling degree, %	75	93	88

Due to the special pore landscape of DUT-126 with its large hexagonal channels ( $d = 22.8 \text{ \AA}$ ), the nitrogen isotherm (Figure 30), measured at 77 K, does not show a classical “Type Ia” isotherm, like its two polymorphs DUT-67 and DUT-69. Similar to DUT-68, whose isotherm possesses a slope untypical for mere microporous materials, the isotherm of DUT-126 is of “Type Ib” and features a step, indicating the presence of small mesopores. The step starts in the low pressure region ( $p/p_0 > \sim 0.04$ ) with an uptake of  $\sim 210 \text{ cm}^3 \text{ g}^{-1}$  and the isotherm reaches its plateau at higher pressures with an uptake of  $305 \text{ cm}^3 \text{ g}^{-1}$ .

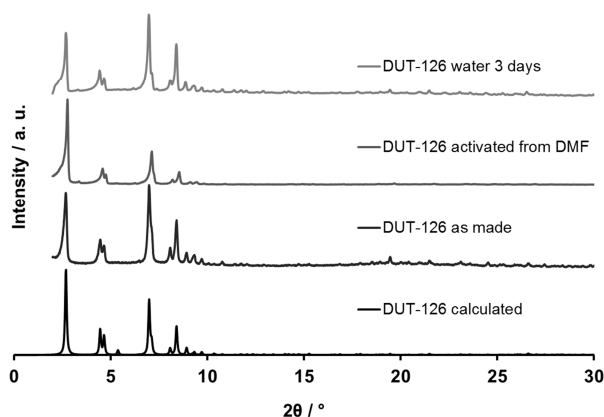


**Figure 30.** Left: Nitrogen adsorption (blank symbols) and desorption (solid symbols) isotherms measured at 77 K for DUT-126 (black circles), DUT-67 (red diamonds), and DUT-68 (green triangles). Right: Water vapour adsorption (solid symbols) and desorption (blank symbols) isotherm, measured at 298 K for DUT-126 (black circles), DUT-67 (red diamonds) and DUT-68 (green triangles).<sup>247</sup>

To estimate the hydrophobicity of DUT-126, a water physisorption isotherm was measured at 298 K and compared to that of DUT-67 and DUT-68. The form of the water vapour isotherm of DUT-126 is S-shaped, similar to the isotherms of the polymorphic frameworks (Figure 30). A step occurs in the pressure region between 0.45 and 0.55, where almost 50% are adsorbed, indicating that water molecules start to fill the mesoporous channels at this point. Contrary to the isotherms of DUT-67 and DUT-68, which have a typical saturation plateau, the adsorption branch of DUT-126 at relative pressures  $> \sim 0.6$  has a steeper slope. In addition, the whole run of the isotherm is shifted to higher relative pressures, pointing to a more hydrophobic surface. Furthermore, the pore volume derived by water adsorption amounts only to  $0.36 \text{ cm}^3 \text{ g}^{-1}$ . Thus, the water pore filling degree accounts to 75%, which is significantly lower than the ones of DUT-67 (93%) and DUT-68 (88%). The smaller pore filling degree for water together with the water isotherm’s shape, demonstrate the more hydrophobic character of

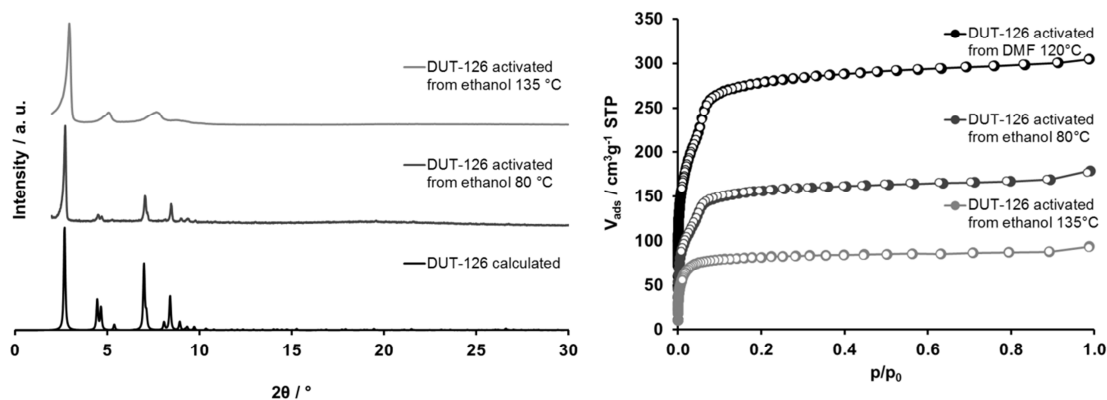
DUT-126, which originates from the trifluoroacetate modulator, located inside the hexagonal channels and the completely truncated triangular bipyramidal pores.

Despite of its hydrophobic properties, the isotherm of DUT-126 has a hysteresis, which does not close even at low relative pressures. Such a hysteresis indicates a partial degradation of the framework. During water removal from the framework, capillary forces are occurring, which are responsible for the degradation process. An indicator that capillary forces and not instability against hydrolysis is the cause of framework destruction is the high stability of DUT-126 in water. Stored under water for three days, DUT-126 shows no loss in crystallinity (Figure 31). Unlike its polymorphs, which exhibit a high chemical stability<sup>122</sup>, DUT-126 is more susceptible for degradation if solvents such as water and ethanol are removed directly from the framework.



**Figure 31.** PXRD patterns of DUT-126, calculated (black), as made (dark grey), dried from DMF at 120 °C (grey) and soaked in water for 3 days (light grey).

After drying from ethanol at 85 °C, the porosity is reduced to almost 50%, the specific surface area is reduced to 594 m<sup>2</sup> g<sup>-1</sup> and the total pore volume to 0.27 m<sup>3</sup> g<sup>-1</sup>. At a higher activation temperature of 135 °C, the porosity loss is increased and the framework loses even its mesoporous character, observable in the resulting “Type-Ia” isotherm, obtained with nitrogen at 77 K (Figure 32). Even an exchange of ethanol with supercritical carbon dioxide to prevent capillary forces during the activation process did not preserve the porosity. PXRD data confirm the framework degradation (Figure 32). The reduced stability is likely based on the orientation of the linker molecules in the crystal structure and the resulting high surface tension they are exposed to.

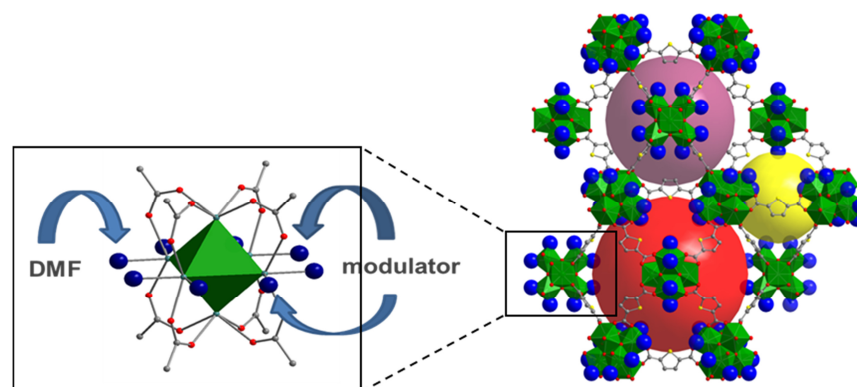


**Figure 32.** Left: PXRD diffraction patterns of DUT-126, calculated (black), activated from ethanol at 80 °C (dark grey) and at 135 °C (light grey). Right: Nitrogen physisorption isotherms at 77 K (adsorption: solid symbols, desorption blank symbols) of DUT-126 activated from DMF at 120 °C (black circles), from ethanol at 80 °C (dark grey circles) and from ethanol at 135 °C (light grey circles).

The thermal stability of DUT-126 was investigated with the help of TG/DTA measurements on a pre-activated sample (120 °C) under air atmosphere. The framework starts to release coordinated DMF molecules not before 180 °C and trifluoroacetate molecules below 250 °C (Figure A 1 b). This assignment is made based on the theoretical composition of DUT-126 and on the boiling points of the ligands. The thermal release of terminal ligands can have an impact on the framework stability and can contribute to its decomposition. In vacuum, the release starts at significantly lower temperatures. Therefore, the activation should be done at moderate temperatures and the application of this MOF is limited to such cases, which do not involve too high temperatures.

## 5.2 Post-synthetic inner surface functionalization of DUT-67†

A promising way to introduce new functionalities on the inner surface of MOFs can be a functionalization of the metal cluster. Yet, this approach is limited to MOFs that contain free coordination sites. Therefore, only MOFs with reduced cluster connectivity are suited. In case of Zr-based MOFs, this includes a broad range of various structures. The proof of concept was already demonstrated on NU-1000, where terminal -OH groups were replaced by benzoic acid, perfluoropentanoic acid, and perfluorodecanoic acid.<sup>138, 155</sup> In this work, the Zr-based MOF DUT-67 is used to place various kinds of functionalities into its framework, such as hydrophobic fluorinated ligands (chapter 5.2.1), chiral- (chapter 5.2.2) and fluorescent molecules (chapter 5.2.3). Most of these molecules are not suitable to be used directly as modulator agent in the synthesis. Either they are too bulky to allow a network formation, an undesired phase is formed or just an amorphous non-porous product is built. Therefore the post-synthetic approach, where the pristine modulator is replaced by other functional carboxylates, seems ideal to introduce new functionalities in a desired MOF under preservation of its structure. This approach is less complex and less expensive in comparison to other approaches, like linker functionalization routes<sup>255</sup>, since no special synthetic protocol of organic components are involved, and commercially available monocarboxylic acids can be utilized.



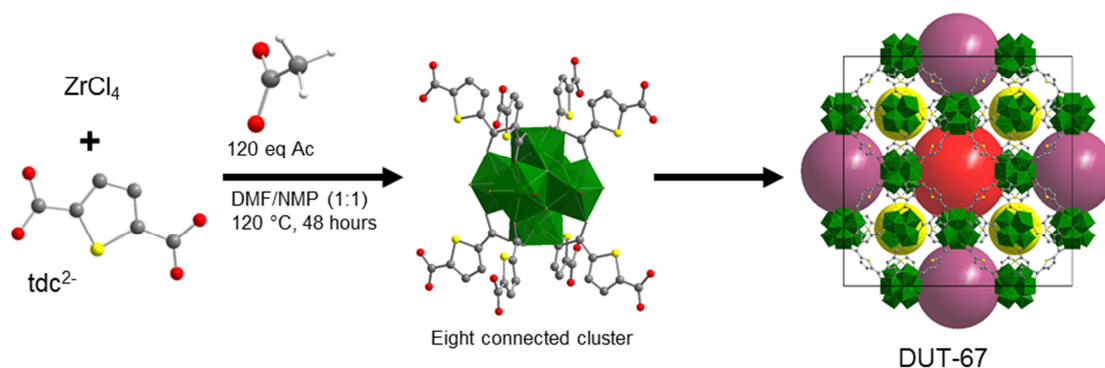
**Figure 33.** Left:  $Zr_6(\mu_3-O)_4(\mu_3-OH)_4^{12+}$  cluster in DUT-67. The blue spheres represent the coordination sites of the modulator, terminal -OH ligands or DMF molecules. Right: Pore packing of DUT-67. Zirconium-clusters are shown in green, carbon atoms in dark grey, oxygen atoms in red and sulphur atoms in yellow. Hydrogen atoms are omitted for clarity.<sup>248</sup>

† parts of this chapter were literally adopted from publication<sup>248</sup>. Reprinted with permission from F. Drache, V. Bon, C. Marschelke, A. Synytska, and S. Kaskel, Postsynthetic Inner-Surface Functionalization of the Highly Stable Zirconium-Based Metal–Organic Framework DUT-67, *Inorganic Chemistry* 2016, 55, 7206-7213. Copyright 2016 American Chemical Society.

The cluster configuration of DUT-67 is ideal for such a post-synthetic functionalization approach. In contrast to UiO-type frameworks, where the clusters are connected by twelve linker molecules giving **fcu** topology, the connectivity of the cluster of DUT-67 is reduced to eight and the topology changes to **reo** type. Due to charge balancing reasons, the cluster features two monocarboxylate anions, which are used as modulator in the synthesis. Furthermore, solvent molecules, such as DMF, are also coordinated to the cluster (Figure 33).

### 5.2.1 Synthesis and characterization of DUT-67 with various modulators

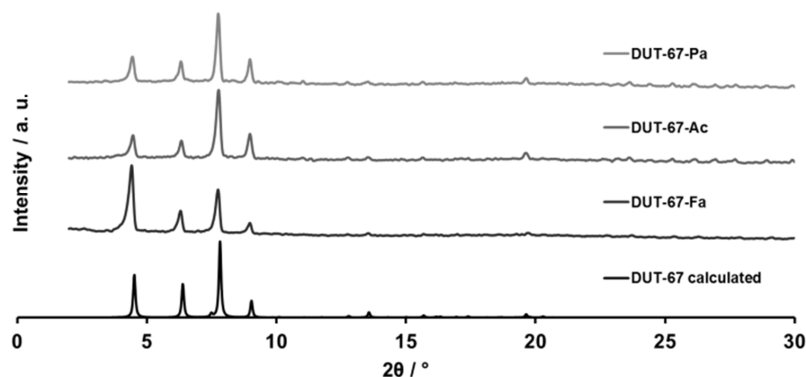
As mentioned in chapter 2.1.2, DUT-67 is synthesised by the reaction of  $ZrCl_4$  with the linker  $H_2tdc$ . In the original publication<sup>122</sup>, acetic acid was used as modulator. Then, a framework with the composition  $Zr_6(\mu_3-O)_4(\mu_3-OH)_4(tdc)_4(CH_3COO)_2(OH)_2$  is formed (Figure 34).



**Figure 34.** Reaction scheme of DUT-67 and synthesis conditions as reported in reference<sup>122</sup>. Zirconium-clusters are shown in green, carbon atoms in grey, oxygen atoms in red, sulphur atoms in yellow and hydrogen atoms in white.

In this work, the smallest possible modulator – formic acid – was chosen to create a starting material as benchmark. The resulting MOF contains then formate (Fa) as monocarboxylic ligand and is therefore labelled as DUT-67-Fa. It is also possible to use instead of formic acid other small carboxylic acids like acetic acid (HAc) or propionic acid (HPa) as modulator in the synthesis. In these cases, the zirconium cluster bears acetate or propionate as ligands, respectively (FigureA 2, FigureA 3). All three of these modulators lead to frameworks with high crystallinity (Figure 35). The use of carboxylic acids with longer alkyl chains, such as 1-butanoic acid as well as 2-butanoic acid, did not result in a crystalline framework formation. The DUT-67 frameworks bearing formate, acetate or propionate as ligands on the cluster do not differ significantly in their porosity (Table 8). But nevertheless, the more steric space the modulator requires in the network, the smaller the pore volume. The theoretical pore volumes are reduced by  $0.02 \text{ cm}^3 \text{ g}^{-1}$  per additional alkyl unit of the modulator. Hence, the theoretical

pore volume of DUT-67-Pa is reduced to  $0.58 \text{ cm}^3 \text{ g}^{-1}$ , whereas DUT-67-Ac has a theoretical pore volume of  $0.60 \text{ cm}^3 \text{ g}^{-1}$  and DUT-67-Fa of  $0.62 \text{ cm}^3 \text{ g}^{-1}$ .



**Figure 35.** PXRD patterns of DUT-67 (as made) with formic acid (dark grey), acetic acid (grey) and propionic acid (light grey) as modulator in the synthesis.

**Table 8.** Textural properties of DUT-67-Fa, DUT-67-Ac and DUT-67-Pa.

MOF	DUT-67-Fa	DUT-67-Ac	DUT-67-Pa
Theoretical pore volume, $\text{cm}^3 \text{ g}^{-1}$	0.62	0.60	0.58
Theoretical surface area, $\text{m}^2 \text{ g}^{-1}$	2152	2080	2128
Pore volume derived from nitrogen adsorption, $\text{cm}^3 \text{ g}^{-1}$	0.47	0.47	0.46
Surface area (BET) derived from nitrogen adsorption, $\text{m}^2 \text{ g}^{-1}$	1143	1171	1063
Pore volume derived from water vapour adsorption, $\text{cm}^3 \text{ g}^{-1}$	0.40	0.41	0.40
Water pore filling degree*, in %	85	87	87
Pore volume derived from $\text{N}_2$ adsorption isotherm for materials after $\text{H}_2\text{O}$ adsorption/desorption, $\text{cm}^3 \text{ g}^{-1}$	0.31	0.38	0.37
Loss of porosity after $\text{H}_2\text{O}$ desorption, in %	34	20	20

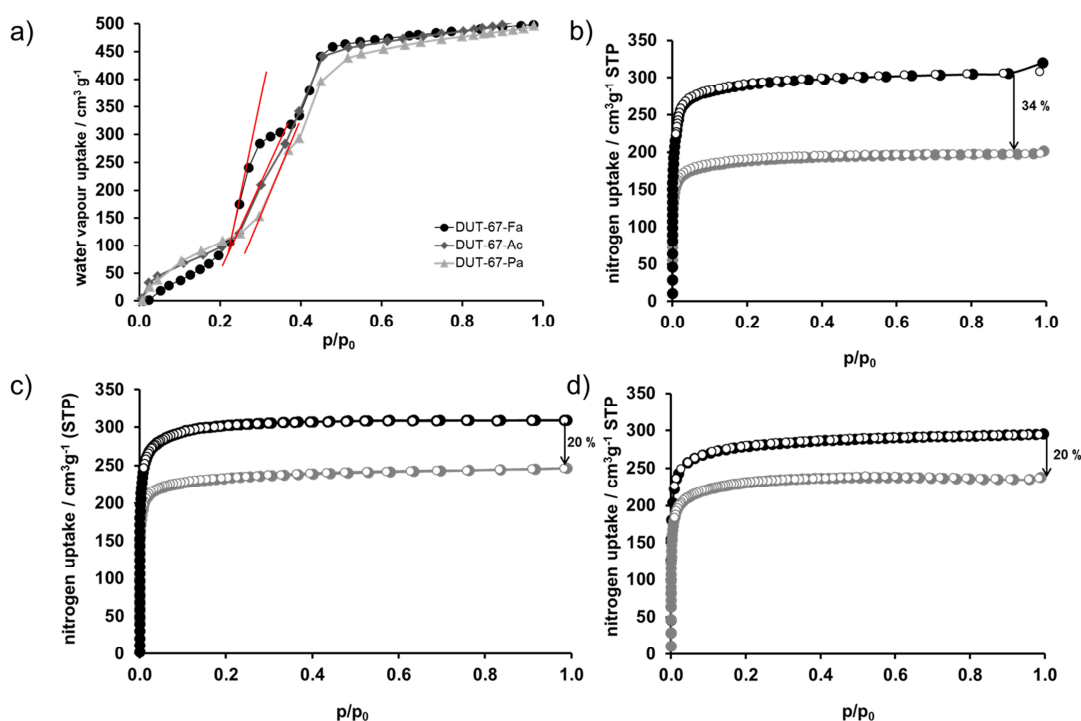
\* Calculated as pore volume calculated from  $\text{H}_2\text{O}$  divided by the pore volume calculated from  $\text{N}_2$ . Both pore volumes were calculated at  $p/p_0 = 0.97$ .

In the experimentally derived pore volumes, the differences are less pronounced. Here, the pore volume of DUT-67-Fa and DUT-67-Ac amounts to  $0.47 \text{ cm}^3 \text{ g}^{-1}$ , whereas the pore volume for DUT-67-Pa is  $0.48 \text{ cm}^3 \text{ g}^{-1}$ . In general, the theoretical pore volumes and surface areas are higher than the experimental ones, which can originate from several factors, such as



defects, partial collapse of pores during the thermal activation process or insufficient activation. It is also worth to mention that additional clusters were localised crystallographically in the structure of DUT-67, which could not be removed by the standard washing process. These clusters can therefore also contribute to porosity loss.

If DUT-67 is exposed to water vapour and if the water is desorbed from the framework, a decrease in porosity takes place. This decrease is dependent on the polarity of the modulator and how well it can shield the metal cluster. Therefore, the loss of porosity after water removal should be less with increasing hydrophobicity of the used modulator. The polarity of DUT-67 is slightly increased if modulators with longer alkyl chains were used, which can be seen in the reduced slope of the water physisorption isotherms in the pressure range of  $p/p_0 = 0.2-0.4$  (red lines in Figure 36 a) of DUT-67-Fa, DUT-67-Ac and DUT-67-Pa. The smaller the slope of the isotherm, the more hydrophobic is the material. The increased hydrophobicity corresponds with the decreased loss of porosity after water desorption at 100 °C. DUT-67-Fa, which is synthesised with the smallest modulator molecule, loses 37% of its porosity, DUT-67-Ac and DUT-67-Pa, whose modulators consist of carboxylic acids with longer alkyl chains, lose only 20% of their porosity (Figure 36 c-d, Table 8). Therefore, the insertion of highly hydrophobic molecules, such as fluorinated monocarboxylic acids, into the framework should increase drastically the stability of the MOF against water removal.

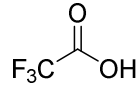
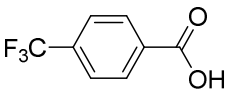
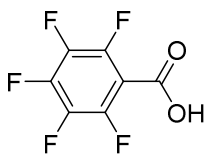



**Figure 36.** a) Water vapour isotherms at 298 K of DUT-67-Fa (black circles), DUT-67-Ac (dark grey diamonds) and DUT-67-Pa (grey triangles). Nitrogen isotherms at 77 K before (black circles) and after (grey circles) water desorption from the framework of b) DUT-67-Fa, c) DUT-67-Ac and d) DUT-67-Pa.

### 5.2.2 Post-synthetic inner surface functionalization of DUT-67 with hydrophobic fluorinated ligands

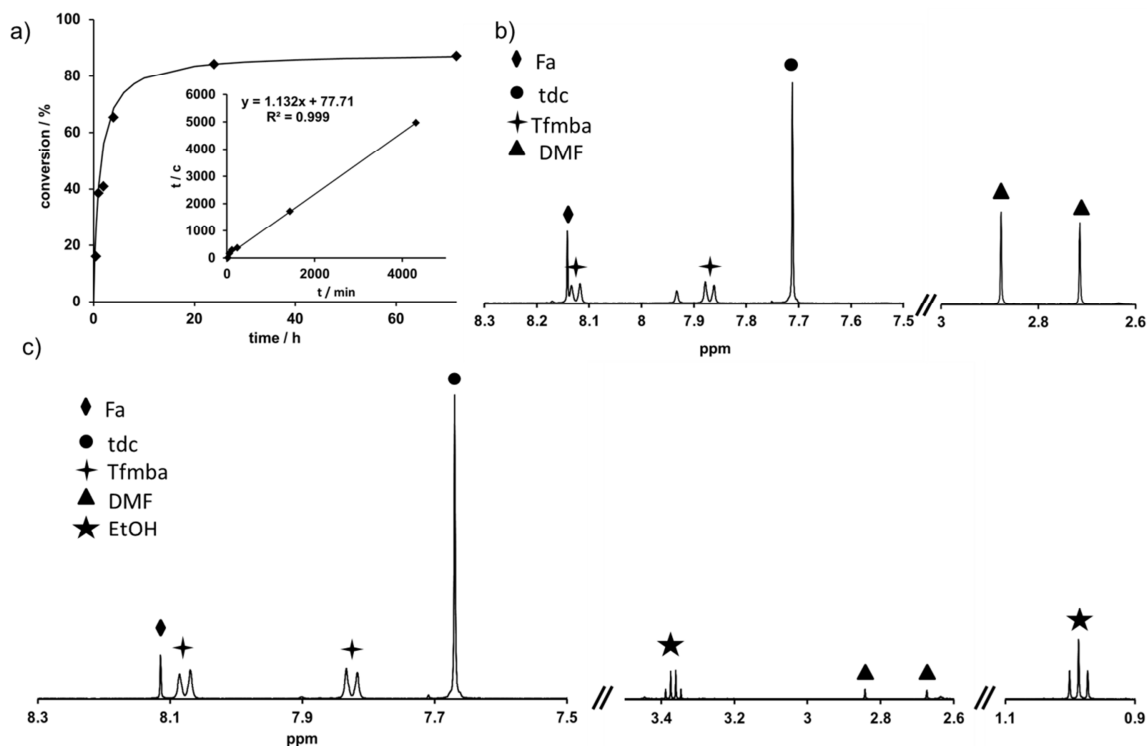
In order to tune the polarity of the inner surface and to investigate the influence of water repellent moieties on moisture stability, DUT-67 was functionalized with the fluorinated monocarboxylic acids trifluoroacetic acid (HTfa), 4-(trifluoromethyl)benzoic acid (HTfmba), pentafluorobenzoic acid (HPfba) and perfluorooctanoic acid (HPfoa) (Table 9). Since these monocarboxylic acids are not suitable as modulators in a direct synthesis or do not form the desired structure of DUT-67, a post-synthetic approach was applied. In this approach the pristine modulator formate is exchanged by the fluorinated mono-carboxylates by exposing the parent DUT-67-Fa to a concentrated solution of these mono-carboxylates at room temperature.

**Table 9.** List of fluorinated carboxylic acids used for the post-synthetic modulator exchange in DUT-67.

Compound	Monocarboxylic acid	Structural formula
DUT-67-Tfa	Trifluoroacetic acid	
DUT-67-Tfmba	4-(Trifluoromethyl)benzoic acid	
DUT-67-Pfba	Pentafluorobenzoic acid	
DUT-67-Pfoa	Perfluorooctanoic acid	

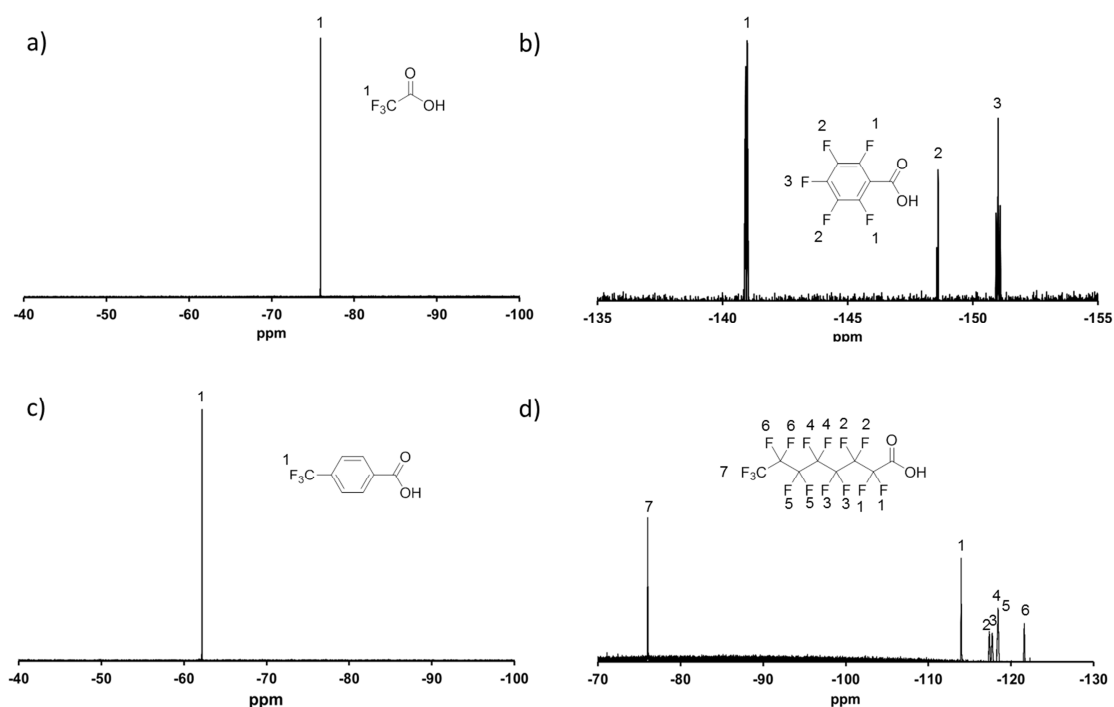
The functionalization with Tfmba was chosen as an example to monitor the exchange rate of the mono-carboxylates. Therefore small parts of the sample were removed from the concentrated solution at distinct times, carefully washed and analysed by  $^1\text{H-NMR}$ . For calculating the conversion of the ligand exchange, the ratio of Tfmba and the linker  $\text{tdc}^{2-}$  were used. The chemical shift in the  $^1\text{H-NMR}$  spectrum of Tfmba is located at 7.87 ppm and 8.13 ppm and the chemical shift of  $\text{tdc}^{2-}$  is at 7.71 ppm (Figure 37 b). The rate of the exchange process follows a pseudo second order, illustrating a successful exchange. After 24 hours the ligand exchange is almost complete and after three days a conversion of 87% could be achieved (Figure 37 a). DMF molecules ( $\delta = 2.85$  ppm, 2.68 ppm, 7.93 ppm) coordinated to

the cluster are retained if the exchange is performed in DMF as solvent. If ethanol is used as solvent, the amount of DMF on cluster decreases drastically to almost zero (Figure 37 c). The DMF molecules are then partially replaced by ethanol ( $\delta = 0.99$  ppm, 3.38 ppm).



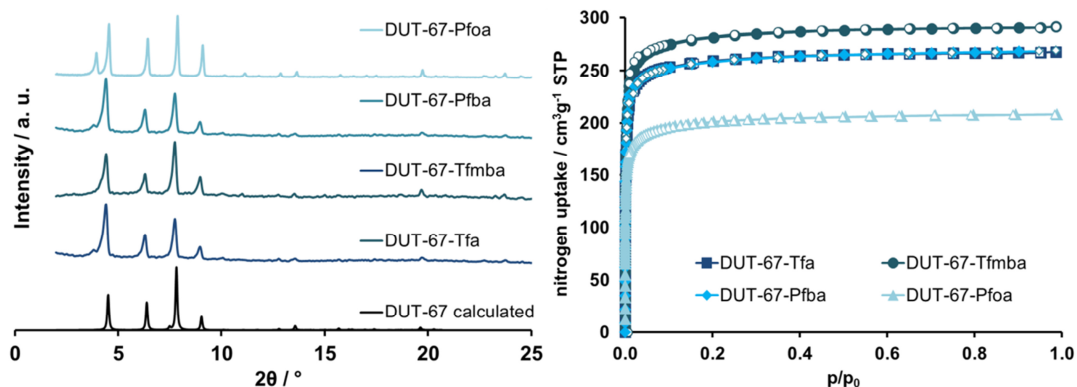
**Figure 37.** a) The kinetic process of functionalization of DUT-67 with Tfmba; b)  $^1\text{H-NMR}$  spectrum of DUT-67-Tfmba if DMF is used as solvent; c)  $^1\text{H-NMR}$  spectrum of DUT-67-Tfmba if ethanol is used as solvent.

Since the other fluorinated monocarboxylates Tfa, Pfba and Pfoa cannot be seen in  $^1\text{H-NMR}$  spectra due to the absence of hydrogen atoms in their structure, the exchange of the modulator can only be seen in the decrease in the amount of the initial modulator formic acid ( $\delta = 8.14$  ppm). In all cases the amount of formic acid is significantly decreased. In addition, the presence of the fluorinated ligands could also be proven by  $^{19}\text{F-NMR}$  measurements. The chemical shifts in  $^{19}\text{F-NMR}$  spectra of Tfmba can be localised at  $\delta = -62.17$  ppm, of Tfa  $\delta = -75.89$  ppm, of Pfba  $\delta = -140.94$  ppm,  $-151.01$  ppm,  $-148.62$  ppm and of Pfoa  $\delta = -76.03$  ppm,  $-113.98$  ppm,  $-117.54$  ppm,  $-117.99$  ppm,  $-118.43$  ppm,  $-118.47$  ppm and  $-121.59$  ppm (Figure 38). Impurities were found in the form of  $\text{SiF}_4$  ( $\delta = -161.79$  ppm) and  $\text{KF}$  ( $\delta = -135.56$  ppm), but are not present in the displayed section of the spectra and are therefore not shown. These impurities originate from the digestion of the samples with  $\text{HCl}$  and  $\text{CsF}$  in a glass vessel. In this process,  $\text{HF}$  is *in-situ* formed and reacts with the glass surface to  $\text{SiF}_4$  until it is neutralized with  $\text{K}_2\text{CO}_3$  to  $\text{KF}$ .



**Figure 38.**  $^{19}\text{F}$ -NMR spectra of digested samples of a) DUT-67-Tfa, b) DUT-67-Pfba, c) DUT-67-Tfmba and d) DUT-67-Pfoa.

After the post-synthetic treatment, the modified DUT-67 analogues retain a high degree of crystallinity (Figure 39 left). Also their porosity remains intact (Figure 39 right). Compared to the theoretical pore volumes, the experimentally derived ones follow the same trend. With increased steric demand of the monocarboxylate ligands the porosity decreases. Therefrom, the experimental pore volumes range from  $0.47 \text{ cm}^3 \text{ g}^{-1}$  (DUT-67-Fa) to  $0.32 \text{ cm}^3 \text{ g}^{-1}$  (DUT-67-Pfba). In Table 10 the theoretical and experimental textural properties are summarized for all DUT-67 materials which have fluorinated ligands incorporated.



**Figure 39.** Left: PXRD pattern of fluorinated DUT-67 activated in vacuum at  $100 \text{ }^\circ\text{C}$ ; Right: Nitrogen isotherms at  $77 \text{ K}$  of DUT-67-Tfa (dark blue squares), of DUT-67-Tfmba (dark blue circles), of DUT-67-Pfba (blue diamonds) and of DUT-67-Pfoa (light blue triangles) activated in vacuum at  $100 \text{ }^\circ\text{C}$ .

**Table 10.** Textural properties of DUT-67 analogues with fluorinated ligands.

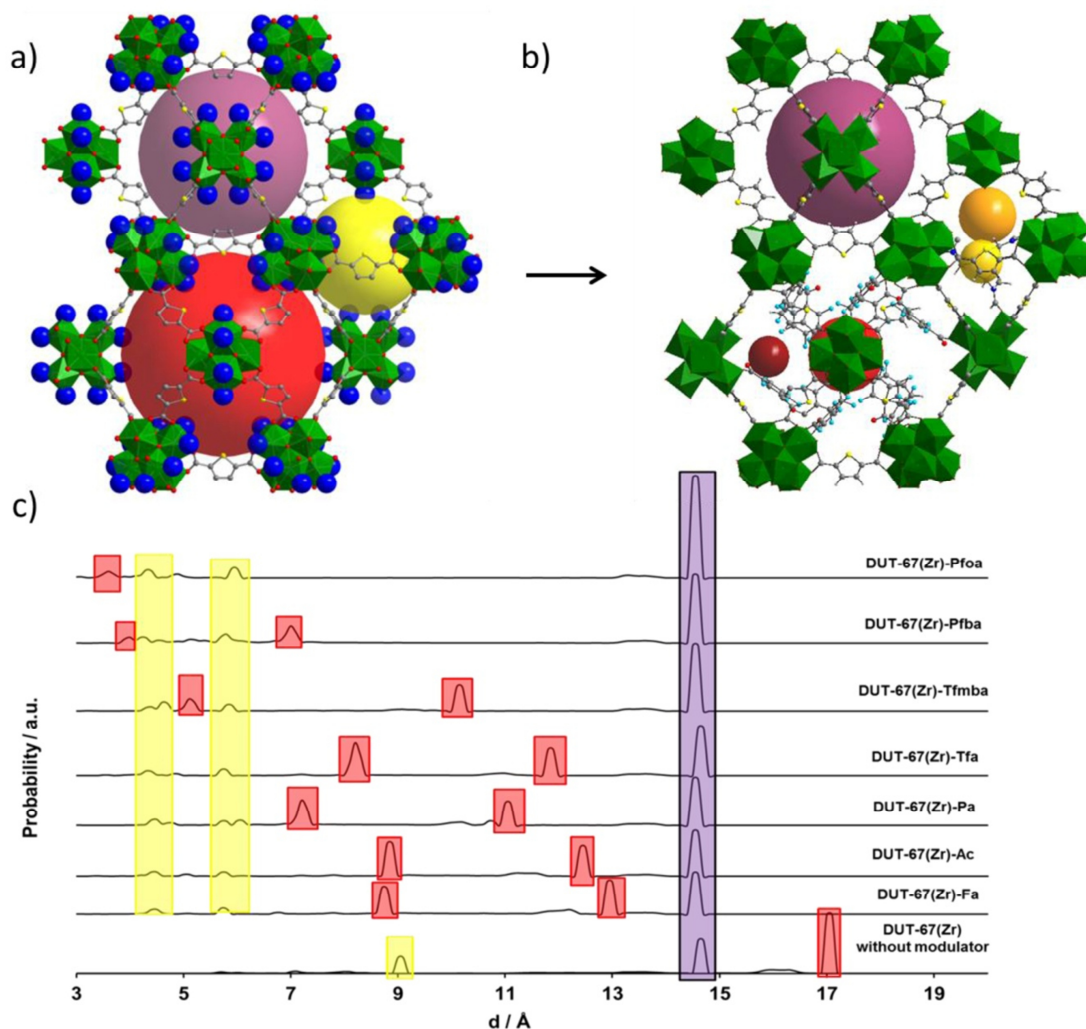
MOF	DUT-67-	DUT-67-	DUT-67-	DUT-67-
	Tfa	Tfmba	Pfba	Pfoa
Theoretical pore volume, cm <sup>3</sup> g <sup>-1</sup>	0.55	0.47	0.46	0.33
Theoretical surface area, m <sup>2</sup> g <sup>-1</sup>	2007	1608	1721	1053
Pore volume derived from nitrogen adsorption, cm <sup>3</sup> g <sup>-1</sup>	0.41	0.45	0.42	0.32
Surface area (BET) derived from nitrogen adsorption, m <sup>2</sup> g <sup>-1</sup>	1012	1111	1021	773
Pore volume derived from water vapour adsorption, cm <sup>3</sup> g <sup>-1</sup>	0.35	0.36	0.35	0.23
Water pore filling degree*, in %	85	80	83	72
Pore volume derived from N <sub>2</sub> adsorption isotherm for materials after H <sub>2</sub> O adsorption/desorption, cm <sup>3</sup> g <sup>-1</sup>	0.38	0.39	0.40	0.32
Loss of porosity after H <sub>2</sub> O desorption, in %	7	13	5	0.3

\* Calculated as pore volume calculated from H<sub>2</sub>O divided by the pore volume calculated from N<sub>2</sub>. Both pore volumes were calculated at p/p<sub>0</sub> = 0.97.

In order to gain deeper insights into the characteristic features of the pores surface of DUT-67, its pore size distribution was investigated and how it changes with different modulator molecules coordinated to the metal cluster. For this investigation, the fluorinated mono-carboxylates as well as the carboxylates, which consist of alkyl chains, were taken into account.

The pore landscape of DUT-67 consists of three different types of pores with individual pore sizes, depending on the kind of coordinated ligands. If the crystal structure of DUT-67 is taken for the calculations, where no mono-carboxylate ligand is present and the vacant positions are only occupied by oxygen atoms, the pore size distribution analysis (performed by Zeo++ program<sup>249</sup>) gives three maxima at 9.1 Å, 14.6 Å, and 17.1 Å (Figure 40). The smallest pore (A) has an octahedral shape and is displayed as yellow sphere in Figure 40. The other two pores are of a cuboctahedral shape, whereas the biggest pore (B) is displayed in red and the middle sized pore (C) in purple. A careful analysis of the crystal structure reveals that all terminal oxygen atoms in pore (C) are oriented outwards from this pore cage. Therefore, a post-synthetic exchange of the modulator does not affect this pore type. In contrast, the inner surface of the cages with centre in the Wyckoff position 8c (octahedral pore, A) and in the

Wyckoff position 4b (cuboctahedral pore, B) are modified by the post-synthetic ligand exchange.

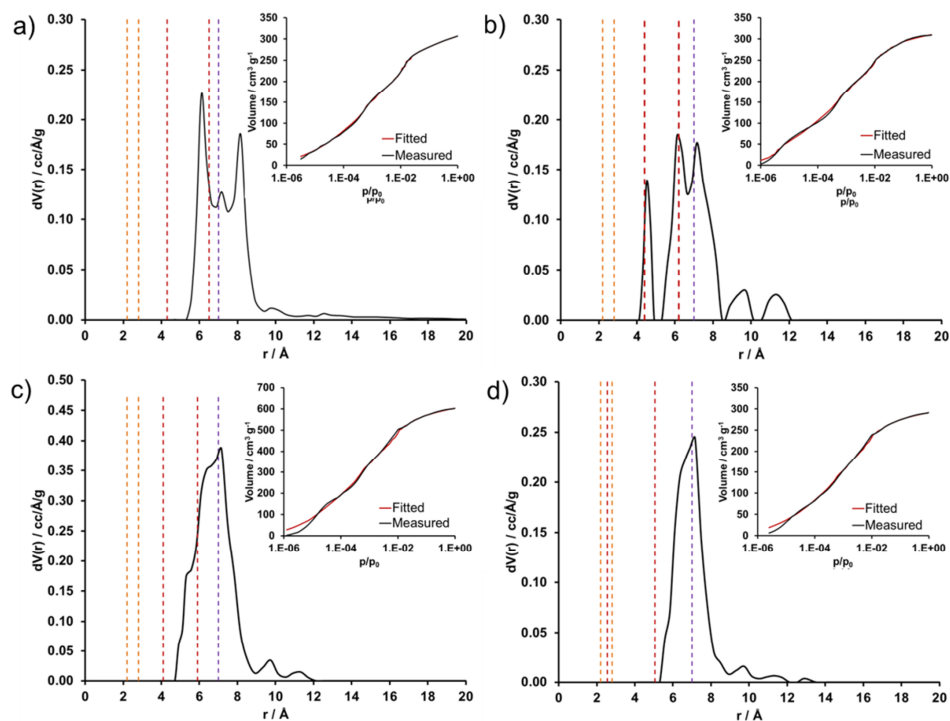


**Figure 40.** a) Pore system of DUT-67 without modulator and solvent molecules; b) Pore system of DUT-67-Pfba: cuboctahedral pore (B) (red sphere in Fig. 17a) is affected by the modulator exchange; octahedral pore (A) (yellow sphere in Fig. 17a) splits by DMF molecules. Zirconium polyhedra are illustrated in green, carbon atoms in dark grey, oxygen atoms in red and sulphur in yellow, nitrogen atoms in dark blue, fluorine atoms in pale blue and hydrogen atoms in white; c) Pore size distribution, calculated for the structural models of DUT-67(Zr) materials containing different modulator molecules, using Zeo++ program.<sup>248</sup>

In order to calculate the pore size distributions of DUT-67 that contain the different monocarboxylate ligands, their crystal structures were simulated. Because a defined amount of DMF is always coordinated to the cluster in DUT-67, three DMF molecules were placed in the small octahedral pore (A). Their presence leads to a formal splitting of the pore space into two voids with much smaller pore size. Zeo++ program identifies this pore as two different pores with 4.4 Å and 5.7 Å in diameter (marked yellow in Figure 40). The steric size of most

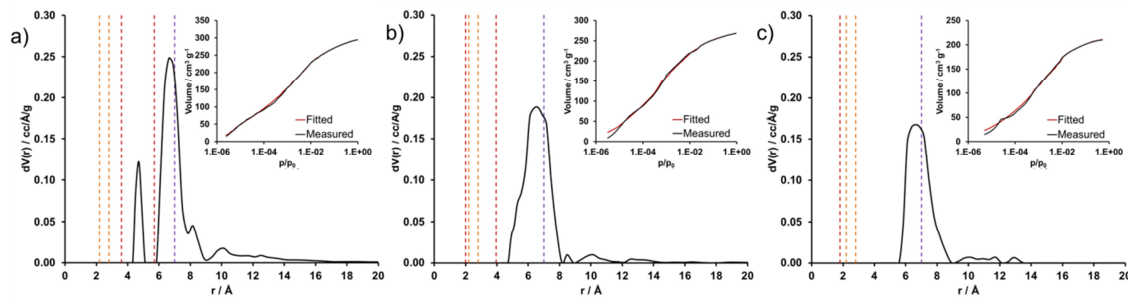
of the mono-carboxylate ligands is too large to be located in the small pore (A). Therefore, these ligands were placed in the bigger cuboctahedral pore (B) in the crystal structure simulations. There, the pore space is also divided into two voids (marked red in Figure 40). After insertion of the monocarboxylate ligands, the size of this pore type ranges from originally 17.1 Å for a hypothetical structure without modulator molecules to 3.6 Å for a structure containing the long perfluorinated alkylcarboxylate Pfoa. It has to be mentioned that the positions of DMF and modulator molecules on the cluster are statistically disordered within the above mentioned cages and the model for the calculation is only an approximation. Nonetheless the structural models describe well the changes on the inner surface of the material and are helpful for understanding the functionalization process in detail.

To compare the pore sizes calculated on the basis of the simulated structures with the experimentally observed pore size distributions, NLDFT methods were applied to N<sub>2</sub> adsorption isotherms at 77 K of the corresponding MOFs. The best fit could be achieved using a silica kernel based on a spherical and cylindrical pore model. At relative pressures higher than 10<sup>-5</sup>, the calculated and measured isotherms are in good agreement. At lower pressures, deviations are observed, which can be attributed to inappropriate equilibration or quadrupole interactions, a common problem in high resolution nitrogen adsorption isotherms.<sup>194</sup> For this reason, the pore sizes estimated for the smallest pore (A) cannot be considered to reflect realistic values and are therefore not considered. In case of the unmodified DUT-67-Fa the pore size distribution show three distinct maxima, which represent the three different pore types (Figure 41 a). The maximum at 14.3 Å can be attributed to the cuboctahedral pore (C), which does not contain any modulator molecules inside. The same pore size could be determined for DUT-67-Ac, DUT-67-Tfa and DUT-67-Tfmba (Figure 41 b-d), which is in good agreement with the calculated pore size from the simulated structures. The size of the cuboctahedral pore (B), where the ligand exchange takes place, decreases with the size of the incorporated ligand. Whereas the pore size of this pore type for DUT-67-Fa is with a diameter of 16.3 Å very close to the calculated pore size of 17.1 Å for the structure without any modulator, the pore sizes of the other compounds are significantly reduced. The diameter of this pore type could be determined to 12.4 Å for DUT-67-Ac and to an approximate diameter of 12.7 Å for DUT-67-Tfa and DUT-67-Tfmba. Despite the different sizes of the incorporated ligands, the determined pore diameters are quite similar, which can be explained with a varying degree of ligand exchange.



**Figure 41.** Pore size distributions derived by nitrogen isotherms at 77 K for a) DUT-67-Fa; b) DUT-67-Ac; c) DUT-67-Tfa and d) DUT-67-Tfmba. The coloured dotted lines correspond to the pore sizes of the simulated structures calculated by Zeo++ program. The yellow lines are attributed to the theoretical radii of the octahedral pore (A), the red lines to the cuboctahedral pore (B) and the purple line to the cuboctahedral pore (C).

The broadening and the overlapping of the peaks in the pore size distribution of DUT-67 originate from the rotational mobility of the ligands inside the pores. For DUT-67-Pa, DUT-67-Pfba and DUT-67-Pfoa the peaks are stronger overlapping than in the other cases (Figure 42). Therefore, the pore diameter of these compounds could not be determined exactly. Only an average pore size is determined, which cannot differentiate between the two pore types. As expected, the average pore diameter of DUT-67-Pa is with 13.2 Å larger than the average pore diameters of DUT-67-Pfba and DUT-67-Pfoa, which could be determined to be 12.7 Å.

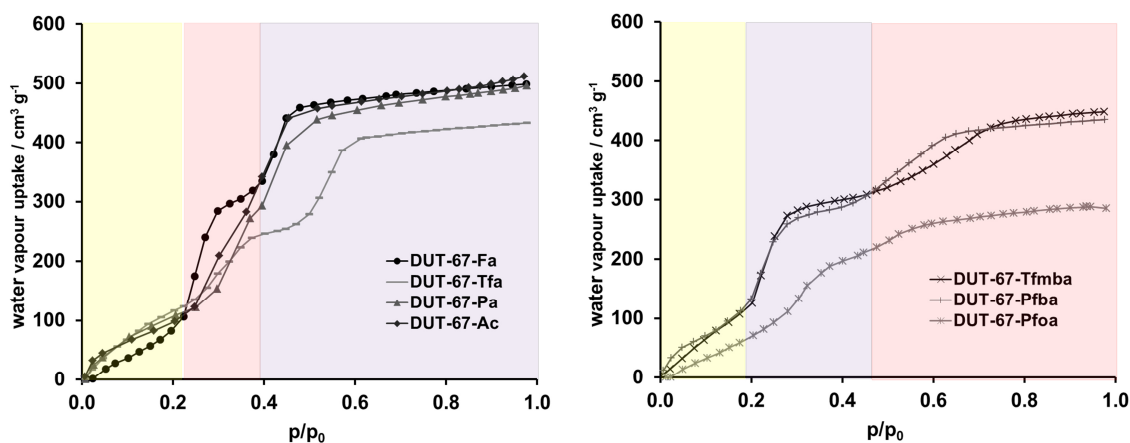


**Figure 42.** Pore size distributions derived by nitrogen isotherms at 77 K for a) DUT-67-Pa; b) DUT-67-Pfba and c) DUT-67-Pfoa. The coloured dotted lines correspond to the pore sizes of the simulated structures calculated by Zeo++ program. The yellow lines are attributed to the theoretical radii of the octahedral pore (A), the red lines to the cuboctahedral pore (B) and the purple line to the cuboctahedral pore (C).



The significant differences between the post-synthetically functionalized DUT-67 and the DUT-67 with alkyl-carboxylate as modulators are observed in water vapour adsorption isotherms, which reveal the pore filling process. Thus, the respective water vapour physisorption isotherms were studied thoroughly to fathom the influence of the incorporated ligands on the surface properties.

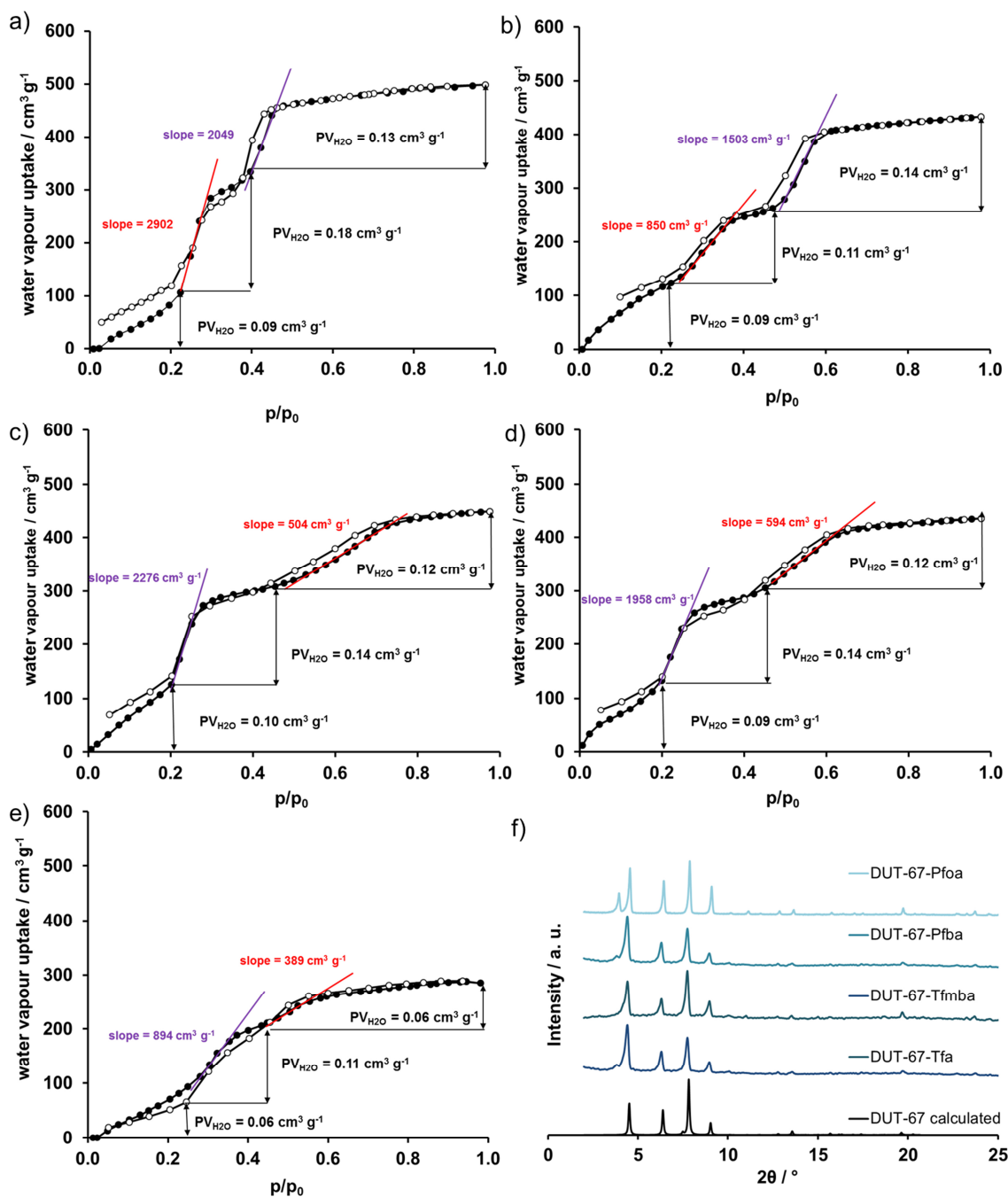
In general, the isotherms of DUT-67 consist of three distinct steps, representing the three different pore types discussed above. The first step ends at a relative pressure of 0.2 and is attributed to the filling of small octahedral pore (A). Up to this pressure, the DUT-67 with fluorinated ligands show no differences in the slope of the adsorption branch compared to DUT-67-Fa, DUT-67-Ac or DUT-67-Pa, indicating that the inner surface of the smallest pore is not affected by modulator exchange. This leads to the conclusion that this pore type offers no space for modulator exchange and that the free coordination sites, which are directing in this type of pore, are only occupied with DMF molecules. The second plateau in the isotherm of DUT-67-Fa starts at relative pressures around 0.3 and is attributed to the filling of the larger cuboctahedral pore (B), whose surface is most prone to be affected by modulator chemistry. Therefore the major differences in water adsorption isotherms including different ligands are visible in the isotherm step, which is responsible for filling of this pore type. As discussed in chapter 5.2.1, modulators with longer alkyl chains than formate provoke a decreased slope of the isotherm in the corresponding pressure region as well as a shift of the saturation point to higher humidity. Such a changed adsorption progress is a clear indicator that the hydrophobicity of this particular cage is increased and depends thereby on the used modulator. The third step of the isotherm of DUT-67-Fa starts at a relative pressure of 0.4. Its slope is smaller than the one of the second step, indicating a more hydrophobic surface. The isotherms slope of DUT-67-Ac and DUT-67-Pa are quite identical in this pressure range. Therefore, the third step of these isotherms can be referred to the filling of the cuboctahedral pore (C), where no free coordination sites of the cluster are located and only  $\text{tdc}^{2-}$  linker molecules decorate the pore walls. Modulator molecules do not affect the surface properties in this pore type, since they do not protrude into it. Thus, a similar progress of the corresponding isotherms step and a filling of this pore at similar relative pressures are expected. Summarizing, the use of different modulators in the synthesis of DUT-67 influences only the pore filling of the cuboctahedral pore (B), where the exchange of modulator takes place. A similar pore filling mechanism can be assumed for the fluorinated DUT-67-Tfa that could be obtained only utilizing post-synthetic modulator exchange (Figure 43 left).



**Figure 43.** Water vapour adsorption isotherms at 298 K: Left: DUT-67-Fa (black circles), DUT-67-Ac (dark grey diamonds), DUT-67-Pa (grey triangles) and DUT-67-Tfa (light grey stripes). Right: DUT-67-Tfmba (dark grey twisted crosses), DUT-67-Pfba (grey crosses) and DUT-67-Pfoa (light grey stars). The background colour represents the filling of the corresponding pore (yellow: small octahedral pore, purple: cuboctahedral pore without modulator, red: cuboctahedral pore with modulator).<sup>248</sup>

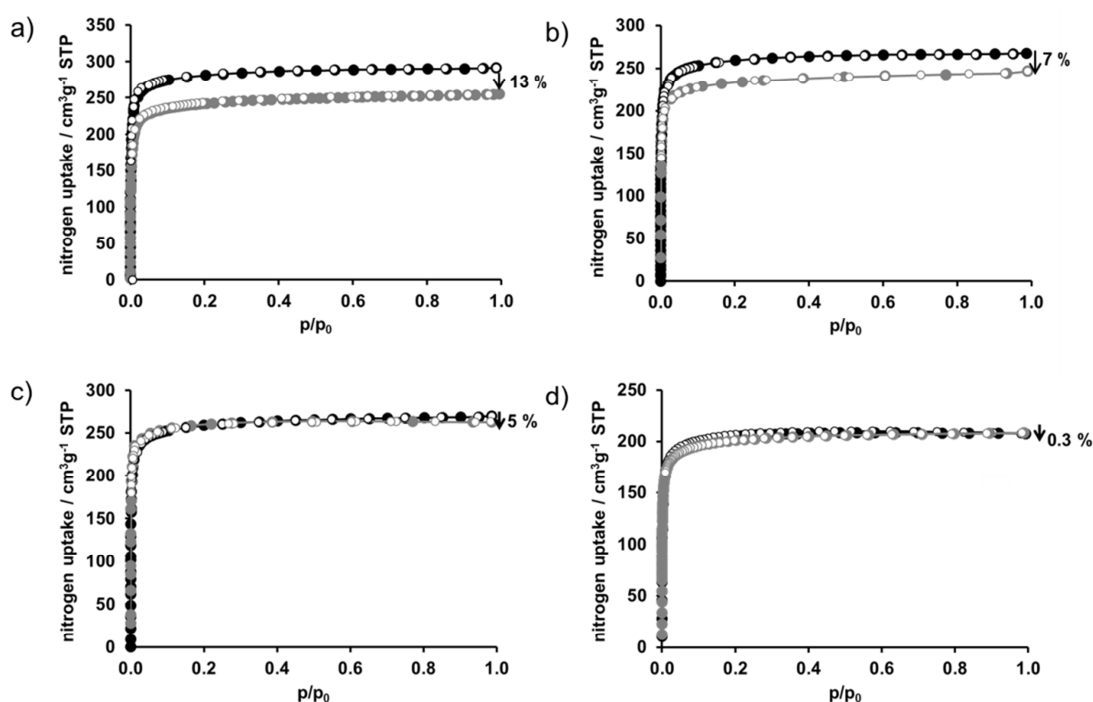
If more sterically demanding fluorinated monocarboxylic acids are used for the post-synthetic exchange, the pore filling mechanism for DUT-67-Tfmba, DUT-67-Pfba, and DUT-67-Pfoa changes drastically. The large fluorinated carboxylic acids shield the polar zirconium cluster and repel water molecules from the cuboctahedral pore (B), causing a switching of the pore filling order of the two different cubocathedral pore types. Now, the cuboctahedral pore (C), which has no free coordination sites, corresponds to the second step in the water adsorption isotherm (Figure 43 right). This assumption is supported by the comparison of the corresponding slopes in water adsorption isotherms (Figure 44 a-d). Thus, the slope of the second step in DUT-67-Pfba and DUT-67-Tfmba water adsorption isotherms correspond exactly to the third step of parent DUT-67-Fa. At the same time, the slopes of the third step in adsorption isotherms of DUT-67-Pfba, DUT-67-Tfmba and DUT-67-Pfoa are extremely small. The isotherms reach saturation at  $p/p_0 = 0.68$  (Pfba),  $p/p_0 = 0.78$  (Pfmba) and  $p/p_0 \approx 0.6$  (Pfoa) that is significantly higher in comparison with the water adsorption isotherm of DUT-67-Fa, showing saturation at  $p/p_0 = 0.5$ . Furthermore, the pore volume of the cuboctahedral pore (C), calculated from the third step of the DUT-67-Fa water adsorption isotherm is with  $0.13 \text{ cm}^3 \text{ g}^{-1}$  similar to the pore volume calculated for DUT-67-Tfa and similar to the pore volumes of the second steps of DUT-67-Pfba and DUT-67-Tfmba isotherms ( $V_p = 0.14 \text{ cm}^3 \text{ g}^{-1}$ ). Similar calculations for the cuboctahedral pore (B) with modulator molecules inside result in  $0.11 \text{ cm}^3 \text{ g}^{-1}$  for DUT-67-Tfa ( $p/p_0 = 0.2-0.57$ ),  $0.12 \text{ cm}^3 \text{ g}^{-1}$  for DUT-67-Pfba ( $p/p_0 > 0.47$ ) and DUT-67-Tfmba ( $p/p_0 > 0.55$ ). These values are significantly

smaller than  $0.18 \text{ cm}^3 \text{ g}^{-1}$ , which is calculated from the second step of the DUT-67-Fa isotherm ( $p/p_0 = 0.22-0.4$ ).



**Figure 44.** Water adsorption (solid symbols) and desorption (blank symbols) isotherms at 298 K of DUT-67-Fa (a), DUT-67-Tfa (b), DUT-67-Tfmba (c), DUT-67-Pfba (d) and DUT-67-Pfoa (e). The red lines represent the slope of the isotherm for the pore filling of the cuboctahedral pore B (red sphere in Figure 40), and the purple lines represent the slope of the isotherm for the pore filling of the cuboctahedral pore C (purple sphere in Figure 40). PXRD patterns (f) of DUT-67 with the exchanged modulators pentafluorobenzoic acid (Pfba), trifluoromethybenzoic acid (Tfmba), trifluoroacetic acid (Tfa), and perfluorooctanoic acid (Pfoa) after water desorption and activation in vacuum at  $100^\circ \text{C}$ .

Based on the isotherm slopes and pore volumes, calculated for the different pore types it is concluded that fluorinated species, introduced into the pores not only hinder water adsorption in the pores, but also affect the pore filling mechanism and even cause a reversal of the pore filling sequence. In the case of DUT-67-Pfoa, the flexibility of the alkyl chains and fluorination degree of the octanoic acid affects all steps in the water adsorption isotherm (Figure 44 e). Thus, Pfoa is the only tested modulator molecule, which is able to influence the hydrophobicity of both cuboctahedral pore types. This could be enabled due to the nearly complete blocking of the cuboctahedral pore (B), hindering water molecules to diffuse into the cuboctahedral pore (C) with no terminating ligands inside. The water vapour adsorption isotherms of all DUT-67 analogues show a hysteretic behaviour. In contrast to the DUT-67 containing alkyl carboxylate ligands, the hysteresis loops of the fluorinated DUT-67 are almost closing during desorption, indicating a reversibility of the process and improved water stability.



**Figure 45.** Nitrogen isotherms at 77 K of a) DUT-67-Tfmba; b) DUT-67-Tfa; c) DUT-67-Pfba and d) DUT-67-Pfoa before (black circles) and after (grey circles) water desorption and activation in vacuum at 100 °C.

The increased stability could also be demonstrated by measuring the porosity of DUT-67 samples after the water adsorption/desorption process. Thereby, the samples were activated at relatively harsh temperatures of 100 °C. As mentioned in the previous chapter, the use of

propionic acid or acetic acid as modulator decreases the loss of porosity from 34% (DUT-67-Fa) to 20% after water desorption. The introduction of fluorinated ligands stabilizes the framework against water desorption significantly. The loss of porosity is then reduced to 13% for DUT-67-Tfmba, to 7% for DUT-67-Tfa and to 5% for DUT-67-Pfba. In case of DUT-67-Pfoa the porosity loss could be minimized to even 0.3% (Table 10, Figure 45). In addition, not only porosity, but also crystallinity is preserved after water desorption in vacuum at 100 °C. The PXRD patterns of all functionalized DUT-67 (Figure 44 f), and even of DUT-67-Fa, match well the calculated one, confirming phase purity and a high degree of crystallinity.

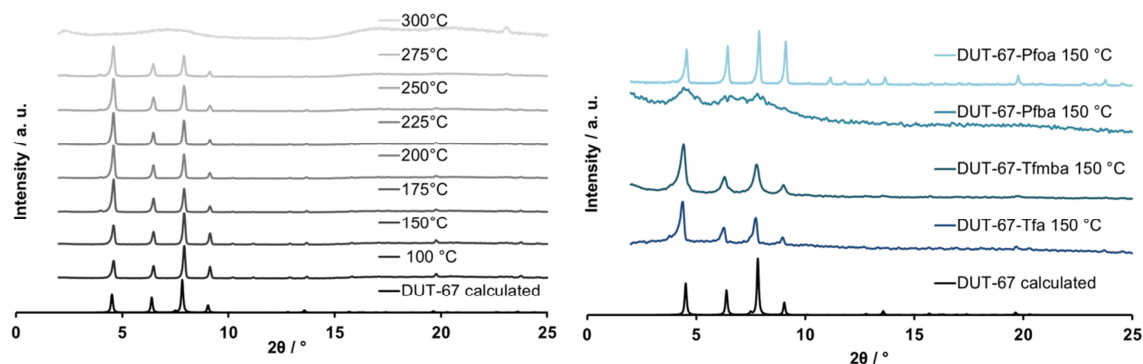
The observation was made that if DUT-67-Fa gets in contact with water, it soaks up the water and sinks down. In contrast, the fluorinated DUT-67 floats on the top of the surface of the water. Therefore, the increased hydrophobicity of the fluorinated DUT-67 was also verified by water contact angle measurements (Figure 46). To enable the contact angle measurements, the materials were compressed to pellets. In case of DUT-67-Fa, a contact angle could not be determined. Due to its hydrophilic properties the water droplet was completely absorbed. On the contrary, no significant water absorption was observed for all other investigated samples. DUT-67-Ac, DUT-67-Pa and DUT-67-Tfa behave similar hydrophilic, displaying an advancing contact angle close to 60°. In case of the fluorinated DUT-67, where the sequence of the pore filling with water is switched, the contact angles are significant higher and reach up to 119°. With such high contact angles the functionalized DUT-67 can be regarded as more hydrophobic materials. The increasing hydrophobicity is thereby in good agreement with the stability increases during water removal.

Compound	DUT67-Fa	DUT67-Ac	DUT67-Pa	DUT67-Tfa	DUT-67-Pfba	DUT-67-Tfmba	DUT67-Pfoa
Advancing angle / °	-	69 ± 3	63 ± 2	62 ± 1	83.5 ± 0.8	103 ± 1	119 ± 0.5

Figure 46. Advancing water contact angle for investigated compounds.<sup>248</sup>

To investigate the thermal stability of DUT-67 materials with the various ligands, TGA/DTA measurements were carried out (FigureA 5, FigureA 6). In general, DMF molecules are released in air at temperatures higher than 150 °C, whereas the linker tdc<sup>2-</sup> starts to be released at ~ 280 °C. This is in good agreement with *in situ* thermo XRD measurements of DUT-67-Fa, where the transition from a crystalline to an amorphous material takes place at

temperatures between 275-300 °C. The release of the modulators and the fluorinated monocarboxylates take place at lower temperatures. In case of DUT-67-Fa, the release of the modulator formate, which takes place at temperatures higher than 217 °C, does not lead to framework collapse. If more bulky ligands are involved, the thermal stability of the framework is reduced.



**Figure 47.** Left: *in situ* thermo PXR measurements of DUT-67-Fa; Right: PXR patterns of fluorinated DUT-67 which were activated in vacuum at 150 °C.

PXR measurements show that the functionalized DUT-67 materials become less crystalline if they are activated in vacuum at 150 °C (Figure 47). DUT-67-Pfba becomes even amorphous. DUT-67-Pfoa is the only exception; it seems to be stable under these conditions. In addition, the fluorinated ligands form weaker bonds to the Zr-cluster than the alkyl-carboxylates due to decreased basicity. Therefore, the release of the fluorinated ligands starts at lower temperatures (Table 11). However, activation in vacuum at 100 °C is uncritical for all compounds. At this temperature, the crystallinity is preserved (Figure 44 f).

**Table 11.** Monocarboxylic ligand release temperature.

Ligand	pKa	Temperature of modulator loss according to TGA / °C
Propionic acid (HPa)	4.87	239
Acetic acid (HAc)	4.76	236
Formic acid (HFa)	3.75	217
Trifluoromethylbenzoic acid (HTfmba)	3.6	200
Pentafluorobenzoic acid (HPfba)	1.6	190
Trifluoroacetic acid (Tfa)*	0.23	197 - 237
Perfluorooctanoic acid (HPfoa)	0	174

\* The exact temperature could not be determined, due to the peaks overlap.

### 5.2.3 Post-synthetic inner surface functionalization of DUT-67 with chiral ligands

With the post-synthetic functionalization approach, the incorporation of chiral ligands into DUT-67 is also possible. The chiral functionalization opens new fields of supposable applications, like enantioselective catalysis or the separation of enantiomers. Since the crystal size distribution is very homogenous (Figure 48) and the crystal size is tuneable by the amount of modulator used in the synthesis, DUT-67 should be suitable as column packing material for e.g. high-performance liquid chromatography (HPLC).

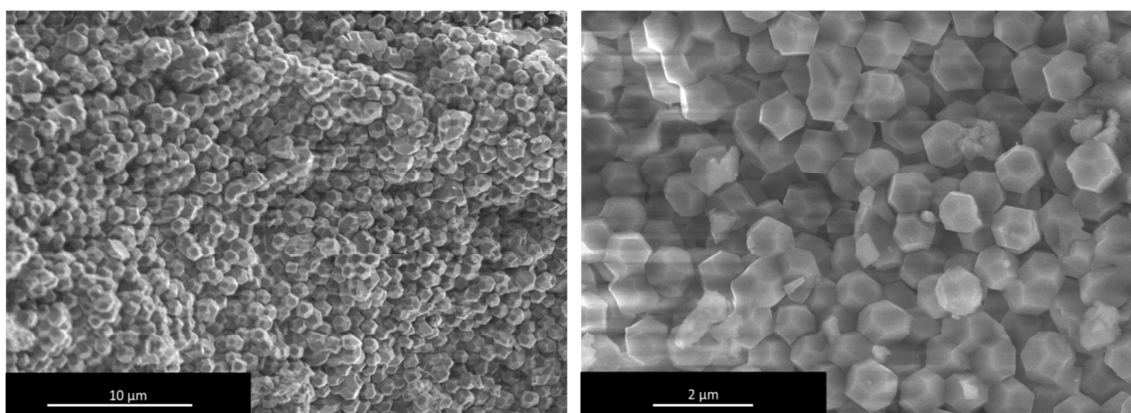
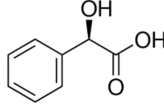
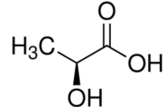
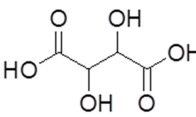


Figure 48. SEM images of DUT-67-Ma at different resolutions.

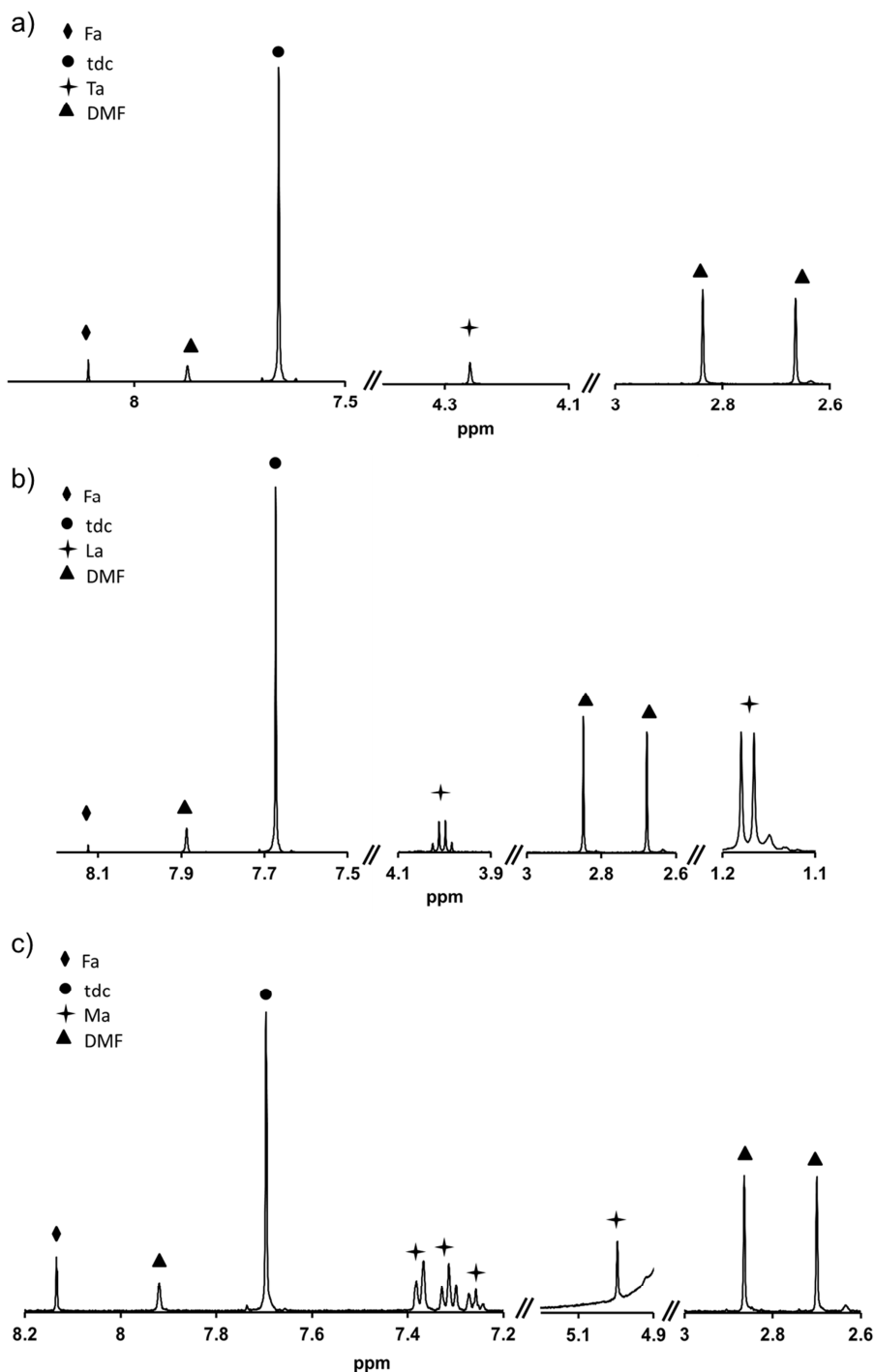
In this work, the chiral carboxylic acids, tartaric acid (HTa), mandelic acid (HMa) and lactic acid (HLa) were used (Table 12) for the functionalization.

Table 12. List of chiral carboxylic acids used for the post-synthetic modulator exchange in DUT-67.

Compound	Carboxylic acid	Structural formula
DUT-67-Ma	(R)-(-)-Mandelic acid	
DUT-67-La	L-(+)-Lactic acid	
DUT-67-Ta	DL-Tartaric acid	

Their successful incorporation into DUT-67 is proven by  $^1\text{H-NMR}$  measurements of the digested samples (Figure 49): the chemical shift of the exchanged modulator tartaric acid can

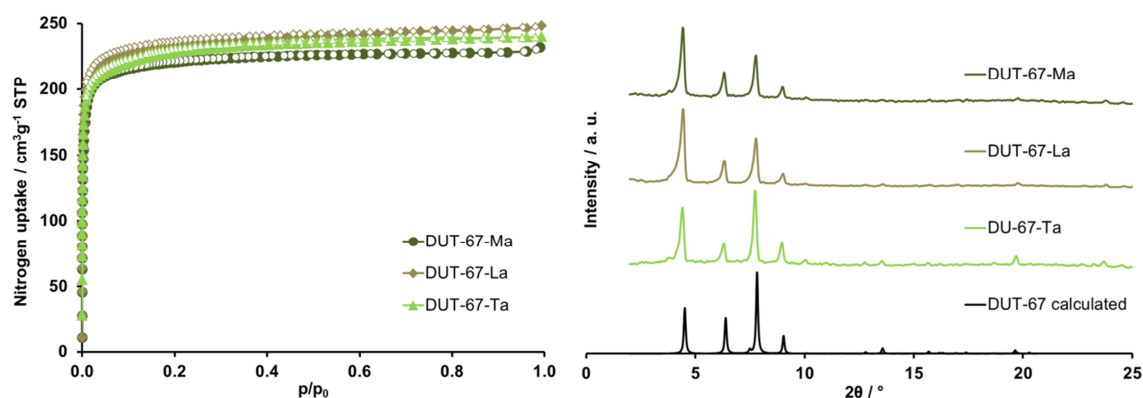
be assigned to 4.26 ppm, of lactic acid to 1.17 ppm and to 4.0 ppm and of mandelic acid to 4.97 ppm, 7.23 ppm, 7.28 ppm and 7.34 ppm. The exchange rate can be determined by the integration and comparison of the respective peaks of the chiral ligands and the tdc<sup>2-</sup> linker in the <sup>1</sup>H-NMR spectra. Whereas DUT-67-Ma and DUT-67-Ta show exchange rates of 12% and 16%, respectively, the modulator formate is completely replaced with lactate in DUT-67-La.



**Figure 49.** Details of the <sup>1</sup>H-NMR spectra of digested samples of a) DUT-67-Ta, b) DUT-67-La and d) DUT-67-Ma.



Similar to the introduction of the hydrophobic fluorinated ligands, the exchange of the hydrophilic chiral ligands with the pristine modulator formate does not affect the degree of crystallinity significantly (Figure 50 right). The PXRD patterns remained unchanged and the crystal morphology is also preserved, which can be seen in SEM images (Figure 48). The functionalized DUT-67 analogues are still porous, whereas the specific surface area as well as the total pore volume are decreased compared to parent MOF DUT-67-Fa, which exhibited a pore volume of  $0.47 \text{ cm}^3 \text{ g}^{-1}$  and a specific surface area of  $1143 \text{ m}^2 \text{ g}^{-1}$  (Table 13, Figure 50 left). The pore volumes of these chiral functionalized MOFs are quite similar if activated at  $100 \text{ }^\circ\text{C}$ . In detail, the pore volume of DUT-67-Ta amounts to  $0.37 \text{ cm}^3 \text{ g}^{-1}$ , of DUT-67-La to  $0.38 \text{ cm}^3 \text{ g}^{-1}$  and of DUT-67-Ma to  $0.36 \text{ cm}^3 \text{ g}^{-1}$ .

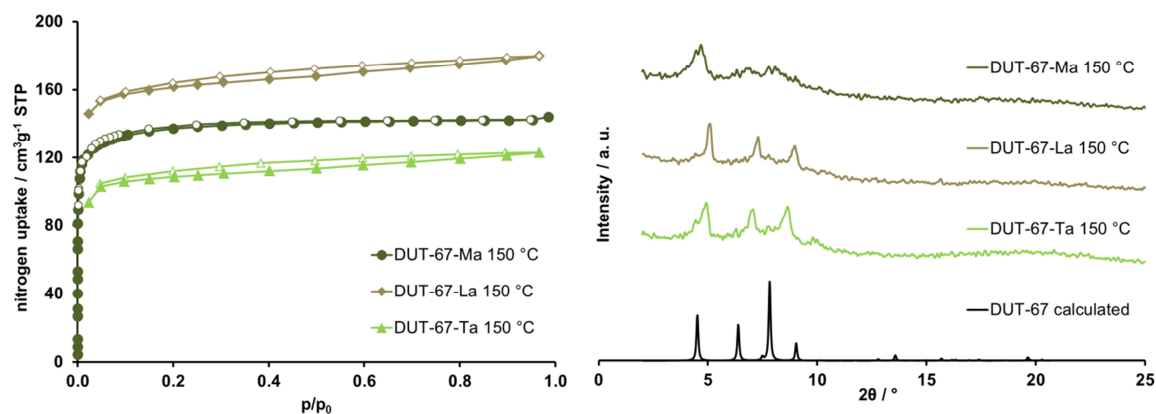


**Figure 50.** Left: nitrogen isotherms at 77 K of DUT-67-Ma (dark green circles), of DUT-67La (ochre diamonds) and DUT-67-Ta (light green triangles) activated in vacuum at  $100 \text{ }^\circ\text{C}$ ; Right: PXRD patterns of DUT-67-Ma, DUT-67-La and DUT-67-Ta after activation in vacuum at  $100 \text{ }^\circ\text{C}$ .

**Table 13.** Textural properties of chiral functionalized DUT-67.

MOF	DUT-67-	DUT-67-	DUT-67-
	Ma	La	Ta
Pore volume derived from nitrogen adsorption after activation at $100 \text{ }^\circ\text{C}$ , $\text{cm}^3 \text{ g}^{-1}$	0.36	0.38	0.37
Surface area (BET) derived from nitrogen adsorption after activation at $100 \text{ }^\circ\text{C}$ , $\text{m}^2 \text{ g}^{-1}$	855	902	868
Pore volume derived from nitrogen adsorption after activation at $150 \text{ }^\circ\text{C}$ , $\text{cm}^3 \text{ g}^{-1}$	0.22	0.25	0.17
Surface area (BET) derived from nitrogen adsorption after activation at $150 \text{ }^\circ\text{C}$ , $\text{m}^2 \text{ g}^{-1}$	534	547	368

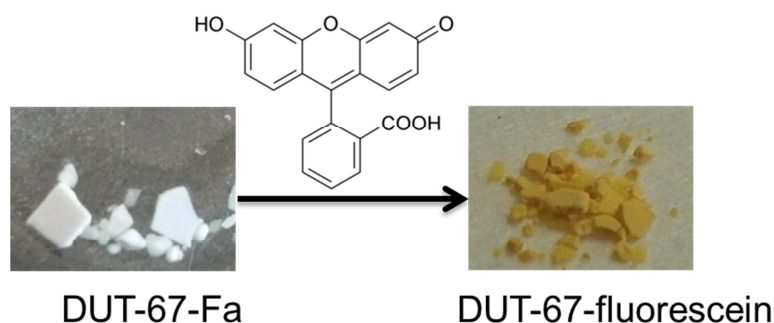
If the activation temperature is increased to 150 °C, a drastic loss of porosity takes place. The pore volumes are reduced to 0.22 cm<sup>3</sup> g<sup>-1</sup> for DUT-67-Ma, to 0.25 cm<sup>3</sup> g<sup>-1</sup> for DUT-67-La and even to 0.17 cm<sup>3</sup> g<sup>-1</sup> for DUT-67-Ta. Accordingly, the crystallinity is also seriously affected at this high temperature – the bragg-reflections in PXRD are broadened and a significant amount of an amorphous phase is formed (Figure 51). Therefore, an application of these materials is limited to lower temperatures.



**Figure 51.** Left: nitrogen isotherms at 77 K of DUT-67-Ma (dark green circles), of DUT-67La (ochre diamonds) and DUT-67-Ta (light green triangles) activated in vacuum at 150 °C; Right: PXRD patterns of DUT-67-Ma, DUT-67-La and DUT-67-Ta after activation in vacuum at 150 °C.

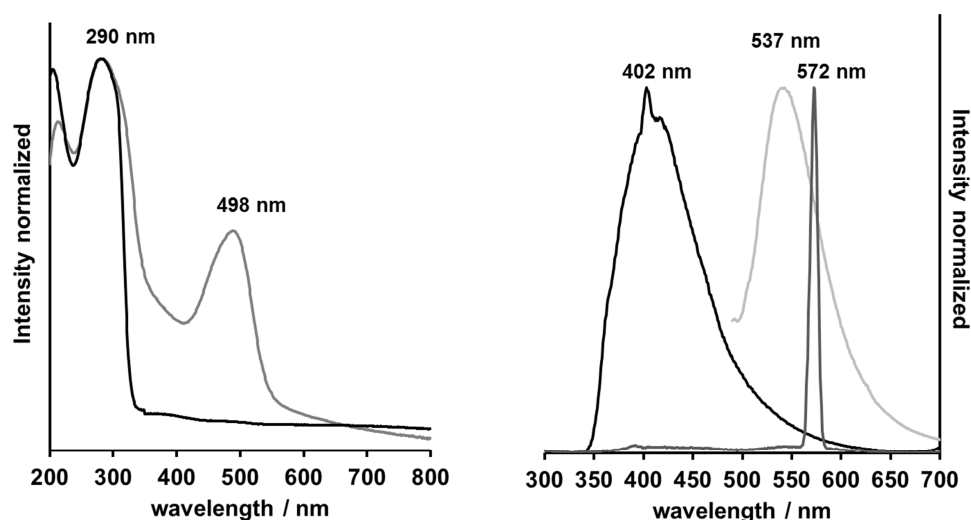
### 5.2.4 Post-synthetic inner surface functionalization of DUT-67 with fluorescein

The post-synthetic approach is also applicable to change the optical properties of the MOF. Dyes can be adsorbed in the pores of DUT-67, if their kinetic diameter is not too big to enter through the pore windows. For example, if DUT-67 gets into contact with a solution of indigo, it is stained in a blue colour. Though, the coloration will not last if the MOF is washed with pure solvent (DMF), since indigo has no functional group to coordinate strongly enough to the metal cluster and is released by the washing. Contrary, the fluorescein dye contains a carboxylic group, which can coordinate to the zirconium cluster.



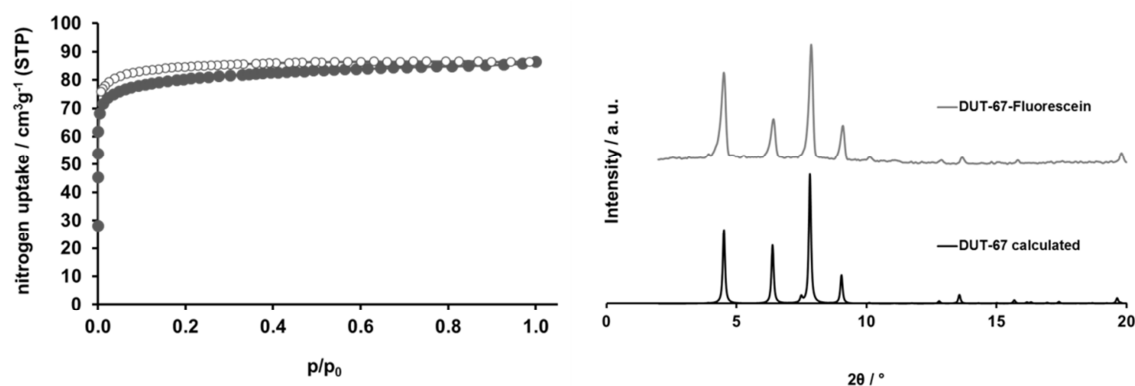
**Figure 52.** Incorporation of fluorescein dye in DUT-67.

Therefore it is not possible to remove the coordinated dye by simply washing the MOF several times with ethanol. After the incorporation of fluorescein, the colour of DUT-67 changes from white to yellow (Figure 52).



**Figure 53.** Left: UV/Vis absorption spectra of DUT-67-Fa (black curve) and DUT-67-fluorescein (grey curve); Right: Fluorescence spectra of DUT-67-Fa (black curve) and DUT-67-fluorescein (dark grey curve) excited at 290 nm and of DUT-67-fluorescein (light grey curve) excited at 485 nm.

Thus, the UV-Vis-absorption spectrum is changing. DUT-67-Fa has an absorption maximum at 290 nm, whereas DUT-67-fluorescein has an additional maximum at 498 nm, which originates from the fluorescein dye (Figure 53 left). The absorption maximum of fluorescein in the solid state described in literature is at 496 nm and in the solvated state at 434 nm for the neutral form, at 453 nm and 472 nm for the anionic form and at 490 nm for the dianionic form. DUT-67-Fa has its fluorescence emission maximum at 402 nm if excited at 290 nm. With the presence of fluorescein in the framework, the emission spectrum has a bathochromic shift and its maximum is then located at 572 nm. If DUT-67-fluorescein is excited at 485 nm, the emission maximum is shifted to 537 nm (Figure 53 right), while DUT-67-Fa does not show any significant emission behaviour for both excitation wavelengths. The fluorescence emission spectrum of formic acid given by the literature has a peak at 310 nm and a broad continuum in the range from 330 nm to 500 nm if excited with higher energy (123.9 nm).<sup>256</sup> In the case of fluorescein, the anionic and the dianionic forms are known to be fluorescent. Both have an emission maximum at around 517 nm if excited above 300 nm. The emission spectrum of the anionic form is broader and has a shoulder peak at approximately 550 nm.<sup>257</sup> After the incorporation of the fluorescein dye, DUT-67 is still highly crystalline (Figure 54). Yet, the porosity is decreased with the incorporation of such a sterically demanding ligand. The total pore volume derived from nitrogen physisorption isotherm at 77 K is only  $0.13 \text{ cm}^3 \text{ g}^{-1}$  and the specific surface area amounts to  $313 \text{ m}^2 \text{ g}^{-1}$ . Nevertheless, the porosity of DUT-67-fluorescein is still sufficient for potential applications. Fluorescein is known for showing pH-dependent intensity changes in its fluorescence spectra. It is also known that fluorescein is changing its colour if bromine is present. Therefore, it is imaginable to use DUT-67-fluorescein as a non-solvable sensor for bromine or for different pH-values.

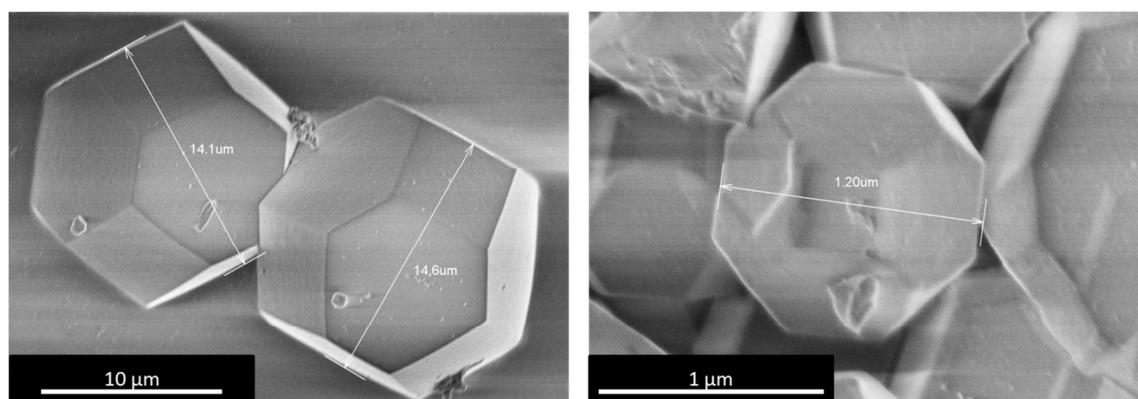


**Figure 54.** Left: nitrogen isotherm at 77 K of DUT-67-Fluorescein activated in vacuum at 100 °C; Right: PXRD pattern of DUT-67-Fluorescein

### 5.3 Post-synthetic treatment of DUT-67 with inorganic acids

To create open metal sites in Zr- or Hf-based MOFs with reduced connectivity, the treatment with inorganic acids is an effective method to remove modulator molecules selectively. For the purpose to get chloride or sulphate anions as counter anions for the metal cluster, several synthetic routes are suited. The attempt to synthesise a crystalline MOF by a direct synthesis of DUT-67 with HCl as modulator failed. A post-synthetic treatment of DUT-67-Fa with inorganic acids leads to a highly crystalline material, whose modulator molecules as well as DMF molecules are replaced by acid anions. In case of a fine powder of DUT-67, a low concentrated (2 wt%) solution of HCl or H<sub>2</sub>SO<sub>4</sub> and a short time of four hours suffice to remove all pristine modulator molecules and partially DMF molecules. A treatment of DUT-67 crystals of a size of ~1.2 μm with a 2wt% HCl solution for four hours (Figure 55) results in a metal/chlorine ratio of 6:4 (according to elemental analysis), as well as crystals of ~15 μm size, according to single crystal X-ray diffraction analysis.

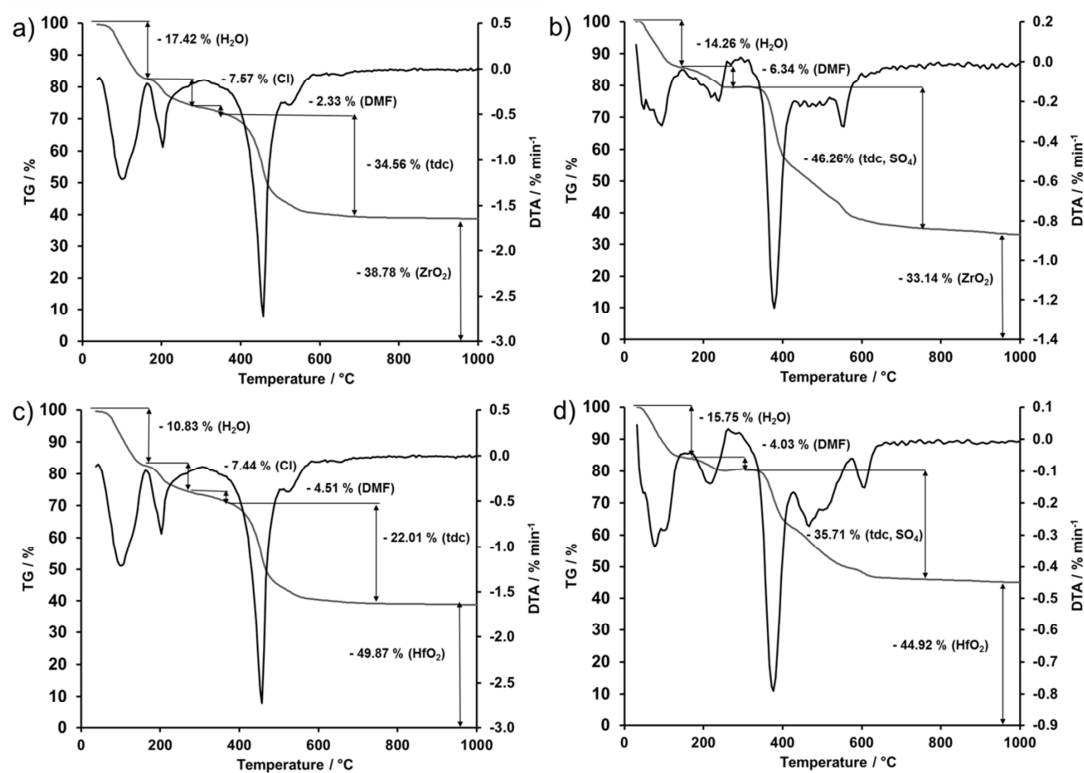
The rate of the removal of modulator molecules, as well as the presence of chloride or sulphate anions depends on several factors, such as time of treatment and concentration of the acidic solution. The resulting compositions, derived from elemental analysis and TG/DTA measurements (Figure 56), of a four hours treatment of DUT-67 with a size of ~1.2 μm are listed in Table 14. It is also worth to mention that a treatment with a 5 wt% solution of H<sub>2</sub>SO<sub>4</sub> for 24 hours results into a complete decomposition of the MOF.



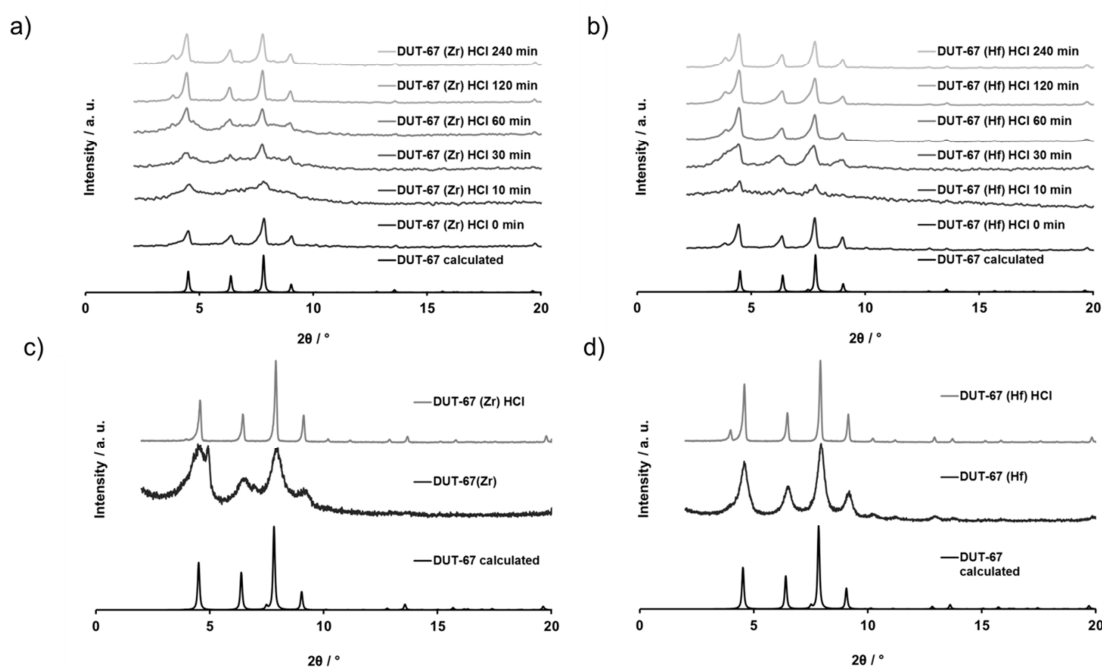
**Figure 55.** SEM images of DUT-67\_HCl of different sizes at different resolutions. The left image shows crystals that were used for single crystal X-ray analysis. The right image shows crystals that were used for a further characterization.

**Table 14.** Compositions of DUT-67(Zr) and DUT-67(Hf) which were treated with a 2wt% solution of HCl or H<sub>2</sub>SO<sub>4</sub> for 4 h.

MOF	Composition according to EA		Composition according to TG/DTA
	<i>found</i>	<i>calculated</i>	
<b>DUT-67(Zr)_HCl</b>	Zr <sub>6</sub> (μ <sub>3</sub> -O) <sub>4</sub> (OH) <sub>4</sub> (tdc) <sub>4</sub> Cl <sub>4</sub> (DMF)(EtOH) <sub>2</sub> C 22.40%, H 2.34%, N 0.82%, S 8.23%, Cl 8.89%	Zr <sub>6</sub> (μ <sub>3</sub> -O) <sub>4</sub> (OH) <sub>4</sub> (tdc) <sub>4</sub> Cl <sub>4</sub> (DMF)(EtOH) <sub>2</sub> C 22.34%, H 1.87%, N 0.84%, S 7.69%, Cl 8.51%	Zr <sub>6</sub> (μ <sub>3</sub> -O) <sub>4</sub> (OH) <sub>4</sub> (tdc) <sub>3.9</sub> Cl <sub>4.1</sub> (DMF) <sub>0.6</sub> (H <sub>2</sub> O) <sub>18.5</sub>
<b>DUT-67(Zr)_H<sub>2</sub>SO<sub>4</sub></b>	Zr <sub>6</sub> (μ <sub>3</sub> -O) <sub>2</sub> (μ <sub>3</sub> -OH) <sub>6</sub> (tdc) <sub>4</sub> (SO <sub>4</sub> ) <sub>3</sub> (DMF)(EtOH) <sub>2</sub> C 20.38%, H 2.03%, N 0.63%, S 12.35%	Zr <sub>6</sub> (μ <sub>3</sub> -O) <sub>2</sub> (μ <sub>3</sub> -OH) <sub>6</sub> (tdc) <sub>x</sub> (SO <sub>4</sub> ) <sub>y</sub> (DMF) <sub>1.9</sub> (H <sub>2</sub> O) <sub>17.7</sub> C 20.51%, H 1.83%, N 0.77%, S 12.36%	Zr <sub>6</sub> (μ <sub>3</sub> -O) <sub>2</sub> (μ <sub>3</sub> -OH) <sub>6</sub> (tdc) <sub>x</sub> (SO <sub>4</sub> ) <sub>y</sub> (DMF) <sub>1.9</sub> (H <sub>2</sub> O) <sub>17.7</sub>
<b>DUT-67(Hf)_HCl</b>	Hf <sub>6</sub> (μ <sub>3</sub> -O) <sub>4</sub> (OH) <sub>4</sub> (tdc) <sub>4</sub> Cl <sub>4</sub> (DMF) <sub>2.5</sub> (EtOH) <sub>2</sub> C 19.11%, H 1.26%, N 1.55%, S 6.34%, Cl 6.15%	Hf <sub>6</sub> (μ <sub>3</sub> -O) <sub>4</sub> (OH) <sub>4</sub> (tdc) <sub>4</sub> Cl <sub>4</sub> (DMF) <sub>2.5</sub> (EtOH) <sub>2</sub> C 18.54%, H 1.82%, N 1.52%, S 5.58%, Cl 6.16%	Hf <sub>6</sub> (μ <sub>3</sub> -O) <sub>4</sub> (OH) <sub>4</sub> (tdc) <sub>4</sub> Cl <sub>4.4</sub> (DMF) <sub>2.5</sub> (H <sub>2</sub> O) <sub>15.3</sub>
<b>DUT-67(Hf)_H<sub>2</sub>SO<sub>4</sub></b>	Hf <sub>6</sub> (μ <sub>3</sub> -O) <sub>2</sub> (μ <sub>3</sub> -OH) <sub>6</sub> (tdc) <sub>4</sub> (SO <sub>4</sub> ) <sub>3</sub> (DMF)(EtOH) <sub>2</sub> C 16.26%, H 1.77%, N 0.69%, S 9.81%	Hf <sub>6</sub> (μ <sub>3</sub> -O) <sub>2</sub> (μ <sub>3</sub> -OH) <sub>6</sub> (tdc) <sub>x</sub> (SO <sub>4</sub> ) <sub>y</sub> (DMF) <sub>1.6</sub> (H <sub>2</sub> O) <sub>24.6</sub> C 15.92%, H 1.42%, N 0.60%, S 9.60%	Hf <sub>6</sub> (μ <sub>3</sub> -O) <sub>2</sub> (μ <sub>3</sub> -OH) <sub>6</sub> (tdc) <sub>x</sub> (SO <sub>4</sub> ) <sub>y</sub> (DMF) <sub>1.6</sub> (H <sub>2</sub> O) <sub>24.6</sub>

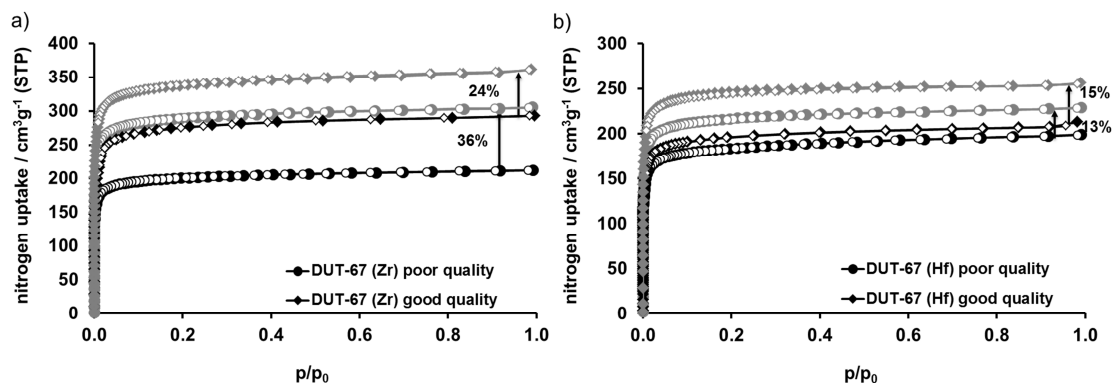
**Figure 56.** TG/DTA measurements of a) DUT-67(Zr)\_HCl, b) DUT-67(Zr)\_H<sub>2</sub>SO<sub>4</sub>, c) DUT-67(Hf)\_HCl and d) DUT-67(Hf)\_H<sub>2</sub>SO<sub>4</sub> in air.

During the acidic treatment process, using a 2 wt% HCl solution, the crystallinity of DUT-67 was monitored *via* PXRD measurements (Figure 57 a-b). The diffraction patterns show that after a short time (10-30 min) their crystallinity decreases and the Bragg-reflections are broadening. Then, after two hours, a highly crystalline material is formed, indicating that a recrystallization process takes place. Furthermore, the observation was made that a sample of DUT-67 with poor crystallinity and very broad Bragg-reflections shows after acidic treatment with HCl clearly defined and sharp reflections (Figure 57 c-d), which supports the thesis of a recrystallization- and healing process.



**Figure 57.** a) PXRD patterns of DUT-67(Zr), which is treated with a 2wt% solution of HCl at different times; b) PXRD patterns of DUT-67(Hf) which is treated with a 2wt% solution of HCl at different times; c) PXRD patterns of DUT-67(Zr) with poor quality as synthesised (dark grey) and after a treatment with a 2wt% solution of HCl for 24 hours (light grey); d) PXRD patterns of DUT-67(Hf) with poor quality as synthesised (dark grey) and after a treatment with a 2wt% solution of HCl for 24 hours (light grey).

The acidic treatment has also an influence on the porosity. For instance, for a sample of DUT-67(Zr), which was of very poor quality and low pore volume of  $0.33 \text{ cm}^3 \text{ g}^{-1}$  the porosity could be increased to  $0.45 \text{ cm}^3 \text{ g}^{-1}$  (increase of 36%) after 24 h of treatment. Correspondingly, an increase of porosity of 13% for DUT-67(Hf) from  $0.31 \text{ cm}^3 \text{ g}^{-1}$  to  $0.35 \text{ cm}^3 \text{ g}^{-1}$  occurred. If the longer reaction time is applied to already good porous MOFs with pore volumes of  $0.45 \text{ cm}^3 \text{ g}^{-1}$  (DUT-67(Zr)) and  $0.34 \text{ cm}^3 \text{ g}^{-1}$  (DUT-67(Hf)), the pore volumes could even be improved to  $0.56 \text{ cm}^3 \text{ g}^{-1}$  (DUT-67(Zr)\_HCl) and to  $0.39 \text{ cm}^3 \text{ g}^{-1}$  (DUT-67(Hf)\_HCl) (Figure 58).



**Figure 58.** Nitrogen physisorption isotherms at 77 K of a) DUT-67 (Zr) and b) DUT-67 (Hf) of poor quality (circles) and good quality (diamonds) before (black) and after (grey) the treatment of 2 wt% HCl solution (24 h).

The treatment time of only four hours results in porosity values which are very similar to those of the unmodified DUT-67. The total pore volumes for DUT-67(Zr) and its acid treated analogues range between  $0.46 \text{ cm}^3 \text{ g}^{-1}$  and  $0.48 \text{ cm}^3 \text{ g}^{-1}$ . For DUT-67(Hf) the total pore volumes remain unchanged with a value of  $0.33 \text{ cm}^3 \text{ g}^{-1}$  (Table 15).

**Table 15.** Textural properties of pristine DUT-67 and of DUT-67 that was treated with an acidic solution for four hours.

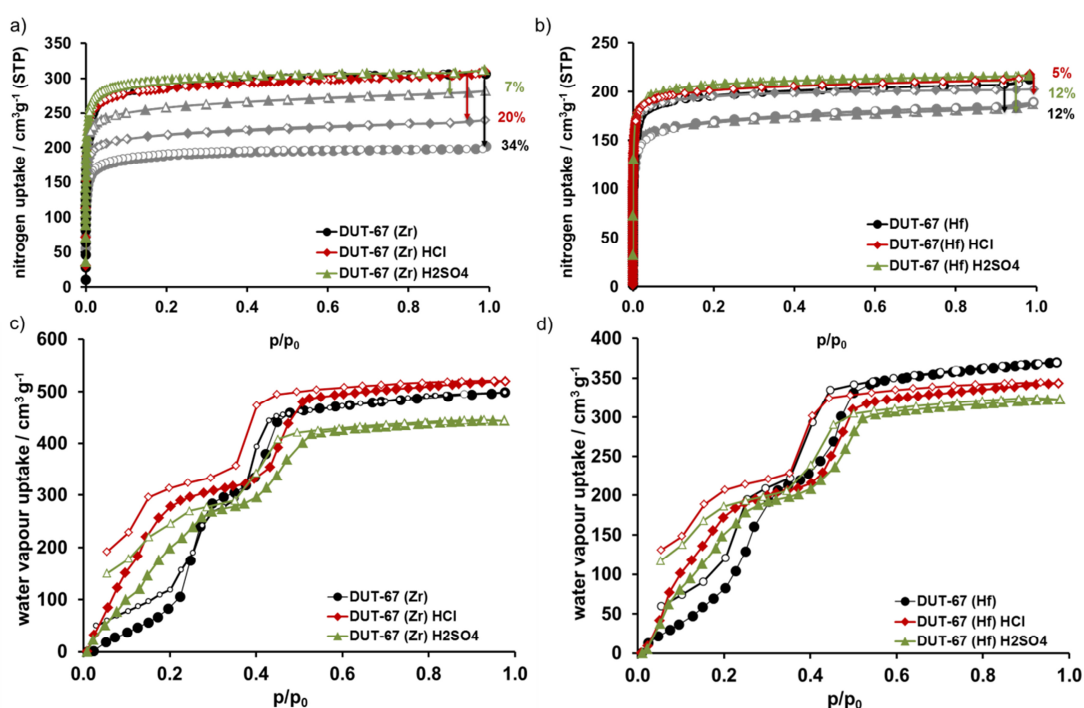
MOF	DUT-67 (Zr)	DUT-67 (Zr)_HCl	DUT-67 (Zr)_H <sub>2</sub> SO <sub>4</sub>	DUT-67 (Hf)	DUT-67 (Hf)_HCl	DUT-67 (Hf)_H <sub>2</sub> SO <sub>4</sub>
Pore volume derived from nitrogen adsorption, $\text{cm}^3 \text{ g}^{-1}$	0.47	0.46	0.48	0.33	0.33	0.33
Surface area (BET) derived from nitrogen adsorption, $\text{m}^2 \text{ g}^{-1}$	1143	1013	1153	763	791	798
Pore volume derived from water vapour adsorption, $\text{cm}^3 \text{ g}^{-1}$	0.40	0.42	0.37	0.30	0.28	0.28
Water pore filling degree*, in %	85	91	77	91	85	85
Pore volume derived from N <sub>2</sub> adsorption isotherm for materials after H <sub>2</sub> O adsorption/desorption, $\text{cm}^3 \text{ g}^{-1}$	0.31	0.37	0.45	0.29	0.31	0.29
Loss of porosity after H <sub>2</sub> O desorption, in %	34	20	7	12	6	12

\* Calculated as pore volume calculated from H<sub>2</sub>O divided by the pore volume calculated from N<sub>2</sub>. Both pore volumes were calculated at  $p/p_0 = 0.97$ .

Consequently, water physisorption measurements were performed on acid treated samples and the resulting isotherms are analysed analogously as described for the fluorinated DUT-67 in chapter 5.2.2 (Figure 599 c-d). As mentioned, the adsorption isotherm of DUT-67 contains three steps, representing the three different pore types: I) a small octahedral pore, II) a



cuboctahedral pore with open metal sites and, III) a cuboctahedral pore without open metal sites. The pore without open metal sites (respectively without modulator molecules), which corresponds to the last step in the isotherm, cannot be changed in its hydrophilic/hydrophobic properties. This becomes visible in the unchanged slope of the isotherm in the corresponding pressure region ( $p/p_0 > 0.35$ ). In contrast, the first and the second step ( $p/p_0 < 0.35$ ) are affected for DUT-67\_HCl and DUT-67\_H<sub>2</sub>SO<sub>4</sub> and their slopes are significantly steeper in comparison to the pristine DUT-67. This behaviour indicates a much more hydrophilic character of the pores, where the modulator molecules were removed or replaced by the counter ions Cl<sup>-</sup> or SO<sub>4</sub><sup>2-</sup>.

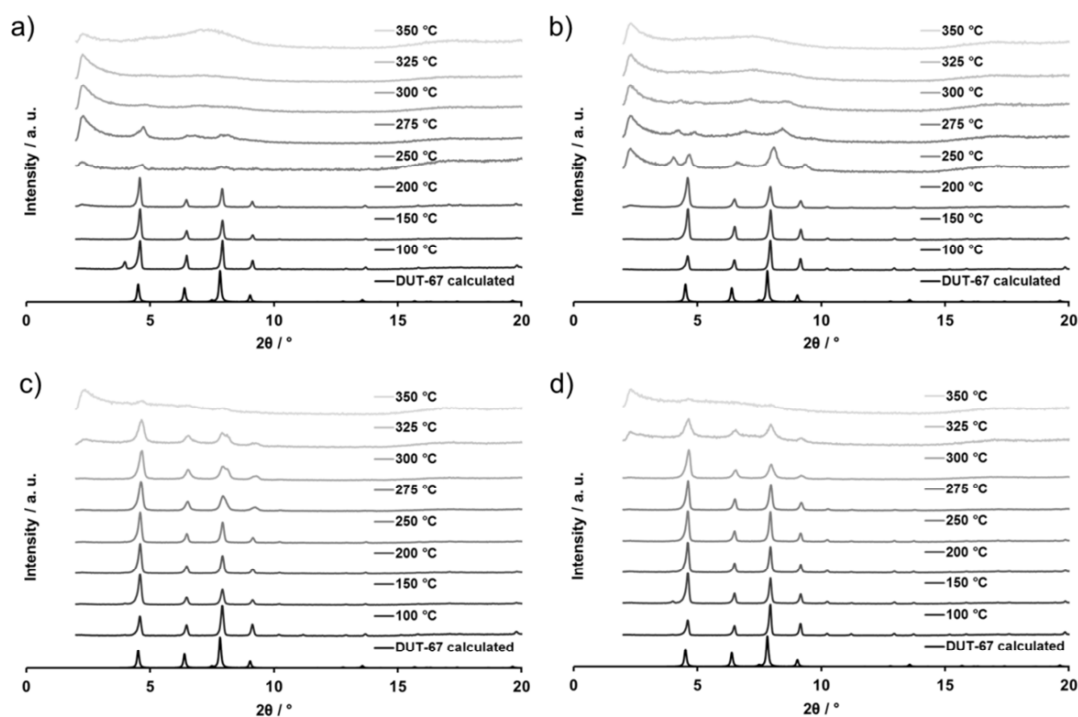


**Figure 59.** Nitrogen physisorption isotherms of a) Zr based and b) Hf based DUT-67 (black circles), DUT-67 HCl (red diamonds) and DUT-67\_H<sub>2</sub>SO<sub>4</sub> (green triangles) at 77 K. The grey coloured isotherms correspond to DUT-67 (circles), DUT-67\_HCl (diamonds) and DUT-67\_H<sub>2</sub>SO<sub>4</sub> (triangles), which were activated at 100 °C after water desorption. Water adsorption/desorption isotherms of c) DUT-67 (Zr) (black circles) and of d) DUT-67(Hf) and the acid treated analogues DUT-67\_HCl (red diamonds) and DUT-67\_H<sub>2</sub>SO<sub>4</sub> (green triangles) at 298 K.

Despite the more hydrophilic character of DUT-67\_HCl and DUT-67\_H<sub>2</sub>SO<sub>4</sub>, the stability of these frameworks after activation from water at 100 °C under vacuum is increased. While for pristine DUT-67(Zr) a decrease in its total pore volume of 34% after water removal was observed, DUT-67(Zr)\_HCl losses porosity of 20% and DUT-67(Zr)\_H<sub>2</sub>SO<sub>4</sub> of only 7%. A similar trend is observed for the Hf-based DUT-67. The unmodified DUT-67(Hf), as well as

DUT-67(Hf)\_H<sub>2</sub>SO<sub>4</sub> loses 12% of porosity, while the loss of porosity for DUT-67(Hf)\_HCl is reduced to 6% (Figure 59 a-b, Table 15).

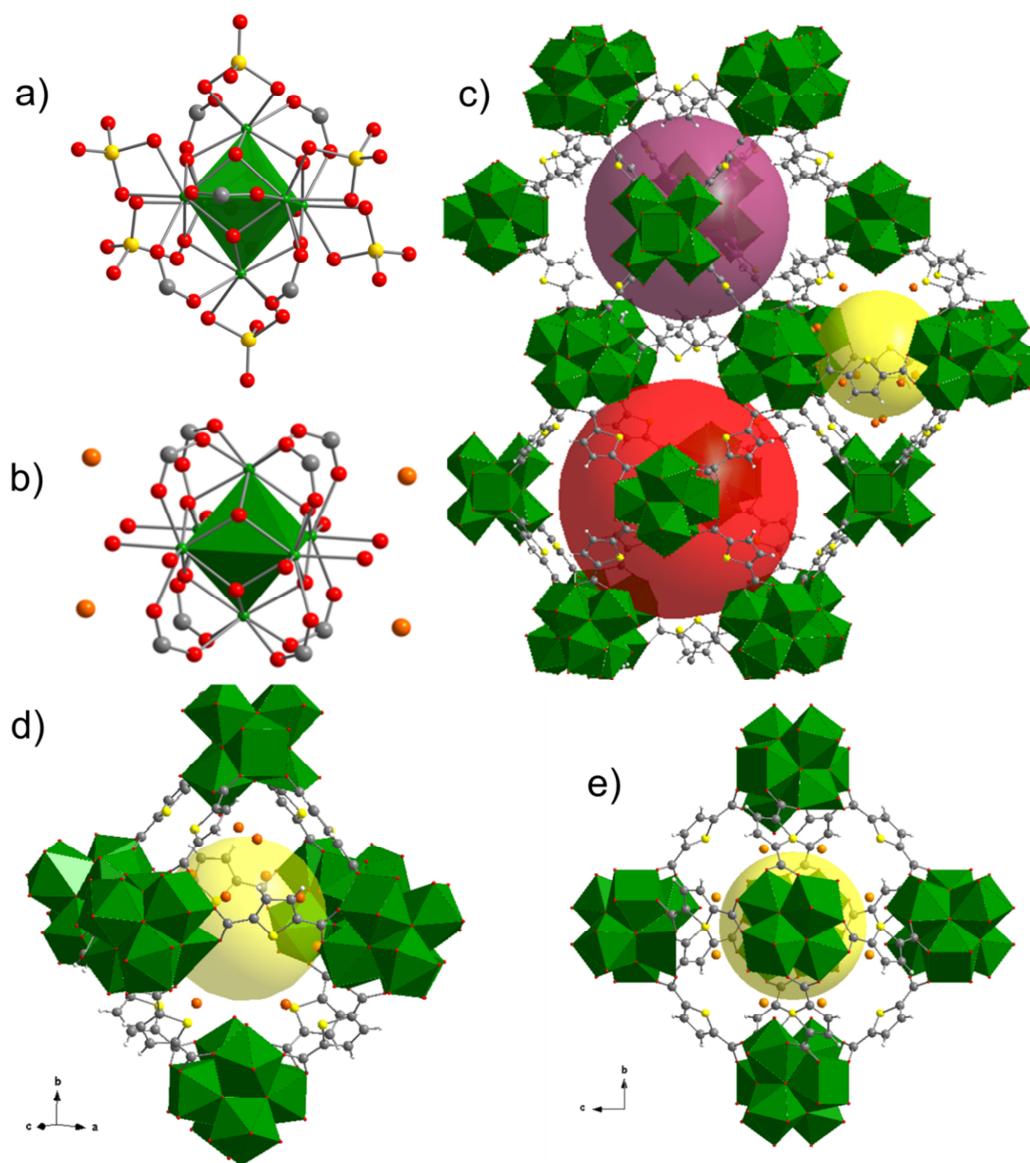
Furthermore, the thermal stability of DUT-67 is influenced by the acidic treatment (Figure 60). For the pristine Zr- and Hf-based DUT-67, the thermal decomposition takes place at temperatures between 275 and 300 °C. The sulphated analogues even show some residual crystallinity at 325 °C. Contrary, the chlorinated analogues are less stable and lose their crystallinity at significantly lower temperatures between 200 and 250 °C. In this temperature region, the chloride anion is removed from the network and small parts of the tdc<sup>2-</sup>-linker begin to decompose, according to TG-MS measurements (FigureA 7). The linker release at lower temperatures is likely caused by the chloride removal and the resulting lack of charge balance, which has to be compensated.



**Figure 60.** Thermo-PXRD patterns of a) DUT-67(Zr)\_HCl, b) DUT-67(Hf)\_HCl, c) DUT-67(Zr)\_H<sub>2</sub>SO<sub>4</sub> and d) DUT-67(Hf)\_H<sub>2</sub>SO<sub>4</sub>.

Single crystal X-ray diffraction analysis of DUT-67(Zr)\_HCl indicate that chlorine is present in the structure. The chlorine anions, which could be determined with partial occupancy of 10.7% after refinement, could be located on a mirror plane *m* corresponding to the 96*k* Wyckoff position in the unit cell. These positions are located next to the metal cluster and are separated from the μ<sub>3</sub>-oxygen atoms O6 by a distance of 3.353 Å, which is characteristic for weak O-H...Cl interactions (Figure 61 b). Therefore, the chlorine anions are likely bonded to

the  $\mu_3$ -OHs by Van der Waals forces and hydrogen bonds. The positions of the chlorine anions regarding to the pore packing are located only in the smallest hydrophilic octahedral pore (yellow sphere, Figure 61 c-e), wherein twelve chlorine anions are present per octahedral pore. As mentioned before, the acidic treatment also reduces the amount of modulator significantly. Therefore, the free coordination sites are only occupied by -OH or water molecules which can be thermally removed. Thus, the metal clusters are not shielded and are accessible for other molecules, which is important for an application in Lewis acid based catalysis.



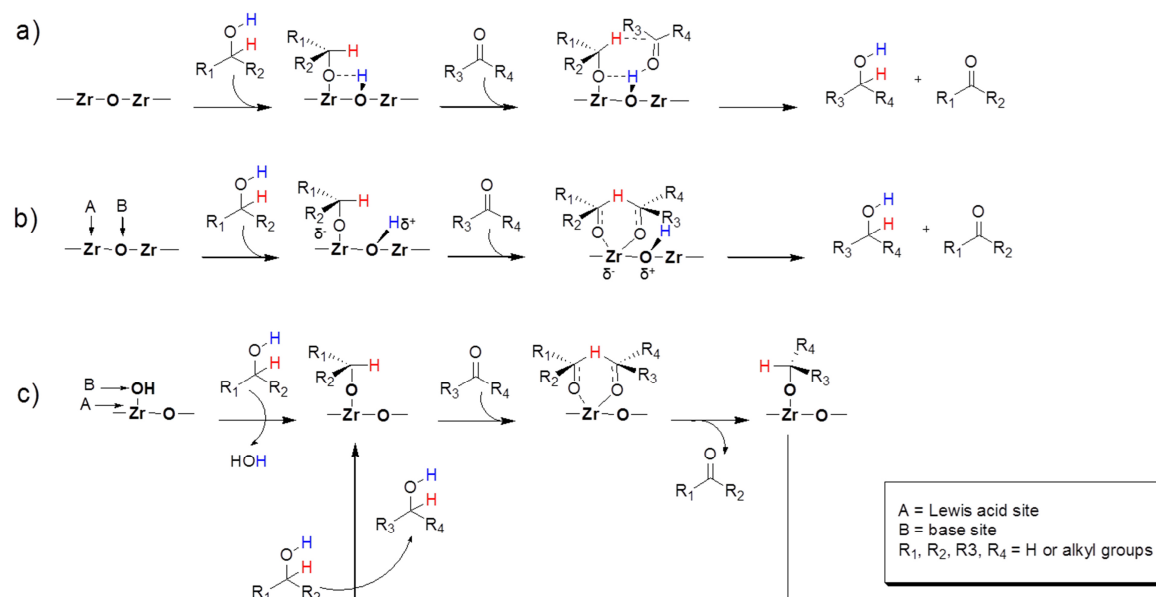
**Figure 61.** a) Local environment of the zirconium cluster of MOF-808(Zr)<sub>2</sub>(SO<sub>4</sub>)<sub>2</sub>. b) Local environment of the zirconium cluster of DUT-67(Zr)<sub>2</sub>(Cl)<sub>2</sub>. c) Pore packing of DUT-67\_HCl. The colored spheres represent three different pores: small octahedral micropore in yellow, small cuboctahedral pore in violet, big cuboctahedral pore in red. d-e) Position of chlorine anions in the small octahedral pore (yellow sphere) displayed in different viewing directions. Zr atoms are shown in green, carbon in dark grey, oxygen in red, sulfur in yellow, chlorine in orange and hydrogen in white.

In contrast, according to Jiang *et al.*<sup>156</sup>, Zr-based MOFs, which are treated with sulphuric acid, feature the sulphate anions on the corners and/or the edges of the octahedral Zr-cluster (Figure 61 a). In this position they block the catalytic Lewis acid centres on one hand, and on the other hand they can hinder substrates to reach the residual catalytic metal centres due to their sterically demanding size.

To get an insight into the acid strengths of the materials and how it changes after the acid treatment, the Hammett indicator method<sup>258-259</sup> was applied. The Hammett acidity  $H_0$  allows a qualitative statement about the ability of a material to convert a neutral base to its conjugated acid. If an adsorbed indicator changes the colour to its acidic form, it means that the acid strength of the material is equal or lower than the  $pK_a$  value of the indicator. For the UiO-66 and UiO-67 materials, as well as the (Zr- and Hf-based) pristine DUT-67, the  $H_0$  acid strength ranges between  $+6.8 > H_0 > +3.3$ . In contrast, the DUT-67 materials, which were treated with sulphuric and hydrochloric acid, increased their acid strength to  $+1.5 > H_0 > -3$  (FigureA 8). Since the Hammett indicator method responds to Lewis and Brønsted acid sites, a base exchange with a 0.1 N aqueous solution of ammonium acetate with a subsequent pH measurement were applied to DUT-67 materials according to the procedure of Holm *et al.*<sup>260</sup> which provides an evaluation of the strength of Brønsted acid sites alone. The pristine DUT-67(Zr) has an acid strength of 6.3 and DUT-67(Hf) has a reduced acid strength of 6.8. With the hydrochloric acid treatment, the Zr- as well as the Hf-based MOFs increase their protonic acid strength slightly to 5.8.

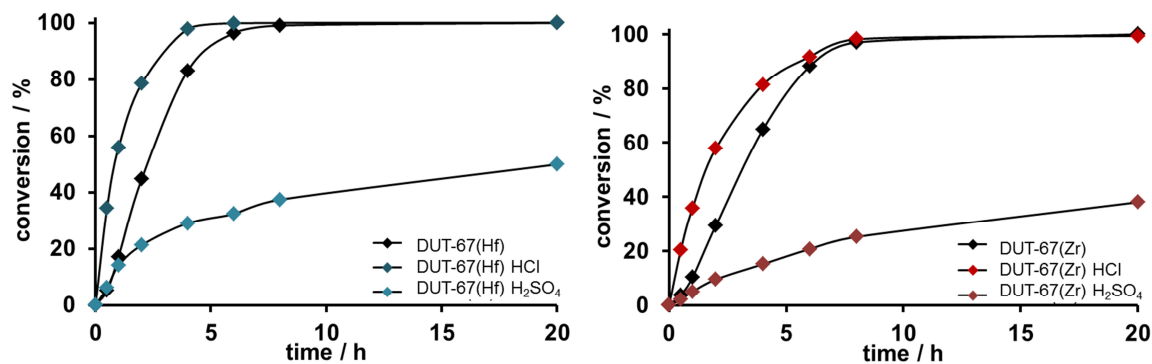
### 5.4 Catalytic studies of DUT-67 in Meerwein-Ponndorf-Verley reduction

The catalytic transfer hydrogenation is an efficient and highly selective way to introduce hydrogen to substrates from organic molecules, instead of high-pressure hydrogen gas. Recently, the focus is on upgrading biomass-derived feedstocks, where for example furfural-derivatives are exploited to produce  $\gamma$ -valerolactone<sup>261-263</sup>. Using alcohols as hydrogen donor to transfer it to aldehydes and ketones is known since 1925 when Meerwein, Verley and Ponndorf published their discovery<sup>264-266</sup>. The Meerwein-Ponndorf-Verley reduction of ketones and aldehydes is performed under mild conditions and is highly chemoselective. Even easily reducible groups, such as unsaturated carbon moieties, carbon-halogen bonds or nitriles are not affected. In the past, the reaction was performed over homogenous catalysts, mainly metal alkoxides. Due to the fact that they are used in large excess and out of separation problems, heterogeneous catalysts are preferred. By a rational design of the catalyst, in respect to hydrophobicity of the surface or pore size distribution, a competitive adsorption of reactants can be controlled, and therefore influence the product distribution of e.g. biomass feedstocks. Established heterogeneous catalysts for MPV reduction are catalysts with Lewis acid sites, such as metal oxides, zirconium-functionalized silicas and zeolites. Nevertheless, they have some disadvantages, like low conversion MPV rates, high calcination temperatures (> 400 °C) or small pore windows in case of zeolites. Therefore, the employment of MOFs, with their tuneable pore dimensions, as catalysts for MPV reduction is promising.



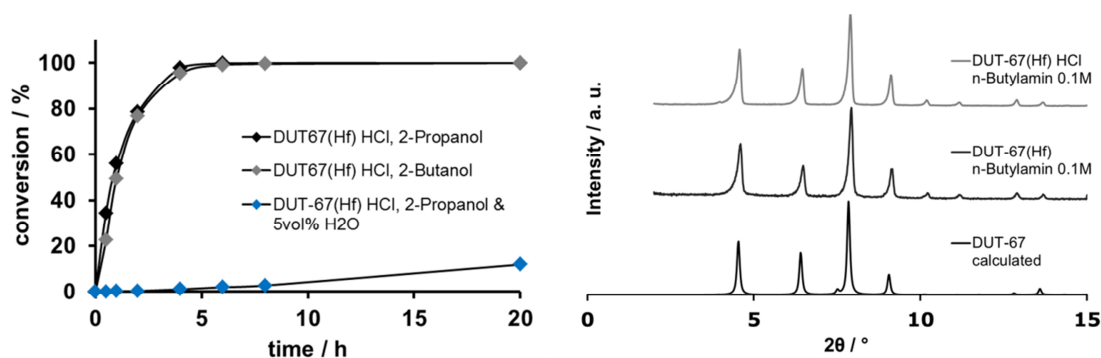
**Figure 62.** Possible reaction mechanisms of the hydrogen transfer in MPV reduction on heterogeneous Zr-based catalysts.<sup>66</sup> Adapted with permission from M. J. Gilkey, B. Xu, Heterogeneous Catalytic Transfer Hydrogenation as an Effective Pathway in Biomass Upgrading. ACS Catalysis 2016, 6 (3), 1420-1436. Copyright 2016 American Chemical Society.

The mechanism of MPV catalysis involves Lewis acid sites as active centres as well as neighbouring base sites (Figure 62).<sup>66</sup> DUT-67 provides both, free coordination sites and base sites in terms of hydroxylated M6 clusters (M = Zr, Hf). DUT-67 in its as synthesised form has two modulator molecules per metal cluster as well as coordinated DMF molecules, which occupy the catalytic active centres. As stated above, an acidic treatment with HCl of Zr- or Hf-based MOFs with reduced connectivity decreases the amount of their modulators significantly. Therefore the free coordination sites of the metal cluster are not shielded and are accessible for other molecules, what becomes important for an application in Lewis acid based catalysis. As mentioned, the chlorine anions are most probably located next to the  $\mu_3$ -oxygen atoms, leaving space for substrates to reach the free coordination metal sites. In contrast, Zr- and Hf-based MOFs which are treated with sulphuric acid feature the sulphate anions on the corners and/or the edges of the octahedral metal cluster, blocking the catalytic Lewis acid centres. This assumption is confirmed by the catalytic performance of DUT-67 and its acid treated analogues DUT-67\_HCl and DUT-67\_H<sub>2</sub>SO<sub>4</sub> (Figure 63). As model reaction the catalytic hydrogen transfer from 2-propanol to cyclohexanone was chosen to show the potential of DUT-67 and its modified analogues as catalyst for MPV reactions. With DUT-67 as catalyst a fast conversion of cyclohexanone to cyclohexanol, without formation of any side-products, was observed. DUT-67(Hf) converts 99% and DUT-67(Zr) 97% of cyclohexanone to cyclohexanol after eight hours if 2-propanol is used as solvent. A change of the solvent, which functions also as proton donator, from 2-propanol to 2-butanol, does not impact the reaction rate under the used conditions (Figure 64 left). Because DUT-67 is a quite hydrophilic material, the presence of water in the reaction mixture leads to a deactivation of the catalyst. If 5 vol% of water is added to the reaction mixture, only 12% of cyclohexanone after 20 hours is converted (Figure 64 left).



**Figure 63.** Catalytic performance of Hf based (left) and Zr based (right) DUT-67 (black diamonds), DUT-67 HCl (dark blue/red diamonds) and DUT-67 H<sub>2</sub>SO<sub>4</sub> (light blue/red diamonds) for MPV reduction of cyclohexanone at 120 °C with 2-propanol as solvent.

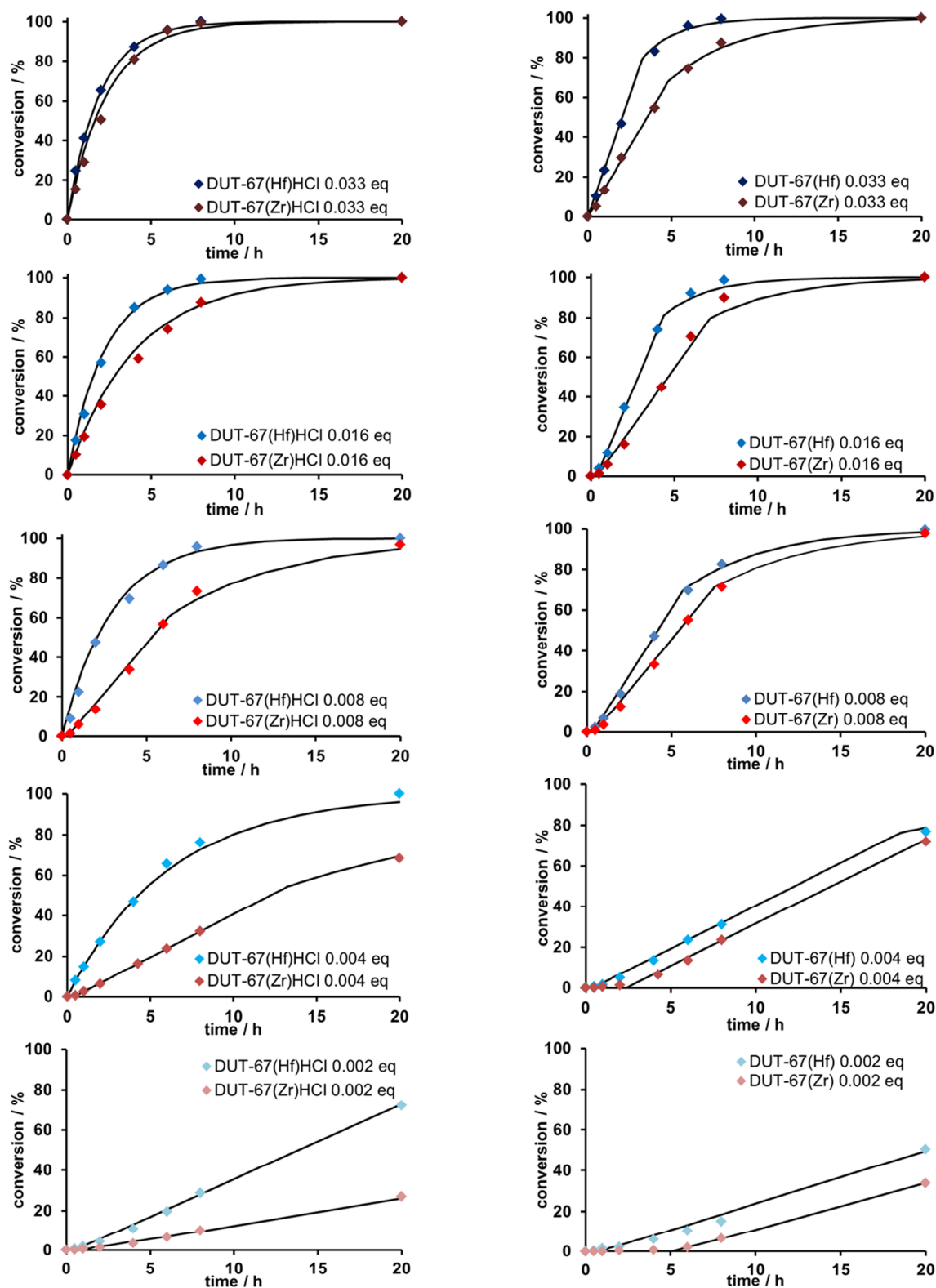
Remarkably, the Hf-based DUT-67 show better catalytic performance than the Zr-based ones. One reason for this behaviour is that the difference of electronegativity of Hf to oxygen ( $\Delta EN = 2.14$ ) is slightly bigger than the one of Zr to oxygen ( $\Delta EN = 2.11$ ). As mentioned, the treatment of DUT-67 with HCl results in an increased performance, compared to the pristine MOF due to an increased amount of accessible active sites and an increased acid strength (from  $+6.8 > H_0 > +3.3$  for DUT-67 to  $+1.5 > H_0 > -3$  for DUT-67\_HCl). On the contrary, the sulphated DUT-67 shows a drastic decrease in the catalytic performance, despite its increased acid strength ( $+1.5 > H_0 > -3$ ) due to the blocked catalytic sites.



**Figure 64.** Left: Catalytic performance of Hf-based DUT-67\_HCl for MPV reduction of cyclohexanone at 120 °C with 2-propanol (black diamonds), 2-butanol (grey diamonds) and with 2-propanol containing 5vol% water (blue diamonds) as solvent. Right: PXRD patterns of DUT-67(Hf) (dark grey) and DUT-67(Hf)\_HCl in a 0.1 M *n*-butylamine solution after 24 h.

To calculate the number of acid sites on the catalyst surface, a titration with *n*-butylamine solution with Hammett indicators according the procedure of Benesi *et al.*<sup>267-268</sup> was done. For this purpose, 15 mg of catalyst were brought each into contact with a defined amount of 0.1 M *n*-butylamine solution in 0.05 ml steps ranging from 0.1 ml to 0.6 ml in a closed vessel for several hours of equilibration. After that, the respective Hammett indicator was added to check if the used base amount was sufficient to block the free acid sites on the metal clusters. To make sure that the MOFs are stable under these conditions, their crystallinity was checked by PXRD after 24 hours of exposure to the base (Figure 64 right). After six hours of equilibration time, 2.3 eq of acid sites per metal cluster, which are accessible for *n*-butylamine could be determined for DUT-67(Zr) and 1.7 eq for DUT-67(Hf). As expected, the amount of free acid sites of DUT-67(Zr)\_HCl is higher with 4.3 eq, as well as DUT-67(Hf)\_HCl with 4.0 eq. These values are in good agreement with the theoretical amount, which is given by the crystal structure and the composition of the MOF. Since DUT-67 is an eight connected MOF and bears two modulator molecules per metal cluster, it leaves two metal atoms per cluster occupied, which can function as Lewis acid site. If these two modulators are removed by the

acid treatment, four metal atoms per cluster are exposed as acid site.



**Figure 65.** Catalytic performance of DUT-67\_HCl (left) and DUT-67 (right), Hf-based (blue diamonds) and Zr-based (red diamonds) for MPV reduction of cyclohexanone at 120 °C for different amount of catalyst used during the reaction (0.033 eq, 0.016 eq, 0.008 eq, 0.004 eq and 0.002 eq). The kinetic progresses were fitted for pseudo zero order (linear range) and for pseudo first order (non-linear range).



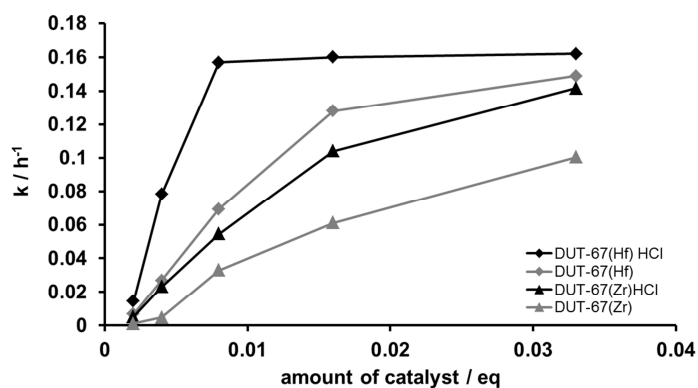
To get an insight into the reaction kinetics and to understand the mechanism, which takes place during the reaction, the catalyst amount for DUT-67 and DUT-67\_HCl was varied in the MPV reaction (Figure 65). In general, the rate determining step of MPV reactions is the formation of the transition state, a six membered ring intermediate, consisting of the Lewis acid site, the proton donating alcohol and the aldehyde<sup>269</sup> (Figure 62). Despite the MPV reduction should follow a higher reaction order – over DUT-67 the reactions show at least for four hours a behaviour of a pseudo zero order reaction, which is expressed as a linear range of conversion (FigureA 9). Here, the rate limiting factor is now the number of accessible catalytic active sites. For higher conversion rates, a sufficient number of active sites are present and the reaction order changes into a pseudo first order, where the influence of the concentration of the aldehyde gets prominent (FigureA 10). The less of catalyst is used in the reaction, the more time it takes to generate the change in reaction order. Furthermore, especially with lower catalyst amount, at low conversion rates, the reaction over DUT-67 show an S-shaped form. The deferred conversion indicates a proceeding activation step. The remaining coordinated modulator molecules blocking the active centres need to be displaced at first by the substrate. In contrast, the kinetics of the DUT-67\_HCl catalysed reactions do not show such an activation process due to the fact that most of the modulator – and DMF molecules were eliminated before by the HCl treatment. In addition, the HCl treated DUT-67 follows a pseudo first order reaction rate, indicating that enough active sites are accessible right from the start of the reaction. A pseudo zero order kinetic over a longer time is observed only for very low amount of catalyst (0.002 eq for DUT-67(Hf)\_HCl and  $\leq 0.008$  eq for DUT-67(Zr)\_HCl).

A plot of the initial rates (0.5-2 h) illustrates additionally the mechanisms taking place (Figure 66, FigureA 11). For both DUT-67(Zr)\_HCl and DUT-67(Hf)\_HCl a linear correlation between 0.002 eq and 0.008 eq of catalyst indicates that the rate limiting factor in this region is the intrinsic activity of the catalyst. With a doubled amount of catalyst the initial rate constants approximately doubles until they are not increasing anymore and the plots are turned into a plateau, where mass transport and diffusion become the rate limiting steps. Consequently, the kinetic rates of the conversion cannot be increased by higher catalyst amount. For very small amounts of catalyst (0.002 eq), the initial rate constants are much smaller than expected due to the inhibited conversion at low reaction times. This phenomenon is more pronounced for the untreated DUT-67, because of the coordinated modulator molecules, which need to be displaced firstly. Out of this reason, the corresponding initial

rates are smaller than the ones of the acid treated MOFs and more catalyst is needed to reach the plateau.

**Table 16.** The calculated initial rate constants ( $k/h^{-1}$ ) of DUT-67 and its HCl treated analogues.

eq	DUT-67(Hf)_HCl	DUT-67(Hf)	DUT-67(Zr)_HCl	DUT-67(Zr)
<b>0.033</b>	0.162	0.149	0.142	0.086
<b>0.016</b>	0.160	0.128	0.104	0.072
<b>0.008</b>	0.157	0.069	0.054	0.061
<b>0.004</b>	0.078	0.185	0.023	0.025
<b>0.002</b>	0.015	0.007	0.005	0.014

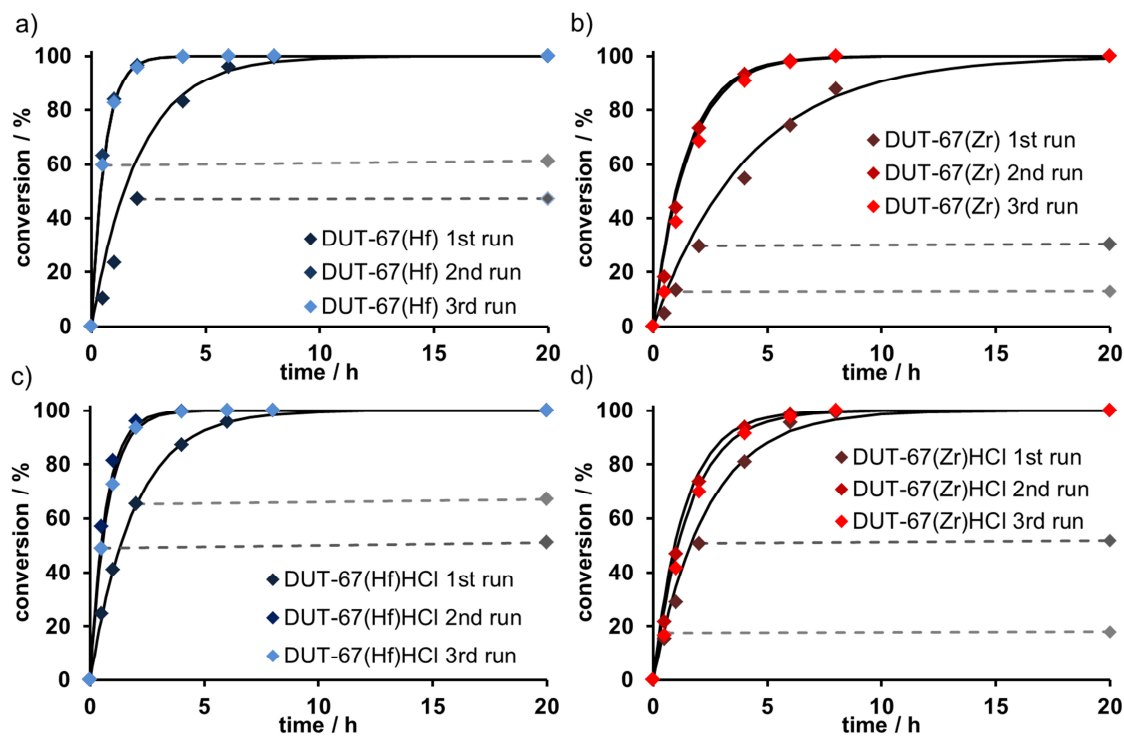


**Figure 66.** Plot of the initial rate constants vs. different amounts of DUT-67(Hf) (grey diamonds), DUT-67(Hf)\_HCl (black diamonds), DUT-67(Zr) (grey triangles) and DUT-67(Zr)\_HCl (black triangles).

Furthermore, the recyclability and stability of DUT-67 were tested. In both cases – for DUT-67 and DUT-67\_HCl – the catalytic performance after the first run is drastically increased (Table 17). The TOFs for DUT-67(Hf)\_HCl have an almost three-fold increase in the second and third run in comparison to the first run and for DUT-67(Hf) the values have even almost a six-fold increase. In case of Hf-based DUT-67 the TOFs range between 8.4 and 11.0  $h^{-1}$  and in case of Zr-based DUT-67 the TOFs range between 4.1–4.3  $h^{-1}$  in the third cycle.

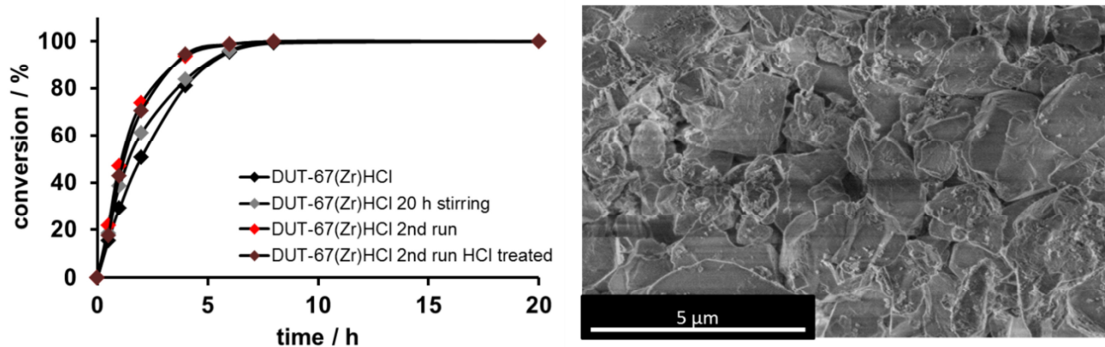
**Table 17.** Catalytic activity of the fresh and reused catalysts in MPV reduction of cyclohexanone (reaction conditions: 0.6 mmol of cyclohexanone, 39 mmol 2-propanol, 20  $\mu$ mol catalyst, 120  $^{\circ}$ C, 250 rpm). The turnover frequency was calculated for 30% yield of cyclohexanol based on theoretical amount of Lewis acid site (four acid sites/mol MOF).

catalyst	TOF/mol mol $^{-1}$ h $^{-1}$		
	1st run	2nd run	3rd run
DUT-67(Hf)_HCl	3.4	9.3	8.4
DUT-67(Hf)	1.9	11.0	11.0
DUT-67(Zr)_HCl	2.7	4.7	4.1
DUT-67(Zr)	1.1	4.6	4.3



**Figure 67.** Catalytic performance of a) DUT-67(Hf), b) DUT-67(Zr), c) DUT-67(Hf)\_HCl and d) DUT-67(Zr)\_HCl for MPV reduction of cyclohexanone at 120 °C for the first (dark blue/red diamonds), the second (blue/red diamonds) and the third run (light blue/red diamonds). The curves were fitted as pseudo first order (black line). The grey diamonds represent the conversion after the catalysts were removed from the reaction medium.

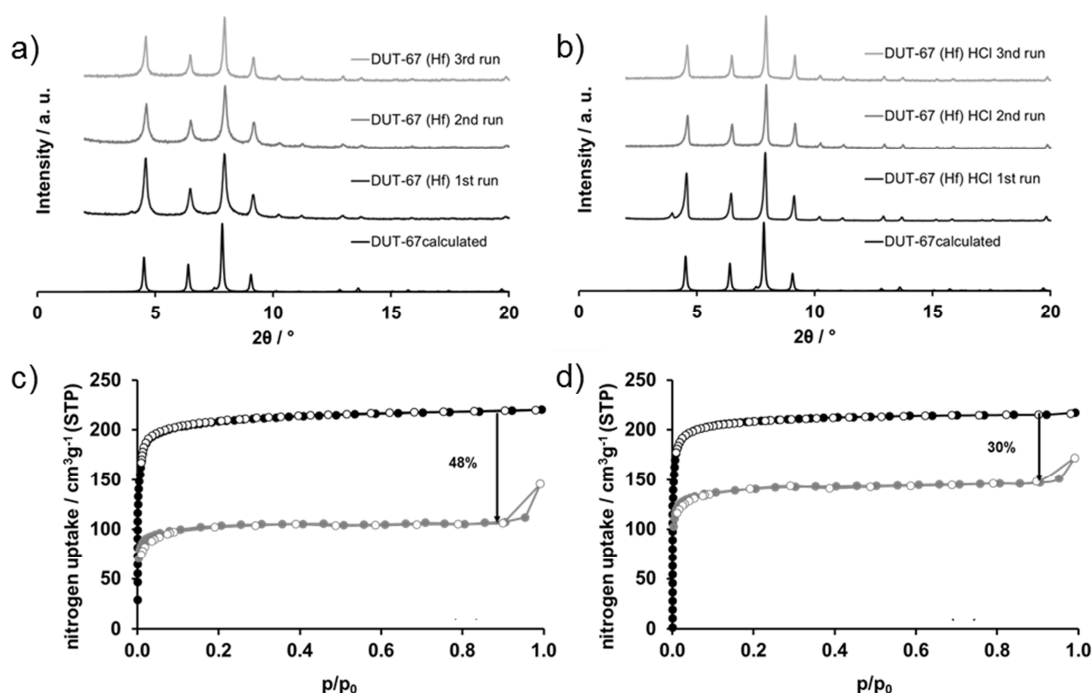
Such an improvement can be explained by two different factors. First, the catalyst is stirred at 250 rpm, which crushes the particles and reduces the particle size during the reaction. In this way, the mass transport is promoted. To verify this assumption, the catalyst was stirred in 2-propanol at room temperature for 20 hours before the catalysis was carried out. As expected, the stirred catalyst shows a slightly higher reaction rate (Figure 68 left).



**Figure 68.** Left: Catalytic performance of DUT-67(Zr)\_HCl (black diamonds), of DUT-67(Zr)\_HCl stirred 20 h in 2-propanol at room temperature at 250 rpm before usage (grey diamonds), of second cycle of DUT-67(Zr)\_HCl (light red diamonds) and of DUT-67(Zr)\_HCl that was washed with diluted HCl solution after the first catalytic cycle (dark red diamonds) for MPV reduction of cyclohexanone at 120 °C. Right: SEM image of DUT-67(Zr)\_HCl after the first catalytic cycle, stirred at 250 rpm.

The second reason is a complete elimination of modulator molecules after the first cycle. Even the chlorine in DUT-67\_HCl is removed from the framework and cannot be traced anymore in TG/MS analysis (Figure A 12). Furthermore, the acid strength is reduced to  $+6.8 > H_0 > +3.3$ , proved by Hammet indicators. Thus, after catalysis, DUT-67 and DUT-67\_HCl can be considered as the same material. Accordingly, the performance of the acid and the non-acid treated MOFs are almost equal. If the catalyst is treated with a solution of HCl after the first catalytic cycle, the acid strength is increased to  $+1.5 > H_0 > -3$  again, yet the performance is not rising (Figure 68 left). This proves that the acid strength in this range plays a minor role for the performance in MPV reduction and that the amount as well as the accessibility of Lewis acid sites on the metal cluster (no modulator molecules present) and the particle size influences the reaction rate primarily.

Furthermore, the Hf-based catalysts were tested if some metal ions are leached during the reaction by hot filtration test. After a small part of the solution was filtered off and treated under the same conditions, further conversion was observed for none of the catalysts even after the third run (Figure 67). Hence, the catalysts remain intact and show unchanged PXRD patterns (Figure 69 a-b). Contrary to DUT-67(Hf)\_HCl, the Bragg-reflections of DUT-67(Hf) are slightly broadened.



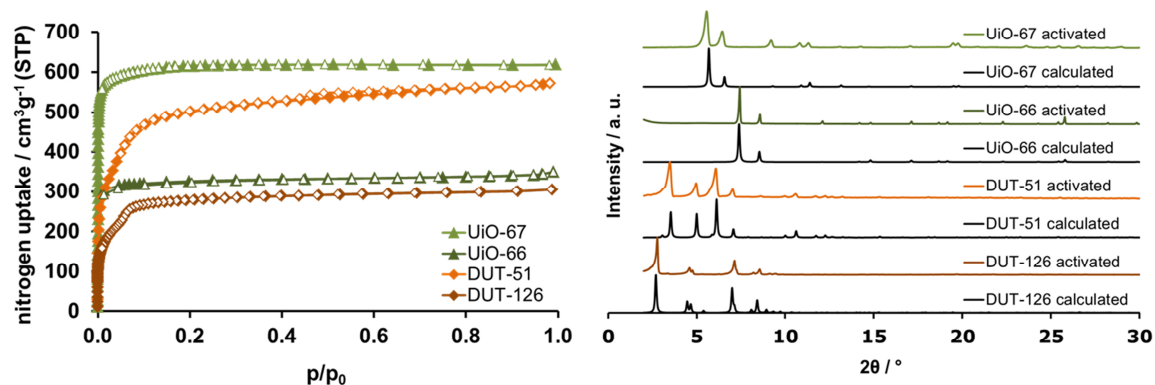
**Figure 69.** PXRD patterns of DUT-67(Hf) (a) and of DUT-67(Hf)\_HCl (b) after the first (dark grey line), the second (grey line) and the third (light grey line) run of MPV reduction of cyclohexanone at 120 °C, as well as nitrogen isotherms at 77 K of DUT-67(Hf) (c) and DUT-67(Hf)\_HCl (d) before (black circles) and after the third run (grey circles).

Despite the well preserved crystallinity, the porosity is decreased. After three cycles, the total pore volume ( $p/p_0 = 0.90$ ) of DUT-67(Hf)\_HCl is reduced to 30% and the pore volume of DUT-67(Hf) to 48% (Figure 69 c-d). Thermogravimetric analysis shows that the ratio of linker to metal did not change in comparison to the as synthesised MOFs (Table 18). Therefore, no significant leaching of linker molecules or metal ions happens during the catalytic reaction.

**Table 18.** Compositions and porosity of DUT-67(Hf) and DUT-67(Hf)\_HCl after the usage as catalyst for MPV reduction of cyclohexanone at 120 °C for the third time.

MOF after 3 <sup>rd</sup> run in MPV reduction	Composition according to TG/DTA	tPV ( $p/p_0 = 0.90$ )/cm <sup>3</sup> g <sup>-1</sup>
DUT-67(Hf)	Hf <sub>6</sub> (μ <sub>3</sub> -O) <sub>4</sub> (μ <sub>3</sub> -OH) <sub>4</sub> (tdc) <sub>4.06</sub> (OH) <sub>4</sub> (H <sub>2</sub> O) <sub>13.7</sub>	0.17
DUT-67(Hf)_HCl	Hf <sub>6</sub> (μ <sub>3</sub> -O) <sub>4</sub> (μ <sub>3</sub> -OH) <sub>4</sub> (tdc) <sub>3.98</sub> (OH) <sub>4</sub> (H <sub>2</sub> O) <sub>18.5</sub>	0.23

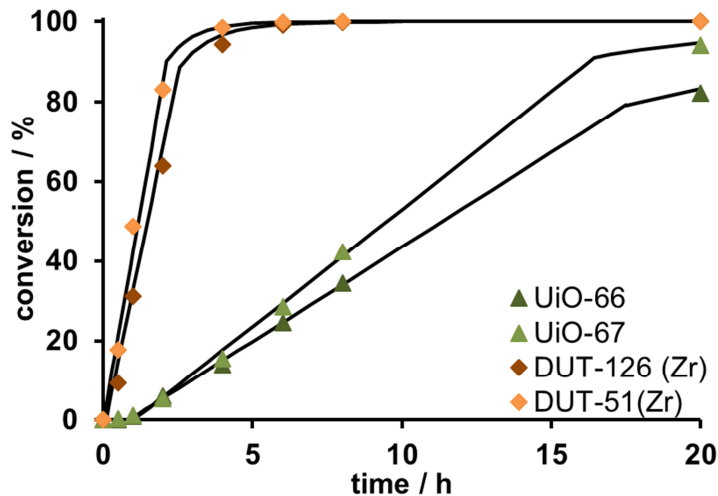
Furthermore, the catalytic activities of four other Zr-based MOFs were tested – UiO-66, UiO-67, DUT-126 and DUT-51 (Table 19). UiO-66 was synthesised with benzoic acid (Ba) as modulator, whereas acetic acid (Ac) was chosen as modulator for UiO-67. Both MOFs – UiO-66 and UiO-67 – consist of twelve-connected clusters. They are known to exhibit defects, which provide free coordination sites on metal cluster. The used UiOs in this work feature 0.8 (UiO-66) and 2.7 (UiO-67) acid sites per metal cluster, determined by titration with *n*-butylamine. According to TG measurements, the composition of these two compounds are Zr<sub>6</sub>(μ<sub>3</sub>-O)<sub>4</sub>(μ<sub>3</sub>-OH)<sub>4</sub>(bpdc)<sub>4</sub>(Ac)<sub>1.4</sub>(OH)<sub>3</sub> (UiO-67) and Zr<sub>6</sub>(μ<sub>3</sub>-O)<sub>4</sub>(μ<sub>3</sub>-OH)<sub>4</sub>(bdc)<sub>4.9</sub>(Ba)<sub>1.5</sub>OH (UiO-66) (FigureA 13 a-b). Therefore, the number of free coordination sites determined by TG measurement is 2.65 for UiO-67 and 0.78 for UiO-66 and are in good agreement with values obtained from titration experiments. The acid strength of both MOFs are with  $+6.8 > H_0 > +3.3$  the same as for DUT-67. The quality of the used samples was monitored by PXRD and nitrogen physisorption measurements. UiO-66 as well as UiO-67 show high crystallinity and porosity (Figure 70). UiO-66 has a specific surface area of 1263 m<sup>2</sup> g<sup>-1</sup> and a total pore volume of 0.54 cm<sup>3</sup> g<sup>-1</sup>, while UiO-67 has a higher specific surface area of 2451 m<sup>2</sup> g<sup>-1</sup> and a total pore volume of 0.96 cm<sup>3</sup> g<sup>-1</sup>. Both, UiO-66 and UiO-67, show poor performance in MPV reduction of cyclohexanone. Up to eight hours, the kinetic plot follows a pseudo zero order. For calculating the TOF values, the modulator molecules were neglected, since they are removed during the catalytic process. Thus, the considered numbers of free acid sites are 4.1 for UiO-67 and 2.3 for UiO-66. The TOF is with 0.5 h<sup>-1</sup> (UiO-66) and 0.4 h<sup>-1</sup> (UiO-67) much smaller than the one of DUT-67.



**Figure 70.** Left: nitrogen physisorption isotherms at 77 K of UiO-66 (dark green triangles), UiO-67 (light green triangles), DUT-126 (dark orange diamonds) and DUT-51 (light orange diamonds); Right: PXRD pattern of calculated (black lines) and of activated samples (coloured lines) of UiO-66 (dark green), UiO-67 (light green), DUT-126 (dark orange) and DUT-51 (light orange).

The other two tested Zr-based MOFs, DUT-126 and DUT-51, are based on eight-connected clusters and should have four free acid sites per metal cluster. The compositions of both MOFs are analysed by TG/DTA analysis. DUT-126, which consist of the same linker (tdc) as DUT-67, has the composition  $Zr_6(\mu_3-O)_4(\mu_3-OH)_4(tdc)_4(tfa)_4(DMF)_{2.3}(H_2O)_{13}$  and DUT-51, which is isorecticular to DUT-67 and has dithieno[3,2-b;2',3'-d]-thiophene-2,6-dicarboxylate (dttdc) as linker, has the composition  $Zr_6(\mu_3-O)_4(\mu_3-OH)_4(dttdc)_3(Fa)_2(OH)_4(DMF)_{1.1}(H_2O)_{2.9}$ . Thus the used sample of DUT-51 exhibits also missing linker defects, wherein six acid sites per metal cluster are present. In contrast, the determined composition of DUT-126 does not point to missing linker defects and the presence of four metal sites per metal cluster could be confirmed, if modulator molecules are neglected. The used MOFs show high crystallinity according to PXRD analysis (Figure 70). In case of porosity, DUT-126 is comparable to DUT-67 with a specific surface area of  $1297 \text{ m}^2 \text{ g}^{-1}$  and a total pore volume of  $0.48 \text{ cm}^3 \text{ g}^{-1}$ . Contrary, DUT-51 exhibits a significantly higher porosity with a specific surface are of  $1989 \text{ m}^2 \text{ g}^{-1}$  and a total pore volume of  $0.88 \text{ cm}^3 \text{ g}^{-1}$ . DUT-51 should have similar intrinsic activity as DUT-67. Its acid strength is in the same range of  $+6.8 > H_0 > +3.3$ . DUT-126 has with  $+3.3 > H_0 > +1.5$  a slightly higher acid strength due to the fact that trifluoroacetic acid instead of formic acid is used as modulator agent during synthesis. However, DUT-51 and DUT-126 have larger pores in comparison to DUT-67 – the pores of DUT-51 are  $14.3 \text{ \AA}$ ,  $18.8 \text{ \AA}$  and  $24.6 \text{ \AA}$  in diameter in contrast to DUT-67, whose pores are  $9.0 \text{ \AA}$ ,  $14.6 \text{ \AA}$  and  $17.0 \text{ \AA}$  in size. As well as DUT-51, DUT-126 has mesoporous channels ( $d = 22.8 \text{ \AA}$ ) which can function as transport pores. Thus, the mass transport and diffusion should be enhanced and should lead to higher conversion rates. Indeed, the TOFs are increased from  $1.1 \text{ h}^{-1}$

(DUT-67) to  $2.5 \text{ h}^{-1}$  (DUT-126) and to  $2.3 \text{ h}^{-1}$  (DUT-51). Despite their superior performance, DUT-67 has some advantages, such as thermal and chemical stability, commercially available linker, short synthesis time, good reproducibility and an overall easy synthesis, which is feasible to scale up.



**Figure 71.** Catalytic performance of Zr-based DUT-51 (orange diamonds), DUT-126 (brown diamonds), UiO-66 (light green triangles) and UiO-67 (dark green triangles) for MPV reduction of cyclohexanone at  $120 \text{ }^\circ\text{C}$ . The curves were fitted as pseudo zero order (linear range) and pseudo first order (non-linear range) (FigureA 14).

**Table 19.** Catalytic activity of various Zr-based MOFs in MPV reduction of cyclohexanone. (reaction conditions:  $0.6 \text{ mmol}$  of cyclohexanone,  $39 \text{ mmol}$  2-propanol,  $20 \text{ } \mu\text{mol}$  catalyst,  $120 \text{ }^\circ\text{C}$ ,  $250 \text{ rpm}$ ) The Turnover frequencies were calculated for 30% yield of cyclohexanol based on experimental amount of Lewis acid sites: 4 acid sites/mol MOF for DUT-67 and DUT-126, 6 acid sites/mol MOF for DUT-51, 4.1 acid sites/mol MOF for UiO-67 and 2.3 acid sites/mol MOF for UiO-66.

catalyst	TOF / $\text{mol mol}^{-1} \text{ h}^{-1}$	Amount of catalytic active sites in $20 \text{ } \mu\text{mol}$ MOF / $\text{mmol}$
UiO-66	0.5	0.05
UiO-67	0.4	0.08
DUT-67	1.1	0.08
DUT-51	2.3	0.11
DUT-126	2.5	0.08

To compare the catalytic activity of DUT-67 with other catalysts, the TOFs of some established heterogeneous catalysts are listed in Table 20. Metal oxides, such as MgO and  $\text{TiO}_2$  have relatively low conversion rates. A previously reported  $\text{ZrO}_2$  material shows quite good activity, due to the high density of base sites despite the Lewis acid sites<sup>269</sup>, pointing out the importance of neighbouring acid and base sites. Zirconosilicates as well as Zr-SBA-15 exhibit moderate TOFs. Nevertheless, their TOF values are in the same range as for DUT-67

materials in their second cycle. Furthermore DUT-67 can compete with some zeolites, which have usually very high conversion rates in MPV reactions.<sup>270-274</sup>

**Table 20** TOFs of reported heterogeneous catalyst for MPV reduction of cyclohexanone with 2-propanol or 2-butanol as proton donator.

Entry	catalyst	Temperature / °C	TOF / mol mol <sup>-1</sup> h <sup>-1</sup>	Reference
1	MgO-1 <sup>a</sup>	82	0.002	275
2	MgO-2 <sup>a</sup>	82	0.004	275
3	MgO-3 <sup>a</sup>	82	0.007	275
4	ZrO <sub>2</sub>	120	27.3	269
5	TiO <sub>2</sub>	120	0.28	269
6	ZS-0 <sup>b</sup>	82	6	276
7	ZS-1 <sup>b</sup>	82	9.6	276
8	ZS-5 <sup>b</sup>	82	11.4	276
9	conv-Zr-MFI (Si/Zr=150) <sup>c</sup>	85	0.3	277
10	meso-Zr-MFI (Si/Zr=150) <sup>d</sup>	85	7.4	277
11	conv-Zr-MFI (Si/Zr=100) <sup>c</sup>	85	0.3	277
12	meso-Zr-MFI (Si/Zr=100) <sup>d</sup>	85	8.9	277
13	Ti-beta zeolite	100	1.2	270
14	Al-beta zeolite	100	7.0	270
15	Sn-beta zeolite	100	109.0	270
16	Zr-SBA-15 <sup>c</sup>	110	7.2	278

<sup>a</sup> nanocrystalline magnesium oxide. TOFs were calculated by given yields after 16 h based on catalyst amount, <sup>b</sup> partially crystalline zirconosilicate, <sup>c</sup> conventional MFI-type zirconosilicates, <sup>d</sup> mesoporous MFI-type zirconosilicates, <sup>e</sup> TOF calculated by given yield of cyclohexanol after 1 hour based on reported meq of acid sites.

With the mentioned features, it can be summarised that DUT-67 is a suitable catalyst for the Meerwein-Ponndorf-Verley reduction of cyclohexanone remaining stable under the catalytic conditions. Furthermore, the catalytic performance significantly increases after the first run, likely due to the removal of remaining ligands on the metal cluster during the catalytic process. This effect can be seen in particular for the pristine DUT-67. Here, TOFs are up to approximately 6 times as high as in the second and third run. The comparison of the catalytic performance of DUT-67 with those of other Zr-based MOFs, which has a similar amount of free acid sites and similar acid strengths, demonstrates the importance of the accessibility and the size of the pores. MOFs with smaller pore windows such as UiO-66 and UiO-67 have TOFs that are only at half the level of DUT-67(Zr), while the TOFs of DUT-51 and DUT-126, which have distinct mesoporous transport pores, are doubled compared to DUT-67(Zr).



### 5.5 DUT-122 and its application as sensor material†

Due to their high porosity and the ability to concentrate molecules in their frameworks, MOFs are highly suited as sensor materials. Thereby, the sensing characteristics can originate from the linker or the metal cluster. Because most MOFs exhibit low chemical stability, the use of Zr-based MOFs, which are known for higher stability, is promising. Since the Zr-clusters of MOFs do not possess luminescent properties, the luminescence has to originate from the linker or the metal cluster has to be doped with rare earth metals, for example. Thereby, not only the linker itself is responsible for the luminescence properties, also the type of the metal cluster, the orientation of the linker in the crystal structure and the structure of the SBU affect the separation of the linker and influence directly the emission properties. These circumstances make tuneable emission properties possible and give consideration to use MOFs also as phosphors in solid state lighting applications, like white lighting LEDs.<sup>279</sup> An incorporation of functional moieties into desired MOFs for tuning their luminescence properties under maintenance of important characteristics such as topology, porosity and pore accessibility is mostly feasible using the isorecticular approach, a pre-functionalization of the linker, or a post-synthetic modification of the framework, as described in the previous chapters.

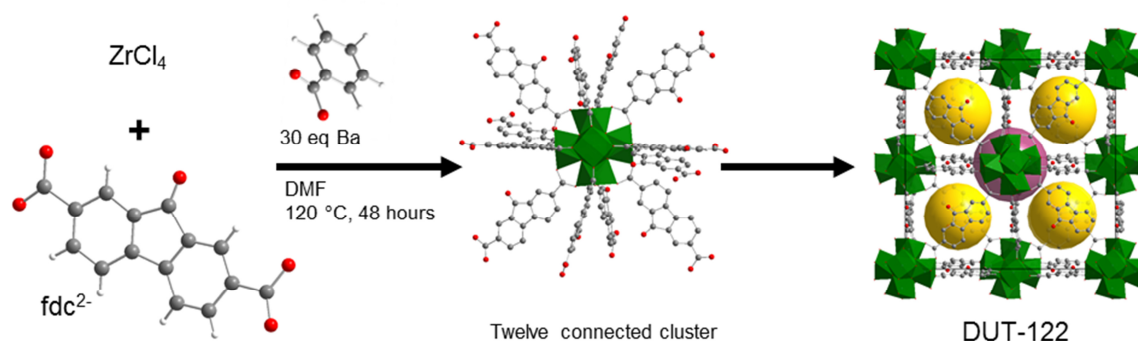
To incorporate new luminescence properties into UiO-67, the isorecticular approach can be utilized by choosing 9-fluorenone-2,7-dicarboxylic acid (H<sub>2</sub>fdc) as linker in the synthesis. The bent linker shows strong luminescence and therefore the MOF adapts the photoluminescence properties of the linker. Since H<sub>2</sub>fdc is well known for its solvchromatic shifts in fluorescence emission spectra<sup>280-283</sup> and Zr-based MOFs are mostly chemically stable, H<sub>2</sub>fdc can be reacted with ZrCl<sub>4</sub> to create a MOF isorecticular to UiO-67, which should be suitable as sensor material. Here, the resulting MOF will be labelled as DUT-122, yet the same compound was already published under the name BUT-10<sup>24</sup>, where it proved its value in separation of carbon dioxide over nitrogen and methane. It is worth to mention that in 2010, Furman *et al.*<sup>284-285</sup> reported six different MOFs that contain H<sub>2</sub>fdc as linker molecule. By changing the metal species, different structures were obtained and led to tuneable emission colours. Yet, none of them were tested for their potential application as sensor material.

---

†parts of this chapter were literally adopted from publication<sup>246</sup>. Reprinted with permission from F. Drache, V. Bon, I. Senkovska, M. Adam, A. Eychmüller, and S. Kaskel, Vapochromic Luminescence of a Zirconium-Based Metal–Organic Framework for Sensing Applications, *European Journal of inorganic chemistry* 2016, 2016, 4483-4489. Copyright 2016 John Wiley and Sons.

### 5.5.1 Synthesis and characterization of DUT-122

The MOF DUT-122 is synthesised in a solvothermal reaction of  $\text{H}_2\text{fdc}$  with  $\text{ZrCl}_4$  and with benzoic acid (Ba) as modulator (Figure 72). The resulting compound has a composition of  $\text{Zr}_6(\mu_3\text{-O})_4(\mu_3\text{-OH})_4(\text{fdc})_{5.2}(\text{OH})_2(\text{H}_2\text{O})$ , according to elemental- and thermogravimetric analysis (Figure 76) and has thus missing linker defects. The found composition is: C 45.02%, H 2.14% and Zr 21.98%. These values are in good agreement with the calculated amounts that are C 44.28%, H 1.87% and Zr 25.87%. It is also possible to use  $\text{HfCl}_4$  instead of  $\text{ZrCl}_4$  in the synthesis. Then, an isomorphous MOF is obtained.



**Figure 72.** Reaction scheme of DUT-122 and synthesis conditions. The coordination sphere of  $\text{Zr}_6(\mu_3\text{-O})_4(\mu_3\text{-OH})_4^{12+}$  cluster is surrounded by twelve fluorenone dicarboxylate molecules. The resulting crystal structure contains two types of pores. The yellow spheres represent the smaller tetrahedral pores and the purple sphere represents the octahedral pore. Zirconium-clusters are shown in green, carbon atoms in grey, oxygen atoms in red, sulphur atoms in yellow and hydrogen atoms in white.

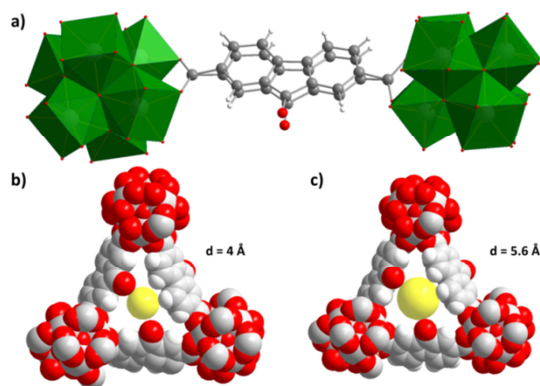
The crystal structures of DUT-122 for Zr- and Hf-based versions were determined by single crystal X-ray diffraction, both crystallizes in the cubic symmetry. The analysis of the diffraction data for the extinctions suggests the primitive lattice and the presence of a glide plane that is characteristic for the  $Pa\bar{3}$  space group. Such lowering of the symmetry in comparison with UiO-type frameworks, which crystallize in  $Fm\bar{3}m$ , can be explained by the lowering of the molecular symmetry of the ligand. Despite the use of a bent ligand, which has an angle between carboxylates of nearly  $160^\circ$ , the formation of the 12-connected framework with **fcu** topology was still possible. Therefore, from the structural point of view, the created framework can be considered as isorecticular to UiO-67. The distances between carboxylate carbon atoms are also comparable and amounts to 9.834(7) Å for DUT-122(Zr) and 10.103(5) Å for UiO-67. At the same time, the presence of the additional two atoms in the ligand molecule strongly influences the textural properties of the material. The theoretical surface area is with 2465  $\text{m}^2 \text{g}^{-1}$  smaller for DUT-122(Zr) than the theoretical surface area for UiO-67 with 3042  $\text{m}^2 \text{g}^{-1}$ . Correspondingly, the theoretical total pore volume is also decreased from 1.06  $\text{cm}^3 \text{g}^{-1}$  (UiO-67) to 0.83  $\text{cm}^3 \text{g}^{-1}$  (DUT-122(Zr)). In addition, the diameter of the

octahedral pore of DUT-122(Zr) is only 9.4 Å and the diameter of the tetrahedral pore is 8.4 Å. These values are also significantly smaller, compared to the pore dimensions of UiO-67, whose pore diameters are 12.0 Å and 9.6 Å. Besides, the decreasing of the surface area, pore volume and pore sizes, the pore accessibility of DUT-122(Zr) is also slightly affected (Table 21). Because four fluorenone oxygen moieties are directed – and thus protrude into the octahedral pore, the pore windows of the tetrahedral pores are not equivalent. The pore limiting diameter is therefore much smaller than that for UiO-67, whose dimension is 5.60 Å. In contrast, the diameters of the pore windows of DUT-122(Zr) range between 4.00 Å and 5.60 Å due to a disorder of the ligands (Figure 73). Hence, in one alternative position of the ligands the pore limiting diameter of DUT-122(Zr) is finally equal to the one of UiO-67. It is worth to mention that due to the rotational disorder of the ligands, molecules like benzene or toluene, which have a kinetic diameter of 5.8 Å, can still enter the framework through the pore windows.

**Table 21.** Textural properties and pore size of UiO-67 and DUT-122<sup>[a]</sup>.

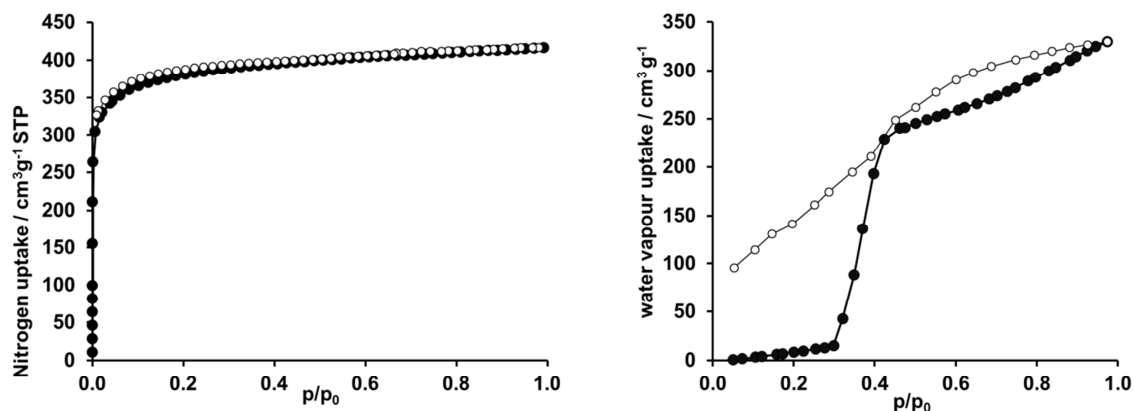
	UiO-67	DUT-122(Zr)
Geometrical surface area, m <sup>2</sup> g <sup>-1</sup>	3041	2465
Geometrical total pore volume, cm <sup>3</sup> g <sup>-1</sup>	1.057	0.828
Pore limiting diameter, Å	5.60	4.15
Maximum pore diameter, Å	12.58	9.40
Diameter of tetrahedral pore, Å	9.6	8.4
Diameter of octahedral pore, Å	12.0	9.4
Solvent accessible void, %	69.5	63.7

[a] The crystal structure with unresolved disorder was used for the calculations.



**Figure 73.** Structural analysis of the pore windows considering the disorder of the ligand molecules: a) ball and sticks representation of two alternative positions; b) pore window with two ligand molecules in position A and one ligand molecule in position B; c) pore window with two ligand molecules in position B and one ligand molecule in position A. Zirconium clusters are shown in green, carbon atoms in grey, oxygen in red, sulphur in yellow and hydrogen in white.<sup>246</sup>

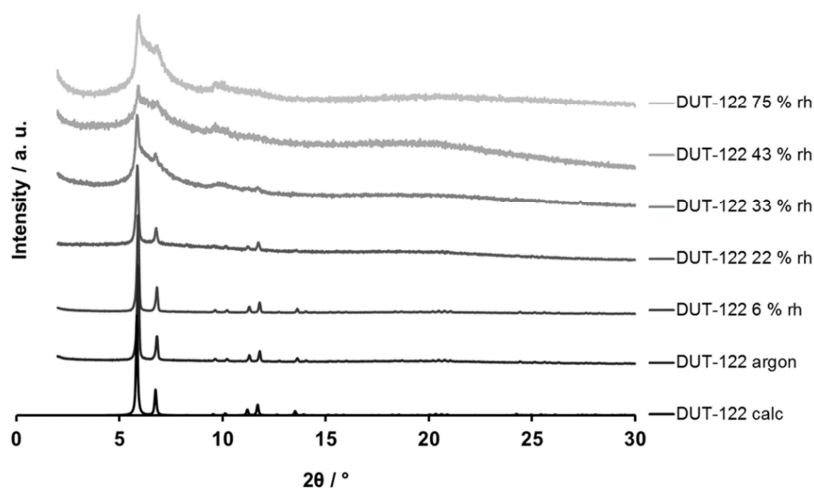
According to the crystal structure analysis, the solvent accessible void volume for DUT-122(Zr) reaches 63.7%. The experimental total pore volume, which was derived from nitrogen physisorption experiment at 77 K, is with  $0.65 \text{ cm}^3 \text{ g}^{-1}$  significantly smaller than the theoretical one. The experimental surface area is with  $1428 \text{ m}^2 \text{ g}^{-1}$  also lower compared to the theoretical surface area. The  $\text{N}_2$  physisorption isotherm corresponds to a classical “Typ Ia” isotherm according to IUPAC<sup>194</sup> classification and shows a maximum uptake of  $417 \text{ cm}^3 \text{ g}^{-1}$  at standard temperature and pressure (Figure 74 left).



**Figure 74.** Left: nitrogen isotherm of DUT-122(Zr) that was activated from DMF in vacuum at 120 °C at 77 K; Right: water vapour isotherm of DUT-122(Zr) that was activated from DMF in vacuum at 120 °C at 298 K.

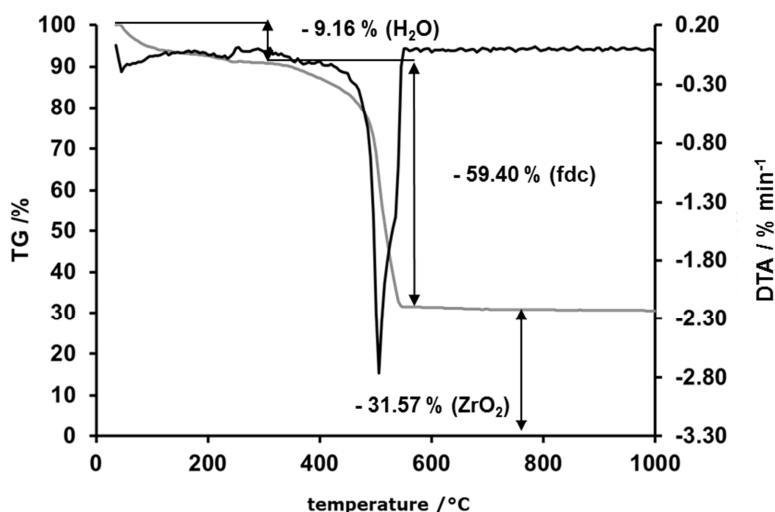
The water vapour isotherm of DUT-122(Zr) is S-shaped (Figure 74 right) and can be assigned to a “Type V” isotherm. Until a relative pressure of 0.3, only an insignificant water uptake of  $15 \text{ cm}^3 \text{ g}^{-1}$  is observed. After this point the isotherm shows a distinct step and its slope increases drastically. It reaches a maximum water uptake at a relative pressure of 0.97 with  $330 \text{ cm}^3 \text{ g}^{-1}$ . At this relative pressure, the pore volume for water is estimated to  $0.266 \text{ cm}^3 \text{ g}^{-1}$ . Consequently the pore filling degree for DUT-122(Zr) is only 41%. Nevertheless, DUT-122(Zr) shows a semi-hydrophilic character. The network itself should be hydrophobic, due to the fact, that the organic linker molecules shield the hydrophilic zirconium cluster completely. Because of defects, which can expose the metal cluster to water molecules, and due to the polar keto group of the fluorenone linker molecules, the framework is more hydrophilic and induces the step in the water vapour isotherm. Therefore the framework of DUT-122(Zr) is more hydrophilic than UiO-67, which does not adsorb a significant amount of water up to a relative pressure of 0.5.<sup>286</sup> The large hysteresis in the isotherm indicates the presence of strong forces for desorption process between the inner surface of DUT-122(Zr) and the water molecules, whereas the removal of water molecules destroys the framework partly. Furthermore, the stability of DUT-122(Zr) against moisture was tested by PXRD

measurements (Figure 75). For this purpose, the MOF sample was exposed to certain humidity level in a desiccator for two hours. Up to a humidity level of 22%, DUT-122(Zr) remains crystalline. At humidity levels higher than 33%, the diffraction pattern does not show distinct Bragg-reflections anymore and the framework starts to decompose. These results are in good agreement with the water vapour isotherm, where the significant water uptake also starts at a relative humidity of  $\sim 30\%$  and the hysteresis starts to be more prominent at this relative humidity level.



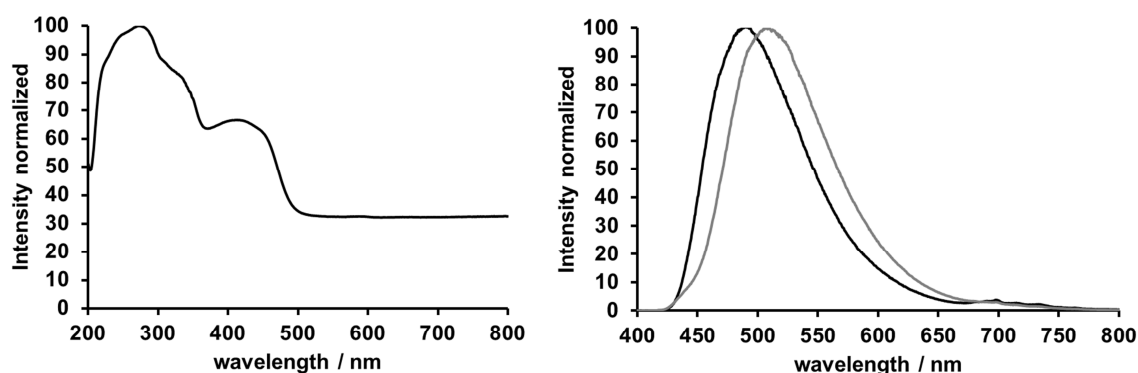
**Figure 75.** PXRD patterns of DUT-122 in inert argon atmosphere and in different relative humidity (rh) levels.

In addition, the thermal stability was checked by TG/DTA measurements. In air, DUT-122(Zr) is thermally stable up to a temperature of 400 °C (Figure 76). At lower temperatures, a dehydration process takes place, where adsorbed water is removed from the framework.



**Figure 76.** TG/DTA analysis of DUT-122(Zr) in air.

The optical properties of DUT-122(Zr) were investigated by solid state UV/Vis – and fluorescence measurements. The absorption spectrum has a global maximum at  $\sim 275$  nm and a local maximum at  $\sim 425$  nm at room temperature. In between these maxima, a local minimum does exist at a wavelength of around 370 nm (Figure 77 left). The fluorescence emission spectra of the pure linker H<sub>2</sub>fdc and of DUT-122(Zr), which were recorded in argon atmosphere at an excitation wavelength of 368 nm, consist of broad emission peaks with FWHM of 93 nm (H<sub>2</sub>fdc) and 95 nm (DUT-122(Zr)) (Figure 77 right). With regard to their emission maxima, the emission profiles differ from each other. The free ligand H<sub>2</sub>fdc has its emission maximum at a wavelength of 508 nm, whereas the emission maximum of DUT-122(Zr) is shifted 21 nm to higher wavelengths and is located at 487 nm. Such shifted wavelength maxima were already observed for other fluorenone based MOFs<sup>284-285, 287</sup> and are a well-known phenomenon, which is based on changes in the band structure. The band structures of frameworks depend i.a. on the type of the metal cations, which have an electron withdrawing effect on the linker molecules. Furthermore, the increased distances between linker molecules influence the emission spectra and are responsible for increased quantum yields. Due to  $\pi$ -stacking that causes fluorescence quenching<sup>288-289</sup>, the free ligand H<sub>2</sub>fdc has a photoluminescence quantum yield of only 0.75% at an excitation wavelength of 368 nm in argon atmosphere. At the same conditions, DUT-122(Zr) has a doubled photoluminescence quantum yield of 1.44%. This quantum yield is comparable to other reported fluorenone based frameworks<sup>284-285, 287, 290</sup>, but is nevertheless very low and therefore not appropriate for solid state lighting applications.



**Figure 77.** Left: Solid state UV/VIS spectrum of DUT-122(Zr). Right: The fluorescence spectra of the pristine linker H<sub>2</sub>fdc (grey) and DUT-122(Zr) (black) in the solid state at an excitation wavelength of 368 nm, measured in argon atmosphere.<sup>246</sup>

### 5.5.2 Application as solvent vapour sensor

Since the energies of the singlet states and  $n-\pi^*$  of the triplet state of the  $H_2fdc$  molecule are solvent dependent, making the intersystem crossing from S1 to T1 ( $\pi-\pi^*$ ) inefficient in polar solvents<sup>280-281</sup>, an employment of DUT-122 as a solvent vapour sensor is the logical consequence. Frameworks, that contain the  $fdc$ -linker, should be therefore sensitive to polar solvents and their photoluminescence properties, such as their emission spectra, quantum yields and the fluorescence lifetimes should be affected. As mentioned, the maximum of the emission spectra of DUT-122(Zr) in argon atmosphere in its activated state, with all solvent molecules removed, is located at 487 nm. Non-polar solvents without a  $\pi$ -system, like heptane and cyclohexane do not cause a significant shift of the emission maximum ( $\lambda_{max} = 488-489$  nm) in saturated vapour atmosphere, as well as polar solvents without a carbonyl or hydroxyl group, like dichloromethane or acetonitrile (Figure 78). In contrast, the vapours of non-polar solvents that contain a  $\pi$ -system, like toluene or benzene, provoke a small hypsochromic shift to  $\lambda_{max} = 481$  nm. A significant hypsochromic shift in the emission spectra is caused by vapours of polar solvents that contain a carbonyl function and by ethers. For instance, acetone provokes a smaller emission shift to  $\lambda_{max} = 484$  nm, diethylether to  $\lambda_{max} = 480$  nm, dioxane and ethylacetate to  $\lambda_{max} = 479$  nm and tetrahydrofuran to even  $\lambda_{max} = 477$  nm. Contrary, vapours of alcohols and water induce a bathochromic shift in the emission spectra, ranging from  $\lambda_{max} = 504$  nm for 2-butanol to  $\lambda_{max} = 536$  nm for water. The trend is observed that with increasing polarity the maximum of the emission profile is shifted to lower energies in the order 2-butanol < 2-propanol < 1-propanol < ethanol < methanol < water. Inferential, the shifts in the emission spectra are not only dependent on the solvent polarity, but also on specific interactions between the solvent molecules and the chromophore linker  $fdc$ , which can include hydrogen bond formations or weak van der Waals interactions. For instance, the O-H groups of water and alcohols are able to induce vibrational coupling, leading to non-radiative transitions<sup>285</sup>.

In case of water, the solvent dependent emission shift was investigated not only for a saturated atmosphere, but also for different levels of relative humidity RH (Figure 78). The spectral shift increases with higher relative humidity and correlates with the response factor (39),

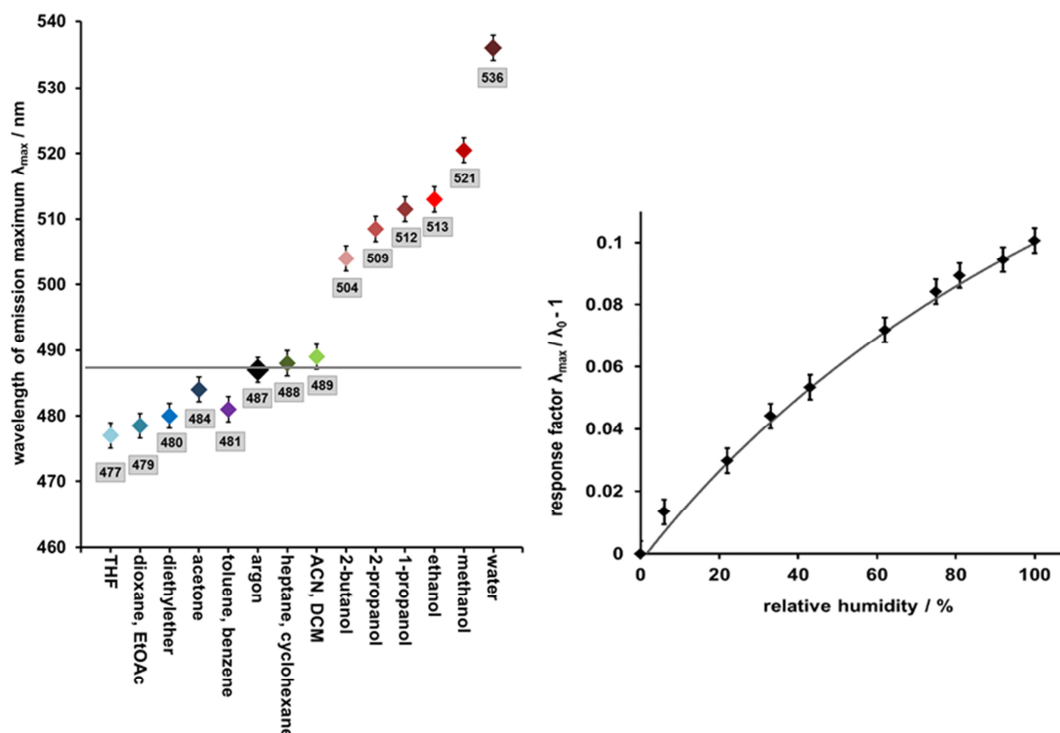
$$RF = \lambda_{max}/\lambda_0 - 1 \quad (39)$$

wherein  $\lambda_0$  is the emission maximum of DUT-122(Zr) in argon atmosphere.

The response factor follows the Langmuir isotherm model (40):

$$RF = \frac{b \cdot RF_m \cdot RH}{1 + b \cdot RH} \quad (40)$$

Thereby,  $RF_m$  could be fitted to a value of 0.2786 and the equilibrium constant  $b$  to a value of 0.0057.



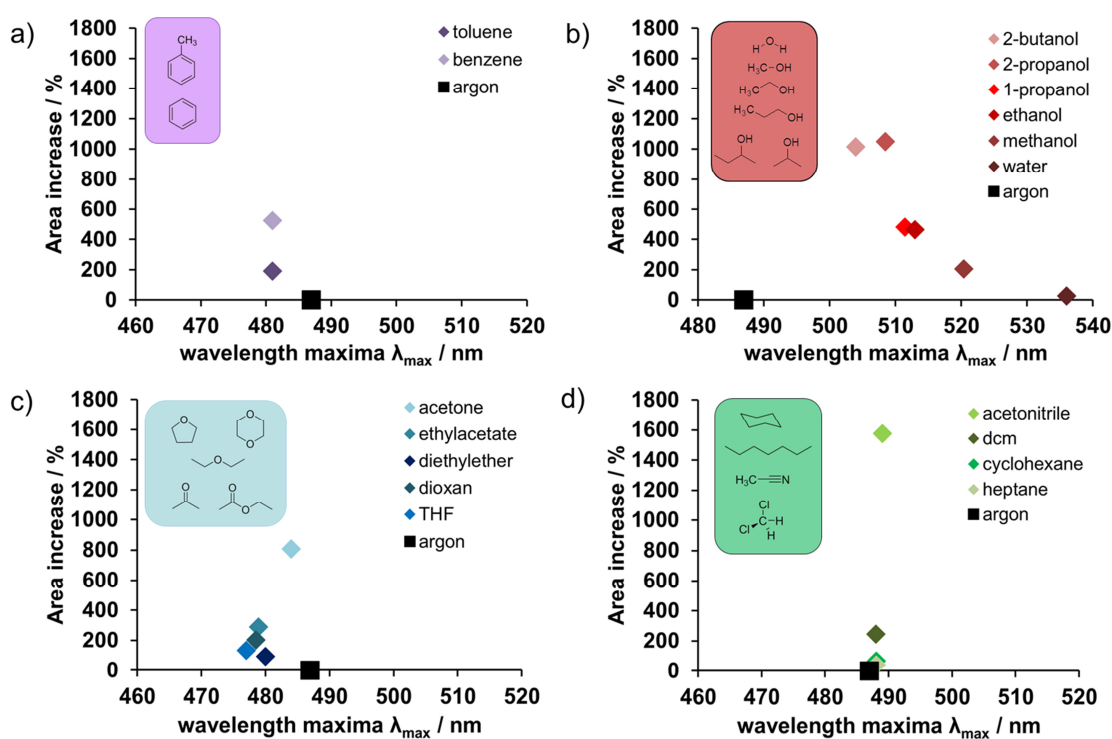
**Figure 78.** Left: wavelengths of emission peak maxima of DUT-122(Zr) obtained in a saturated atmosphere of various solvents. The emission wavelength maximum of DUT-122(Zr) in argon atmosphere is located at 487 nm (black diamond, grey line). The blue diamonds represent solvents which induce a shift to higher energies. The green diamonds corresponds to solvents which are not able to trigger a spectral shift. The red diamonds correspond to the solvents causing shifts to lower energies. Right: correlation between the shift in the emission maximum wavelength of DUT-122(Zr) and relative humidity.<sup>246</sup>

The adaptability of the Langmuir model indicates that chemisorption takes place when DUT-122 comes in contact with water. Up to a relative humidity of 75%, the response time is very fast and the spectral shift can be observed within a few seconds. At higher humidity levels, the corresponding spectral shift has a slower kinetic rate and needs several hours to reach the equilibrium state. This phenomenon is very likely due to the framework transformation, which takes place at such high humidity levels (Figure 75). The adsorption of water (and alcohols) into DUT-122 induces also a visible change from pale yellow in activated state to dark yellow in hydrated state. In contrast, the linker  $H_2fdc$  itself in the solid state does not show any spectral shift, if exposed to solvent vapour. The inability of the linker in solid state to show a responsive behaviour to solvents, points out the importance of the highly ordered



MOF for the application as a sensor, which provides accessibility for solvent molecules by its pore system.

It is worth to mention that the presence of solvent vapours does not only induce shifts of the emission maxima in the fluorescence spectra, it provokes also changes in the intensities of the emission peaks. Since the fluorescence spectra were recorded only in one specific angle, the impact of scattering effects to the resulting emission spectra is not minimized. Therefore, the determined areas of the emission peaks are only an approximation (Figure 79, FigureA 15-17). But nevertheless, they give a good estimation how the intensity changes if DUT-122(Zr) is exposed to a saturated atmosphere of a specific solvent. Thus, solvents with a similar shift in the emission maximum can be distinguished.



**Figure 79.** Wavelengths of emission peak maxima and the area increase of the emission peaks of DUT-122(Zr) obtained in a saturated atmosphere of various solvents. The emission wavelength maximum of DUT-122(Zr) in argon atmosphere is located at 487 nm (black diamond). The purple diamonds represent aromatic solvents which provoke a spectral shift to higher energies. The blue diamonds represent solvents which induce a shift to higher energies and contain oxygen in their structure. The green diamonds corresponds to solvents which are not able to trigger a significant spectral shift. The red diamonds correspond to the solvents causing shifts to lower energies.

For example, toluene ( $\lambda_{\max} = 481$  nm) shows only an area increase of  $\sim 190\%$  and the area of benzene ( $\lambda_{\max} = 481$  nm) has significantly increased with  $\sim 525\%$ . Whereas the non-polar solvents heptane and cyclohexane ( $\lambda_{\max} = 488$  nm) show an area increase of only 40-65%, the more polar dichloromethane ( $\lambda_{\max} = 489$  nm) has an increase of  $\sim 240\%$  and acetonitrile ( $\lambda_{\max} = 489$  nm) exhibits an increase of even 1575%. In case of polar solvents, which contain

an -OH function, the trend is reversed. Here, the area increase caused by the most polar solvent water is the lowest with 28%, whereas for molecules with longer alkyl chains and with bigger size the area increase of the emission peaks gets higher.

Furthermore, fluorescence decay curves were recorded to compare the fluorescence lifetimes of DUT-122(Zr) and the free ligand H<sub>2</sub>fdc and to investigate the impact of the presence of 75% relative humidity on these lifetimes (Figure 80, Table 22-26). All fluorescence decay curves were measured for the excitation wavelengths  $\lambda_{\text{ex}} = 290$  nm,  $\lambda_{\text{ex}} = 368$  nm and  $\lambda_{\text{ex}} = 410$  nm, which represent the maxima and the local minimum of the UV-Vis solid state absorption spectrum of DUT-122(Zr), with emission wavelengths in the range of 362 nm and 528 nm. For all excitation wavelengths, the general trend – the higher the emission wavelength, the higher the fluorescence lifetime – is followed. Thereby, the fluorescence decays for the excitation wavelength of 290 nm have the longest lifetimes and for the excitation wavelength of 368 nm the shortest lifetimes. An exception is given for the excitation wavelength of 368 nm at an emission wavelength of 528 nm, where an unusual long lifetime of 6 ns for DUT-122 and 32 ns for H<sub>2</sub>fdc appears. Their fluorescence decay curves even do not reach the zero level after 100 ns. Due to the rigid nature of the MOF, thermal vibrations and non-radiative relaxation transitions are inhibited. Therefore, fluorescence decays of linker molecules in the solid state are in general faster than the ones of MOFs. In case of DUT-122(Zr), the difference of the fluorescence lifetimes between the pristine linker and the MOF are in the range of 0-2 ns. Similar decreases in fluorescence lifetimes are observed for DUT-122(Zr), when it is exposed to 75% relative humidity. The only exception again is the fluorescence decay for the excitation wavelength of 368 nm at the emission wavelength of 528 nm. Here, the fluorescence lifetime is increased from 6 ns to 23 ns.

**Table 22.** Fluorescence lifetimes (ns) of H<sub>2</sub>fdc as well of DUT-122(Zr) in argon atmosphere and in 75% relative humidity. The excitation wavelength used is  $\lambda_{\text{ex}} = 290$  nm.

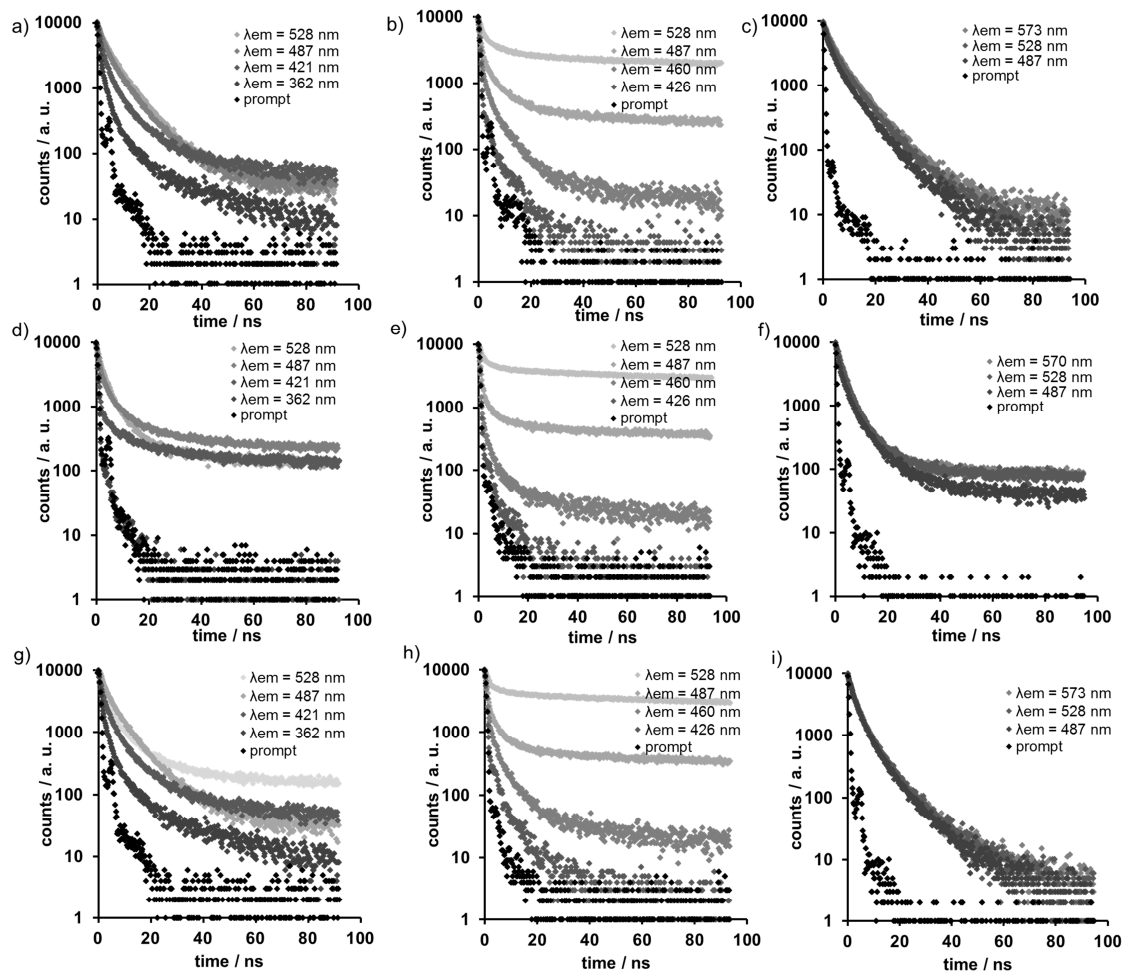
$\lambda_{\text{em}} / \text{nm}$	DUT-122	H <sub>2</sub> fdc	DUT-122 75% RH
362	1.50	1.34	0.89
421	2.31	2.50	1.27
487	4.11	2.94	2.09
528	4.82	2.78	2.77

**Table 23.** Fluorescence lifetimes (ns) of H<sub>2</sub>fdc as well of DUT-122(Zr) in argon atmosphere and in 75% relative humidity. The excitation wavelength used is  $\lambda_{ex} = 368$  nm.

$\lambda_{em} / \text{nm}$	DUT-122	H <sub>2</sub> fdc	DUT-122 75% RH
409	0.90	0.97	0.76
426	1.02	0.97	0.88
487	1.60	1.65	1.34
528	6.09	32.19	23.14

**Table 24.** Fluorescence lifetimes (ns) of H<sub>2</sub>fdc as well of DUT-122(Zr) in argon atmosphere and in 75% relative humidity. The excitation wavelength used is  $\lambda_{ex} = 410$  nm.

$\lambda_{em} / \text{nm}$	DUT-122	H <sub>2</sub> fdc	DUT-122 75% RH
487	3.06	3.02	2.15
528	4.09	3.15	3.07
570	4.72	2.97	3.29



**Figure 80.** Fluorescence decay curves of DUT-122(Zr) in argon atmosphere (a-c), of DUT-122(Zr) in 75% relative humidity (d-f) and of the free linker molecule H<sub>2</sub>fdc (g-i) excited at wavelengths at  $\lambda_{ex} = 290$  nm (a, d, g), at  $\lambda_{ex} = 368$  nm (b, e, h) and at  $\lambda_{ex} = 410$  nm (c, f, i) for various emission wavelengths, ranging from 362 nm to 573 nm.

In conclusion, a UiO-67 analogue MOF – namely DUT-122 – could be synthesised; it is highly porous if activated from DMF in vacuum at 120 °C and shows luminescent behaviour caused by its linker H<sub>2</sub>fdc. These luminescent properties were analysed in detail. For this purpose, UV-Vis absorption spectra, fluorescence emission spectra, fluorescence lifetimes and quantum yields were measured for DUT-122 in argon atmosphere as well as for the linker in its solid state. The fluorescence emission maximum of DUT-122 of 487 nm differs with from the pristine linker's wavelength located at 508 nm. Compared to the linker, the quantum yield of DUT-122 is higher and the fluorescence lifetimes are generally longer. Furthermore, the fluorescence lifetimes of DUT-122 decrease when water is adsorbed. Also the location of the emission maximum of DUT-122 changes with the presence of water. This emission maximum wavelength shift is thereby dependent on the relative humidity. In a relative humidity of 100%, the emission maximum is shifted to 536 nm. Emission maximum wavelength shift is also provoked by other solvent molecules depending on their polarity and the presence of protic functional groups. Non-polar aromatic solvents and polar aprotic solvents induce a hypsochromic shift, whereas polar protic solvents induce a bathochromic shift. Non-polar non-aromatic solvents without an oxygen function do not provoke an emission maximum wavelength emission shift but an increase of the emission intensity. Other solvents types increase the emission intensity of DUT-122, too. Hence, DUT-122 is a promising material for solvent vapour sensing applications.

## 6. CONCLUSIONS AND OUTLOOK

The aim of the work was to exploit the modulating approach, to modify the structure and properties of Zr-MOFs, based on their reduced cluster connectivity. The role of modulator as structure directing agent was demonstrated on DUT-126, a fourth polymorph in the Zr-tdc-system. With the use of polar trifluoroacetic acid as modulator in the synthesis the structure of DUT-126 is formed that is not accessible with the modulators used for the other polymorphic MOFs – formic, acetic or propionic acid. The new DUT-126 structure has **hbr** topology, which has not been observed in MOF chemistry so far. The new MOF has similar textural properties compared to the already known structures of DUT-67, DUT-68 and DUT-69.

To functionalize the inner surface, DUT-67 was utilized as a model to study the influence of modulator molecules on the hydrophobicity of the whole framework and its impact on the framework stability against water removal. It is well known that Zr-based MOFs are often sensitive to water removal from their pores, due to strong capillary forces acting between the framework inner surface and the adsorbed layer. It could be shown that with increasing length of the alkyl chain of the modulator the porosity loss, which occurs after activation from water, could be reduced. If acetic acid or propionic acid were used as modulator during the synthesis instead of formic acid, the loss of porosity could be reduced from 34% to 20%. Thereby, the increased stability of the given framework structure is obviously dependent on the polarity and the steric demand of the modulator, which is shielding the metal cluster against water molecules and decreases the interaction between the framework and water molecules. Thus, a selective functionalization of the inner surface of DUT-67 by a post-synthetic modulator exchange with fluorinated monocarboxylates resulted in minimized porosity loss after water removal to less than 0.5% and to increased hydrophobic properties.

Importantly, it could be shown that the functionalization does not only affect the slopes of water vapour isotherms but changes also the sequential pore filling mechanism due to the special pore environment of DUT-67. Only one pore type out of three is functionalized by the post-synthetic modulator exchange, because one pore type is too small for the exchange and the other one exhibits no necessary free coordination sites. The hypothesis of the switched pore filling sequence was verified by careful analysis of water vapour isotherms and of experimental – and theoretical pore size distributions of all modified DUT-67 analogues.

Due to the increased stability and the tuneable water adsorption properties, such functionalized MOFs are a potential candidate for adsorption-based heat-exchange- and solar cooling applications. For that purpose, the pressure range of significant water adsorption

uptake is an important factor and a stepwise adsorption is desired. A small pressure change should be sufficient to induce the adsorption/desorption process and, out of efficiency reasons, the full capacity of the adsorbent material should be utilized in this pressure range.<sup>50</sup>  
<sup>52</sup> To prove the practicability for such applications, the long term stability of these tuned MOFs should be investigated by multiple water adsorption/desorption cycles.

The applicability of the modulator exchange to other desired modifications was tested on chiral functionalization. To insert the chiral component into the MOF, the same post-synthetic procedure was carried out. In comparison to other functionalization approaches, the used post-synthetic functionalization protocol is easy and simple – the MOF is just soaked in a concentrated solution of the wanted molecule, which ideally is a carboxylic acid, at room temperature. In this work, the chiral carboxylates tartaric acid, lactic acid and mandelic acid were coordinated to the metal cluster of DUT-67 under preservation of crystallinity and with only minor porosity loss. A possible application of these chiral DUT-67 materials is the use as adsorbent for the separation of chiral molecules, for example as stationary phase in HPLC columns. As well, these materials could be utilized as catalysts for enantioselective reactions in the future.

For several applications, such as Lewis acid based catalysis, the presence of open metal sites is of interest. The feasibility to remove coordinated mono-dentate carboxylates under preservation of the framework by treatment with diluted solutions of inorganic acids could be shown on DUT-67, which was used again as a model substance. While a treatment of DUT-67 with sulphuric acid resulted in a shielding of the metal clusters with coordinated  $\text{SO}_4^{2-}$  anions, a treatment with hydrochloric acid resulted in free coordination sites and the  $\text{Cl}^-$  anions are probably located in the vicinity to the  $\mu_3\text{-OHs}$  of the metal cluster. The acidic treatment was examined on Zr- and Hf-based DUT-67 and it could be shown that the thermal stability and the stability against water removal is positively affected in comparison to the parental DUT-67, where formate is still coordinated to the metal cluster. Furthermore, an application of these materials as heterogenous catalysts was demonstrated for the MPV reduction of cyclohexanone. A detailed analysis of the influence of the catalyst amount on the conversion rates and the impact of the coordinated ligand on the activity of the catalyst at low conversion times was carried out. Therefore, acid treated and non-acid treated DUT-67s were used for the catalytic reaction, wherein the MOFs without any remaining modulator molecules showed TOF values ~2 times higher than the pristine DUT-67 with coordinated modulators. That the

presence of modulator molecules slows down the catalytic reaction rate could be particularly seen in reactions where only a small amount of catalyst was used. In these cases, the reaction rate follows an S-shape slope, indicating that the coordinated modulator molecules are only displaced from the catalytic active centres during the catalytic reaction. This assumption is supported by the fact that after the first catalytic run, no modulator molecules could be found anymore in the MOF structure and the TOF values are increased significantly in the second and the third run. Stability and recycling tests showed that DUT-67 is an appropriate heterogenous catalyst for this type of catalytic reaction. In comparison with the Zr-based UiO-66 and UiO-67, DUT-67 clearly outperformed these MOFs. In contrast, the Zr-based MOFs DUT-126 and the isorecticular DUT-51 showed better performance in the reduction of cyclohexanone in the first catalytic cycle, likely because of their bigger pores, which enable improved mass transport. Nevertheless, DUT-67 has some advantages in comparison to DUT-51 and DUT-126, such as higher stability, a commercially available linker, high yields in the synthesis and lower production costs. In general, it should be considered if the given MOF is suitable for the desired catalytic reaction. For example, for reactions involving substrates with bigger kinetic diameter, MOFs are the better choice than zeolites, which show also good catalytic performance but have usually small pore windows and therefore limited accessibility. The potential application of DUT-67 materials as catalysts for other catalytic reactions, such as esterification of carboxylic acids or isomerization of terpenes, and the influence of the acidic treatment on the performance of the respective reaction showed first promising results (which are not part of this thesis) and are worth further investigations.

The application of the twelve-connected Zr-based MOF DUT-122 as a photoluminescent sensor material to different solvent vapours was also demonstrated in this thesis. The high porosity of MOFs makes them attractive for such applications. Analyte molecules can be easily enriched into the framework *via* adsorption, leading to increased sensitivity and facile accessibility of responsive centres, providing fast sorption kinetics and short response times. It could be shown that DUT-122 is sensitive to various solvent vapours, which induce photoluminescent shifts and intensity changes of the emission profile within seconds. Depending on the polarity and the functionality of the respective solvent and their influence on the emission profile, four compound classes could be distinguished: i) polar -OH containing solvents like water and alcohols, which provoke an emission shift to lower energies, ii) non-polar aliphatic – and polar compounds without any oxygen-containing function, which induce no shift, iii) molecules with oxygen function such as carbonyls and ethers, which provoke a shift of the emission profile to higher energies, iv) as well as non-

polar aromatic molecules like benzene or toluene. In case of water, the vapour pressure dependence on the wavelength shift and its influence on fluorescence lifetimes were also studied. The solvent-dependent emission shift increases with higher humidity and correlates with a response factor that follows the Langmuir isotherm model. In 100% relative humidity, the fluorescence maximum of DUT-122 shifts from 487 nm to 536 nm ( $\lambda_{\text{ex}} = 368$  nm), which is the highest spectral shift observed for all tested solvent vapours. In addition, the fluorescence lifetime decreases at higher humidity levels, which could be exemplarily shown for the case of 75 % relative humidity.

Despite a lot of MOF structures are known, the synthesis and exploration of new structures based on zirconium or hafnium is still attractive, since they overcome the main weak point of MOFs to a certain extent – their sensitivity against moisture and other solvents. The increased stability and the possibility of easy functionalization of these MOFs, which was demonstrated in this thesis, opens new application fields that may involve moisture, like the previous mentioned applications as sensor for solvent vapours and water, as catalyst or as adsorbent for heat pumps and chillers.



---

## 7. REFERENCES

1. Davis, B. H.; Sing, K. S. W., Historical Aspects. In *Handbook of Porous Solids*, Wiley-VCH Verlag GmbH: 2008; pp 1-23.
2. Ballschmiter, K., Transport and Fate of Organic Compounds in the Global Environment. *Angew. Chem., Int. Ed. Engl.* **1992**, *31* (5), 487-515.
3. Mondloch, J. E.; Katz, M. J.; Isley Iii, W. C.; Ghosh, P.; Liao, P.; Bury, W.; Wagner, G. W.; Hall, M. G.; DeCoste, J. B.; Peterson, G. W.; Snurr, R. Q.; Cramer, C. J.; Hupp, J. T.; Farha, O. K., Destruction of chemical warfare agents using metal-organic frameworks. *Nat. Mater.* **2015**, *14* (5), 512-516.
4. Moon, S.-Y.; Liu, Y.; Hupp, J. T.; Farha, O. K., Instantaneous Hydrolysis of Nerve-Agent Simulants with a Six-Connected Zirconium-Based Metal-Organic Framework. *Angew. Chem., Int. Ed.* **2015**, *54* (23), 6795-6799.
5. Montoro, C.; Linares, F.; Quartapelle Procopio, E.; Senkovska, I.; Kaskel, S.; Galli, S.; Masciocchi, N.; Barea, E.; Navarro, J. A. R., Capture of Nerve Agents and Mustard Gas Analogues by Hydrophobic Robust MOF-5 Type Metal-Organic Frameworks. *J. Am. Chem. Soc.* **2011**, *133* (31), 11888-11891.
6. Batten Stuart, R.; Champness Neil, R.; Chen, X.-M.; Garcia-Martinez, J.; Kitagawa, S.; Öhrström, L.; O’Keeffe, M.; Paik Suh, M.; Reedijk, J., Terminology of metal-organic frameworks and coordination polymers (IUPAC Recommendations 2013). *Pure Appl. Chem.* **2013**, Vol. 85, p 1715.
7. Alezi, D.; Belmabkhout, Y.; Suyetin, M.; Bhatt, P. M.; Weseliński, Ł. J.; Solovyeva, V.; Adil, K.; Spanopoulos, I.; Trikalitis, P. N.; Emwas, A.-H.; Eddaoudi, M., MOF Crystal Chemistry Paving the Way to Gas Storage Needs: Aluminum-Based soc-MOF for CH<sub>4</sub>, O<sub>2</sub>, and CO<sub>2</sub> Storage. *J. Am. Chem. Soc.* **2015**, *137* (41), 13308-13318.
8. Dincă, M.; Long, J. R., Hydrogen Storage in Microporous Metal-Organic Frameworks with Exposed Metal Sites. *Angew. Chem., Int. Ed.* **2008**, *47* (36), 6766-6779.
9. Li, Y.; Yang, R. T., Gas Adsorption and Storage in Metal-Organic Framework MOF-177. *Langmuir* **2007**, *23* (26), 12937-12944.
10. Murray, L. J.; Dinca, M.; Long, J. R., Hydrogen storage in metal-organic frameworks. *Chem. Soc. Rev.* **2009**, *38* (5), 1294-1314.
11. Suh, M. P.; Park, H. J.; Prasad, T. K.; Lim, D.-W., Hydrogen Storage in Metal-Organic Frameworks. *Chem. Rev.* **2012**, *112* (2), 782-835.
12. Zhao, D.; Yuan, D.; Zhou, H.-C., The current status of hydrogen storage in metal-organic frameworks. *Energy Environ. Sci.* **2008**, *1* (2), 222-235.
13. Li, B.; Wen, H.-M.; Zhou, W.; Chen, B., Porous Metal-Organic Frameworks for Gas Storage and Separation: What, How, and Why? *J. Phys. Chem. Lett.* **2014**, *5* (20), 3468-3479.
14. Banerjee, D.; Cairns, A. J.; Liu, J.; Motkuri, R. K.; Nune, S. K.; Fernandez, C. A.; Krishna, R.; Strachan, D. M.; Thallapally, P. K., Potential of Metal-Organic Frameworks for Separation of Xenon and Krypton. *Acc. Chem. Res.* **2015**, *48* (2), 211-219.
15. Banerjee, D.; Simon, C. M.; Plonka, A. M.; Motkuri, R. K.; Liu, J.; Chen, X.; Smit, B.; Parise, J. B.; Haranczyk, M.; Thallapally, P. K., Metal-organic framework with optimally selective xenon adsorption and separation. *Nat. Commun.* **2016**, *7*, 11831.
16. Burd, S. D.; Ma, S.; Perman, J. A.; Sikora, B. J.; Snurr, R. Q.; Thallapally, P. K.; Tian, J.; Wojtas, L.; Zaworotko, M. J., Highly Selective Carbon Dioxide Uptake by [Cu(bpy-n)<sub>2</sub>(SiF<sub>6</sub>)] (bpy-1 = 4,4'-Bipyridine; bpy-2 = 1,2-Bis(4-pyridyl)ethene). *J. Am. Chem. Soc.* **2012**, *134* (8), 3663-3666.

17. Bux, H.; Liang, F.; Li, Y.; Cravillon, J.; Wiebecke, M.; Caro, J., Zeolitic Imidazolate Framework Membrane with Molecular Sieving Properties by Microwave-Assisted Solvothermal Synthesis. *J. Am. Chem. Soc.* **2009**, *131* (44), 16000-16001.
18. Herm, Z. R.; Wiers, B. M.; Mason, J. A.; van Baten, J. M.; Hudson, M. R.; Zajdel, P.; Brown, C. M.; Masciocchi, N.; Krishna, R.; Long, J. R., Separation of Hexane Isomers in a Metal-Organic Framework with Triangular Channels. *Science* **2013**, *340* (6135), 960-964.
19. Huang, Y.-L.; Jiang, L.; Lu, T.-B., Modulation of Gas Sorption Properties through Cation Exchange within an Anionic Metal-Organic Framework. *ChemPlusChem* **2016**, *81* (8), 780-785.
20. Li, J.-R.; Kuppler, R. J.; Zhou, H.-C., Selective gas adsorption and separation in metal-organic frameworks. *Chem. Soc. Rev.* **2009**, *38* (5), 1477-1504.
21. Liu, D.; Ma, X.; Xi, H.; Lin, Y. S., Gas transport properties and propylene/propane separation characteristics of ZIF-8 membranes. *J. Membr. Sci.* **2014**, *451*, 85-93.
22. Qiu, S.; Xue, M.; Zhu, G., Metal-organic framework membranes: from synthesis to separation application. *Chem. Soc. Rev.* **2014**, *43* (16), 6116-6140.
23. Van de Voorde, B.; Bueken, B.; Denayer, J.; De Vos, D., Adsorptive separation on metal-organic frameworks in the liquid phase. *Chem. Soc. Rev.* **2014**, *43* (16), 5766-5788.
24. Wang, X.; Li, L.; Wang, Y.; Li, J.-R.; Li, J., Exploiting the pore size and functionalization effects in UiO topology structures for the separation of light hydrocarbons. *CrystEngComm* **2017**, *19* (13), 1729-1737.
25. Zhao, Z.; Ma, X.; Kasik, A.; Li, Z.; Lin, Y. S., Gas Separation Properties of Metal Organic Framework (MOF-5) Membranes. *Ind. Eng. Chem. Res.* **2013**, *52* (3), 1102-1108.
26. Valvekens, P.; Vermoortele, F.; De Vos, D., Metal-organic frameworks as catalysts: the role of metal active sites. *Catal. Sci. Technol.* **2013**, *3* (6), 1435-1445.
27. Rimoldi, M.; Howarth, A. J.; DeStefano, M. R.; Lin, L.; Goswami, S.; Li, P.; Hupp, J. T.; Farha, O. K., Catalytic Zirconium/Hafnium-Based Metal-Organic Frameworks. *ACS Catal.* **2017**, *7* (2), 997-1014.
28. Gascon, J.; Corma, A.; Kapteijn, F.; Llabrés i Xamena, F. X., Metal Organic Framework Catalysis: Quo vadis? *ACS Catal.* **2014**, *4* (2), 361-378.
29. Zhu, L.; Liu, X.-Q.; Jiang, H.-L.; Sun, L.-B., Metal-Organic Frameworks for Heterogeneous Basic Catalysis. *Chem. Rev.* **2017**, *117* (12), 8129-8176.
30. Huang, Y.-B.; Liang, J.; Wang, X.-S.; Cao, R., Multifunctional metal-organic framework catalysts: synergistic catalysis and tandem reactions. *Chem. Soc. Rev.* **2017**, *46* (1), 126-157.
31. Liu, J.; Chen, L.; Cui, H.; Zhang, J.; Zhang, L.; Su, C.-Y., Applications of metal-organic frameworks in heterogeneous supramolecular catalysis. *Chem. Soc. Rev.* **2014**, *43* (16), 6011-6061.
32. Isaeva, V. I.; Kustov, L. M., The application of metal-organic frameworks in catalysis (Review). *Pet. Chem.* **2010**, *50* (3), 167-180.
33. Farrusseng, D.; Aguado, S.; Pinel, C., Metal-Organic Frameworks: Opportunities for Catalysis. *Angew. Chem., Int. Ed.* **2009**, *48* (41), 7502-7513.
34. Allendorf, M. D.; Bauer, C. A.; Bhakta, R. K.; Houk, R. J. T., Luminescent metal-organic frameworks. *Chem. Soc. Rev.* **2009**, *38* (5), 1330-1352.
35. Hu, Z.; Deibert, B. J.; Li, J., Luminescent metal-organic frameworks for chemical sensing and explosive detection. *Chem. Soc. Rev.* **2014**, *43* (16), 5815-5840.
36. Kreno, L. E.; Leong, K.; Farha, O. K.; Allendorf, M.; Van Duyne, R. P.; Hupp, J. T., Metal-Organic Framework Materials as Chemical Sensors. *Chem. Rev.* **2012**, *112* (2), 1105-1125.
37. Kumar, P.; Deep, A.; Kim, K.-H., Metal organic frameworks for sensing applications. *TrAC Trends Anal. Chem.* **2015**, *73*, 39-53.

38. Yi, F.-Y.; Chen, D.; Wu, M.-K.; Han, L.; Jiang, H.-L., Chemical Sensors Based on Metal–Organic Frameworks. *ChemPlusChem* **2016**, *81* (8), 675-690.
39. Zhao, D.; Cui, Y.; Yang, Y.; Qian, G., Sensing-functional luminescent metal-organic frameworks. *CrystEngComm* **2016**, *18* (21), 3746-3759.
40. Sun, C.-Y.; Qin, C.; Wang, X.-L.; Su, Z.-M., Metal-organic frameworks as potential drug delivery systems. *Expert Opin. Drug Delivery* **2013**, *10* (1), 89-101.
41. Al Haydar, M.; Abid, H. R.; Sunderland, B.; Wang, S., Metal organic frameworks as a drug delivery system for flurbiprofen. *Drug Des., Dev. Ther.* **2017**, *11*, 2685-2695.
42. Chowdhury, M. A., The applications of metal-organic-frameworks in controlled release of drugs. *Rev. J. Chem.* **2017**, *7* (1), 1-22.
43. Mihad, I.; Rana, S.; Ghaleb, A. H., Anti-cancer Drug Delivery Using Metal Organic Frameworks (MOFs). *Curr. Med. Chem.* **2017**, *24* (2), 193-214.
44. Cai, W.; Chu, C.-C.; Liu, G.; Wang, Y.-X. J., Metal–Organic Framework-Based Nanomedicine Platforms for Drug Delivery and Molecular Imaging. *Small* **2015**, *11* (37), 4806-4822.
45. Horcajada, P.; Gref, R.; Baati, T.; Allan, P. K.; Maurin, G.; Couvreur, P.; Férey, G.; Morris, R. E.; Serre, C., Metal–Organic Frameworks in Biomedicine. *Chem. Rev.* **2012**, *112* (2), 1232-1268.
46. Rojas, S.; Devic, T.; Horcajada, P., Metal organic frameworks based on bioactive components. *J. Mater. Chem. B* **2017**, *5* (14), 2560-2573.
47. de Lange, M. F.; Ottevanger, C. P.; Wiegman, M.; Vlugt, T. J. H.; Gascon, J.; Kapteijn, F., Crystals for sustainability - structuring Al-based MOFs for the allocation of heat and cold. *CrystEngComm* **2015**, *17* (2), 281-285.
48. de Lange, M. F.; Zeng, T.; Vlugt, T. J. H.; Gascon, J.; Kapteijn, F., Manufacture of dense CAU-10-H coatings for application in adsorption driven heat pumps: optimization and characterization. *CrystEngComm* **2015**, *17* (31), 5911-5920.
49. Demir, H.; Mobedi, M.; Ülkü, S., A review on adsorption heat pump: Problems and solutions. *Renewable Sustainable Energy Rev.* **2008**, *12* (9), 2381-2403.
50. Ehrenmann, J.; Henninger, S. K.; Janiak, C., Water Adsorption Characteristics of MIL-101 for Heat-Transformation Applications of MOFs. *Eur. J. Inorg. Chem.* **2011**, *2011* (4), 471-474.
51. Falcaro, P.; Ricco, R.; Doherty, C. M.; Liang, K.; Hill, A. J.; Styles, M. J., MOF positioning technology and device fabrication. *Chem. Soc. Rev.* **2014**, *43* (16), 5513-5560.
52. Jeremias, F.; Frohlich, D.; Janiak, C.; Henninger, S. K., Water and methanol adsorption on MOFs for cycling heat transformation processes. *New J. Chem.* **2014**, *38* (5), 1846-1852.
53. An, J.; Geib, S. J.; Rosi, N. L., Cation-Triggered Drug Release from a Porous Zinc–Adeninate Metal–Organic Framework. *J. Am. Chem. Soc.* **2009**, *131* (24), 8376-8377.
54. An, J.; Farha, O. K.; Hupp, J. T.; Pohl, E.; Yeh, J. I.; Rosi, N. L., Metal-adeninate vertices for the construction of an exceptionally porous metal-organic framework. *Nat. Commun.* **2012**, *3*, 604.
55. Dreischarf, A. C.; Lammert, M.; Stock, N.; Reinsch, H., Green Synthesis of Zr-CAU-28: Structure and Properties of the First Zr-MOF Based on 2,5-Furandicarboxylic Acid. *Inorg. Chem.* **2017**, *56* (4), 2270-2277.
56. Rose, M.; Weber, D.; Lotsch, B. V.; Kremer, R. K.; Goddard, R.; Palkovits, R., Biogenic metal–organic frameworks: 2,5-Furandicarboxylic acid as versatile building block. *Microporous and Mesoporous Mater.* **2013**, *181*, 217-221.
57. Li, H.-H.; Niu, Z.; Chen, L.; Jiang, H.-B.; Wang, Y.-P.; Cheng, P., Three luminescent metal-organic frameworks constructed from trinuclear zinc(ii) clusters and furan-2,5-dicarboxylate. *CrystEngComm* **2015**, *17* (27), 5101-5109.

58. Reinsch, H.; Waitschat, S.; Chavan, S. M.; Lillerud, K. P.; Stock, N., A Facile "Green" Route for Scalable Batch Production and Continuous Synthesis of Zirconium MOFs. *Eur. J. Inorg. Chem.* **2016**, 2016 (27), 4490-4498.
59. Hu, Z.; Peng, Y.; Kang, Z.; Qian, Y.; Zhao, D., A Modulated Hydrothermal (MHT) Approach for the Facile Synthesis of UiO-66-Type MOFs. *Inorg. Chem.* **2015**, 54 (10), 4862-4868.
60. Hu, Z.; Castano, I.; Wang, S.; Wang, Y.; Peng, Y.; Qian, Y.; Chi, C.; Wang, X.; Zhao, D., Modulator Effects on the Water-Based Synthesis of Zr/Hf Metal-Organic Frameworks: Quantitative Relationship Studies between Modulator, Synthetic Condition, and Performance. *Cryst. Growth Des.* **2016**, 16 (4), 2295-2301.
61. Leng, K.; Sun, Y.; Li, X.; Sun, S.; Xu, W., Rapid Synthesis of Metal-Organic Frameworks MIL-101(Cr) Without the Addition of Solvent and Hydrofluoric Acid. *Cryst. Growth Des.* **2016**, 16 (3), 1168-1171.
62. Klimakow, M.; Klobes, P.; Thünemann, A. F.; Rademann, K.; Emmerling, F., Mechanochemical Synthesis of Metal-Organic Frameworks: A Fast and Facile Approach toward Quantitative Yields and High Specific Surface Areas. *Chem. Mater.* **2010**, 22 (18), 5216-5221.
63. Crawford, D.; Casaban, J.; Haydon, R.; Giri, N.; McNally, T.; James, S. L., Synthesis by extrusion: continuous, large-scale preparation of MOFs using little or no solvent. *Chem. Sci.* **2015**, 6 (3), 1645-1649.
64. Jacoby, M., Materials Chemistry: Metal-Organic Frameworks Go Commercial. *Chem. Eng. News* **2013**, 91 (51), 34-35.
65. Schaate, A.; Roy, P.; Godt, A.; Lippke, J.; Waltz, F.; Wiebcke, M.; Behrens, P., Modulated Synthesis of Zr-Based Metal-Organic Frameworks: From Nano to Single Crystals. *Chem. - Eur. J.* **2011**, 17 (24), 6643-6651.
66. Gilkey, M. J.; Xu, B., Heterogeneous Catalytic Transfer Hydrogenation as an Effective Pathway in Biomass Upgrading. *ACS Catal.* **2016**, 6 (3), 1420-1436.
67. Stuart R. Batten, N. R. C., Xiao-Ming Chen, Javier Garcia-Martinez, Susumu Kitagawa, Lars Öhrström, Michael O'Keeffe, Myunghyun Paik Suh, Jan Reedijk, Terminology of metal-organic frameworks and coordination polymers (IUPAC Recommendations 2013). *Pure Appl. Chem.* **2013**, 85 (8), 1715-1724.
68. Martin, K. V., Polymerization through Coordination. *J. Am. Chem. Soc.* **1958**, 80 (1), 233-236.
69. Bottei, R. S.; Gerace, P. L., Preparation and thermal stabilities of some metal chelate polymers of naphthazarin. *J. Inorg. Nucl. Chem.* **1961**, 23 (3), 245-251.
70. Aleksandr, A. B.; Matveeva, N. G., Polymeric Chelate Compounds. *Russ. Chem. Rev.* **1960**, 29 (3), 119.
71. Rode, V. V.; Rukhadze, E. G.; Terent'ev, A. P., Chelate Polymers. *Russ. Chem. Rev.* **1963**, 32 (12), 666.
72. Bailar, J. C., Jr., Coordination Polymers. *Prep. Inorg. React.* **1964**, 1 (1), 1-27.
73. Hoskins, B. F.; Robson, R., Infinite polymeric frameworks consisting of three dimensionally linked rod-like segments. *J. Am. Chem. Soc.* **1989**, 111 (15), 5962-5964.
74. Hoskins, B. F.; Robson, R., Design and construction of a new class of scaffolding-like materials comprising infinite polymeric frameworks of 3D-linked molecular rods. A reappraisal of the zinc cyanide and cadmium cyanide structures and the synthesis and structure of the diamond-related frameworks  $[\text{N}(\text{CH}_3)_4][\text{CuI}\text{ZnII}(\text{CN})_4]$  and  $\text{CuI}[4,4',4'',4''']\text{-tetracyanotetraphenylmethane}[\text{BF}_4 \cdot x\text{C}_6\text{H}_5\text{NO}_2]$ . *J. Am. Chem. Soc.* **1990**, 112 (4), 1546-1554.
75. Yaghi, O. M.; Li, H., Hydrothermal Synthesis of a Metal-Organic Framework Containing Large Rectangular Channels. *J. Am. Chem. Soc.* **1995**, 117 (41), 10401-10402.
76. Li, H.; Eddaoudi, M.; O'Keeffe, M.; Yaghi, O. M., Design and synthesis of an exceptionally stable and highly porous metal-organic framework. *Nature* **1999**, 402 (6759), 276-279.

- 
77. Farha, O. K.; Özgür Yazaydın, A.; Eryazici, I.; Malliakas, C. D.; Hauser, B. G.; Kanatzidis, M. G.; Nguyen, S. T.; Snurr, R. Q.; Hupp, J. T., De novo synthesis of a metal–organic framework material featuring ultrahigh surface area and gas storage capacities. *Nat. Chem.* **2010**, *2* (11), 944-948.
  78. Eddaoudi, M.; Kim, J.; Rosi, N.; Vodak, D.; Wachter, J.; O’Keeffe, M.; Yaghi, O. M., Systematic Design of Pore Size and Functionality in Isoreticular MOFs and Their Application in Methane Storage. *Science* **2002**, *295* (5554), 469-472.
  79. Shekhah, O.; Wang, H.; Paradinas, M.; Ocal, C.; Schubach, B.; Terfort, A.; Zacher, D.; Fischer, R. A.; Woll, C., Controlling interpenetration in metal-organic frameworks by liquid-phase epitaxy. *Nat. Mater.* **2009**, *8* (6), 481-484.
  80. Zhang, J.; Wojtas, L.; Larsen, R. W.; Eddaoudi, M.; Zaworotko, M. J., Temperature and Concentration Control over Interpenetration in a Metal–Organic Material. *J. Am. Chem. Soc.* **2009**, *131* (47), 17040-17041.
  81. Deshpande, R. K.; Waterhouse, G. I. N.; Jameson, G. B.; Telfer, S. G., Photolabile protecting groups in metal-organic frameworks: preventing interpenetration and masking functional groups. *Chem. Commun.* **2012**, *48* (10), 1574-1576.
  82. Deshpande, R. K.; Minnaar, J. L.; Telfer, S. G., Thermolabile Groups in Metal–Organic Frameworks: Suppression of Network Interpenetration, Post-Synthetic Cavity Expansion, and Protection of Reactive Functional Groups. *Angew. Chem., Int. Ed.* **2010**, *49* (27), 4598-4602.
  83. Farha, O. K.; Eryazici, I.; Jeong, N. C.; Hauser, B. G.; Wilmer, C. E.; Sarjeant, A. A.; Snurr, R. Q.; Nguyen, S. T.; Yazaydın, A. Ö.; Hupp, J. T., Metal–Organic Framework Materials with Ultrahigh Surface Areas: Is the Sky the Limit? *J. Am. Chem. Soc.* **2012**, *134* (36), 15016-15021.
  84. Deng, H.; Grunder, S.; Cordova, K. E.; Valente, C.; Furukawa, H.; Hmadeh, M.; Gándara, F.; Whalley, A. C.; Liu, Z.; Asahina, S.; Kazumori, H.; O’Keeffe, M.; Terasaki, O.; Stoddart, J. F.; Yaghi, O. M., Large-Pore Apertures in a Series of Metal-Organic Frameworks. *Science* **2012**, *336* (6084), 1018-1023.
  85. Haldar, R.; Sikdar, N.; Maji, T. K., Interpenetration in coordination polymers: structural diversities toward porous functional materials. *Mater. Today* **2015**, *18* (2), 97-116.
  86. Schnobrich, J. K.; Koh, K.; Sura, K. N.; Matzger, A. J., A Framework for Predicting Surface Areas in Microporous Coordination Polymers. *Langmuir* **2010**, *26* (8), 5808-5814.
  87. Sarkisov, L., Accessible Surface Area of Porous Materials: Understanding Theoretical Limits. *Adv.Mater.* **2012**, *24* (23), 3130-3133.
  88. Koh, K.; Wong-Foy, A. G.; Matzger, A. J., A Porous Coordination Copolymer with over 5000 m<sup>2</sup>/g BET Surface Area. *J. Am. Chem. Soc.* **2009**, *131* (12), 4184-4185.
  89. Furukawa, H.; Ko, N.; Go, Y. B.; Aratani, N.; Choi, S. B.; Choi, E.; Yazaydın, A. Ö.; Snurr, R. Q.; O’Keeffe, M.; Kim, J.; Yaghi, O. M., Ultrahigh Porosity in Metal-Organic Frameworks. *Science* **2010**, *329* (5990), 424-428.
  90. Grunker, R.; Bon, V.; Muller, P.; Stoeck, U.; Krause, S.; Mueller, U.; Senkovska, I.; Kaskel, S., A new metal-organic framework with ultra-high surface area. *Chem. Commun.* **2014**, *50* (26), 3450-3452.
  91. Stoeck, U.; Krause, S.; Bon, V.; Senkovska, I.; Kaskel, S., A highly porous metal-organic framework, constructed from a cuboctahedral super-molecular building block, with exceptionally high methane uptake. *Chem. Commun.* **2012**, *48* (88), 10841-10843.
  92. Stoeck, U.; Senkovska, I.; Bon, V.; Krause, S.; Kaskel, S., Assembly of metal-organic polyhedra into highly porous frameworks for ethene delivery. *Chem. Commun.* **2015**, *51* (6), 1046-1049.
  93. Low, J. J.; Benin, A. I.; Jakubczak, P.; Abrahamian, J. F.; Faheem, S. A.; Willis, R. R., Virtual High Throughput Screening Confirmed Experimentally: Porous Coordination Polymer Hydration. *J. Am. Chem. Soc.* **2009**, *131* (43), 15834-15842.
-

- 
94. Bosch, M.; Zhang, M.; Zhou, H.-C., Increasing the Stability of Metal-Organic Frameworks. *Adv. Chem.* **2014**, *2014*, 8.
  95. Burtch, N. C.; Jasuja, H.; Walton, K. S., Water Stability and Adsorption in Metal-Organic Frameworks. *Chem. Rev.* **2014**, *114* (20), 10575-10612.
  96. Gu, Z.-Y.; Wang, G.; Yan, X.-P., MOF-5 Metal-Organic Framework as Sorbent for In-Field Sampling and Preconcentration in Combination with Thermal Desorption GC/MS for Determination of Atmospheric Formaldehyde. *Anal. Chem.* **2010**, *82* (4), 1365-1370.
  97. Greathouse, J. A.; Allendorf, M. D., The Interaction of Water with MOF-5 Simulated by Molecular Dynamics. *J. Am. Chem. Soc.* **2006**, *128* (33), 10678-10679.
  98. Tan, K.; Nijem, N.; Canepa, P.; Gong, Q.; Li, J.; Thonhauser, T.; Chabal, Y. J., Stability and Hydrolyzation of Metal Organic Frameworks with Paddle-Wheel SBUs upon Hydration. *Chem. Mater.* **2012**, *24* (16), 3153-3167.
  99. Liang, Z.; Marshall, M.; Chaffee, A. L., CO<sub>2</sub> adsorption, selectivity and water tolerance of pillared-layer metal organic frameworks. *Microporous and Mesoporous Mater.* **2010**, *132* (3), 305-310.
  100. Akiyama, G.; Matsuda, R.; Sato, H.; Hori, A.; Takata, M.; Kitagawa, S., Effect of functional groups in MIL-101 on water sorption behavior. *Microporous and Mesoporous Mater.* **2012**, *157*, 89-93.
  101. Jasuja, H.; Jiao, Y.; Burtch, N. C.; Huang, Y.-g.; Walton, K. S., Synthesis of Cobalt-, Nickel-, Copper-, and Zinc-Based, Water-Stable, Pillared Metal-Organic Frameworks. *Langmuir* **2014**, *30* (47), 14300-14307.
  102. Banerjee, R.; Phan, A.; Wang, B.; Knobler, C.; Furukawa, H.; O'Keeffe, M.; Yaghi, O. M., High-Throughput Synthesis of Zeolitic Imidazolate Frameworks and Application to CO<sub>2</sub> Capture. *Science* **2008**, *319* (5865), 939-943.
  103. Liu, Y.; Kravtsov, V. C.; Larsen, R.; Eddaoudi, M., Molecular building blocks approach to the assembly of zeolite-like metal-organic frameworks (ZMOFs) with extra-large cavities. *Chem. Commun.* **2006**, (14), 1488-1490.
  104. Choi, H. J.; Dinca, M.; Dailly, A.; Long, J. R., Hydrogen storage in water-stable metal-organic frameworks incorporating 1,3- and 1,4-benzenedipyrzolate. *Energy Environ. Sci.* **2010**, *3* (1), 117-123.
  105. Colombo, V.; Galli, S.; Choi, H. J.; Han, G. D.; Maspero, A.; Palmisano, G.; Masciocchi, N.; Long, J. R., High thermal and chemical stability in pyrazolate-bridged metal-organic frameworks with exposed metal sites. *Chem. Sci.* **2011**, *2* (7), 1311-1319.
  106. Park, K. S.; Ni, Z.; Côté, A. P.; Choi, J. Y.; Huang, R.; Uribe-Romo, F. J.; Chae, H. K.; O'Keeffe, M.; Yaghi, O. M., Exceptional chemical and thermal stability of zeolitic imidazolate frameworks. *Proc. Natl. Acad. Sci.* **2006**, *103* (27), 10186-10191.
  107. Liu, X.; Li, Y.; Ban, Y.; Peng, Y.; Jin, H.; Bux, H.; Xu, L.; Caro, J.; Yang, W., Improvement of hydrothermal stability of zeolitic imidazolate frameworks. *Chem. Commun.* **2013**, *49* (80), 9140-9142.
  108. Chui, S. S. Y.; Lo, S. M. F.; Charmant, J. P. H.; Orpen, A. G.; Williams, I. D., A chemically functionalizable nanoporous material[Cu<sub>3</sub>(TMA)<sub>2</sub>(H<sub>2</sub>O)<sub>3</sub>]. *Science* **1999**, *283*, 1148-1150.
  109. Pöpl, A.; Jee, B.; Icker, M.; Hartmann, M.; Himsl, D., Untersuchungen zur chemischen Stabilität von Cu<sub>3</sub>(btc)<sub>2</sub> (HKUST-1) durch N<sub>2</sub>-Adsorption, Röntgenpulverdiffraktometrie und EPR-Spektroskopie. *Chem. Ing. Tech.* **2010**, *82* (7), 1025-1029.
  110. Küssgens, P.; Rose, M.; Senkowska, I.; Fröde, H.; Henschel, A.; Siegle, S.; Kaskel, S., Characterization of metal-organic frameworks by water adsorption. *Microporous and Mesoporous Mater.* **2009**, *120* (3), 325-330.
-

111. Férey, G.; Mellot-Draznieks, C.; Serre, C.; Millange, F.; Dutour, J.; Surblé, S.; Margiolaki, I., A Chromium Terephthalate-Based Solid with Unusually Large Pore Volumes and Surface Area. *Science* **2005**, *309* (5743), 2040-2042.
112. Férey, G.; Serre, C.; Mellot-Draznieks, C.; Millange, F.; Surblé, S.; Dutour, J.; Margiolaki, I., A Hybrid Solid with Giant Pores Prepared by a Combination of Targeted Chemistry, Simulation, and Powder Diffraction. *Angew. Chem., Int. Ed.* **2004**, *43* (46), 6296-6301.
113. Guillerm, V.; Ragon, F.; Dan-Hardi, M.; Devic, T.; Vishnuvarthan, M.; Campo, B.; Vimont, A.; Clet, G.; Yang, Q.; Maurin, G.; Férey, G.; Vittadini, A.; Gross, S.; Serre, C., A Series of Isorecticular, Highly Stable, Porous Zirconium Oxide Based Metal–Organic Frameworks. *Angew. Chem., Int. Ed.* **2012**, *51* (37), 9267-9271.
114. Cavka, J. H.; Jakobsen, S.; Olsbye, U.; Guillou, N.; Lamberti, C.; Bordiga, S.; Lillerud, K. P., A New Zirconium Inorganic Building Brick Forming Metal Organic Frameworks with Exceptional Stability. *J. Am. Chem. Soc.* **2008**, *130* (42), 13850-13851.
115. Sarkisov, L.; Harrison, A., Computational structure characterisation tools in application to ordered and disordered porous materials. *Mol. Simul.* **2011**, *37* (15), 1248-1257.
116. DeCoste, J. B.; Peterson, G. W.; Jasuja, H.; Glover, T. G.; Huang, Y.-g.; Walton, K. S., Stability and degradation mechanisms of metal-organic frameworks containing the  $Zr_6O_4(OH)_4$  secondary building unit. *J. Mater. Chem. A* **2013**, *1* (18), 5642-5650.
117. Mondloch, J. E.; Katz, M. J.; Planas, N.; Semrouni, D.; Gagliardi, L.; Hupp, J. T.; Farha, O. K., Are  $Zr_6$ -based MOFs water stable? Linker hydrolysis vs. capillary-force-driven channel collapse. *Chem. Commun.* **2014**, *50* (64), 8944-8946.
118. Canivet, J.; Fateeva, A.; Guo, Y.; Coasne, B.; Farrusseng, D., Water adsorption in MOFs: fundamentals and applications. *Chem. Soc. Rev.* **2014**, *43* (16), 5594-5617.
119. Furukawa, H.; Gándara, F.; Zhang, Y.-B.; Jiang, J.; Queen, W. L.; Hudson, M. R.; Yaghi, O. M., Water Adsorption in Porous Metal–Organic Frameworks and Related Materials. *J. Am. Chem. Soc.* **2014**, *136* (11), 4369-4381.
120. Kandiah, M.; Nilsen, M. H.; Usseglio, S.; Jakobsen, S.; Olsbye, U.; Tilset, M.; Larabi, C.; Quadrelli, E. A.; Bonino, F.; Lillerud, K. P., Synthesis and Stability of Tagged UiO-66 Zr-MOFs. *Chem. Mater.* **2010**, *22* (24), 6632-6640.
121. Jiang, H.-L.; Feng, D.; Wang, K.; Gu, Z.-Y.; Wei, Z.; Chen, Y.-P.; Zhou, H.-C., An Exceptionally Stable, Porphyrinic Zr Metal–Organic Framework Exhibiting pH-Dependent Fluorescence. *J. Am. Chem. Soc.* **2013**, *135* (37), 13934-13938.
122. Bon, V.; Senkowska, I.; Baburin, I. A.; Kaskel, S., Zr- and Hf-Based Metal–Organic Frameworks: Tracking Down the Polymorphism. *Cryst. Growth Des.* **2013**, *13* (3), 1231-1237.
123. Katz, M. J.; Brown, Z. J.; Colon, Y. J.; Siu, P. W.; Scheidt, K. A.; Snurr, R. Q.; Hupp, J. T.; Farha, O. K., A facile synthesis of UiO-66, UiO-67 and their derivatives. *Chem. Commun.* **2013**, *49* (82), 9449-9451.
124. Vandichel, M.; Hajek, J.; Vermoortele, F.; Waroquier, M.; De Vos, D. E.; Van Speybroeck, V., Active site engineering in UiO-66 type metal-organic frameworks by intentional creation of defects: a theoretical rationalization. *CrystEngComm* **2015**, *17* (2), 395-406.
125. Van de Voorde, B.; Stassen, I.; Bueken, B.; Vermoortele, F.; De Vos, D.; Ameloot, R.; Tan, J.-C.; Bennett, T. D., Improving the mechanical stability of zirconium-based metal-organic frameworks by incorporation of acidic modulators. *J. Mater. Chem. A* **2015**, *3* (4), 1737-1742.
126. Gutov, O. V.; Hevia, M. G.; Escudero-Adán, E. C.; Shafir, A., Metal–Organic Framework (MOF) Defects under Control: Insights into the Missing Linker Sites and Their Implication in the Reactivity of Zirconium-Based Frameworks. *Inorg. Chem.* **2015**, *54* (17), 8396-8400.
127. Vermoortele, F.; Bueken, B.; Le Bars, G.; Van de Voorde, B.; Vandichel, M.; Houthoofd, K.; Vimont, A.; Daturi, M.; Waroquier, M.; Van Speybroeck, V.; Kirschhock, C.; De Vos, D. E.,

- Synthesis Modulation as a Tool To Increase the Catalytic Activity of Metal–Organic Frameworks: The Unique Case of UiO-66(Zr). *J. Am. Chem. Soc.* **2013**, *135* (31), 11465-11468.
128. Wu, H.; Chua, Y. S.; Krungleviciute, V.; Tyagi, M.; Chen, P.; Yildirim, T.; Zhou, W., Unusual and Highly Tunable Missing-Linker Defects in Zirconium Metal–Organic Framework UiO-66 and Their Important Effects on Gas Adsorption. *J. Am. Chem. Soc.* **2013**, *135* (28), 10525-10532.
129. Liang, W.; Coghlan, C. J.; Ragon, F.; Rubio-Martinez, M.; D'Alessandro, D. M.; Babarao, R., Defect engineering of UiO-66 for CO<sub>2</sub> and H<sub>2</sub>O uptake - a combined experimental and simulation study. *Dalton Trans.* **2016**, *45* (11), 4496-4500.
130. Li, B.; Zhu, X.; Hu, K.; Li, Y.; Feng, J.; Shi, J.; Gu, J., Defect creation in metal-organic frameworks for rapid and controllable decontamination of roxarsone from aqueous solution. *J. Hazard. Mater.* **2016**, *302*, 57-64.
131. Wang, K.; Li, C.; Liang, Y.; Han, T.; Huang, H.; Yang, Q.; Liu, D.; Zhong, C., Rational construction of defects in a metal–organic framework for highly efficient adsorption and separation of dyes. *Chem. Eng. J.* **2016**, *289*, 486-493.
132. Ghosh, P.; Colon, Y. J.; Snurr, R. Q., Water adsorption in UiO-66: the importance of defects. *Chem. Commun.* **2014**, *50* (77), 11329-11331.
133. Øien, S.; Wragg, D.; Reinsch, H.; Svelle, S.; Bordiga, S.; Lamberti, C.; Lillerud, K. P., Detailed Structure Analysis of Atomic Positions and Defects in Zirconium Metal–Organic Frameworks. *Cryst. Growth Des.* **2014**, *14* (11), 5370-5372.
134. Bueken, B.; Reinsch, H.; Reimer, N.; Stassen, I.; Vermoortele, F.; Ameloot, R.; Stock, N.; Kirschhock, C. E. A.; De Vos, D., A zirconium squarate metal-organic framework with modulator-dependent molecular sieving properties. *Chem. Commun.* **2014**, *50* (70), 10055-10058.
135. Cliffe, M. J.; Wan, W.; Zou, X.; Chater, P. A.; Kleppe, A. K.; Tucker, M. G.; Wilhelm, H.; Funnell, N. P.; Coudert, F.-X.; Goodwin, A. L., Correlated defect nanoregions in a metal–organic framework. *Nat. Commun.* **2014**, *5*, 4176.
136. Taylor, J. M.; Dekura, S.; Ikeda, R.; Kitagawa, H., Defect Control To Enhance Proton Conductivity in a Metal–Organic Framework. *Chem. Mater.* **2015**, *27* (7), 2286-2289.
137. Cliffe, M. J.; Hill, J. A.; Murray, C. A.; Coudert, F.-X.; Goodwin, A. L., Defect-dependent colossal negative thermal expansion in UiO-66(Hf) metal-organic framework. *Phys. Chem. Chem. Phys.* **2015**, *17* (17), 11586-11592.
138. Deria, P.; Bury, W.; Hod, I.; Kung, C.-W.; Karagiari, O.; Hupp, J. T.; Farha, O. K., MOF Functionalization via Solvent-Assisted Ligand Incorporation: Phosphonates vs Carboxylates. *Inorg. Chem.* **2015**, *54* (5), 2185-2192.
139. Garibay, S. J.; Cohen, S. M., Isoreticular synthesis and modification of frameworks with the UiO-66 topology. *Chem. Commun.* **2010**, *46* (41), 7700-7702.
140. Yee, K.-K.; Reimer, N.; Liu, J.; Cheng, S.-Y.; Yiu, S.-M.; Weber, J.; Stock, N.; Xu, Z., Effective Mercury Sorption by Thiol-Laced Metal–Organic Frameworks: in Strong Acid and the Vapor Phase. *J. Am. Chem. Soc.* **2013**, *135* (21), 7795-7798.
141. Ragon, F.; Campo, B.; Yang, Q.; Martineau, C.; Wiersum, A. D.; Lago, A.; Guillerm, V.; Hemsley, C.; Eubank, J. F.; Vishnuvarthan, M.; Taulelle, F.; Horcajada, P.; Vimont, A.; Llewellyn, P. L.; Daturi, M.; Devautour-Vinot, S.; Maurin, G.; Serre, C.; Devic, T.; Clet, G., Acid-functionalized UiO-66(Zr) MOFs and their evolution after intra-framework cross-linking: structural features and sorption properties. *J. Mater. Chem. A* **2015**, *3* (7), 3294-3309.
142. Yi, X.-C.; Xi, F.-G.; Qi, Y.; Gao, E.-Q., Synthesis and click modification of an azido-functionalized Zr(IV) metal-organic framework and a catalytic study. *RSC Adv.* **2015**, *5* (2), 893-900.



143. Gui, B.; Meng, X.; Chen, Y.; Tian, J.; Liu, G.; Shen, C.; Zeller, M.; Yuan, D.; Wang, C., Reversible Tuning Hydroquinone/Quinone Reaction in Metal–Organic Framework: Immobilized Molecular Switches in Solid State. *Chem. Mater.* **2015**, *27* (18), 6426-6431.
144. Kutzscher, C.; Nickerl, G.; Senkowska, I.; Bon, V.; Kaskel, S., Proline Functionalized UiO-67 and UiO-68 Type Metal–Organic Frameworks Showing Reversed Diastereoselectivity in Aldol Addition Reactions. *Chem. Mater.* **2016**, *28* (8), 2573-2580.
145. Phang, W. J.; Jo, H.; Lee, W. R.; Song, J. H.; Yoo, K.; Kim, B.; Hong, C. S., Superprotonic Conductivity of a UiO-66 Framework Functionalized with Sulfonic Acid Groups by Facile Postsynthetic Oxidation. *Angew. Chem., Int. Ed.* **2015**, *127* (17), 5231-5235.
146. Gonzalez, M. I.; Bloch, E. D.; Mason, J. A.; Teat, S. J.; Long, J. R., Single-Crystal-to-Single-Crystal Metalation of a Metal–Organic Framework: A Route toward Structurally Well-Defined Catalysts. *Inorg. Chem.* **2015**, *54* (6), 2995-3005.
147. Wang, C.; Xie, Z.; deKrafft, K. E.; Lin, W., Doping Metal–Organic Frameworks for Water Oxidation, Carbon Dioxide Reduction, and Organic Photocatalysis. *J. Am. Chem. Soc.* **2011**, *133* (34), 13445-13454.
148. Fei, H.; Sampson, M. D.; Lee, Y.; Kubiak, C. P.; Cohen, S. M., Photocatalytic CO<sub>2</sub> Reduction to Formate Using a Mn(I) Molecular Catalyst in a Robust Metal–Organic Framework. *Inorg. Chem.* **2015**, *54* (14), 6821-6828.
149. Marshall, R. J.; Forgan, R. S., Postsynthetic Modification of Zirconium Metal-Organic Frameworks. *Eur. J. Inorg. Chem.* **2016**, *2016* (27), 4310-4331.
150. Kim, M.; Cahill, J. F.; Fei, H.; Prather, K. A.; Cohen, S. M., Postsynthetic Ligand and Cation Exchange in Robust Metal–Organic Frameworks. *Journal of the American Chemical Society* **2012**, *134* (43), 18082-18088.
151. Karagiari, O.; Bury, W.; Mondloch, J. E.; Hupp, J. T.; Farha, O. K., Solvent-Assisted Linker Exchange: An Alternative to the DeNovo Synthesis of Unattainable Metal–Organic Frameworks. *Angew. Chem., Int. Ed.* **2014**, *53* (18), 4530-4540.
152. Nickerl, G.; Senkowska, I.; Kaskel, S., Tetrazine functionalized zirconium MOF as an optical sensor for oxidizing gases. *Chem. Commun.* **2015**, *51* (12), 2280-2282.
153. Fei, H.; Shin, J.; Meng, Y. S.; Adelhardt, M.; Sutter, J.; Meyer, K.; Cohen, S. M., Reusable Oxidation Catalysis Using Metal-Monocatecholato Species in a Robust Metal–Organic Framework. *J. Am. Chem. Soc.* **2014**, *136* (13), 4965-4973.
154. Fei, H.; Cohen, S. M., Metalation of a Thiocatechol-Functionalized Zr(IV)-Based Metal–Organic Framework for Selective C–H Functionalization. *J. Am. Chem. Soc.* **2015**, *137* (6), 2191-2194.
155. Deria, P.; Chung, Y. G.; Snurr, R. Q.; Hupp, J. T.; Farha, O. K., Water stabilization of Zr6-based metal-organic frameworks via solvent-assisted ligand incorporation. *Chem. Sci.* **2015**.
156. Jiang, J.; Gándara, F.; Zhang, Y.-B.; Na, K.; Yaghi, O. M.; Klemperer, W. G., Superacidity in Sulfated Metal–Organic Framework-808. *J. Am. Chem. Soc.* **2014**, *136* (37), 12844-12847.
157. Puchberger, M.; Kogler, F. R.; Jupa, M.; Gross, S.; Fric, H.; Kickelbick, G.; Schubert, U., Can the Clusters Zr<sub>6</sub>O<sub>4</sub>(OH)<sub>4</sub>(OOCR)<sub>12</sub> and [Zr<sub>6</sub>O<sub>4</sub>(OH)<sub>4</sub>(OOCR)<sub>12</sub>]<sub>2</sub> Be Converted into Each Other? *Eur. J. Inorg. Chem.* **2006**, *2006* (16), 3283-3293.
158. DeCoste, J. B.; Demasky, T. J.; Katz, M. J.; Farha, O. K.; Hupp, J. T., A UiO-66 analogue with uncoordinated carboxylic acids for the broad-spectrum removal of toxic chemicals. *New J. Chem.* **2015**, *39* (4), 2396-2399.
159. Hon Lau, C.; Babarao, R.; Hill, M. R., A route to drastic increase of CO<sub>2</sub> uptake in Zr metal organic framework UiO-66. *Chem. Commun.* **2013**, *49* (35), 3634-3636.
160. Lee, Y.; Kim, S.; Kang, J. K.; Cohen, S. M., Photocatalytic CO<sub>2</sub> reduction by a mixed metal (Zr/Ti), mixed ligand metal-organic framework under visible light irradiation. *Chem. Commun.* **2015**, *51* (26), 5735-5738.

- 
161. Yuan, S.; Chen, Y.-P.; Qin, J.; Lu, W.; Wang, X.; Zhang, Q.; Bosch, M.; Liu, T.-F.; Lian, X.; Zhou, H.-C., Cooperative Cluster Metalation and Ligand Migration in Zirconium Metal–Organic Frameworks. *Angew. Chem., Int. Ed.* **2015**, *54* (49), 14696-14700.
162. Mondloch, J. E.; Bury, W.; Fairen-Jimenez, D.; Kwon, S.; DeMarco, E. J.; Weston, M. H.; Sarjeant, A. A.; Nguyen, S. T.; Stair, P. C.; Snurr, R. Q.; Farha, O. K.; Hupp, J. T., Vapor-Phase Metalation by Atomic Layer Deposition in a Metal–Organic Framework. *J. Am. Chem. Soc.* **2013**, *135* (28), 10294-10297.
163. Klet, R. C.; Wang, T. C.; Fernandez, L. E.; Truhlar, D. G.; Hupp, J. T.; Farha, O. K., Synthetic Access to Atomically Dispersed Metals in Metal–Organic Frameworks via a Combined Atomic-Layer-Deposition-in-MOF and Metal-Exchange Approach. *Chem. Mater.* **2016**, *28* (4), 1213-1219.
164. Kung, C.-W.; Mondloch, J. E.; Wang, T. C.; Bury, W.; Hoffeditz, W.; Klahr, B. M.; Klet, R. C.; Pellin, M. J.; Farha, O. K.; Hupp, J. T., Metal–Organic Framework Thin Films as Platforms for Atomic Layer Deposition of Cobalt Ions To Enable Electrocatalytic Water Oxidation. *ACS Appl. Mater. Interfaces* **2015**, *7* (51), 28223-28230.
165. Meilikhov, M.; Yusenkov, K.; Esken, D.; Turner, S.; Van Tendeloo, G.; Fischer, R. A., Metals@MOFs – Loading MOFs with Metal Nanoparticles for Hybrid Functions. *Eur. J. Inorg. Chem.* **2010**, *2010* (24), 3701-3714.
166. Juan-Alcaniz, J.; Gascon, J.; Kapteijn, F., Metal-organic frameworks as scaffolds for the encapsulation of active species: state of the art and future perspectives. *J. Mater. Chem.* **2012**, *22* (20), 10102-10118.
167. Feng, D.; Jiang, H.-L.; Chen, Y.-P.; Gu, Z.-Y.; Wei, Z.; Zhou, H.-C., Metal–Organic Frameworks Based on Previously Unknown Zr<sub>8</sub>/Hf<sub>8</sub> Cubic Clusters. *Inorg. Chem.* **2013**, *52* (21), 12661-12667.
168. Nguyen, H. G. T.; Schweitzer, N. M.; Chang, C.-Y.; Drake, T. L.; So, M. C.; Stair, P. C.; Farha, O. K.; Hupp, J. T.; Nguyen, S. T., Vanadium-Node-Functionalized UiO-66: A Thermally Stable MOF-Supported Catalyst for the Gas-Phase Oxidative Dehydrogenation of Cyclohexene. *ACS Catal.* **2014**, *4* (8), 2496-2500.
169. Malaestean, I. L.; Speldrich, M.; Ellern, A.; Baca, S. G.; Kogerler, P., Heterometal expansion of oxozirconium carboxylate clusters. *Dalton Trans.* **2011**, *40* (2), 331-333.
170. Katz, M. J.; Moon, S.-Y.; Mondloch, J. E.; Beyzavi, M. H.; Stephenson, C. J.; Hupp, J. T.; Farha, O. K., Exploiting parameter space in MOFs: a 20-fold enhancement of phosphate-ester hydrolysis with UiO-66-NH<sub>2</sub>. *Chem. Sci.* **2015**, *6* (4), 2286-2291.
171. Yang, D.; Bernales, V.; Islamoglu, T.; Farha, O. K.; Hupp, J. T.; Cramer, C. J.; Gagliardi, L.; Gates, B. C., Tuning the Surface Chemistry of Metal Organic Framework Nodes: Proton Topology of the Metal-Oxide-Like Zr<sub>6</sub> Nodes of UiO-66 and NU-1000. *J. Am. Chem. Soc.* **2016**, *138* (46), 15189-15196.
172. Klet, R. C.; Liu, Y.; Wang, T. C.; Hupp, J. T.; Farha, O. K., Evaluation of Bronsted acidity and proton topology in Zr- and Hf-based metal-organic frameworks using potentiometric acid-base titration. *J. Mater. Chem. A* **2016**, *4* (4), 1479-1485.
173. Vermoortele, F.; Vandichel, M.; Van de Voorde, B.; Ameloot, R.; Waroquier, M.; Van Speybroeck, V.; De Vos, D. E., Electronic Effects of Linker Substitution on Lewis Acid Catalysis with Metal–Organic Frameworks. *Angew. Chem., Int. Ed.* **2012**, *51* (20), 4887-4890.
174. Kuwahara, Y.; Kango, H.; Yamashita, H., Catalytic Transfer Hydrogenation of Biomass-Derived Levulinic Acid and Its Esters to  $\gamma$ -Valerolactone over Sulfonic Acid-Functionalized UiO-66. *ACS Sustainable Chem. Eng.* **2017**, *5* (1), 1141-1152.
175. Miao, Z.; Qi, C.; Wensley, A. M.; Luan, Y., Development of a novel Bronsted acid UiO-66 metal-organic framework catalyst by postsynthetic modification and its application in catalysis. *RSC Adv.* **2016**, *6* (71), 67226-67231.
-

- 
176. Qiu, L.-G.; Li, Z.-Q.; Wu, Y.; Wang, W.; Xu, T.; Jiang, X., Facile synthesis of nanocrystals of a microporous metal-organic framework by an ultrasonic method and selective sensing of organoamines. *Chem. Commun.* **2008**, (31), 3642-3644.
177. Zou, X.; Zhu, G.; Hewitt, I. J.; Sun, F.; Qiu, S., Synthesis of a metal-organic framework film by direct conversion technique for VOCs sensing. *Dalton Trans.* **2009**, (16), 3009-3013.
178. Qiu, Y.; Deng, H.; Mou, J.; Yang, S.; Zeller, M.; Batten, S. R.; Wu, H.; Li, J., In situ tetrazole ligand synthesis leading to a microporous cadmium-organic framework for selective ion sensing. *Chem. Commun.* **2009**, (36), 5415-5417.
179. Liu, Y.; Gahungu, G.; Sun, X.; Su, J.; Qu, X.; Wu, Z., Theoretical study on the influence of ancillary and cyclometalated ligands on the electronic structures and optoelectronic properties of heteroleptic iridium(III) complexes. *Dalton Trans.* **2012**, 41 (25), 7595-7603.
180. Aguilera-Sigalat, J.; Bradshaw, D., A colloidal water-stable MOF as a broad-range fluorescent pH sensor via post-synthetic modification. *Chem. Commun.* **2014**, 50 (36), 4711-4713.
181. Yang, J.; Dai, Y.; Zhu, X.; Wang, Z.; Li, Y.; Zhuang, Q.; Shi, J.; Gu, J., Metal-organic frameworks with inherent recognition sites for selective phosphate sensing through their coordination-induced fluorescence enhancement effect. *J. Mater. Chem. A* **2015**, 3 (14), 7445-7452.
182. Xu, X.-Y.; Yan, B., Selective detection and controlled release of Aspirin over fluorescent amino-functionalized metal-organic framework in aqueous solution. *Sens. Actuators, B* **2016**, 230, 463-469.
183. Desai, A. V.; Samanta, P.; Manna, B.; Ghosh, S. K., Aqueous phase nitric oxide detection by an amine-decorated metal-organic framework. *Chem. Commun.* **2015**, 51 (28), 6111-6114.
184. Vellingiri, K.; Boukhvalov, D. W.; Pandey, S. K.; Deep, A.; Kim, K.-H., Luminescent metal-organic frameworks for the detection of nitrobenzene in aqueous media. *Sens. Actuators, B* **2017**, 245, 305-313.
185. Vellingiri, K.; Deep, A.; Kim, K.-H.; Boukhvalov, D. W.; Kumar, P.; Yao, Q., The sensitive detection of formaldehyde in aqueous media using zirconium-based metal organic frameworks. *Sens. Actuators, B* **2017**, 241, 938-948.
186. Nagarkar, S. S.; Saha, T.; Desai, A. V.; Talukdar, P.; Ghosh, S. K., Metal-organic framework based highly selective fluorescence turn-on probe for hydrogen sulphide. *Sci. Rep.* **2014**, 4, 7053.
187. Nagarkar, S. S.; Desai, A. V.; Ghosh, S. K., A Nitro-Functionalized Metal-Organic Framework as a Reaction-Based Fluorescence Turn-On Probe for Rapid and Selective H<sub>2</sub>S Detection. *Chem. - Eur. J.* **2015**, 21 (28), 9994-9997.
188. Li, Y.-A.; Zhao, C.-W.; Zhu, N.-X.; Liu, Q.-K.; Chen, G.-J.; Liu, J.-B.; Zhao, X.-D.; Ma, J.-P.; Zhang, S.; Dong, Y.-B., Nanoscale UiO-MOF-based luminescent sensors for highly selective detection of cysteine and glutathione and their application in bioimaging. *Chem. Commun.* **2015**, 51 (100), 17672-17675.
189. Xu, R.; Wang, Y.; Duan, X.; Lu, K.; Micheroni, D.; Hu, A.; Lin, W., Nanoscale Metal-Organic Frameworks for Ratiometric Oxygen Sensing in Live Cells. *J. Am. Chem. Soc.* **2016**, 138 (7), 2158-2161.
190. Nagarkar, S. S.; Desai, A. V.; Ghosh, S. K., A fluorescent metal-organic framework for highly selective detection of nitro explosives in the aqueous phase. *Chem. Commun.* **2014**, 50 (64), 8915-8918.
191. Yang, N.-N.; Sun, W.; Xi, F.-G.; Sui, Q.; Chen, L.-J.; Gao, E.-Q., Postsynthetic N-methylation making a metal-organic framework responsive to alkylamines. *Chem. Commun.* **2017**, 53 (10), 1747-1750.
192. Carboni, M.; Lin, Z.; Abney, C. W.; Zhang, T.; Lin, W., A Metal-Organic Framework Containing Unusual Eight-Connected Zr-Oxo Secondary Building Units and Orthogonal
-

- Carboxylic Acids for Ultra-sensitive Metal Detection. *Chem. - Eur. J.* **2014**, *20* (46), 14965-14970.
193. Sing, K. S. W., Reporting physisorption data for gas/solid systems with special reference to the determination of surface area and porosity (Recommendations 1984). *Pure Appl. Chem.*, **1985**; *57*, 603.
194. Thommes, M.; Kaneko, K.; Neimark Alexander, V.; Olivier James, P.; Rodriguez-Reinoso, F.; Rouquerol, J.; Sing Kenneth, S. W., Physisorption of gases, with special reference to the evaluation of surface area and pore size distribution (IUPAC Technical Report). *Pure and Appl. Chem.*, **2015**; *87*, 1051.
195. Tanaka, H.; Hiratsuka, T.; Nishiyama, N.; Mori, K.; Miyahara, M. T., Capillary condensation in mesoporous silica with surface roughness. *Adsorption* **2013**, *19* (2), 631-641.
196. Brunauer, S.; Emmett, P. H.; Teller, E., Adsorption of Gases in Multimolecular Layers. *J. Am. Chem. Soc.* **1938**, *60* (2), 309-319.
197. Langmuir, I., The Adsorption of Gases on plane Surfaces of Glass, Mica and Platinum. *J. Am. Chem. Soc.* **1918**, *40* (9), 1361-1403.
198. Langmuir, I., The Constitution and Fundamental Properties of Solids and Liquids. Part I. Solids. *J. Am. Chem. Soc.* **1916**, *38* (11), 2221-2295.
199. Düren, T.; Millange, F.; Férey, G.; Walton, K. S.; Snurr, R. Q., Calculating Geometric Surface Areas as a Characterization Tool for Metal–Organic Frameworks. *J. Phys. Chem. C* **2007**, *111* (42), 15350-15356.
200. Moellmer, J.; Celer, E. B.; Luebke, R.; Cairns, A. J.; Staudt, R.; Eddaoudi, M.; Thommes, M., Insights on Adsorption Characterization of Metal-Organic Frameworks: A Benchmark Study on the Novel soc-MOF. *Microporous Mesoporous Mater.* **2010**, *129* (3), 345-353.
201. Gurvich, L., *J. Phys. Chem. Soc. Russ.* **1915**, *47*, 805-827.
202. Robens, E., Adsorption by powders and porous solids. F. Rouquerol, J. Rouquerol, K. Sing, Academic Press, San Diego 1999, ISBN: 0-12-598920-2, 467 *Vakuum in Forschung und Praxis* **1999**, *11* (3), 191-191.
203. Lippens, B. C.; de Boer, J. H., Studies on pore systems in catalysts. *J. Catal.* **1965**, *4* (3), 319-323.
204. Thomson, W., *Proc. R. Soc. Edinburgh* **1870**, *7*, 63-68.
205. Thomson, W., *Proc. R. Soc. Edinburgh* **1871**, *42*, 448-452.
206. Turner, K., Principles and Practice of Heterogeneous Catalysis By J. M. Thomas and W. J. Thomas. VCH: Weinheim, Germany. 1997. 669 pp. Hardcover: ISBN 3-527-29288-8. ISBN 3-527-29239-X. *Org. Process Res. Dev.* **1997**, *1* (6), 438-438.
207. Barrett, E. P.; Joyner, L. G.; Halenda, P. P., The Determination of Pore Volume and Area Distributions in Porous Substances. I. Computations from Nitrogen Isotherms. *J. Am. Chem. Soc.* **1951**, *73* (1), 373-380.
208. Upstill, C. E.; Evans, R., The surface tension and density profile of simple liquids. *J. Phys. C: Solid State Phys.* **1977**, *10* (15), 2791.
209. Tarazona, P.; Marconi, U. M. B.; Evans, R., Phase equilibria of fluid interfaces and confined fluids. *Mol. Phys.* **1987**, *60* (3), 573-595.
210. Fluids in narrow pores: Adsorption, capillary condensation, and critical points. *J. Chem. Phys.* **1986**, *84* (4), 2376-2399.
211. Evans, R.; Tarazona, P., Theory of Condensation in Narrow Capillaries. *Phys. Rev. Lett.* **1984**, *52* (7), 557-560.
212. ISO-15901-3, Pore size distribution and porosity of solid materials by mercury porosimetry and gas adsorption, Analysis of micropores by gas adsorption. **2007**.

- 
213. Landers, J.; Gor, G. Y.; Neimark, A. V., Density functional theory methods for characterization of porous materials. *Colloids Surf., A* **2013**, *437*, 3-32.
214. Gläser, R.; Weitkamp, J., Surface Hydrophobicity or Hydrophilicity of Porous Solids. In *Handbook of Porous Solids*, Wiley-VCH Verlag GmbH: 2008; pp 395-431.
215. Bragg, W. H.; Bragg, W. L., The Reflection of X-rays by Crystals. *Proc. R. Soc. London, Ser. A* **1913**, *88* (605), 428-438.
216. Massa, W., *Crystal Structure Determination*. Springer, Berlin, Heidelberg: Berlin Heidelberg 2000; p 212.
217. Massa, W., *Kristallstrukturbestimmung*. Vieweg+Teubner Verlag: Wiesbaden, 2011; Vol. 7.
218. Bravais, A., *Abhandlungen über symmetrische Polyeder*. Engelmann, W.: Leipzig, 1890.
219. Bravais, A., *Abhandlung über die Systeme von regelmässig auf einer Ebene oder Raum verteilten Punkten*. Engelmann, W.: Leipzig, 1897.
220. William Henry Bragg, C. H., Max von Laue, *International Tables for Crystallography*. 6th ed.; Springer: 2016; Vol. A: Space-group symmetry.
221. Wyckoff, R. W. G., *The analytical expression of the results of the theory of space-groups* Carnegie Institution of Washington: Washington, 1922.
222. Winn, M. D.; Ballard, C. C.; Cowtan, K. D.; Dodson, E. J.; Emsley, P.; Evans, P. R.; Keegan, R. M.; Krissinel, E. B.; Leslie, A. G. W.; McCoy, A.; McNicholas, S. J.; Murshudov, G. N.; Pannu, N. S.; Potterton, E. A.; Powell, H. R.; Read, R. J.; Vagin, A.; Wilson, K. S., Overview of the CCP4 suite and current developments. *Acta Crystallogr., Sect. D: Biol. Crystallogr.* **2011**, *67* (Pt 4), 235-242.
223. Cie, S. *X-Area*, Stoe & Cie: Darmstadt, Germany, 2002.
224. Sheldrick, G. M. *XPREP*, Bruker AXS Inc.: Madison, Wisconsin, USA, 2005.
225. Harker, D.; Kasper, J. S., Phases of Fourier coefficients directly from crystal diffraction data. *Acta Crystallogr.* **1948**, *1* (2), 70-75.
226. Sayre, D., The squaring method: a new method for phase determination. *Acta Crystallogr.* **1952**, *5* (1), 60-65.
227. Sheldrick, G. M. *SHELXS-97*, University of Göttingen: Germany, 1997.
228. Sheldrick, G. M. *SHELXL-97*, University of Göttingen: Germany, 1997.
229. van der Sluis, P.; Spek, A. L., BYPASS: an effective method for the refinement of crystal structures containing disordered solvent regions. *Acta Crystallogr., Sect. A: Found. Crystallogr.* **1990**, *46* (3), 194-201.
230. Vitalij Pecharsky, P. Z., *Fundamentals of Powder Diffraction and Structural Characterization of Materials, Second Edition*. Springer US: 2009.
231. Data, I. C. f. D. *ICDD (20xx). PDF-4+ 20xx (Database)*, International Centre for Diffraction Data: Newtown Square, PA, USA.
232. Merkys, A.; Vaitkus, A.; Butkus, J.; Okulič-Kazarinas, M.; Kairys, V.; Gražulis, S., COD::CIF::Parser: an error-correcting CIF parser for the Perl language. *J. Appl. Crystallogr.* **2016**, *49* (Pt 1), 292-301.
233. Gražulis, S.; Merkys, A.; Vaitkus, A.; Okulič-Kazarinas, M., Computing stoichiometric molecular composition from crystal structures. *J. Appl. Crystallogr.* **2015**, *48* (Pt 1), 85-91.
234. Gražulis, S.; Daškevič, A.; Merkys, A.; Chateigner, D.; Lutterotti, L.; Quirós, M.; Serebryanaya, N. R.; Moeck, P.; Downs, R. T.; Le Bail, A., Crystallography Open Database (COD): an open-access collection of crystal structures and platform for world-wide collaboration. *Nucleic Acids Res.* **2012**, *40* (Database issue), D420-D427.
-

- 
235. Gražulis, S.; Chateigner, D.; Downs, R. T.; Yokochi, A. F. T.; Quirós, M.; Lutterotti, L.; Manakova, E.; Butkus, J.; Moeck, P.; Le Bail, A., Crystallography Open Database – an open-access collection of crystal structures. *J. Appl. Crystallogr.* **2009**, *42* (Pt 4), 726-729.
236. Downs, R. T. B., K. L.; Gibbs, G. V.; Boisen, M. B., Interactive software for calculating and displaying X-ray or neutron powder diffractometer patterns of crystalline materials. *Am. Mineral.* **1993**, *78*, 1104-1107.
237. Le Bail, A., Inorganic structure prediction with GRINSP. *J. Appl. Crystallogr.* **2005**, *38* (2), 389-395.
238. Caglioti, G.; Paoletti, A.; Ricci, F. P., Choice of collimators for a crystal spectrometer for neutron diffraction. *Nucl. Instrum.* **1958**, *3* (4), 223-228.
239. Boultif, A.; Louër, D., Powder pattern indexing with the dichotomy method. *J. Appl. Crystallogr.* **2004**, *37* (5), 724-731.
240. Werner, P. E.; Eriksson, L.; Westdahl, M., TREOR, a semi-exhaustive trial-and-error powder indexing program for all symmetries. *J. Appl. Crystallogr.* **1985**, *18* (5), 367-370.
241. Inc., A. S. *Materials Studio 2008*; Accelrys Software Inc. : San Diego, 2001-2011.
242. Pawley, G., Unit-cell refinement from powder diffraction scans. *J. Appl. Crystallogr.* **1981**, *14* (6), 357-361.
243. Le Bail, A.; Duroy, H.; Fourquet, J. L., Ab-initio structure determination of LiSbWO<sub>6</sub> by X-ray powder diffraction. *Mater. Res. Bull.* **1988**, *23* (3), 447-452.
244. Rietveld, H., A profile refinement method for nuclear and magnetic structures. *J. Appl. Crystallogr.* **1969**, *2* (2), 65-71.
245. Dr. J. K. Cockcroft, P. P. B., Dr. M. P. Attfield, and others, Advanced Certificate in Powder Diffraction on the Web. <http://pd.chem.ucl.ac.uk/pdnn/solve1/leball.htm> (accessed 30.06.2017).
246. Drache, F.; Bon, V.; Senkovska, I.; Adam, M.; Eychmüller, A.; Kaskel, S., Vapochromic Luminescence of a Zirconium-Based Metal–Organic Framework for Sensing Applications. *Eur. J. Inorg. Chem.* **2016**, *2016* (27), 4483-4489.
247. Drache, F.; Bon, V.; Senkovska, I.; Getzschmann, J.; Kaskel, S., The modulator driven polymorphism of Zr(IV) based metal–organic frameworks. *Philos. Trans. R. Soc., A*, **2017**, 375 (2084).
248. Drache, F.; Bon, V.; Senkovska, I.; Marschelke, C.; Synytska, A.; Kaskel, S., Postsynthetic Inner-Surface Functionalization of the Highly Stable Zirconium-Based Metal–Organic Framework DUT-67. *Inorg. Chem.* **2016**, *55* (15), 7206-7213.
249. Maciej Haranczyk, C. H. R., Thomas F. Willems, Richard L. Martin, Marielle Pinheiro, Christopher Oustrouchov, Berend Smit, Andrew J. Jones, Enrique Iglesia, Daniel Holden, Kim Jelfs, Michael Deem *Zeo++*, Computational Research Division of the Lawrence Berkeley National laboratory 2013.
250. Boultif, A.; Louer, D., Indexing of powder diffraction patterns for low-symmetry lattices by the successive dichotomy method. *J. Appl. Crystallogr.* **1991**, *24* (6), 987-993.
251. *Material Studio 5.0*, Accelrys Software Inc.: San Diego, USA, 2009.
252. Blatov, V. A.; Shevchenko, A. P.; Proserpio, D. M., Applied Topological Analysis of Crystal Structures with the Program Package ToposPro. *Cryst. Growth Des.* **2014**, *14* (7), 3576-3586.
253. O’Keefe, M.; Peskov, M. A.; Ramsden, S. J.; Yaghi, O. M., The Reticular Chemistry Structure Resource (RCSR) Database of, and Symbols for, Crystal Nets. *Acc. Chem. Res.* **2008**, *41* (12), 1782-1789.
254. Willems, T. F.; Rycroft, C. H.; Kazi, M.; Meza, J. C.; Haranczyk, M., Algorithms and tools for high-throughput geometry-based analysis of crystalline porous materials. *Microporous Mesoporous Mater.* **2012**, *149* (1), 134-141.
-

- 
255. Wu, T.; Shen, L.; Luebbbers, M.; Hu, C.; Chen, Q.; Ni, Z.; Masel, R. I., Enhancing the stability of metal-organic frameworks in humid air by incorporating water repellent functional groups. *Chem. Commun.* **2010**, 46 (33), 6120-6122.
256. Suto, M.; Wang, X.; Lee, L. C., Fluorescence yields from photodissociative excitation of formic acid, methyl formate, and acetic acid in the vacuum-ultraviolet region. *J. Phys. Chem.* **1988**, 92 (13), 3764-3768.
257. Sjöback, R.; Nygren, J.; Kubista, M., Absorption and fluorescence properties of fluorescein. *Spectrochim. Acta, Part A* **1995**, 51 (6), L7-L21.
258. Hammett, L. P.; Deyrup, A. J., A Series of simple basic Indicators. I The Acidity Functions of Mixtures of Sulphuric and Perchloric Acids with Water. *J. Am. Chem. Soc.* **1932**, 54 (7), 2721-2739.
259. Walling, C., The Acid Strength of Surfaces. *J. Am. Chem. Soc.* **1950**, 72 (3), 1164-1168.
260. Holm, V. C. F.; Bailey, G. C.; Clark, A., Acidity Studies of Silica-Alumina Catalysts. *J. Phys. Chem.* **1959**, 63 (2), 129-133.
261. Winoto, H. P.; Ahn, B. S.; Jae, J., Production of  $\gamma$ -valerolactone from furfural by a single-step process using Sn-Al-Beta zeolites: Optimizing the catalyst acid properties and process conditions. *J. Ind. Eng. Chem.* **2016**, 40, 62-71.
262. Zhu, S.; Xue, Y.; Guo, J.; Cen, Y.; Wang, J.; Fan, W., Integrated Conversion of Hemicellulose and Furfural into  $\gamma$ -Valerolactone over Au/ZrO<sub>2</sub> Catalyst Combined with ZSM-5. *ACS Catal.* **2016**, 6 (3), 2035-2042.
263. Gürbüz, E. I.; Gallo, J. M. R.; Alonso, D. M.; Wettstein, S. G.; Lim, W. Y.; Dumesic, J. A., Conversion of Hemicellulose into Furfural Using Solid Acid Catalysts in  $\gamma$ -Valerolactone. *Angew. Chem., Int. Ed.* **2013**, 52 (4), 1270-1274.
264. Verley, A., Exchange of functional groups between two molecules. Exchange of alcohol and aldehyde groups. *Bull. Soc. Chim. Fr.* **1925**, 37, 537-542.
265. Meerwein, H.; Schmidt, R., Ein neues Verfahren zur Reduktion von Aldehyden und Ketonen. *Justus Liebigs Ann. Chem.* **1925**, 444 (1), 221-238.
266. Ponndorf, W., Der reversible Austausch der Oxydationsstufen zwischen Aldehyden oder Ketonen einerseits und primären oder sekundären Alkoholen andererseits. *Angew. Chem.* **1926**, 39 (5), 138-143.
267. Benesi, H. A., Acidity of Catalyst Surfaces. II. Amine Titration Using Hammett Indicators. *J. Phys. Chem.* **1957**, 61 (7), 970-973.
268. Benesi, H. A., Acidity of Catalyst Surfaces. I. Acid Strength from Colors of Adsorbed Indicators. *J. Am. Chem. Soc.* **1956**, 78 (21), 5490-5494.
269. Komanoya, T.; Nakajima, K.; Kitano, M.; Hara, M., Synergistic Catalysis by Lewis Acid and Base Sites on ZrO<sub>2</sub> for Meerwein-Ponndorf-Verley Reduction. *J. Phys. Chem. C* **2015**, 119 (47), 26540-26546.
270. Corma, A.; Domine, M. E.; Valencia, S., Water-resistant solid Lewis acid catalysts: Meerwein-Ponndorf-Verley and Oppenauer reactions catalyzed by tin-beta zeolite. *J. Catal.* **2003**, 215 (2), 294-304.
271. Corma, A.; Domine, M. E.; Nemeth, L.; Valencia, S., Al-Free Sn-Beta Zeolite as a Catalyst for the Selective Reduction of Carbonyl Compounds (Meerwein-Ponndorf-Verley Reaction). *J. Am. Chem. Soc.* **2002**, 124 (13), 3194-3195.
272. Koehle, M.; Lobo, R. F., Lewis acidic zeolite Beta catalyst for the Meerwein-Ponndorf-Verley reduction of furfural. *Catal. Sci. Technol.* **2016**, 6 (9), 3018-3026.
273. van der Waal, J. C.; Creighton, E. J.; Kunkeler, P. J.; Tan, K.; van Bekkum, H., Beta-type zeolites as selective and regenerable catalysts in the Meerwein-Ponndorf-Verley reduction of carbonyl compounds. *Top. Catal.* **1997**, 4 (3), 261-268.
-

274. Wang, J.; Okumura, K.; Jaenicke, S.; Chuah, G.-K., Post-synthesized zirconium-containing Beta zeolite in Meerwein–Ponndorf–Verley reduction: Pros and cons. *Appl. Catal., A* **2015**, *493*, 112-120.
275. Heidari, H.; Abedini, M.; Nemati, A.; Amini, M. M., Nanocrystalline Magnesium Oxide as a Versatile Heterogeneous Catalyst for the Meerwein–Ponndorf–Verley Reduction of Cyclohexanone into Cyclohexanol: Effect of Preparation Method of Magnesium Oxide on Yield. *Catal. Lett.* **2009**, *130* (1), 266-270.
276. Li, G.; Fu, W. H.; Wang, Y. M., Meerwein–Ponndorf–Verley reduction of cyclohexanone catalyzed by partially crystalline zirconosilicate. *Catal. Commun.* **2015**, *62*, 10-13.
277. Zhao, Z.; Liu, Y.; Wu, H.; Li, X.; He, M.; Wu, P., Hydrothermal synthesis of mesoporous zirconosilicate with enhanced textural and catalytic properties with the aid of amphiphilic organosilane. *Microporous Mesoporous Mater.* **2009**, *123* (1–3), 324-330.
278. Iglesias, J.; Melero, J.; Morales, G.; Moreno, J.; Segura, Y.; Paniagua, M.; Cambra, A.; Hernández, B., Zr-SBA-15 Lewis Acid Catalyst: Activity in Meerwein Ponndorf Verley Reduction. *Catalysts* **2015**, *5* (4), 1911.
279. Gong, Q.; Hu, Z.; Deibert, B. J.; Emge, T. J.; Teat, S. J.; Banerjee, D.; Mussman, B.; Rudd, N. D.; Li, J., Solution Processable MOF Yellow Phosphor with Exceptionally High Quantum Efficiency. *J. Am. Chem. Soc.* **2014**, *136* (48), 16724-16727.
280. Kobayashi, T.; Nagakura, S., Picosecond time-resolved spectroscopy and the intersystem crossing rates of anthrone and fluorenone. *Chem. Phys. Lett.* **1976**, *43* (3), 429-434.
281. Andrews, L. J.; Derouede, A.; Linschitz, H., Photophysical processes in fluorenone. *J. Phys. Chem.* **1978**, *82* (21), 2304-2309.
282. Kandasamy, M.; Velraj, G.; Kalaichelvan, S., Vibrational spectra, NMR and HOMO–LUMO analysis of 9-fluorenone-2-carboxylic acid. *Spectrochim. Acta, Part A* **2013**, *105*, 176-183.
283. Zwarich, R.; Bree, A., A study of the excited electronic states of 9-fluorenone. *J. Mol. Spectrosc.* **1974**, *52* (3), 329-343.
284. Furman, J. D.; Warner, A. Y.; Teat, S. J.; Mikhailovsky, A. A.; Cheetham, A. K., Tunable, Ligand-Based Emission from Inorganic–Organic Frameworks: A New Approach to Phosphors for Solid State Lighting and Other Applications. *Chem. Mater.* **2010**, *22* (7), 2255-2260.
285. Furman, J. D.; Melot, B. C.; Teat, S. J.; Mikhailovsky, A. A.; Cheetham, A. K., Towards enhanced ligand-centred photoluminescence in inorganic-organic frameworks for solid state lighting. *Phys. Chem. Chem. Phys.* **2011**, *13* (17), 7622-7629.
286. Ko, N.; Hong, J.; Sung, S.; Cordova, K. E.; Park, H. J.; Yang, J. K.; Kim, J., A significant enhancement of water vapour uptake at low pressure by amine-functionalization of UiO-67. *Dalton Trans.* **2015**, *44* (5), 2047-2051.
287. Yan, D.; Gao, R.; Wei, M.; Li, S.; Lu, J.; Evans, D. G.; Duan, X., Mechanochemical synthesis of a fluorenone-based metal organic framework with polarized fluorescence: an experimental and computational study. *J. Mater. Chem. C* **2013**, *1* (5), 997-1004.
288. Yuan, M.-S.; Wang, D.-E.; Xue, P.; Wang, W.; Wang, J.-C.; Tu, Q.; Liu, Z.; Liu, Y.; Zhang, Y.; Wang, J., Fluorenone Organic Crystals: Two-Color Luminescence Switching and Reversible Phase Transformations between  $\pi$ – $\pi$  Stacking-Directed Packing and Hydrogen Bond-Directed Packing. *Chem. Mater.* **2014**, *26* (7), 2467-2477.
289. Mahmoud, R.; Rogalska, E.; Solimando, R.; Rogalski, M., Stacking phenomena in polyaromatic compounds. *Thermochim. Acta* **1999**, *325* (2), 119-124.
290. Wang, H.; Yang, J.; Sun, J.; Xu, Y.; Wu, Y.; Dong, Q.; Wong, W.-Y.; Hao, Y.; Zhang, X.; Li, H., Optical and Electroluminescent Studies of White-Light-Emitting Copolymers Based on Poly(9,9-dioctylfluorene) and Fluorenone Derivatives. *Macromol. Chem. Phys.* **2014**, *215* (11), 1060-1067.



---

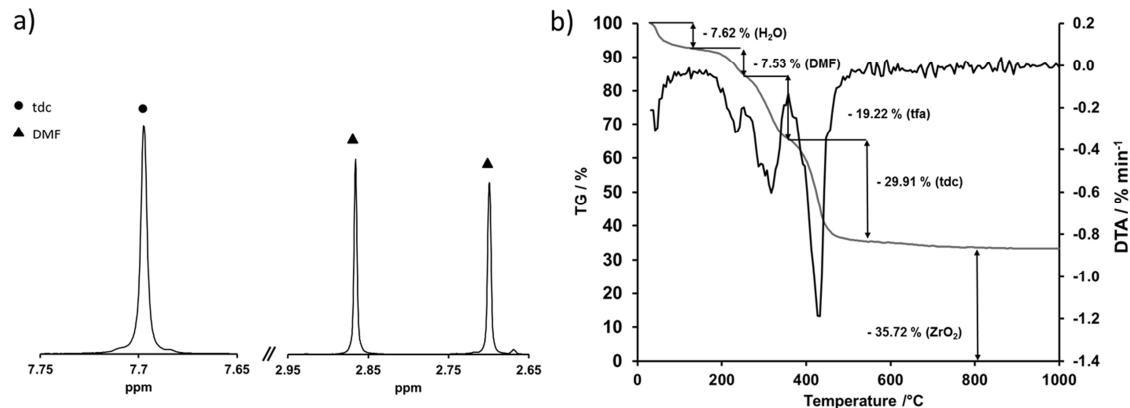
**8. LIST OF ABBREVIATIONS**

Ac	Acetate
Ar	Aryl
Ba	Benzoate
BASF	Badische Anilin und Soda Fabrik
BDC	1,4-Benzenedicarboxylate
BET	Brunnauer-Emmet-Teller
Bipy	2,2'-Bipyridine-5,5'-dicarboxylate
BJH	Barrett-Joyner-Halenda
Bpdc	Biphenyldicarboxylate
BTC	1,3,5-Benzene-tricarboxylate
Dabco	1,4-Diazabicyclo[2.2.2]octane
DFT	Density Functional Theory
DMF	N,N-Dimethylformamide
DMNP	Dimethyl 4-nitrophenyl phosphate
DMSO	Dimethyl sulfoxide
dttdc	Dithieno[3,2-b;2',3'-d]-thiophene-2,6-dicarboxylate
DUT	Dresden University of Technology
EA	Elemental Analysis
EN	Electronegativity
eq	equivalents
Fa	Formate
fdc	9-Fluorenone-2,7-dicarboxylate
FWHM	Full Width at Half-Maximum
GC-MS	Gas Chromatography-Mass Spectroscopy
HKUST	Hong Kong University of Science and Technology
HOMO	Highest Occupied Molecular Orbitals
HPLC	High-Performance Liquid Chromatography
IR	Infrared

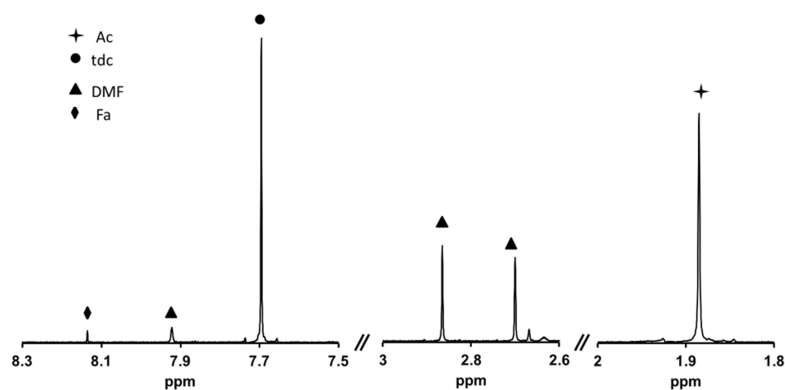
IRMOF	Isoreticular Metal-Organic Framework
IUPAC	International Union of Pure and Applied Chemistry
La	Lactic acid
LED	Light Emitting Diode
LMCT	Ligand-to-Metal Charge Transfer
LUMO	Lowest Unoccupied Molecular Orbitals
Ma	Mandelic acid
MIL	Materials of Institute Lavoisier
MLCT	Metal-to-Ligand Charge Transfer
MOF	Metal-Organic Framework
MPV	Meerwein-Ponndorf-Verley
NLDFT	Non-Local-Density Functional Theory
NMP	N-Methyl-2-pyrrolidone
NMR	Nuclear Magnetic Resonance
NU	Northwestern University
Pa	Propionate
PCN	Porous Coordination Network
Pfba	Pentafluorobenzoate
Pfoa	Perfluorooctanoate
ppb	parts per billion
ppm	parts per million
PSM	Post-Synthetic Modification
PXRD	Powder-X-ray Diffraction
QSDFT	Quenched Solid Density Functional Theory
RCSR	Reticular Chemistry Structure Resource
RH	Relative Humidity
RT	Room Temperature
SALE	Solvent Assisted Linker Exchange
SBA	Santa Barbara Amorphous type material
SBU	Secondary Building Unit

SEM	Scanning Electron Microscopy
SSA	Specific Surface Area
STP	Standard Temperature and Pressure
Ta	Tartaric acid
Tdc	2,5-Thiophenedicarboxylate
Tfa	Trifluoroacetic acid
Tfmba	4-(Trifluoromethyl)benzoate
TG/DTA	Thermogravimetry/Differential Thermal Analysis
TNP	2,4,6-Trinitrophenol
TOF	Turnover Frequency
UiO	University of Oslo
UMCM	University of Michigan Crystalline Material
UV/Vis	Ultraviolet-Visible Spectroscopy
ZIF	Zeolitic Imidazolate Framework

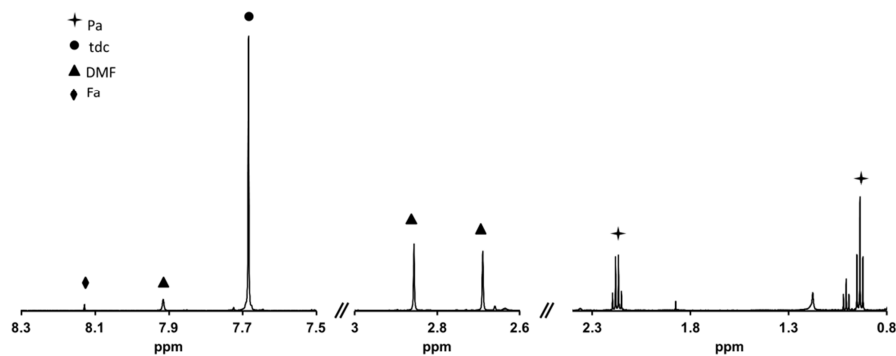
## 9. APPENDIX



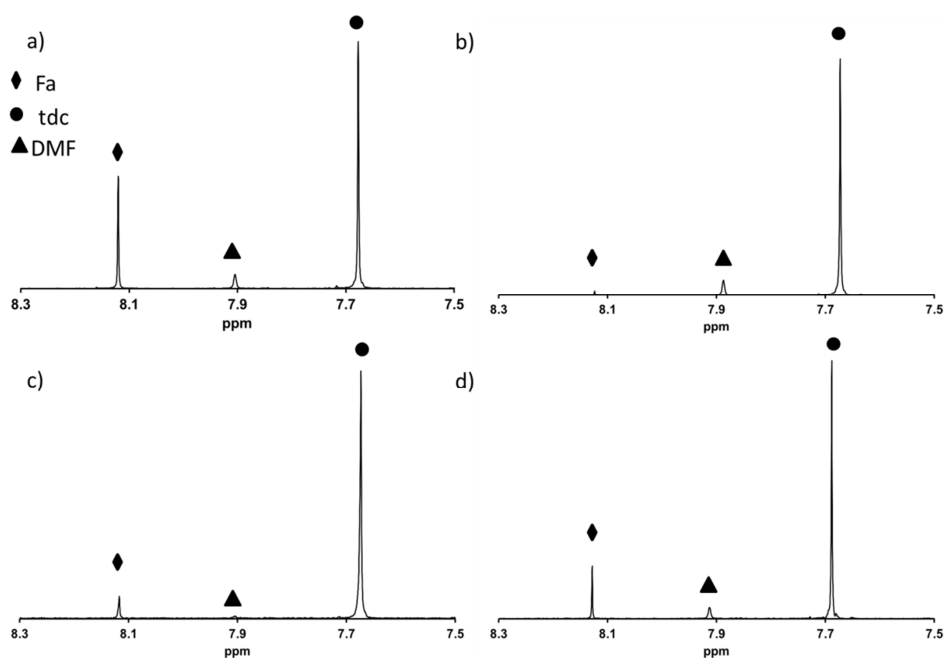
FigureA 1 a)  $^1\text{H-NMR}$  spectrum of DUT-126. b) TG/DTA analysis in air of the dried phase of DUT-126.



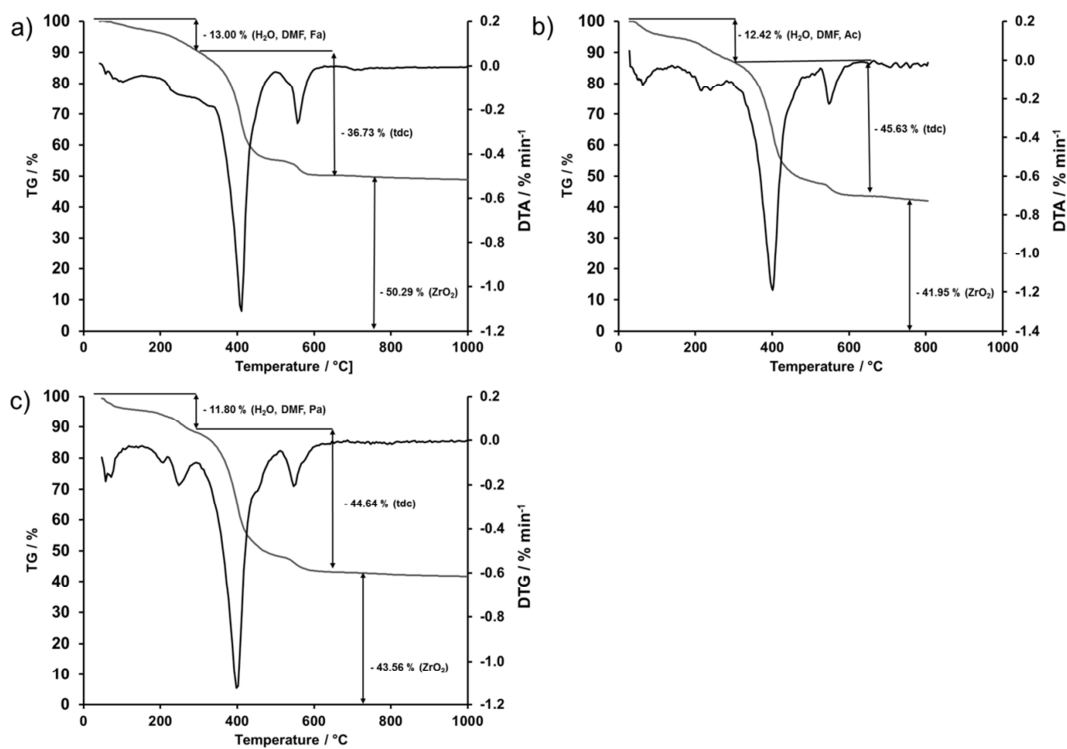
FigureA 2. Detail of the  $^1\text{H-NMR}$  spectra of DUT-67-Ac.  $^1\text{H-NMR}$ : (DMSO/ $\text{DCl}$ ):  $\delta/\text{ppm} = 1.89$  (s, 3H, Ac),  $\delta/\text{ppm} = 7.68$  (s, 2H, tdc),  $\delta/\text{ppm} = 2.85, 2.68$  (s, 3H, DMF),  $\delta/\text{ppm} = 7.9$  (s, 1H, DMF),  $\delta/\text{ppm} = 8.12$  (s, 1H, Fa).



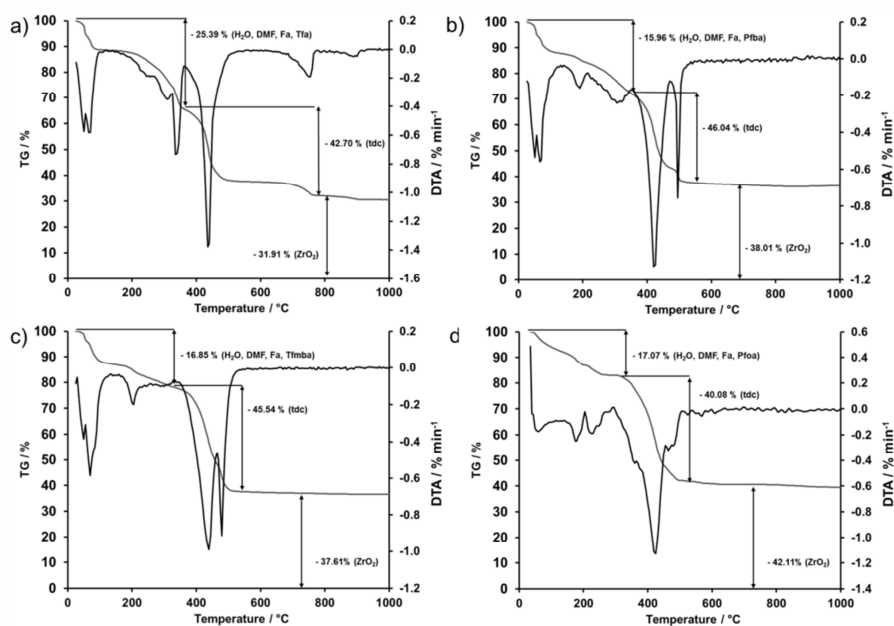
FigureA 3. Detail of the  $^1\text{H-NMR}$  spectra of DUT-67-Pa.  $^1\text{H-NMR}$ : (DMSO/ $\text{DCl}$ ):  $\delta/\text{ppm} = 0.94$  (t, 3H, Pa),  $\delta/\text{ppm} = 2.17$  (q, 2H, Pa),  $\delta/\text{ppm} = 7.68$  (s, 2H, tdc),  $\delta/\text{ppm} = 2.85, 2.68$  (s, 3H, DMF),  $\delta/\text{ppm} = 7.9$  (s, 1H, DMF),  $\delta/\text{ppm} = 8.12$  (s, 1H, Fa).



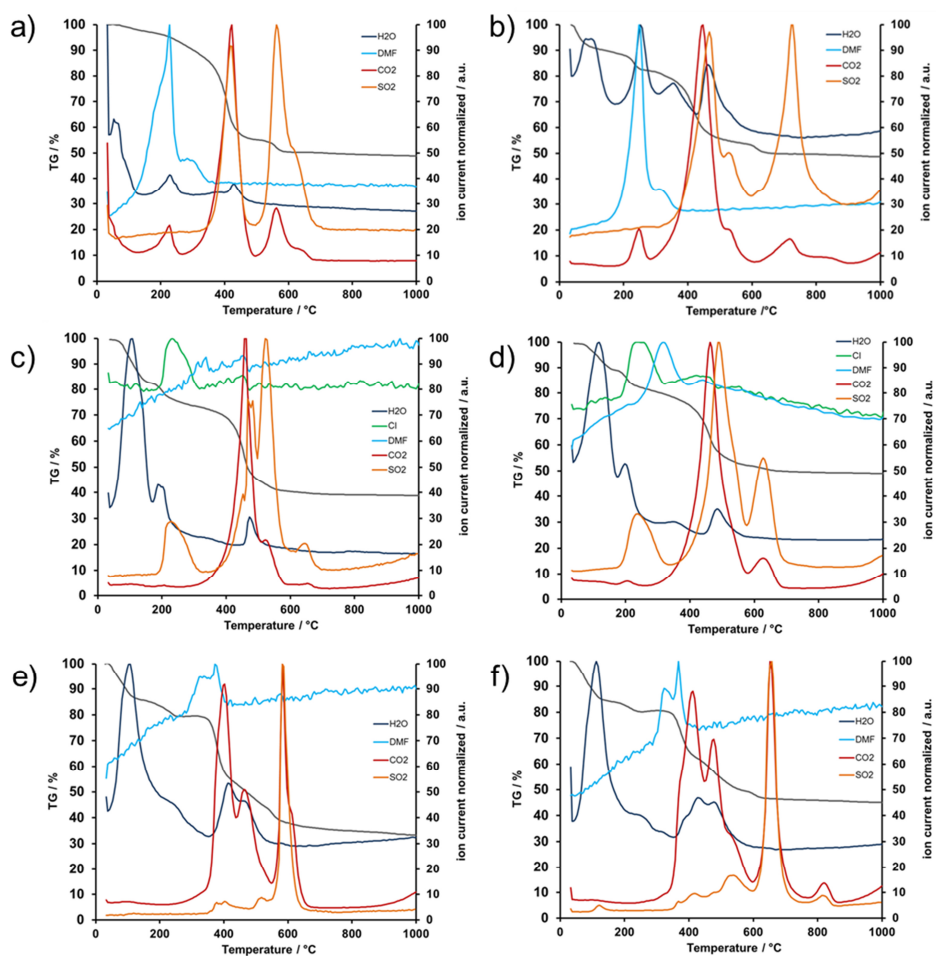
**Figure A 4.** Detail of the  $^1\text{H-NMR}$  spectra of a) DUT-67-Fa, b) DUT-67-Tfa, c) DUT-67-Pfba and d) DUT-67-Pfoa. After the exchange of formate with fluorinated ligands, the signal of formate is significantly reduced.  $^1\text{H-NMR}$  (DMSO/ $D_2O$ ):  $\delta/\text{ppm} = 8.12$  (s, 1H, Fa),  $\delta/\text{ppm} = 7.68$  (s, 2H, tdc),  $\delta/\text{ppm} = 7.9$  (s, 1H, DMF).



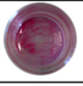
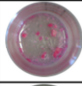
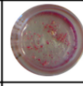
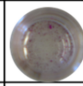
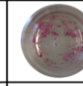
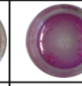
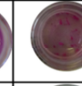
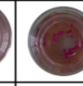
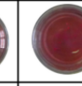
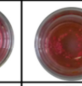
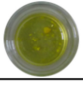
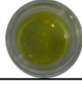

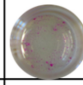
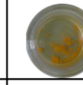
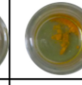
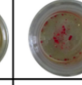
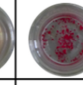
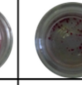
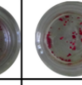



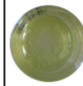
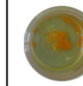
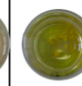
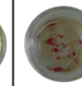
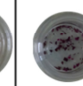
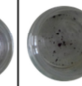
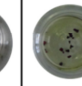



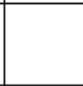
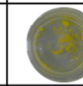
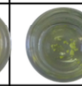
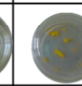
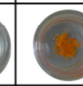
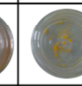
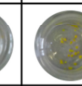










**Figure A 5.** TG analysis (grey line) and DTA analysis (black line) in air of a) DUT-67-Fa, b) DUT-67-Ac and c) DUT-67-Pa activated at 120 °C.



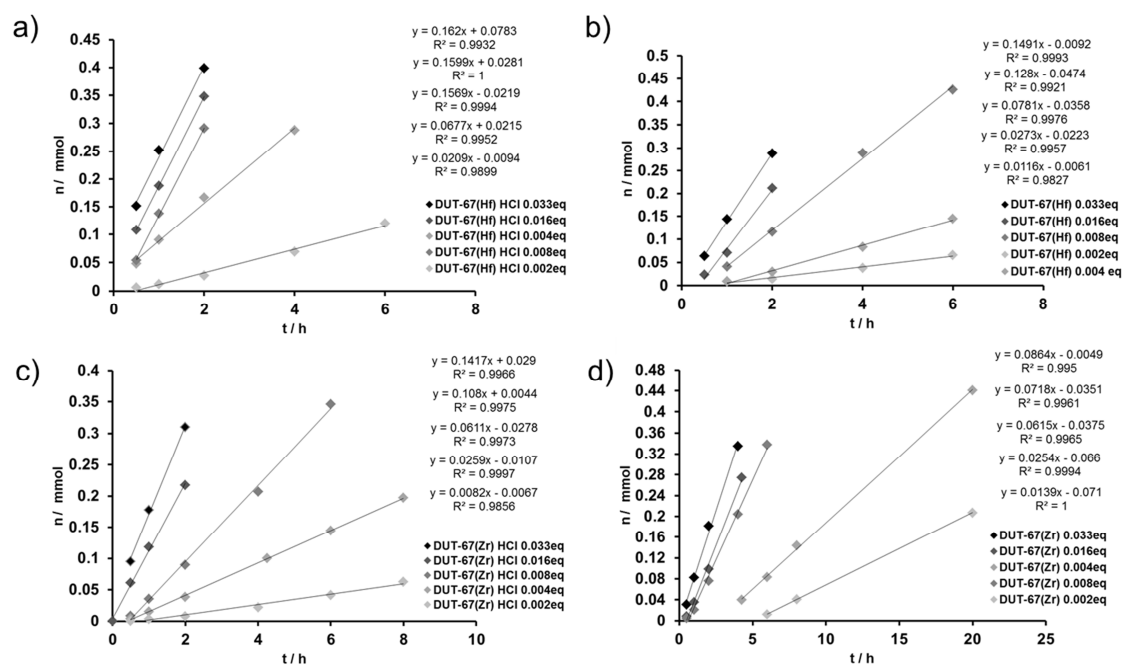
**Figure 6.** TG analysis (grey line) and DTA analysis (black line) in air of a) DUT-67-Tfa, b) DUT-67-Pfba c) DUT-67-Tfmba and d) DUT-67-Pfoa activated at 100 °C.



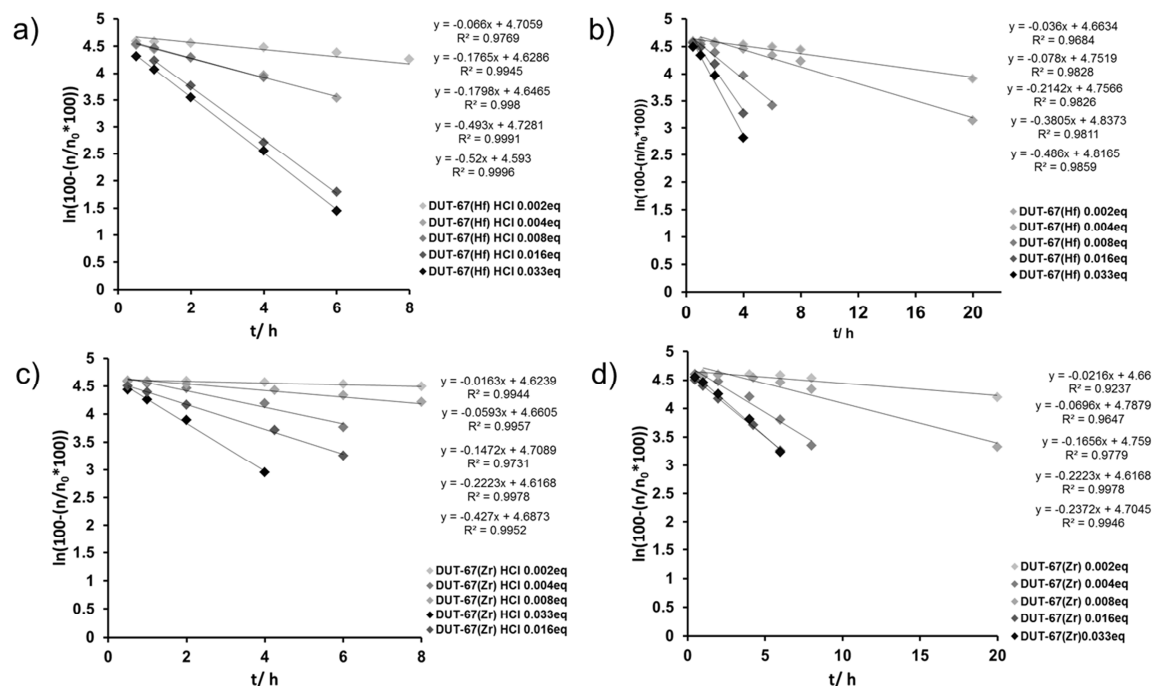
**Figure 7.** TG-MS analysis in air of a) DUT-67(Zr) and b) DUT-67(Hf) containing formate as modulator, of c) DUT-67(Zr)\_HCl, d) DUT-67(Hf)\_HCl, e) DUT-67(Zr)\_H<sub>2</sub>SO<sub>4</sub> and f) DUT-67(Hf)\_H<sub>2</sub>SO<sub>4</sub>.

Hammett indicator	pK <sub>a</sub>	UIO-66	UIO-67	DUT-51(Zr)	DUT-126(Zr)	DUT-67(Zr)	DUT-67(Hf)	DUT-67(Zr) HCl	DUT-67(Hf) HCl	DUT-67(Zr) H <sub>2</sub> SO <sub>4</sub>	DUT-67(Hf) H <sub>2</sub> SO <sub>4</sub>
Neutral red	+ 6.8										
Dimethyl yellow	+ 3.3										
Benzeneazo-diphenylamine	+ 1.5										
Dicinnamal-acetone	- 3										
Anthraquinone	- 8.2										

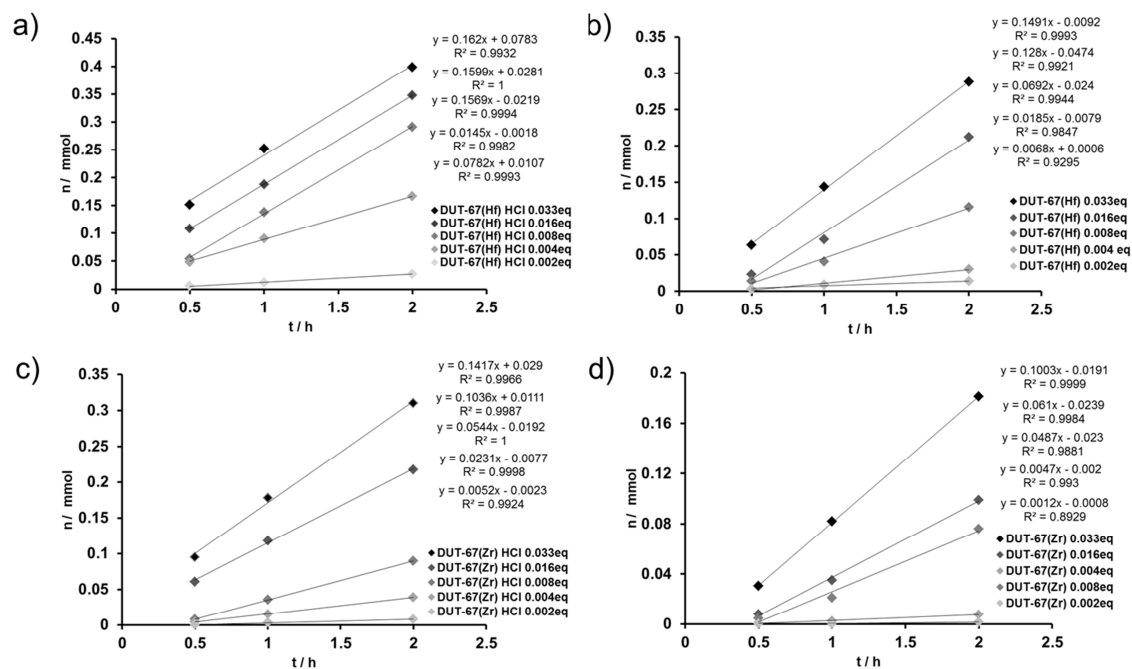
FigureA 8. Colours of various Zr- and Hf-based MOFs with adsorbed Hammet indicators.



FigureA 9. Fitting plots for the pseudo zero order kinetics of a) DUT-67(Hf)\_HCl, b) DUT-67(Hf), c) DUT-67(Zr)\_HCl and d) DUT-67(Zr).

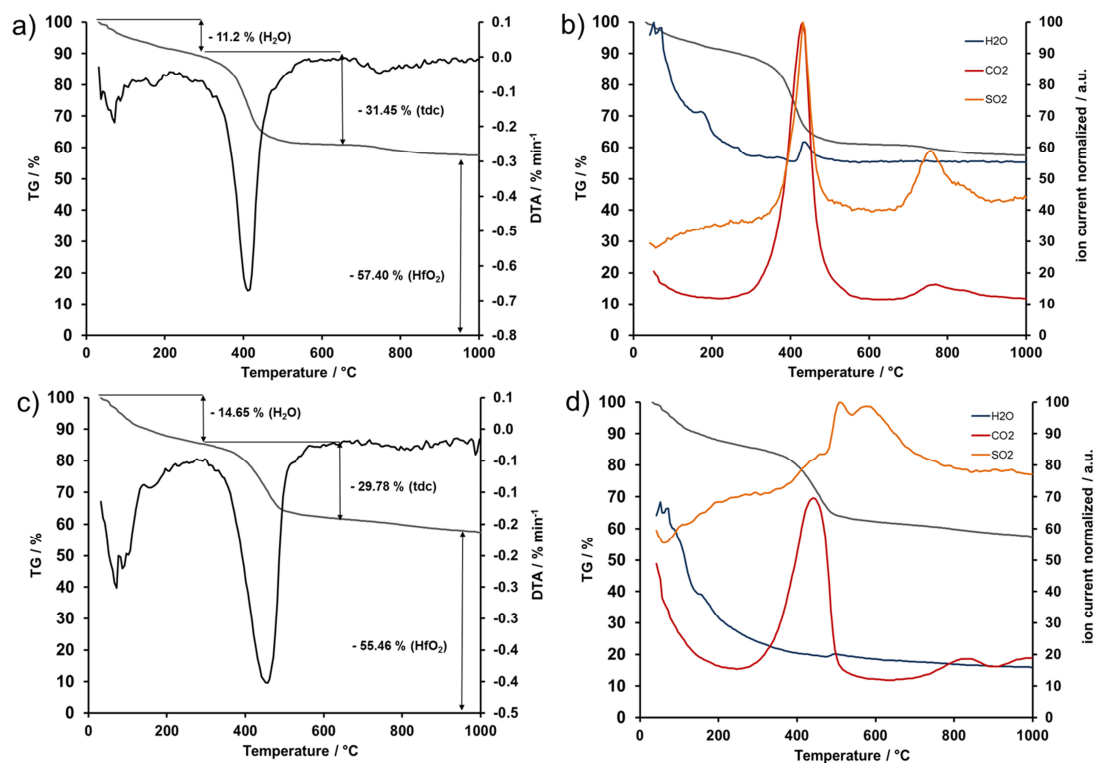


**FigureA 10.** Fitting plots for the pseudo first order kinetics of a) DUT-67(Hf)\_HCl, b) DUT-67(Hf), c) DUT-67(Zr)\_HCl and d) DUT-67(Zr).

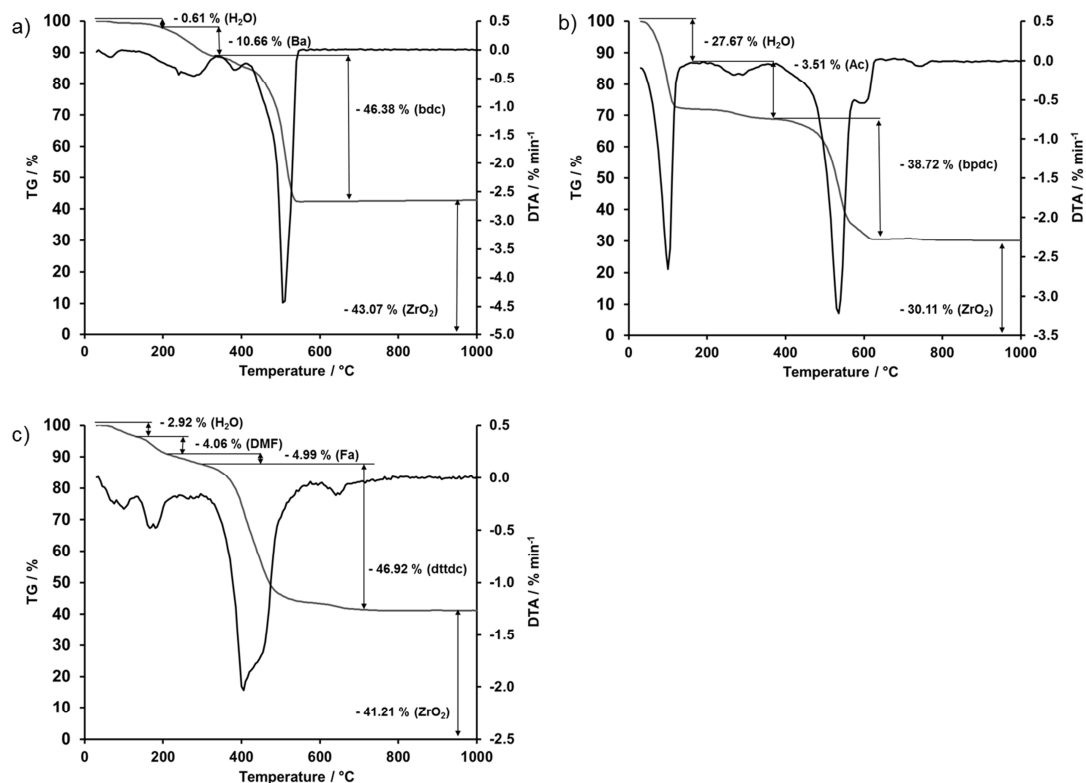


**FigureA 11.** Fitting plots of the initial rate constants of a) DUT-67(Hf)\_HCl, b) DUT-67(Hf), c) DUT-67(Zr)\_HCl and d) DUT-67(Zr).

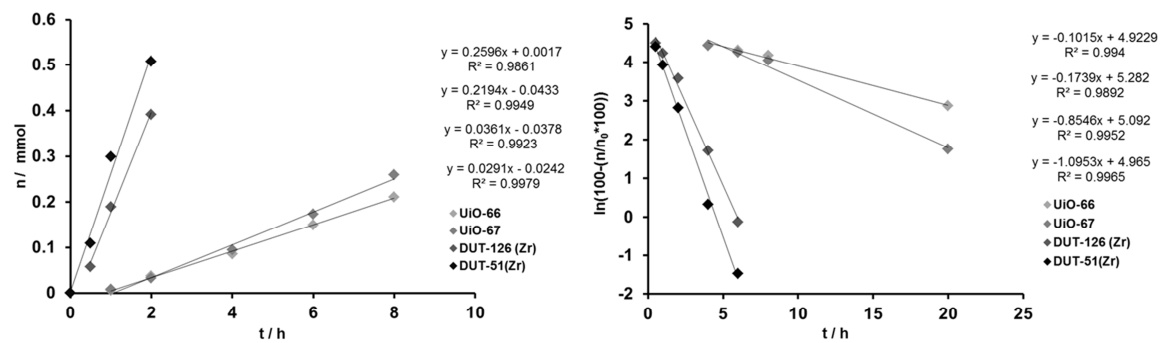




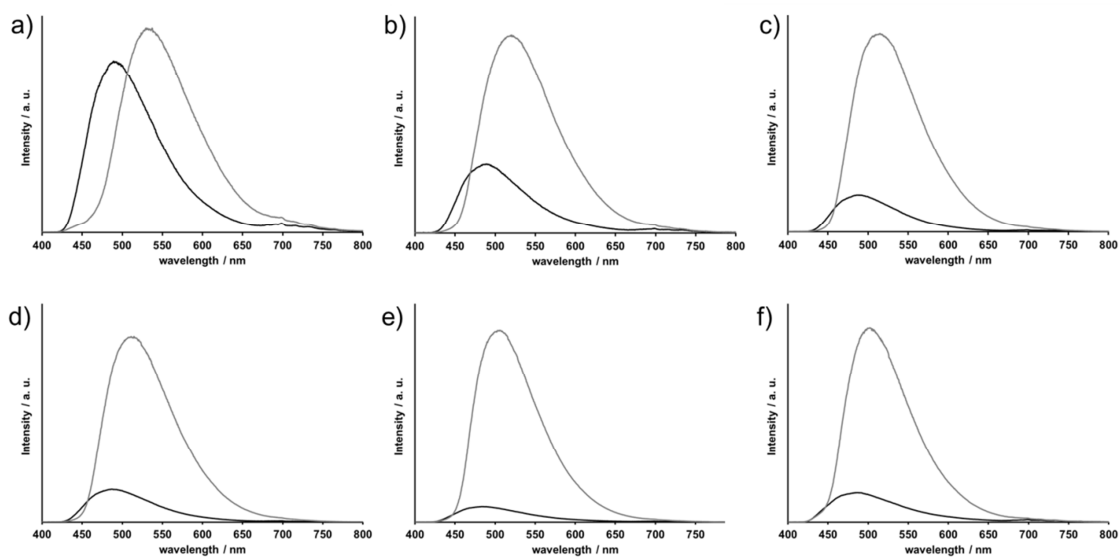
**Figure 12.** TG/DTA (left) and TG/MS (right) measurements in air of DUT-67(Hf) (a-b) and DUT-67(Hf)\_HCl (c-d) after being used for three times as catalyst for the MPV reduction of cyclohexanone at 120°C.



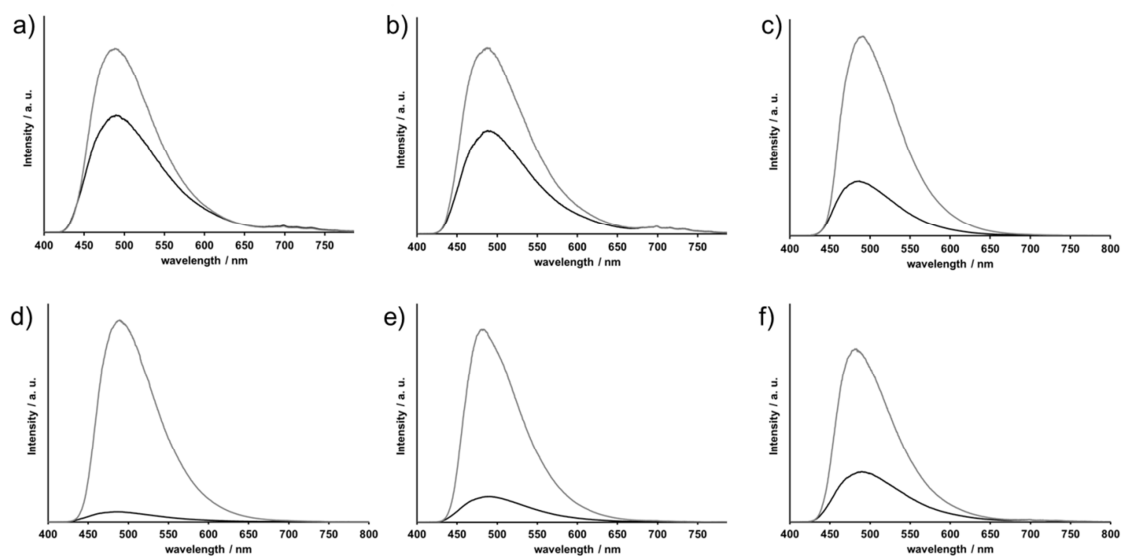
**Figure 13.** TG analysis (grey line) and DTA analysis (black line) in air of a) UiO-66, b) UiO-67 and c) DUT-51 activated at 120 °C.



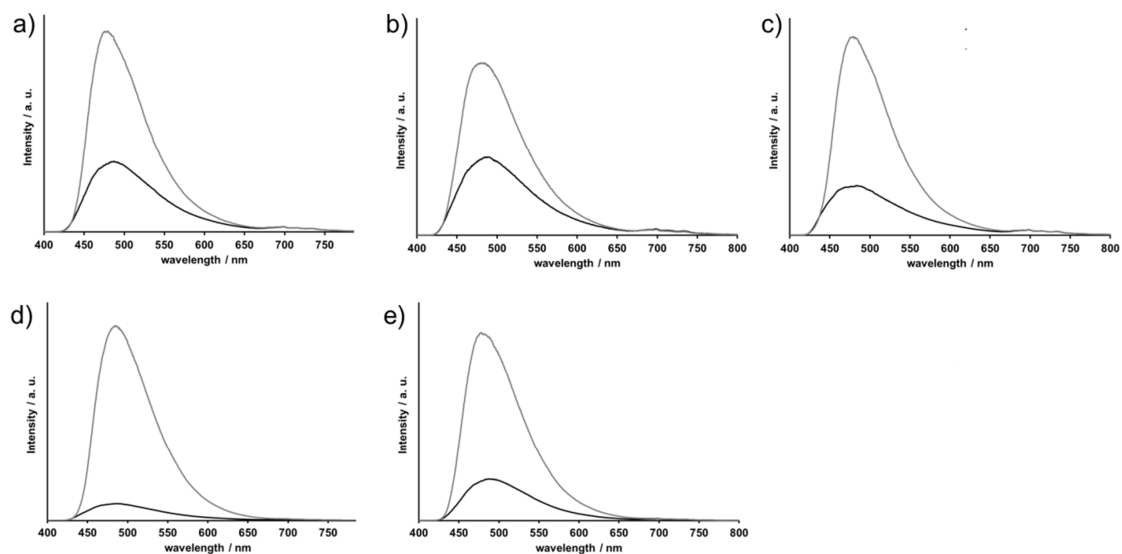
**FigureA 14.** Fitting plots for the pseudo zero order (left) and pseudo first order (right) kinetics of DUT-126 (black diamonds), DUT-51 (dark grey diamonds), UiO-67 (grey diamonds) and UiO-66 (light grey diamonds).



**FigureA 15.** Fluorescence spectra of DUT-122(Zr) in argon atmosphere (black lines) and in saturated solvent vapour atmosphere (grey lines) of a) water, b) methanol, c) ethanol, d) 1-propanol, e) 2-propanol and f) 2-butanol.



**FigureA 16.** Fluorescence spectra of DUT-122(Zr) in argon atmosphere (black lines) and in saturated solvent vapour atmosphere (grey lines) of a) n-heptane, b) cyclohexane, c) dichloromethane, d) acetonitrile, e) benzene and f) toluene.



**FigureA 17.** Fluorescence spectra of DUT-122(Zr) in argon atmosphere (black lines) and in saturated solvent vapour atmosphere (grey lines) of a) tetrahydrofuran, b) diethylether, c) 1,4-dioxane, d) acetone and e) acetylacetate.

## 10. ACKNOWLEDGEMENT

First of all, I want to give my expression of deep gratitude to Prof. Dr. Stefan Kaskel for the opportunity to work under his supervision in his research group and for the interesting topic.

I am also very thankful to Dr. Irena Senkovska, who her supervision, her encouraging support and for many constructive discussions.

I want to highly appreciate the preliminary work of Volodymyr Bon. I am very thankful for his single crystal measurements at Bessy and for the crystal structure solutions he provided and for his fruitful discussions and advise.

I want also acknowledge the contribution of Dr. Jürgen Getzschmann to the structure solution and Rietveld refinement of DUT-126.

Further, I want to gratefully acknowledge Dr. Martin Heise and Dr. Philipp Schlender for helping me with the execution of the thermo XRD measurements.

I want to thank Dr. Ilka Kunert for performing TG/DTA measurements.

I want to acknowledge Alla Synytska for performing contact angle measurements on DUT-67 materials.

Furthermore, I want to express my gratitude to Dr. Marcus Adam, who performed the quantum yield - and fluorescence decay measurements of DUT-122.

I am also thankful to Ulrike Koch and to Susanne Goldberg for performing SEM measurements of various DUT-67 and DUT-126 materials. Many thanks go to Ulrike Koch for being a friend and for the nice and supporting talks after lunch.

I would also like to acknowledge Kerstin Zechel and Heidrun Fröde for the technical assistance of physisorption measurements and thank for their cheerful minds.

Sincere thanks go to Claudia Schenk for helping me to handle the laboratory work as a student research assistant.

Many thanks go to Dr. Matthias Groh, who was always open for long lasting scientific but also political and ethical discussions, even at late hours.

Special thanks go to Prof. Dr. Marcus Rose for introducing me in the world of porous materials during my time as a student research assistant.

I would also like to thank Dr. Marco Drache for inspiring me to study chemistry.

Finally, I extend my gratitude to the other members of my family and to my friends for supporting me all the time and their faith in me.

---

**11. LIST OF PUBLICATIONS****1) Porous phosphorus-based element organic frameworks: A new platform for transition metal catalysts immobilization**

J. Fritsch, F. Drache, G. Nickerl, W. Böhlmann, and S. Kaskel, *Microporous and Mesoporous Materials* **2013**, *172*, 167-173.

**2) Postsynthetic Inner-Surface Functionalization of the Highly Stable Zirconium-Based Metal–Organic Framework DUT-67**

F. Drache, V. Bon, C. Marschelke, A. Synytska, and S. Kaskel, *Inorganic Chemistry* **2016**, *55*, 7206-7213.

**3) Vapochromic Luminescence of a Zirconium-Based Metal–Organic Framework for Sensing Applications**

F. Drache, V. Bon, I. Senkowska, M. Adam, A. Eychmüller, and S. Kaskel, *European Journal of Inorganic Chemistry*, **2016**, *27*, 1099-0682.

**4) The modulator driven polymorphism of Zr(IV) based MOFs**

F. Drache, V. Bon, I. Senkowska, J. Getzschmann, and S. Kaskel, *Phil. Trans. R. Soc. A* **2017**, *375* (2084).

**5) Metal–Organic Frameworks for Thin-Layer Chromatographic Applications**

C. Schenk, C. Kutzscher, F. Drache, S. Helten, I. Senkowska, and S. Kaskel, *ACS Applied Materials & Interfaces* **2017**, *9* (3), 2006-2009.

**6) The origin of the measured chemical shift of  $^{129}\text{Xe}$  in UiO-66 and UiO-67 revealed by DFT investigations**

K. Trepte, J. Schaber, S. Schwalbe, F. Drache, I. Senkowska, S. Kaskel, J. Kortus, E. Brunner and G. Seifert, *Physical Chemistry Chemical Physics*, **2017**, *19*, 10020-10027

**7) Chiral Functionalization of a Zirconium Metal–Organic Framework (DUT-67) as a Heterogeneous Catalyst in Asymmetric Michael Addition Reaction**

K. D. Nguyen, C. Kutzscher, F. Drache, I. Senkowska, and S. Kaskel, *Inorganic Chemistry* **2018**, *57* (3), 1483-1489.

## 12. VERSICHERUNG UND ERKLÄRUNG

Hiermit versichere ich, dass ich die vorliegende Arbeit ohne unzulässige Hilfe Dritter und ohne Benutzung anderer als der angegebenen Hilfsmittel angefertigt habe; die aus fremden Quellen direkt oder indirekt übernommenen Gedanken sind als solche kenntlich gemacht. Die Arbeit wurde bisher weder im Inland noch im Ausland in gleicher oder ähnlicher Form einer anderen Prüfungsbehörde vorgelegt.

Die vorliegende Arbeit wurde am Lehrstuhl für Anorganische Chemie I der Technischen Universität Dresden im Zeitraum von Februar 2013 bis September 2017 unter wissenschaftlicher Betreuung von Herrn Prof. Dr. Stefan Kaskel angefertigt.

Es haben bisher keine früheren erfolglosen Promotionsverfahren stattgefunden.

Hiermit erkenne ich die Promotionsordnung des Bereichs Mathematik und Naturwissenschaften der Technischen Universität Dresden vom 23. Februar 2011, zuletzt geändert durch die Beschlüsse des Bereichsrates vom 15.06.2011 und 18.06.2014 an.

Dresden den 16.02.2018

Franziska Drache